Controlling Nanomaterial Properties with the Angular Momentum of Light

Author

Paula Laborda Lalaguna

Submitted in fulfilment of the requirements for the Degree of Doctor of Philosophy

School of Chemistry

College of Science and Engineering

University of Glasgow

June 17, 2025

Abstract

The properties of nanomaterials can be tailored through structural and geometrical design, chemical functionalization, strain engineering and other techniques. However, many existing methods for property control are either irreversible or depend on complex physical set-ups, limiting their practicality and broader technological implementation. This thesis addresses that challenge by developing a non-contact, all-optical approach that leverages the orbital angular momentum carried by Laguerre-Gaussian beams.

The method is investigated for two different applications. In the first instance, the focus is given to orbital angular momentum transfer from Laguerre-Gaussian beams to two-dimensional (2D) materials. A theoretical framework for calculating optical forces and torques in dielectric media is presented and angular momentum beams are implemented into a numerical simulation software to predict their effects on the 2D materials. Building on this, a novel, non-contact experimental method is developed to induce wrinkling in two common examples of 2D materials, monolayer graphene and WS_2, using the optical torques of Laguerre-Gaussian beams. The out-of-plane deformations and property changes are characterized using various experimental techniques, including electrical conductance measurements, Raman spectroscopy, atomic force microscopy and photoluminescence. The method is reversible and spatially-selective and only limited by sample heterogeneity and monolayer-substrate interactions.

In the second instance, the application of optical angular momentum is extended to chiral sensing. The dynamic control of the optical activity of chiral shuriken metamaterials is demonstrated through numerical simulations and experimental dichroism measurements under varying beam focusing conditions. Together, this thesis highlights the potential of angular momentum beams as a versatile tool for controlling nanomaterial properties with high spatial precision.

Contents

List of abbreviations

AM	Angular momentum
AP	Azimuthal polarization
BS	Beam splitter
CCD	Charge-coupled device
CD	Circular dichroism
CMOS	Complementary metal-oxide semiconductor
CPL	Circularly polarized light
CVD	Chemical vapour deposition
DMD	Digital-mirror device
DPSS	Diode-pumped solid state
EIT	Electromagnetically-induced transparency
EM	Electromagnetic
FEM	Finite-element method
FWHM	Full width at half maximum
HD	Helical dichroism
HG	Hermite-Gaussian
KK	Kramers-Kronig
LH	Left-handed
LG	Laguerre-Gaussian
LP	Linear polarization
NA	Numerical aperture
NMR	Nuclear magnetic resonance

OAM	Orbital angular momentum
ORD	Optical rotatory dispersion
PDE	Partial differential equation
PEM	Photoelastic modulator
PIR	Plasmonic-induced reflectance
PL	Photoluminescence
RH	Right-handed
RMS	Root-mean-square
RP	Radial polarization
SAM	Spin angular momentum
TEM	Transverse-electromagnetic mode
TMDC	Transition metal dichalcogenide
1D	One-dimensional
2D	Two-dimensional
3D	Three-dimensional

Acknowledgments

First, I would like to give my sincere thanks to my supervisor Malcolm Kadodwala, for giving me the opportunity to undertake such an exciting and ambitious project under his supervision. The completion of this thesis would not have been possible without his constant support and guidance throughout these 4 years. I am also extremely grateful for giving me the opportunity to travel around the world to present my research in conferences in Finland, the United States and Japan. My profound thanks extend to Yoshito Tanaka and Shun Hashiyada, whom I had the absolute pleasure to work with at Hokkaido University and who supervised me during the two months spent there. Many thanks to them and the team for being so welcoming and for teaching me about science and Japanese culture. Arigato gozaimasu!

I would like to thank my second supervisor Donald MacLaren for his support and guidance during my PhD project and for being there to talk when needed. His expertise in material science and general advice have been invaluable for the development of this thesis.

Many thanks must go to the *OAM beam community* at Glasgow University and abroad. I would like to thank Kayn Forbes, whose expertise in the chirality aspects of OAM beams has been crucial for the completion of the last chapter of my thesis. I could not thank Kayn enough for all the time spent with us in Zoom meetings discussing science. I would like to thank Sonja Franke-Arnold, Amy McWilliam and Richard Aguiar Maduro, who were always kind enough to help me and answer any questions that I had regarding the experimental optics during my project. I am very thankful to Neel Mackinnon, Stephen Barnett and Jörg Götte. I enjoyed the meetings at Steve's

office learning about the theory and doing maths in the blackboard, and they were always super helpful every time some of the aspects of my thesis got too theoretical to handle.

I would like to give a special thanks to every member of the Kadodwala group that I shared my PhD with. Thanks to Rahul Kumar, Stephanie Wallace, Maryam Hajji, Victor Tabouillot, Shailendra Kumar, Victor Wong, Dominic Koyroytsaltis-McQuire, Martin Kartau, Douglas Murad and Magnus MacMillan for their help within and outside academia. They have been amazing colleagues to work with and I enjoyed sharing the office with them. I will remember all our entertaining conversations with great affection, such as the lectures from Shailu to make us experts in optics but also in the stock market. Special thanks must also go to all the students that I had the pleasure to work with during my PhD. Many thanks to Paul Souchu, that came all the way from France and helped me with the graphene conductance measurements for a solid amount of time of 6 months. Many thanks to Hikaru Yoneji, that came all the way from Osaka and whom I had the pleasure to work with for a month doing Raman spectroscopy of graphene. Thanks to the project students Jordan Andrew and Asma Sarguroh, who I had the pleasure to supervise during their masters. It was great fun to work together with them in the lab and they were always super curious to learn.

Now it is time to thank my Glasgow family, starting with my flatmates. A Simona Bianco, è stato veramente un piacere vivere con te e non potrei ringraziarti mai abbastanza. Abbiamo iniziato l'università e il dottorato insieme e insieme li abbiamo finiti. Sei stata un supporto fondamentale durante il mio dottorato e volevo ringraziarti per essere così. Thanks to Giulia Carfora for the nice concerts, Neapolitan food and long time spent together in Glasgow. Muchas gracias a Maider Uranga por compartir el final del doctorado conmigo. Eskerrik asko! Thanks to Giulia Pellegrino and Zeliha Ertekin for the entertaining lunch breaks and sport sessions. Me gustaría dar las gracias a mi amiga Jenny Cifuentes, a quien tuve el placer de conocer yendo en bici de casualidad. Gracias por todas nuestras aventuras juntas, lo hemos pasado muy bien durante estos años. Massive thanks go to Jessica and Lucía, mis divinas, it was super nice to eat

culurgiones and take so many mystical trips, including that to Boteco do Brasil. Many thanks go to my long time classmates Emmanuelle and Christos, it has been an absolute pleasure to share such a long time together at Glasgow Uni. The thanks extend to everybody in the maths department aka *the black box*, who are too many to be named individually. It has been great to share the PhD with them and in particular I am grateful for the cycling adventures with Francesco Pagliuca, Riccardo Giannini, Sara Villa, Carmen Alonso and Franco Rota that have been very enjoyable. Grazie mille a tutti i miei colleghi delle lezioni d'italiano, con cui ho passato praticamente tutto il dottorato. È stato molto divertente passare ogni mercoledì pomeriggio imparando l'italiano con voi.

Finally, I owe a huge thanks to my friends and family back home. Mis amigas de *El Principado*, del pueblo, David Mur y Almudena Almanzor. Me alegra saber que, a pesar de haber pasado tantos años fuera, nuestra amistad sigue siendo como si no me hubiera ido a ninguna parte. Me gustaría darles las gracias por su apoyo constante. Special thanks must go to my parents Alberto Laborda and Mercedes Lalaguna. Siempre han estado presentes para apoyarme, escucharme y mostrar interés y curiosidad en lo que he estado haciendo, a pesar de no entender gran cosa de lo que digo. Gracias a mis abuelos Antonio y Mercedes, cuyos valores, al igual que los de mis padres, me han convertido en quien soy hoy en día. Gracias a mi hermano Gonzalo y cuñada Elena, tías, tíos y demás familia. To my partner Isacco Nonino, non avrei potuto trovare una persona così bella con cui condividere il mio dottorato. Grazie mille per il tuo supporto, umore e positività nella vita.

I dedicate this thesis to my nephew Mateo, who still has so much time to discover and explore!

Author's declaration

I declare that, except where explicit reference is made to the contribution of others, that this dissertation is the result of my own work and has not been submitted for any other degree at the University of Glasgow or any other institution.

Printed name: PAULA LABORDA LALAGUNA

Signature:

Publications

The results presented in Chapters 3 and 4 are published in:

- **Lalaguna, P. L.**, Souchu, P., Mackinnon, N., Crimin, F., Kumar, R., Chaubey, S. K., Sarguroh, A., McWilliam, A., Ganin, A. Y., MacLaren, D. A., Franke-Arnold, S., Götte, J. G., Barnett, S. M., Gadegaard, N. and Kadodwala, M. "Spatial Control of 2D Nanomaterial Electronic Properties Using Chiral Light Beams". *ACS Nano* **18**, 31, 20401-20411 (2024).

Other publications published during my time in the PhD include:

- Tabouillot, V., Kumar, R., **Lalaguna, P. L.**, Hajji, M., Clarke, R., Karimullah, A. S., Thomson, A. R., Sutherland, A., Gadegaard, N., Hashiyada, S. and Kadodwala, M. "Near-Field Probing of Optical Superchirality with Plasmonic Circularly Polarized Luminescence for Enhanced Bio-Detection". *ACS Photonics* **9**, 11, 3617–3624 (2022).

- Sale, H., Ertekin, Z., **Lalaguna, P. L.**, Kadodwala, M. and Symes, M. D., "Evaluating the native oxide of titanium as an electrocatalyst for oxalic acid reduction". *Chemical Communications* **60**, 6003-6006 (2024).

- Chaubey, S. K., Kumar, R., **Lalaguna, P. L.**, Kartau, M., Bianco, S., Tabouillot, V., Thomson, A. R., Sutherland, A., Lyutakov, O., Gadegaard, N., Karimullah, A. S. and Kadodwala, M., "Ultrasensitive Raman Detection of Biomolecular Conformation at the Attomole Scale using Chiral Nanophotonics". *Small* **20**, 2404536 (2024).

- Giza, M., Kozikov, A., **Lalaguna, P. L.**, Hutchinson, J. D., Verma, V., Vella, B., Kumar, R., Hill, N., Sirbu, D., Arca, E., Healy, N., Milot, R. L., Kadodwala, M. and Docampo, P., "Illuminating the Devolution of Perovskite Passivation Layers". *Small* **5**, 2400234 (2024).

- Vella, B., Fsadni, M. H., Pope, T., Giza, M., Angus, F. J., Shmarov, I., **Lalaguna, P. L.**, Cariello, M., Wilson, C., Kadodwala, M., Penfold, T. J., Docampo, P. and Cooke, G., "Overcoming the mobility penalty introduced by dipole disorder in small-molecule HTM films". *Journal of Materials Chemistry A* **12**, 22844-22858 (2024).

Chapter 1

Introduction

1.1 General introduction

The fact that light carries linear momentum has been a familiar concept in astronomy over centuries and it provides an explanation for a wide range of observed phenomena, including comet tails or perturbations in the orbiting motion of Earth satellites.[1, 2] Perhaps a less familiar concept is that light can also carry angular momentum. While the angular momentum of light has been traditionally associated with the spin angular momentum of circularly-polarized light, dating back to the era of Poynting,[3] the orbital angular momentum exhibited by Laguerre-Gaussian beams is a more recent area of study. Although such beams were already recognized within general laser theory and paraxial optics as early as 1986,[4] it was not until 1992 that Allen *et al.* established that Laguerre-Gaussian beams possess a well-defined amount of orbital angular momentum.[5] Consequently, the field of orbital angular momentum of light began to flourish and, as it happens naturally in science, this breakthrough that was initially presented in a theoretical paper gave rise to practical applications and it expanded onto numerous research areas.

One of the early applications was found in optical manipulation and optical tweezers by Rubinsztein-Dunlop in 1995[6] with the observation that the orbital angular momentum of photons can be transferred to absorptive particles and induce rotational

motion. Nowadays, after slightly more than 30 years undertaking research worldwide, the scientific community has found a wide range of applications and the orbital angular momentum of light is involved in a vast number of different research fields, such as quantum computing,[7–9] optical communications,[10–12] optical activity and chiral detection,[13] imaging[14–16] and others.[17]

This thesis uses the orbital angular momentum of light to control the properties of nanomaterials. In the first instance, the thesis discovers and expands on new applications in the pre-existing research that has been performed in the optical manipulation of matter using the optical forces and torques associated with angular momentum. In the second instance, angular momentum is used for the dynamic modification of the chiral response of periodic nanomaterials. In this thesis, both traditional and new advancements in optics for the generation of angular momentum are combined in an interdisciplinary manner with state-of-the-art characterization and simulation techniques while providing a bridge between optics and material science.

1.2 Thesis overview

The thesis is composed of several chapters. **Chapter 2** introduces the reader to the background and theory of angular momentum of light and Laguerre-Gaussian beams which are relevant to understand the results of this thesis. Special attention is given to two of the applications of angular momentum where research is undertaken in this thesis, namely optical spanners and optical activity.

The rest of the thesis is divided into three result chapters. Each result chapter includes a background introduction and it contains the experimental and computational methods section that is relevant for that chapter.

Chapter 3 includes the theoretical framework where expressions for optical forces and torques are derived in dielectric media. Laguerre-Gaussian beams are implemented in a numerical simulation software and their properties are tested thoroughly in air and compared with theory. Once validated in air, the simulations are performed with the

two-dimensional (2D) materials used in the experiments of the next chapter. The derived expressions from the theory are used to predict angular momentum transfer in the 2D materials and visualize the expected optical forces acting upon them. Laser heating simulations are also performed to conclude that Laguerre-Gaussian beams generate smaller temperature rises compared to Gaussian beams.

Chapter 4 is the experimental verification of **Chapter 3**. This chapter develops a non-contact novel method to induce wrinkling in 2D materials; the method leverages the optical torques of Laguerre-Gaussian beams exploiting the fact that 2D materials undergo out-of-plane deformations with minimal forces. The experimental results are verified with a wide range of experimental techniques, such as conductance measurements, Raman spectroscopy, atomic force microscopy and photoluminescence spectroscopy, in two examples of commonly used 2D materials, monolayer graphene and monolayer WS_2. The results show that the pre-existing wrinkles that are formed intrinscially on the surface after fabrication are amplified with the OAM. This causes a reduction in the conductance of monolayer graphene and a reduction of the band gap in monolayer WS_2. The method is spatially-selective and reversible after a few hours, and it is limited by spatial heterogeneity and monolayer-substrate interactions.

In **Chapter 5**, the angular momentum of light is used for the dynamic control of optical activity in chiral shuriken-shaped metamaterials. The effect is studied by performing numerical simulations and experimental dichroism measurements of different combinations of angular momentum across the entire visible range. The effects are studied for both the weakly- and tightly-focused regimes. In the first instance, expressions for all the focused fields are derived and implemented into a numerical simulation software to account for longitudinal fields. The experimental dichroism in air is compared to the results of previous studies in water. The results using different combinations of angular momentum in this work show that the dichroism can be tuned by the additional OAM carried by circularly-polarized Laguerre-Gaussian beams. The effect is attributed to the superior field gradients and excitation of higher-order modes. The change in optical activity is dynamic, as it is immediately reversed by turning off

the optical components, but limited by the spatial match between the beam and the nanostructure.

Overall, this thesis develops a non-contact, all-optical strategy to tailor the properties of nanomaterials for two different applications, and it highlights the potential of angular momentum beams as a versatile tool for high spatial precision and dynamic property control.

Chapter 2

Background and theory

2.1 The wave equation

The wave equation describes the existence and propagation of electromagnetic (EM) waves and it is derived from Maxwell's equations. According to electrodynamics, Maxwell's equations in differential form are[18, 19]

$$\nabla \cdot \mathbf{E} = \frac{\rho}{\varepsilon_0} \quad \text{(Gauss's law)}, \tag{2.1}$$

$$\nabla \cdot \mathbf{B} = 0 \quad \text{(no name)}, \tag{2.2}$$

$$\nabla \times \mathbf{E} = -\frac{\partial \mathbf{B}}{\partial t} \quad \text{(Faraday's law)}, \tag{2.3}$$

$$\nabla \times \mathbf{B} = \mu_0 \left(\mathbf{J} + \varepsilon_0 \frac{\partial \mathbf{E}}{\partial t} \right) \quad \text{(Maxwell-Ampère's law)}, \tag{2.4}$$

where $\mathbf{E}$ is the electric field, $\mathbf{B}$ magnetic flux density and $\mathbf{J}$ current density (or charge flux density). ρ is the charge density, ε_0 the vacuum permittivity and μ_0 vacuum

permeability. Gauss's and Faraday's laws tell us that the presence of charges and a varying magnetic field produce an electric field, respectively. Equation 2.2 implies that the divergence of the magnetic field is 0 (or that there is no such a thing as magnetic charge). Maxwell-Ampère's law implies that current and a varying electric field induce a magnetic field.[18, 19]

In the case of electromagnetic waves in vacuum, there is no charge and current ($\rho = 0$ and $\mathbf{J} = 0$) so Maxwell's equations in free space become

$$\nabla \cdot \mathbf{E} = 0 \quad \text{(Gauss's law, free space)}, \tag{2.5}$$

$$\nabla \cdot \mathbf{B} = 0 \quad \text{(no name, free space)}, \tag{2.6}$$

$$\nabla \times \mathbf{E} = -\frac{\partial \mathbf{B}}{\partial t} \quad \text{(Faraday's law, free space)}, \tag{2.7}$$

$$\nabla \times \mathbf{B} = \mu_0 \varepsilon_0 \frac{\partial \mathbf{E}}{\partial t} = \frac{1}{c^2} \frac{\partial \mathbf{E}}{\partial t} \quad \text{(Maxwell-Ampère's law, free space)}. \tag{2.8}$$

Taking the curl of equation 2.7, it is obtained that

$$\nabla \times (\nabla \times \mathbf{E}) = -\frac{\partial (\nabla \times \mathbf{B})}{\partial t}. \tag{2.9}$$

We can then use the identity[20, 21]

$$\nabla \times (\nabla \times \mathbf{E}) = \nabla (\nabla \cdot \mathbf{E}) - \nabla^2 \mathbf{E}. \tag{2.10}$$

Since in vacuum $\nabla \cdot \mathbf{E} = 0$, equation 2.10 becomes $\nabla \times (\nabla \times \mathbf{E}) = -\nabla^2 \mathbf{E}$. By equating 2.9 and 2.10 and substituting $\nabla \times \mathbf{B}$ we obtain the wave equation[20, 21]

$$\left(\nabla^2 - \frac{1}{c^2}\frac{\partial^2}{\partial t^2}\right)\mathbf{E} = 0. \tag{2.11}$$

2.1.1 The Helmholtz equation

For monochromatic waves with angular frequency ω, we can separate time and space dependencies of the EM field to write $\mathbf{E}$ as a complex function $\mathbf{E}(\mathbf{r},\mathbf{t}) = \mathbf{E}(\mathbf{r})e^{-i\omega t}$, with the real part being the physically-meaningful electric field. Substituting this into the wave equation 2.11 we obtain a special case of the wave equation called the Helmholtz equation, given by[20, 21]

$$\left(\nabla^2 + k^2\right)\mathbf{E}(\mathbf{r}) = 0, \tag{2.12}$$

where $k = \omega/c$ is the magnitude of the wave vector (wavenumber) in vacuum. The Helmholtz equation has important implications in optics as it describes the existence and propagation of electromagnetic waves.

2.1.2 Paraxial light beams

The paraxial approximation is frequently used in wave optics and it uses the assumption that there is a small angle between an optical ray and the optical axis, in such a way that the beam deviates very slightly from the optical axis as it propagates. This is the case in many problems where the beam propagates mainly in the z direction, and it propagates only slightly in the transverse (x, y) plane.

In a paraxial beam, the wave vector of the beam is given mainly by its z component k_z, and the x and y components, k_x and k_y, respectively, are small. Thus, in the paraxial approximation it is possible to write[22]

$$k_z = k\sqrt{1 - \frac{k_x^2 + k_y^2}{k^2}} \approx k - \frac{k_x^2 + k_y^2}{2k}. \tag{2.13}$$

Equivalently, the main components of the electric field lie in the transverse plane (E_x, E_y) and longitudinal electric fields (E_z) are small. Examples of paraxial light beams include weakly-focused beams, as opposed to tightly-focused beams which are non-paraxial.

Solutions to the paraxial Helmholtz equation include transverse-electromagnetic modes (TEM). Among these, Gaussian beams correspond to the most fundamental mode (TEM_{00}) and this is the most commonly known case as these beams are found in conventional laser beams. The electric field of a paraxial Gaussian beam propagating in the z direction is given by[20]

$$E(\rho, z) = E_0 \frac{w_0}{w(z)} e^{-\frac{\rho^2}{w^2(z)}} e^{ikz + \frac{ik\rho^2}{2R(z)} - i\psi(z)}. \tag{2.14}$$

ρ is simply $\rho = \sqrt{x^2 + y^2}$. As it can be seen in Figure 2.1, expression 2.14 implies that the intensity is concentrated in the middle and it decays exponentially as the radius is increased.

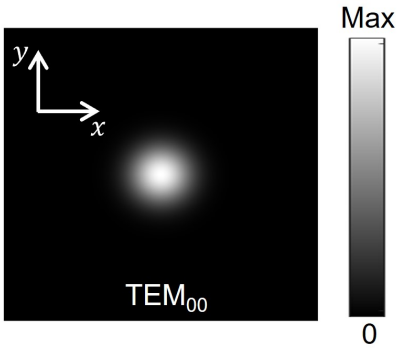

Figure 2.1: Intensity profile of a Gaussian beam (TEM_{00} mode) in the transverse plane.

The term $w(z)$, where

$$w(z) = w_0 \sqrt{1 + \frac{z^2}{z_R^2}} \tag{2.15}$$

corresponds to the beam width of the Gaussian beam, the distance along the transverse plane at which the electric field intensity falls to $1/e$ of its value on axis.[23, 24] w_0 is

defined as the beam waist, beam width of minimum radius at the focal point (the focal point occurs at $z = 0$). $R(z)$ is the wave front curvature

$$R(z) = z\left(1 + \frac{z_R^2}{z^2}\right), \tag{2.16}$$

where z_R is the Rayleigh range, $z_R = \pi w_0^2/\lambda$. The Rayleigh range is defined as the longitudinal distance from the waist plane at which w becomes $\sqrt{2}w_0$.[23, 25] It must be underlined that, for a Gaussian beam to be a solution of the paraxial Helmholtz equation, the beam waist w_0 must be much larger than the beam wavelength ($w_0 \gg \lambda$). This implies that the beam stays roughly collimated over the range $2z_R$[22] and that the beam angle

$$\theta = \frac{2}{kw_0} \tag{2.17}$$

is small. For a light beam that is focused with an objective lens, small θ implies that the numerical aperture of the objective lens, defined as

$$\mathrm{NA} = n \sin\theta, \tag{2.18}$$

is also small. A visual representation of a paraxial Gaussian beam and its main parameters is illustrated in Figure 2.2.

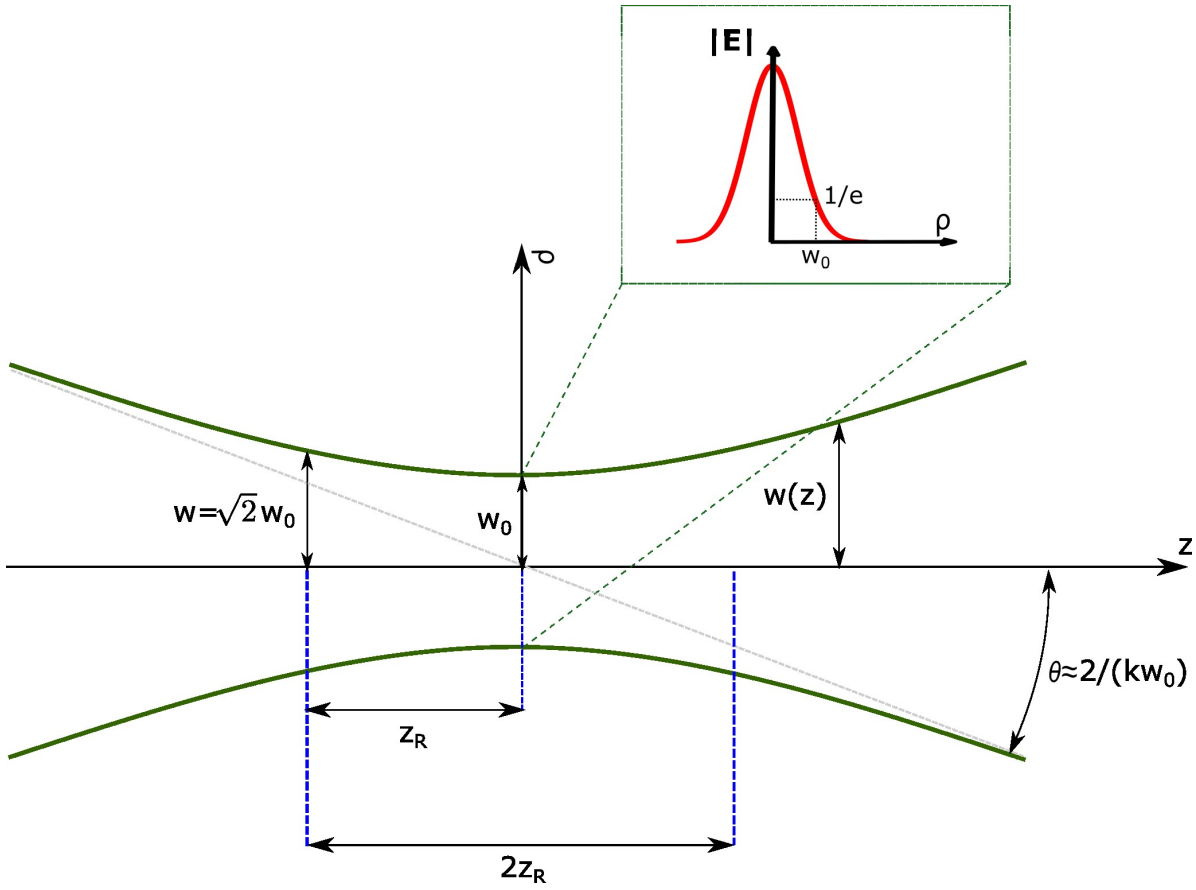

Figure 2.2: Gaussian beam propagating along the z axis, with the main parameters indicated. $w(z)$: beam width; w_0: beam waist ($w(z)$ at $z = 0$); z_R: Rayleigh range. In a paraxial Gaussian beam, the beam stays roughly collimated over the range $2z_R$, and θ is small.[22]

The term $\psi(z)$ in expression 2.14 corresponds to the Gouy phase and it expresses the change in the phase of the Gaussian beam relative to that of a uniform plane wave as it propagates in the longitudinal direction. It is given by[26]

$$\psi(z) = \arctan\left(\frac{z}{z_R}\right). \tag{2.19}$$

Thus, a Gaussian beam that travels from $-\infty$ to ∞ will experience a phase shift relative to a uniform plane wave from $-\pi/2$ to $\pi/2$ due to the Gouy phase.

Other solutions of the paraxial wave equation include higher-order TEM modes, *e.g.* Hermite-Gaussian (HG) modes. Some examples of HG modes are displayed in Figure 2.3. HG modes are rectangularly symmetric and are the combination of a Gaussian function with a Hermite polynomial. HG modes are designated as TEM_{mn}, where m is

the order in the x direction and n the order in the y direction.

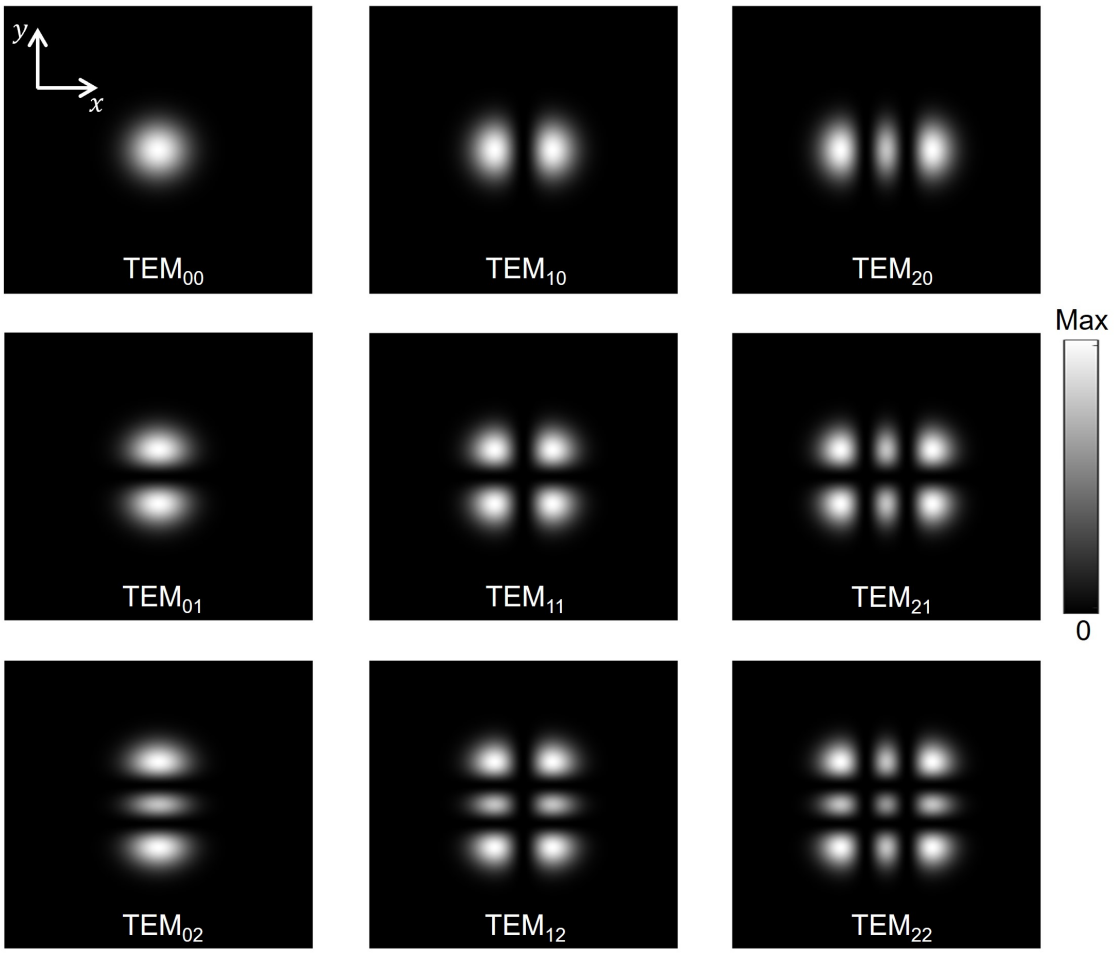

Figure 2.3: Intensity profile of Hermite-Gaussian (rectangular TEM$_{mn}$) modes in the transverse plane. The TEM$_{00}$ mode corresponds to the fundamental Gaussian mode. A MATLAB code was written to generate this figure and it can be found in Appendix A.

Another solution to the paraxial wave equation includes cylindrical TEM modes, such as Laguerre-Gaussian (LG) modes.[4] In 1992, Allen *et al.*[5] made the striking discovery that LG beams possess a well-defined amount of orbital angular momentum.

2.2 Angular momentum of light

Angular momentum of light can be of two types: spin angular momentum and orbital angular momentum, and the sum of the two contributions constitutes the total angular momentum.

To explain the angular momentum of an EM field, we can start by making use of the more familiar example of angular momentum in classical mechanics. According to classical mechanics, an object orbiting around a fixed point acquires an orbital angular momentum **L** defined by the vector product of the position vector **r** and linear momentum **p**, so it is possible to write

$$\mathbf{L} = \mathbf{r} \times \mathbf{p}. \tag{2.20}$$

The magnitude of the angular momentum acquired is given by $L = rp = rmv$, where m is the mass of the object and v the component of the velocity perpendicular to the vector **r**. If the direction of the orbital motion is reversed, the angular momentum vector **L** points in the opposite direction, as illustrated in Figure 2.4.

Figure 2.4: Objects of mass m at position r with linear momentum p rotating around a fixed point with angular velocity ω acquire an angular momentum L defined by $\mathbf{L} = \mathbf{r} \times \mathbf{p}$. The sense of rotation determines the direction of L according to the right-hand rule.

In classical electromagnetism, we can begin to explain the angular momentum of light using the analogy with classical mechanics, although now considering the total angular momentum density of an electromagnetic field, **j**. The total angular momentum density **j** is given by the vector product of the position vector **r** and linear momentum density **p** of an EM field, so it is possible to write[18, 21]

$$\mathbf{p} = \varepsilon_0(\mathbf{E} \times \mathbf{B}), \tag{2.21}$$

$$\mathbf{j} = \mathbf{r} \times \mathbf{p} = \varepsilon_0[\mathbf{r} \times (\mathbf{E} \times \mathbf{B})]. \tag{2.22}$$

Integration of equation 2.22 over volume V results in the total electromagnetic angular momentum in volume V, given by[27]

$$\mathbf{J} = \iiint_V \varepsilon_0[\mathbf{r} \times (\mathbf{E} \times \mathbf{B})]dV. \tag{2.23}$$

The total angular momentum can be separated into spin $\mathbf{S}$ and orbital $\mathbf{L}$ contributions[20]

$$\mathbf{J} = \mathbf{S} + \mathbf{L}. \tag{2.24}$$

2.2.1 Spin angular momentum

Spin angular momentum (SAM) in light beams arises due to helical polarization, such as that found in circularly-polarized light (CPL). To understand polarization, we can consider a monochromatic plane wave travelling in the z direction, so the electric and magnetic fields oscillate in the xy plane and are perpendicular to one another. The electric and magnetic field vectors are therefore given by[18]

$$\mathbf{E}(z,t) = \hat{\mathbf{x}} E_0 \cos(kz - \omega t), \tag{2.25}$$

$$\mathbf{B}(z,t) = \hat{\mathbf{y}} \frac{E_0}{c} \cos(kz - \omega t), \tag{2.26}$$

where k is the wave number $k = 2\pi/\lambda$, $\omega = 2\pi c/\lambda$ is the angular frequency and $\hat{\mathbf{x}}$ and $\hat{\mathbf{y}}$ unit vectors in the x and y directions, respectively. By convention, polarization is described using the orientation of the electric field, so the wave above is polarized in the x direction. As the electric field oscillates in only one plane, it is said to be linearly polarized.

If the electric field rotates in a circular fashion, it is said to be circularly polarized.

To describe CPL, it is useful to describe the electric field vector using two orthogonal vectors, $\mathbf{E_x}(z,t)$ and $\mathbf{E_y}(z,t)$.[18, 28]

$$\mathbf{E}(z,t) = \mathbf{E_x}(z,t) + \mathbf{E_y}(z,t) = \hat{\mathbf{x}}E_0\cos(kz-\omega t) + \hat{\mathbf{y}}E_0\cos(kz-\omega t+\psi), \tag{2.27}$$

where we have introduced the phase difference ψ between the two components. Different values of ψ give rise to different polarization states, as depicted in Figure 2.5. If no phase difference exists between the two components ($\psi = 0$), the wave is linearly polarized, although now the polarization plane is between the x and y axes (Figure 2.5). Suppose now that a phase shift of $\pi/2$ is introduced between the two orthogonal components. If $\psi = -\pi/2$, the y component is $\pi/2$ radians ahead of the x component and the total electric field rotates anticlockwise looking towards the source, therefore the beam is left circularly polarized. If $\psi = \pi/2$, the y component is retarded by $\pi/2$ with respect to the x component, thus the electric field rotates clockwise looking towards the source. Thus, the beam is right-circularly polarized.

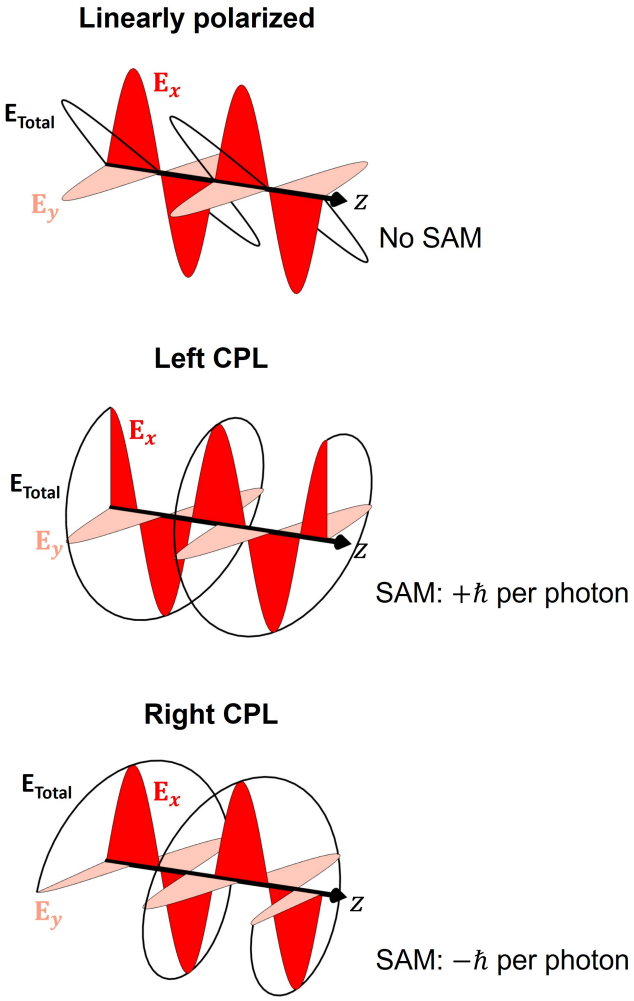

Figure 2.5: Spin angular momentum (SAM) of light beams.

Light beams which are circularly polarized carry spin angular momentum of $\pm\hbar$ per photon, with positive sign for left CPL and negative for right CPL (Figure 2.5).[29, 30] Linearly-polarized light carries no spin angular momentum.

In this thesis, light beams carrying SAM were generated either using quarter wave plates or photoelastic modulators, which are explained in detail in the experimental sections of Chapters 4 and 5, respectively.

2.2.2 Orbital angular momentum

Orbital angular momentum (OAM) is entirely independent on the polarization state under paraxial conditions. Instead, OAM arises due to helical phase fronts.[5, 31] To

help the visualization of helical phase fronts, it is useful to represent each point in the light beam in cylindrical coordinates, rather than cartesian coordinates. In cylindrical coordinates, each point is located at radial distance ρ from the origin, which forms an angle of ϕ with respect to the x axis (called azimuthal angle) and is at distance z along the propagation axis (the z axis), Figure 2.6a.

A light beam with a helical phase front is shown in Figure 2.6b. A surface cross cut is shown at a particular distance along the propagation axis z, and the light beam has been represented as individual wavelets. It can be seen that, going around the azimuthal angle, each wavelet has a different phase. If we trace a line along the points which have the same phase, for example the maxima of the wavelets, it can be seen that the line is a spiral curve, or a helix. This is represented by the dashed line with black crosses in Figure 2.6b.

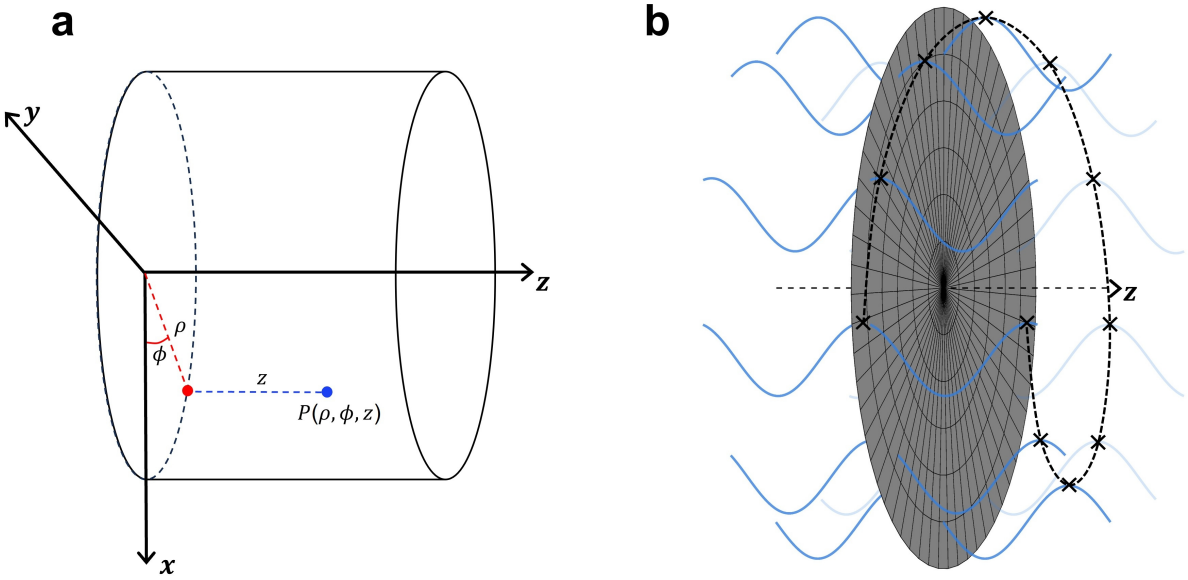

Figure 2.6: (a) Cylindrical coordinates showing a point P located at radial distance ρ, azimuthal angle ϕ and propagation distance z. (b) Light beam with a helical phase front represented as individual wavelets (shown in blue). A helical path following the wavelet maxima has been traced with a dashed black line.

Plane and spherical waves have phase fronts that travel in the same direction as the beam propagates. In other words, surfaces of the same phase are parallel to each other. The Poynting vector, $\mathbf{S} = \frac{1}{\mu_0}\mathbf{E} \times \mathbf{B}$, which describes the energy flux, is normal to the phase front surface and, in both cases it points in the same direction as the propagation axis.[28] In a beam with a helical phase front, however, the Poynting vector follows a

helical path as the phase front is helical.[5, 31–34]

OAM in a light beam is a direct consequence of having a helical phase front. Different light beams with helical phase fronts, and therefore that carry OAM, exist, such as Laguerre-Gaussian beams,[5] Bessel beams,[20, 35–37] Airy beams[38] and Zernike beams.[39] Among these, Laguerre-Gaussian beams are probably the most common type and they are the ones used in this thesis, so an emphasis will be given to introduce the reader to Laguerre-Gaussian beams.

2.2.3 Laguerre-Gaussian beams

Laguerre-Gaussian (LG) beams are generally expressed in cylindrical coordinates and the electric field for a monochromatic beam takes the form[23, 24]

$$E_{l,p}(\rho,\phi,z) = E_0 \frac{C_{l,p}}{\sqrt{w(z)}} e^{-\frac{\rho^2}{w^2(z)}} e^{il\phi} \left(\frac{\rho\sqrt{2}}{w(z)}\right)^{|l|} L_p^{|l|}\left(\frac{2\rho^2}{w^2(z)}\right) e^{ikz-\frac{ik\rho^2}{2R(z)}+i\psi_{l,p}(z)}, \quad (2.28)$$

where l is the topological charge and p the radial number. Close inspection of the expression 2.28 reveals the presence of all the terms that also appear in a Gaussian beam (*cf.* expression 2.14). These include the decrease in intensity as a function of the radius and the beam width, $e^{-\frac{\rho^2}{w^2(z)}}$, and the phase changes as the beam propagates in space due to the wave front curvature $R(z)$ and longitudinal distance kz. Additionally, expression 2.28 contains the terms specific to Laguerre-Gaussian beams. Among these, we can find a generalized Laguerre polynomial given by

$$L_p^{|l|}(x) = \frac{e^x}{p!} x^{-|l|} \frac{d^p}{dx^p}(e^{-x}x^{p+|l|}). \quad (2.29)$$

Special attention requires the dependence on the azimuthal angle, encapsulated in the term $\exp(il\phi)$, where l is an integer called the topological charge. As mentioned earlier, the phase dependency on the azimuthal angle ϕ causes the phase front to be helical and it gives rise to orbital angular momentum.[5] As shown in Figure 2.7, the

topological charge l determines the number of intertwined helices in the phase front, or the number of 2π cycles around the azimuth.[31] If we take a transverse plane of the LG beam as it propagates, the phase will be varying depending on the azimuth. If we get closer to the centre of the beam, each point around the azimuth will coincide with another point of opposite phase. It is then said that LG beams have a phase singularity on axis since the phase is not well-defined at the beam centre.[32, 40] As illustrated in Figure 2.7, this results in a doughnut-shaped intensity profile, where most of the intensity is concentrated in a ring, and the intensity on axis is zero.[40] This is called optical vortex, and therefore LG beams are also frequently called vortex beams in the literature.

As shown in expression 2.28, the electric field of the beam depends on the term $\left(\frac{\rho\sqrt{2}}{w(z)}\right)^{|l|}$, where the radial component depends also on the magnitude of the topological charge. This terms causes the size of the intensity ring to increase in size for larger values of l (Figure 2.7).

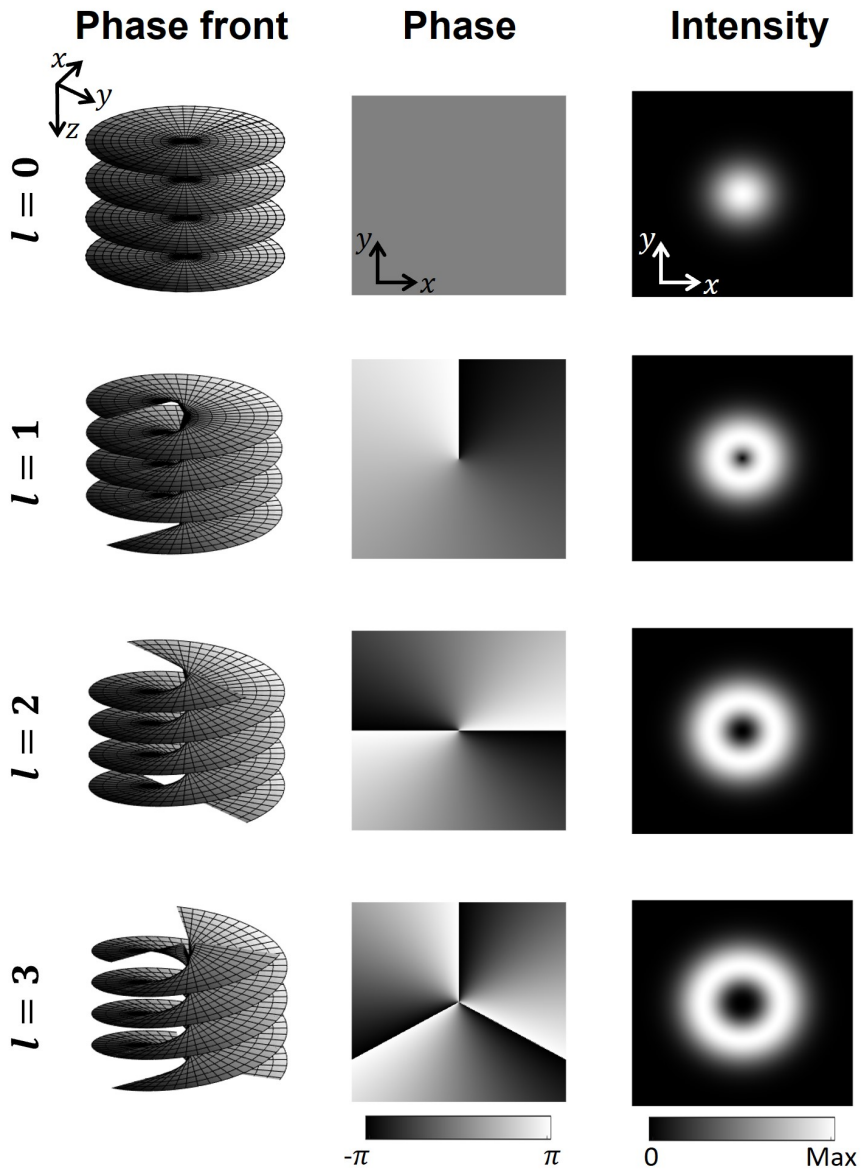

Figure 2.7: Phase front, phase and intensity of LG beams as a function of topological charge l. $l = 0$ results in a Gaussian beam with no phase dependency on the azimuth. $|l| \geq 1$ results in LG beams, whose phase varies around the azimuth cumulatively as $2\pi l$ and the intensity is an annular intensity profile. l determines the number of intertwined helices in the phase front. A MATLAB code was written to produce this figure and it can be found in Appendix A.

The expression for an LG beam includes a normalization constant

$$C_{l,p} = \sqrt{\frac{2p!}{\pi(p + |l|)!}}, \tag{2.30}$$

which is derived from the normalization condition

$$\iint |\mathbf{E}_{l,p}|^2 dxdy = 1. \tag{2.31}$$

Equation 2.31 ensures energy conservation and it implies that the surface integral of the intensity along the transverse plane is 1 for any LG beam.

As shown in equation 2.28, the complete LG mode description includes another integer, p, called radial number, where $p + 1$ denotes the number of concentric rings in the intensity profile.[23] Figure 2.8 shows the intensity of different LG beams for different values of l and p. For $p = 0$, only a ring is observed in the intensity profile. For $p = 1$ and $p = 2$, two and three rings are present, respectively. The radial index p does not affect the amount of OAM that the LG beam carries and LG beams of $p = 0$ are used throughout this thesis, so the radial number will not be discussed any further. Nevertheless, the curious reader can refer to reference [41] which discusses radial modes and the physical interpretation of these.

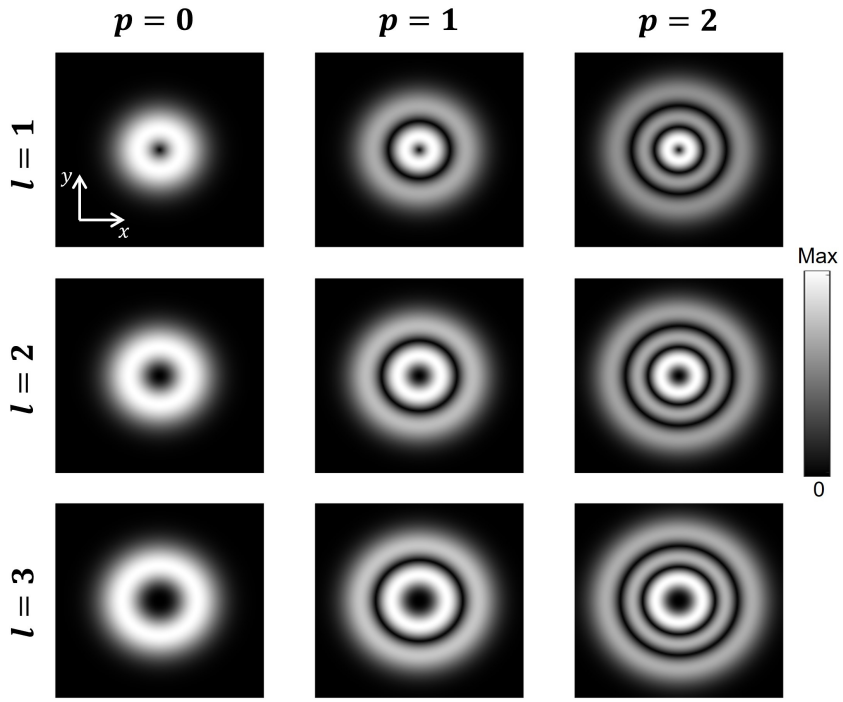

Figure 2.8: Intensity profile of LG beams for varying radial modes (columns) and topological charges (rows). Figure generated using the MATLAB code developed in Appendix A.

In comparison with conventional Gaussian beams, the Gouy phase of LG beams

now depends on l and p, and it is now defined as[4]

$$\psi_{l,p}(z) = (|l| + 2p + 1) \arctan\left(\frac{z}{z_R}\right). \tag{2.32}$$

As stated in the previous section, angular momentum in classical mechanics can be described using equation 2.20. As light is made of photons, orbital angular momentum of light can be described from a quantum-mechanical point of view. In quantum mechanics, observables are described by quantum operators that act on the wave function. Using the position representation, where $\hat{x} = x$, $\hat{y} = y$ and $\hat{z} = z$, the linear momentum operator is[42]

$$\hat{p} = -i\hbar\nabla, \tag{2.33}$$

therefore the orbital angular momentum operator can be written as the vector operator[42]

$$\hat{L} = -i\hbar\ \hat{r} \times \nabla. \tag{2.34}$$

It can be shown that, if the wave function $\psi(\mathbf{r})$ is an angular momentum eigenstate, the magnitude squared operator $\hat{L}^2 = \hat{L}_x^2 + \hat{L}_y^2 + \hat{L}_z^2$ and the z-component operator $\hat{L}_z$ have quantized eigenvalues[20]

$$\hat{L}^2\psi(\mathbf{r}) = L(L-1)\hbar^2\psi(\mathbf{r}), \text{ and} \tag{2.35}$$

$$\hat{L}_z\psi(\mathbf{r}) = m_l\hbar\psi(\mathbf{r}), \tag{2.36}$$

where L and m_l are quantum numers $L = 0,\ 1,\ 2,\ 3$ and $m_l = -L, ..., 0, ..., L$.[20]

Suppose now that we have a Laguerre-Gaussian beam, which has the azimuthally-

dependent term $e^{il\phi}$. From equation 2.34 it is derived that in spherical polar coordinates the $\hat{L_z}$ operator becomes[20]

$$\hat{L_z} = -i\hbar \frac{\partial}{\partial \phi}. \tag{2.37}$$

It follows that modes with the term $e^{il\phi}$ are eigenstates of the operator $\hat{L_z}$, so it is possible to write

$$\hat{L_z}(e^{il\phi}) = -i\hbar \frac{\partial}{\partial \phi}(e^{il\phi}) = -i\hbar \times ile^{il\phi} = -i^2 l\hbar e^{il\phi} = l\hbar e^{il\phi} = L_z e^{il\phi}, \tag{2.38}$$

with eigenvalues $L_z = l\hbar$. Therefore, the orbital angular momentum of an LG mode is $l\hbar$ per photon[5] and the amount of OAM that is carried by the beam increases linearly with l. This is in contrast with beams that only possess spin angular momentum, such as CPL, where the angular momentum amounts to $\pm\hbar$ per photon. Therefore, the angular momentum of LG beams can be tuned at will by varying the topological charge, offering thus a new degree of freedom which can be exploited, for example, in communications.[10] Gaussian beams do not have helical phase fronts, and therefore do not carry orbital angular momentum.

The sign of l determines the handedness of the phase fronts. An example is shown in Figure 2.9. Looking at the phase front towards the source, the phase fronts are rotating anticlockwise for an LG beam $l = 2$ and clockwise for $l = -2$. Similar to SAM, the sign of the topological charge also determines whether the OAM is positive or negative, with positive and negative values associated with left- and right-handed helical phase fronts, respectively (looking towards the beam).

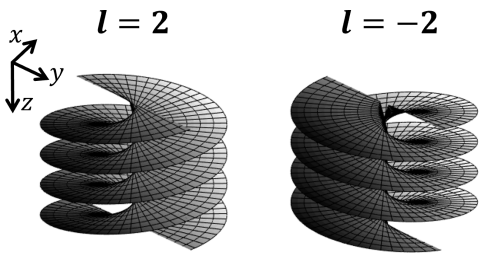

Figure 2.9: Phase front for LG beams $l = 2$ and $l = -2$, showing that the handedness of the phase front is reversed upon changing the sign of the topological charge. Positive and negative values of l are associated with left- and right-handed phase fronts (looking towards the beam). Figure generated using the MATLAB code developed in Appendix A.

As opposed to SAM, OAM is independent of polarization and LG beams can be generated using special optical components. These can be summarized as mode converters, spiral phase plates and diffractive optics. Mode converters involve astigmatic optical components, such as a combination of cylindrical lenses. These combine Hermite-Gaussian beams and modify the Gouy phase in either the x or y direction to yield LG beams. This was the method of choice in early studies regarding LG beams,[5, 43] and the principle is illustrated in Figure 2.10, where an LG_{pl} =LG_{01} beam is generated by combining HG_{01} and HG_{10} beams.

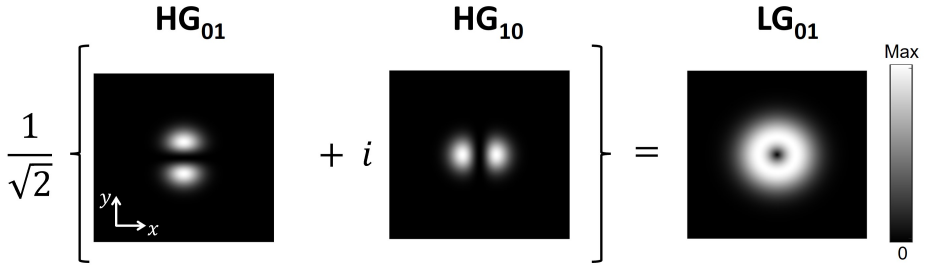

Figure 2.10: Conversion of HG_{01} and HG_{10} modes into LG_{01} using equation A.1. A MATLAB code was written to generate these modes and it can be found in Appendix A.

In this thesis, LG beams were generated either using spiral phase plates or Q-plates, which are explained in detail in the experimental sections of Chapters 4 and 5, respectively.

2.2.4 Spin-orbit conversion

In the case of paraxial light beams ($w_0 \gg \lambda$), the SAM and OAM are given by[44, 45]

$$\mathbf{S} \propto \sigma \frac{\langle \mathbf{k} \rangle}{k}, \tag{2.39}$$

$$\mathbf{L} \propto l \frac{\langle \mathbf{k} \rangle}{k}, \tag{2.40}$$

respectively. $\langle \mathbf{k} \rangle$ is the mean wave vector and k its magnitude. The total angular momentum is given by the sum of both contributions, $\mathbf{J} = \mathbf{S} + \mathbf{L}$.

In the case of non-paraxial light beams, such as tightly-focused beams with a high NA lens ($w_0 \approx \lambda$),[46] spin-orbit conversion takes place.[47] This implies that SAM and OAM are interconverted so equations 2.39 and 2.40 no longer apply. Instead, the SAM and OAM of focused beams are given by[44, 45]

$$\mathbf{S} \propto \sigma \cos\theta \frac{\langle \mathbf{k} \rangle}{k}, \tag{2.41}$$

$$\mathbf{L} \propto [l + \sigma(1 - \cos\theta)] \frac{\langle \mathbf{k} \rangle}{k}, \tag{2.42}$$

where θ is the aperture angle. From equations 2.41 and 2.42 it is clear that the conversion scales with increasing level of focusing. For the maximum aperture angle of $\theta = \pi/2$, it can be seen that a total conversion of 100% takes place. Another important point to notice is that, even though equations 2.41 and 2.42 indicate a redistribution of SAM and OAM, the total angular momentum is conserved and it is still given by $\mathbf{J} = \mathbf{S} + \mathbf{L}$.[45]

Studies in the literature have demonstrated that it is possible to obtain OAM from the SAM of tightly-focused circularly-polarized light.[48–52] SAM to OAM conversion

has been observed in the orbital motion of particles from tightly-focused circularly-polarized Gaussian beams, which had no OAM prior to focusing.[53–55] The reverse process where a tightly-focused vortex beam yields SAM through orbit-to-spin conversion has also been observed.[51]

2.3 Optical manipulation with angular momentum

2.3.1 Conservation laws

Physical quantities such as charge, energy, linear momentum and angular momentum are conserved and therefore they can be transferred from one object to another. For instance, momentum conservation occurs in our daily lives, such as in a game of pool or a cooked *spaghetto* that sticks to a wall.

In electromagnetism, the conservation of such quantities can be expressed *via* local continuity equations. Starting with one of the earliest examples, the continuity equation for charge can be derived from Maxwell's equations and it is expressed as[18]

$$\frac{\partial \rho}{\partial t} = -\nabla \cdot \mathbf{J}, \tag{2.43}$$

where ρ denotes charge density and $\mathbf{J}$ current density (or charge flux density). If we integrate both sides over a volume we obtain

$$\frac{\partial}{\partial t} \iiint_V \rho \, dV = - \iiint_V \nabla \cdot \mathbf{J} \, dV. \tag{2.44}$$

Applying the divergence theorem[19] to the right-hand side of equation 2.44 yields

$$\frac{\partial}{\partial t} \iiint_V \rho \, dV = - \oiint_S \mathbf{J} \cdot d\mathbf{S}. \tag{2.45}$$

Thus, equation 2.45 tells us that if the charge changes in a small volume V, then an

equal amount of charge must flow through the surface enclosing the volume, which implies that the charge is a conserved quantity.

Energy, linear momentum and angular momentum of electromagnetic waves are also conserved, and therefore can be expressed *via* similar continuity equations. The energy density stored in an EM field is given by[18]

$$u_{em} = \frac{1}{2}\left(\varepsilon_0 E^2 + \mu_0^{-1} B^2\right). \tag{2.46}$$

Conservation of the energy of an electromagnetic field is given by Poynting's theorem. In the absence of charge and current, there is no work done on the charges so the mechanical energy density u_{mech} is 0. Therefore, conservation of energy takes the form

$$\frac{\partial u_{em}}{\partial t} = -\nabla \cdot \mathbf{S}. \tag{2.47}$$

$\mathbf{S}$ is the Poynting vector and represents the energy flux density carried by the EM field. It is given by[18]

$$\mathbf{S} = \mu_0^{-1}(\mathbf{E} \times \mathbf{B}). \tag{2.48}$$

The linear momentum density of an EM field is closely related to the Poynting vector, as it is given by[18, 19]

$$\mathbf{g} = \frac{1}{c^2}\mathbf{S} = \frac{1}{c^2}(\mathbf{E} \times \mathbf{H}). \tag{2.49}$$

Both linear and angular momenta of an electromagnetic field are conserved, which can also be expressed by local continuity equations. Note that scalar quantities, such as charge and energy, are related to a vector in the conservation law. However, linear and angular momenta are vectors, and conservation of these is associated with a tensor. Conservation of linear momentum is given by[18]

$$\frac{\partial \mathbf{g}}{\partial t} + \mathbf{f} = -\nabla \cdot \overleftrightarrow{T}, \tag{2.50}$$

where $\mathbf{g}$ is the momentum density (expression 2.49) and $\mathbf{f}$ is the Lorentz force density[18, 19]

$$\mathbf{f} = \rho\mathbf{E} + (\mathbf{J} \times \mathbf{B}). \tag{2.51}$$

$\overleftrightarrow{T}$ is the momentum flux density (also called momentum flux tensor, or Maxwell stress tensor). This tensor is associated with a particular component $i = x, y, z$ in the direction $j = x, y, z$, so overall it contains 9 components. The momentum flux of the i-th component in the j-th direction is given by[27]

$$T_{ij} = -\varepsilon_0 E_i E_j - \mu_0^{-1} B_i B_j + \frac{1}{2}(\varepsilon_o E^2 + \mu_0^{-1} B^2)\delta_{ij}, \tag{2.52}$$

where δ_{ij} is the Kronecker delta function[56]

$$\delta_{ij} = \begin{cases} +1 & \text{if } i = j, \\ 0 & \text{if } i \neq j. \end{cases} \qquad i, j = 1, 2, 3. \tag{2.53}$$

In the case where the momentum density does not depend on time (*e.g.* when a continuous-wave laser is used), the term $\partial\mathbf{g}/\partial t$ vanishes so we are left with an expression where the force density is directly related to the momentum flux density

$$\mathbf{f} = -\nabla \cdot \overleftrightarrow{T}. \tag{2.54}$$

By integrating the force density over a volume and applying the divergence theorem to the right-hand side of expression 2.54 it follows that the force equals the flow of momentum through a surface and it is possible to write[19]

$$\mathbf{F} = \iiint_V \mathbf{f}\, dV = -\oiint_S \overleftrightarrow{T}\, dS. \tag{2.55}$$

As the angular momentum density $\mathbf{j}$ is given by the vector product between the position vector $\mathbf{r}$ and linear momentum density $\mathbf{p}$, from the conservation of linear momentum in expression 2.50 it is obtained that[27]

$$\frac{\partial \mathbf{j}}{\partial t} + \boldsymbol{\tau} = -\nabla \cdot \overleftrightarrow{M}, \tag{2.56}$$

where $\mathbf{j}$ is the angular momentum density, $\boldsymbol{\tau}$ is the torque density ($\boldsymbol{\tau} = \mathbf{r} \times \mathbf{f}$) and $\overleftrightarrow{M}$ the angular momentum flux density or angular momentum flux tensor. The angular momentum flux tensor denotes the angular momentum of the i-th component in the l-th direction and it is given by[27]

$$M_{li} = \varepsilon_{ijk} x_j \left[\frac{1}{2} \delta_{kl} (\varepsilon_0 E^2 + \mu_0^{-1} B^2) - \varepsilon_0 E_k E_l - \mu_0^{-1} B_k B_l \right], \tag{2.57}$$

where ε_{ijk} is the permutation symbol[56]

$$\varepsilon_{ijk} = \begin{cases} +1, & \text{if } ijk = 123,\ 231,\ 312, \\ -1, & \text{if } ijk = 321,\ 132,\ 213, \\ 0, & \text{otherwise.} \end{cases} \tag{2.58}$$

Similar to the linear momentum case, $\partial \mathbf{j}/\partial t = 0$ for a continuous-wave laser so conservation of angular momentum is now given by

$$\boldsymbol{\tau} = -\nabla \cdot \overleftrightarrow{M}, \tag{2.59}$$

and the torque is

$$\mathbf{T} = \iiint_V \boldsymbol{\tau}\, dV = -\oiint_S \overleftrightarrow{M}\, dS. \tag{2.60}$$

2.3.2 Optical spanners

As explained in § 2.3.1, linear and angular momenta are conserved quantities and therefore they can be transferred from a light beam to an object to exert a force or a torque, respectively.

Momentum transfer from a light beam to matter has been traditionally well-known in the case of linear momentum. Conservation of linear momentum is important as it is the underlying principle of optical tweezers, also known as optical trapping. Optical tweezers was firstly developed by Arthur Ashkin, for which he was awarded the Nobel Prize in 2018. The basis of optical trapping is based on the fact that light beams posses linear momentum and, since linear momentum is a conserved quantity, it can be transferred from the beam to an object to exert a force.

In 1970, Ashkin studied the effects of momentum transfer to micron-sized particles, when he realized that there were two types of forces acting on the particles.[57] The first one is due to the radiation pressure force, previously discovered by Maxwell,[58] and it makes the particle move in the propagation direction of the light. As this force originates from scattering and absorption, this force is also called scattering force. The scattering force is proportional to the beam intensity and therefore it scales with laser power.[6] Additionally, Ashkin was able to see that the particles were also drawn to the region of highest intensity due to the intensity gradient when the beam was tightly focused to a small spot. Thus, a new force was discovered and it was named the gradient force, as it goes in the direction of the intensity gradient.[59]

A few years later, Ashkin employed a high NA objective and established that, by tuning the refractive indices of the particle and surrounding medium, the gradient force dominated over the scattering force, effectively trapping the particle due to the high intensity gradient of the tightly-focused beam.[60] This marked the foundations of

optical trapping, which nowadays is used in a wide range of experiments.[61–63]

The principle of optical trapping is illustrated in Figure 2.11. Here, conservation of linear momentum tells us that the particle depicted experiences a force that pushes the particle towards the intensity gradient after tightly-focusing the light by using, for example, a high NA objective.[60]

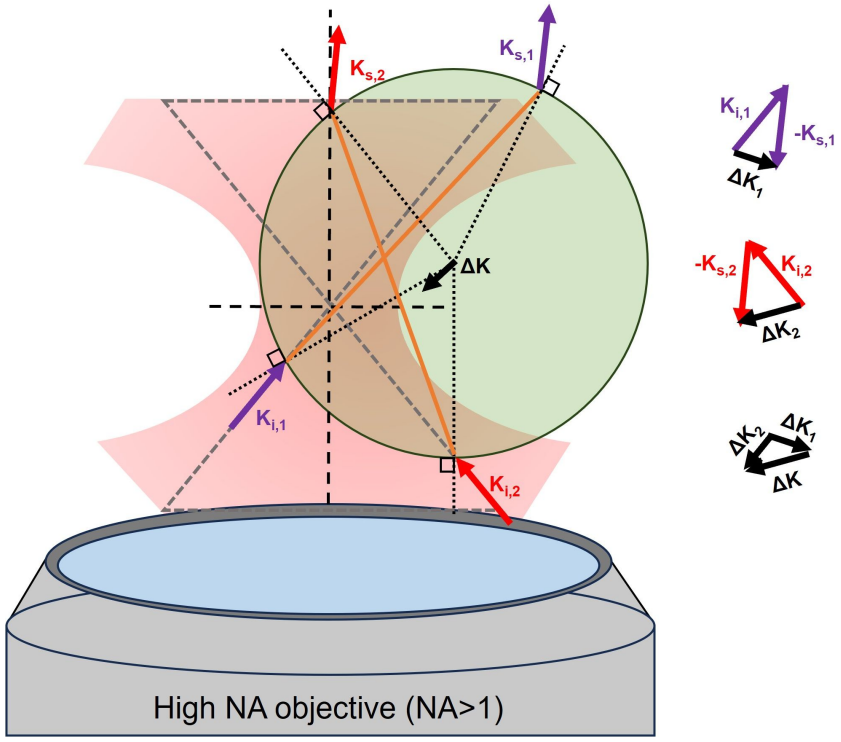

Figure 2.11: Principle of optical trapping. Conservation of linear momentum leads to a force that pushes the particle towards the maximum intensity at the focus. Reproduced from [64].

Recent advances in optical trapping include the use of tightly-focused beams to induce the formation of ionic-liquid droplets that are able to trap dyes[65] and optical trapping combined with plasmonic platforms to trap particles as small as nanoparticles (beyond the diffraction limit).[66]

Similar to the case of linear momentum transfer, which is used to exert a force, it was later discovered that angular momentum transfer can exert a torque. The torque results in the rotation of particles, and therefore this effect was called optical spanners.

The research focusing on angular momentum transfer was pioneered by Poynting[3] and experimentally demonstrated by Beth, who discovered that circularly-polarized light

can transfer spin angular momentum upon a wave plate due to birefringence.[29] The change in the SAM of the beam was used to exert a torque on the quarter wave plate, and the SAM was experimentally measured to be $\hbar$ per photon.[29]

Since the discovery that not only light beams can carry OAM, but the amount of OAM transferred can be tuned up to an infinite number of topological charge,[5] vortex beams have become a topic of particular interest. In early experiments, OAM was transferred to absorptive particles which were subsequently trapped on the beam axis and set into a spinning motion.[6] This optical spanner mechanism, where a torque is induced on the particle due to angular momentum transfer, is analogous to the linear momentum transfer of the beam that can be used to exert a force. For an LG beam which is linearly polarized (no SAM), the torque is given by the total angular momentum per second amounting to[6]

$$\Gamma_z = \frac{P}{\omega} l, \tag{2.61}$$

where P is the excitation power, l topological charge and ω angular frequency. Equation 2.61 suggests that the torque may be increased by either increasing the power or the topological charge l, and the torque applied would reverse in orientation by changing the sign of l. This has been verified in experiments with the rotation of micro particles embedded in vortex beams.[6, 67]

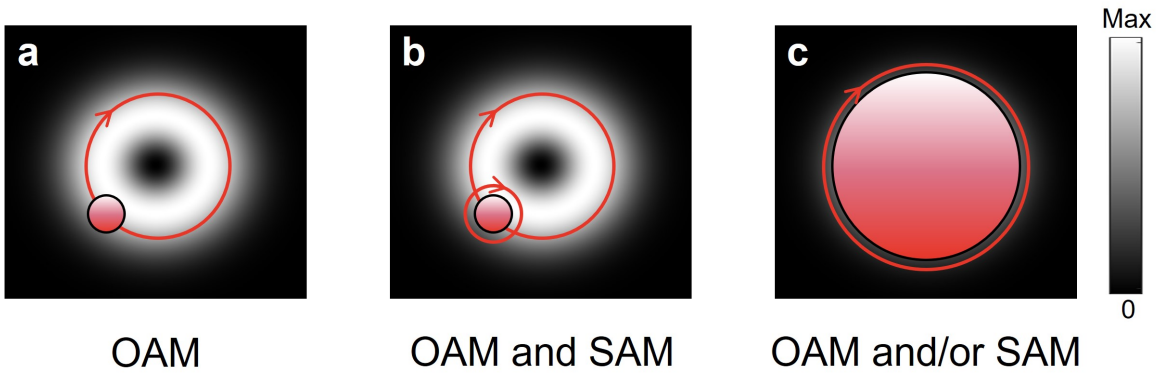

Figure 2.12: Schematic of the types of motion induced by angular momentum transfer. (a,b) A small particle is set into (a) orbital motion due to the azimuthal momentum density carried by OAM beams and (b) same orbital motion as (a) with the additional spinning motion due to SAM. (c) A large particle is set into spinning motion due to OAM, SAM or both. If the particle is transparent and birefringent, only SAM causes the spinning motion.

It is worth mentioning that the interaction of SAM and OAM with matter can yield different or the same results, depending on a variety of factors. This is schematically shown in Figure 2.12. If the beam is larger than the particle, the particle can be trapped off axis with OAM inducing orbital motion (rotation around the beam axis)[67, 68] and SAM inducing spinning motion (rotation around the particle's axis).[69, 70] If the beam carries both OAM and SAM, the particle can spin and orbit at the same time.[71] This makes SAM and OAM physically distinct. In this case, it has been reported that the orbital motion originates from the azimuthally-dependent linear momentum density arising from the helical phase fronts in accordance with the Poynting picture.[34, 72, 73] The azimuthal component of linear momentum density per photon is given by[71]

$$p_\phi = \frac{l\hbar}{\rho} - \frac{\sigma\hbar}{2|u|^2}\frac{\partial|u|^2}{\partial\rho}, \tag{2.62}$$

and it has been observed experimentally using a wavefront sensor.[72] As it is clear from 2.62, the azimuthal momentum (and azimuthal force) will increase with the topological charge.

In the case where the focused beam is smaller than the particle, the effects of SAM and OAM become indistinguishable, and transfer of angular momentum, whether it is

spin, orbital or both, causes the particle to spin, as shown in Figure 2.12c. Following this path, it has been observed that SAM and OAM cause spinning motion of birefringent[74] and absorbing[6] particles, respectively. Furthermore, if the particle is absorbing, both SAM and OAM are transferred to the particle and the particle spins faster or slower depending on whether SAM and OAM add or subtract.[75, 76] Hence, in the presence of OAM and SAM, now the torque given by the total angular momentum per second is

$$\Gamma_z = \frac{P}{\omega}(l + \sigma), \tag{2.63}$$

which also includes the spin polarization contribution σ.[75]

In the case of transparent birefringent particles (*i.e.* where angular momentum transfer is not based on absorption, only on birefringence), only the SAM (but not the OAM) can change, therefore only SAM can make the particle spin.[74]

2.3.3 Recent advances

Since the discovery that optical angular momentum can rotate particles, the optical spanners research began to flourish and expand into different research areas. Recent advances where angular momentum transfer has been used in the optical manipulation of matter include the formation of helical nanoneedles using beams which carry OAM.[77–79] As in the example shown in Figure 2.13, a helical nanoneedle results from mass transport of molten material by the beam, and the handedness of the nanoneedle is determined by the sign of the beam's topological charge. Other examples in material fabrication include the generation of circular nanowires using circularly-polarized light[80] or other 3D chiral structures using vortex beams.[81]

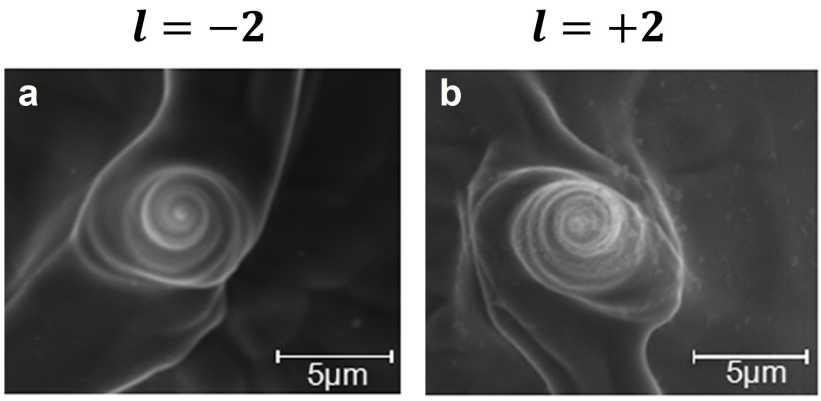

Figure 2.13: SEM image of chiral nanoneedles produced by transport of molten material by an LG beam. The handedness of the nanoneedle is controlled by the handedness of the helical phase front. (a) $l = -2$ and (b) $l = 2$. Figure taken from reference [77].

2.4 Optical activity

Light beams that have spin or/and orbital angular momentum are chiral, due to the polarization or the phase front of the light being helical in nature. Therefore, they can be used to probe the chirality of chiral media.

Chirality is a property of matter that exists in objects that cannot be superimposed onto its mirror image.[82] Chirality can be present in molecules, and molecules that exist as mirror images are called enantiomers. Frequently, but not always, this occurs when a carbon atom has 4 different constituents, as in the example shown in Figure 2.14.

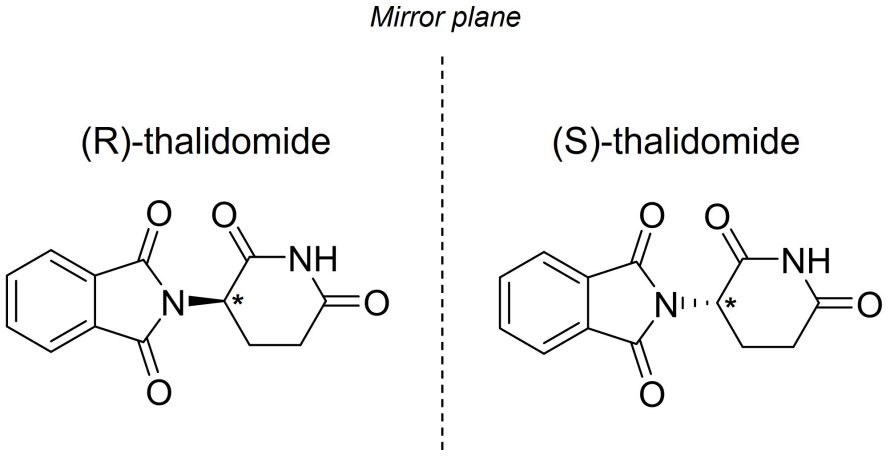

Figure 2.14: Enantiomers of thalidomide, with the chiral centre marked with an asterisk.

Gaining information about the chirality of a system is of crucial importance in many fields including the pharmaceutical industry. Enantiomers interact differently in the body, as many receptors in the body are chiral themselves. A common example to illustrate how important chirality may be is the drug thalidomide. Thalidomide can exist as two enantiomers, (R) and (S)-thalidomide (Figure 2.14). Decades ago, (R)-thalidomide was administered to pregnant women to treat morning sickness; however, under physiological conditions, (R)-thalidomide undergoes conversion to (S)-thalidomide *via* an enol intermediate, which later on was discovered to have caused malformations in new-born babies.[83] Therefore, it is important to ensure that the desired enantiomer is synthesized at high yields and it is equally important to be able to determine what enantiomer is present after the synthesis.

It is not that straight forward to distinguish enantiomers, as they have the same physical properties, such as boiling point, mass, or even same NMR spectrum. However, chiral molecules display optical activity which can be probed using chiroptical techniques. Optical activity was first discovered around 1811, when it was observed that chiral samples rotate linearly-polarized light in opposite directions.[84] This is known as optical rotation. Following this, it was discovered that the optical rotation is different for different wavelengths, an effect that nowadays is known as optical-rotatory dispersion.[85] This formed the foundations of chiroptical techniques.

Nowadays, it is understood that this optical activity phenomenon originates from the coupling of an electric dipole (E1) with either a magnetic dipole (M1) or an electric quadrupole (E2), giving rise to either E1M1 interactions or E1E2 interactions, the latter more commonly found in anisotropic or ordered media.[86, 87] Since E1 transition moments are odd under spatial inversion, but M1 and E2 are even, the E1M1 and E1E2 interactions are odd, which means both interactions will be different for left- and right-handed enantiomers and therefore can distinguish chiral molecules.[88, 89]

Regarding the angular momentum of light, chiral light-matter interactions have been traditionally studied with the spin component of the angular momentum, present in circularly-polarized light, as explained in more detail in § 2.2. The interaction of

circularly-polarized light with chiral media gives rise to conventional techniques such as circular dichroism. The discovery that light can also possess orbital angular momentum,[5] and that this can interact with chiral media,[90] has opened new pathways in the field of optical activity and techniques such as helical dichroism (also called vortex dichroism in some studies) have begun to flourish. In the following sections, conventional chiroptical techniques (that is, optical-rotatory dispersion and circular dichroism) and more recent techniques that use orbital angular momentum (helical dichroism) are described.

2.4.1 Optical-rotatory dispersion

Optical-rotatory dispersion (ORD) is a chiroptical technique that can be used to probe chiral media. ORD is based on the rotation of linearly-polarized light across a range of wavelengths. As explained in § 2.2, the electric field of linearly-polarized light can be regarded as a coherent superposition of LCP and RCP components. The idea is that when linearly-polarized light propagates through an optically-active medium, the LCP and RCP components travel at different speeds, hence they are rotated by different amounts, giving rise to an overall rotation of the electric field vector by an angle[82]

$$\alpha = \frac{1}{2}(\theta_R + \theta_L), \tag{2.64}$$

where θ_R and θ_L is the angle of rotation (in radians) of the RCP and LCP components, respectively, and α the rotation (in radians) of the electric field vector in linearly-polarized light. A schematic of the principle of ORD is shown in Figure 2.15.

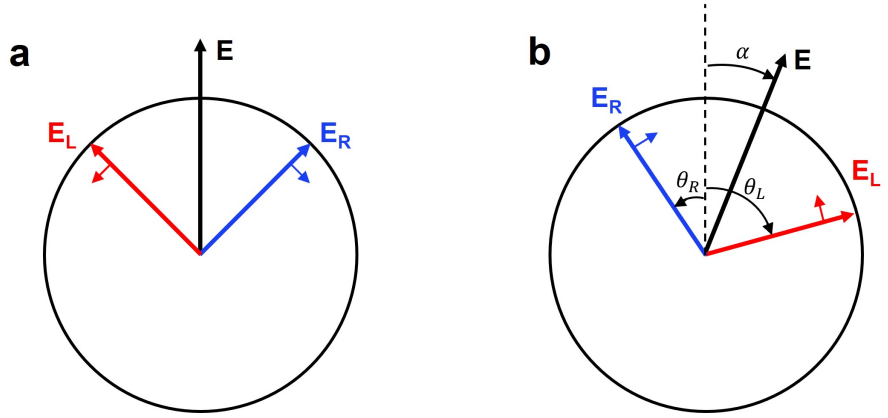

Figure 2.15: Principle of optical rotatory-dispersion. (a) The electric field of linearly-polarized light decomposed into LCP (E_L) and RCP (E_R) components. (b) Rotation experienced by the electric field vector in chiral medium.

The rotation angle α can also be expressed as the difference in refractive indices of the LCP and RCP components

$$\alpha = \frac{\pi}{\lambda}(n_R - n_L), \tag{2.65}$$

with α now having the units of radians per unit length. The difference in refractive indices of LCP and RCP components, $n_R - n_L$, is called circular birefringence.[82]

2.4.2 Circular dichroism

Circular dichroism (CD) is based on the differential absorption of LCP and RCP light by a chiral medium. If again we think of linearly-polarized light as a coherent superposition of LCP and RCP, and one of the components is absorbed more than the other, the light becomes elliptically polarized, as shown schematically in Figure 2.16.

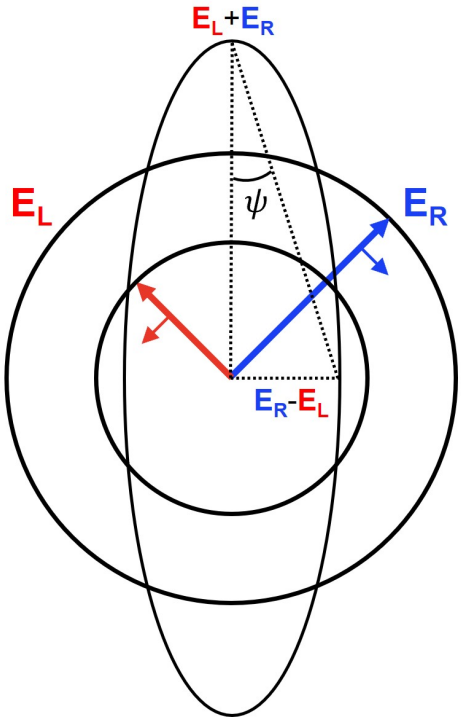

Figure 2.16: Principle of circular dichroism.

The degree of ellipticity is expressed by taking the ratio of the minor and major axes of the ellipse, which correspond to the difference and the sum of LCP and RCP components, respectively. It is therefore given by[82]

$$\psi = \tan\left(\frac{E_R - E_L}{E_R + E_L}\right). \tag{2.66}$$

In radians per unit length, the ellipticity is typically written as

$$\psi = \frac{\pi}{\lambda}(k_R - k_L), \tag{2.67}$$

where $k_R - k_L$ is the difference in imaginary refractive indices, that is, absorption, of RCP and LCP, which gives rise to circular dichroism.

As CD depends on the imaginary part of the refractive index, as opposed to ORD which depends on the real part of the refractive index, the CD and ORD spectra can be derived from each other using some mathematical relations called Kramers-Kronig (KK) relations[91–93]

$$\alpha(\omega) = \frac{2}{\pi} PV \int_0^\infty \frac{\omega' \psi(\omega')}{\omega'^2 - \omega^2} d\omega', \tag{2.68}$$

$$\psi(\omega) = -\frac{2\omega}{\pi} PV \int_0^\infty \frac{\alpha(\omega')}{\omega'^2 - \omega^2} d\omega', \tag{2.69}$$

where ω' is the excitation angular frequency and PV is the Cauchy principal value of the integral.[91–93] KK relations can be useful, as they can be used to derive the CD spectra from the ORD spectra and viceversa.[94]

2.4.3 Helical dichroism

Since the discovery that light beams can also have orbital angular momentum,[5] researches began to ponder whether OAM can be used to discriminate chiral systems in the way SAM does. In early theoretical studies, it was concluded that OAM cannot engage with chiral media under the dipole approximation, that is, *via* E1M1 interactions, and that only the spin part was responsible for the chiral response.[95] Some experimental studies followed afterwards, reporting no interaction between OAM and chiral media.[96, 97]

It was later on found that the reason why no interaction between OAM and chiral media was initially found is because the focus had been on the E1M1 interaction and the dipole approximation,[95, 98] and the early studies overlooked the possibility that OAM can actually engage with electric quadrupoles (E2).[99] Thus, an experimental study conducted by Brullot *et al.*[90] reported the first helical dichroism (HD) spectrum ever measured in which OAM, *via* quadrupolar E2 excitation, enabled to distinguish between small quantities of chiral enantiomers. In an analogous manner to CD, helical dichroism is the difference in absorption between beams with left- (positive topological charge) and right-handed (negative topological charge) helical phase fronts, so it is possible to write

$$\mathrm{HD} = 2\frac{I_{l^+} - I_{l^-}}{I_{l^+} + I_{l^-}}, \tag{2.70}$$

where l^+ denotes positive topological charge and l^- negative topological charge.[90] As the topological charge can be any integer, as opposed to SAM which is restricted to the helicity values of $\sigma = 1$ and $\sigma = -1$, the difference for many different topological charges is frequently reported, as shown in Figure 2.17. Note that in HD, it is implicit that only OAM is present in the beam to rule out the effects of SAM, so HD is collected with linearly-polarized light. In the case that both SAM and OAM are present in the beam, the dichroism is frequently called "circular helical dichroism" or "circular vortex dichroism".[100, 101]

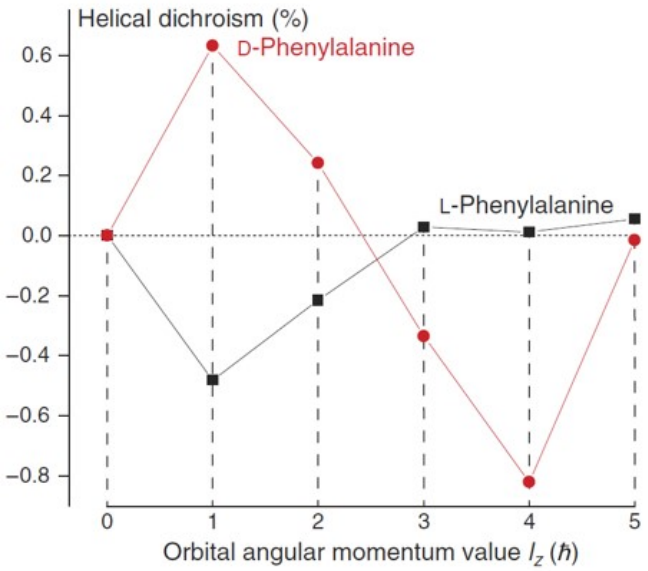

Figure 2.17: First example of helical dichroism ever measured, which allowed to distinguish phenylalanine enantiomers. Figure taken from reference [90].

Nowadays it is understood that the E2 interactions are driven by the electric field gradient. For paraxial beams carrying OAM the field gradient is given by[13, 99]

$$\nabla \mathbf{E}_{\mathbf{LG}}^{l,p=\mathbf{0}} = \left[\hat{\boldsymbol{\rho}}\left(\frac{|l|}{\rho} - \frac{2\rho}{w_0^2}\right) + \hat{\boldsymbol{\phi}}\frac{il}{\rho} + ik\hat{\boldsymbol{z}}\right]\mathbf{E}_{\mathbf{LG}}^{l,p=\mathbf{0}}, \tag{2.71}$$

where $\hat{\boldsymbol{\rho}}$, $\hat{\boldsymbol{\phi}}$ and $\hat{\boldsymbol{z}}$ are unit vectors in cylindrical coordinates. As it can be seen from

equation 2.71, the field gradient has transverse (ρ, ϕ) and longitudinal (z) components. Most importantly, the azimuthal gradient (ϕ) depends on both the magnitude and sign of the topological charge l, which means that not only the E2 excitation will depend on the handedness of the helical phase fronts, but also on its magnitude.[13, 99] Note that the excitation of E2 modes with paraxial beams still requires some degree of orientational order or anisotropy as in the case of conventional CD,[99, 102] and note that the OAM can only engage in E1E2 interactions in the case of circularly-polarized LG beams, whereas the first possible interaction for linearly-polarized LG beams is of the E2E2 order.[13, 99]

Another way that OAM can interact with chiral material is by matching the beam size and material dimensions, as seen in Figure 2.18. In this way large helical dichroism has been observed for specific topological charges where the beam size matches that of the structure, which has allowed for the distinction of single small chiral structures where no CD was observed.[103, 104]

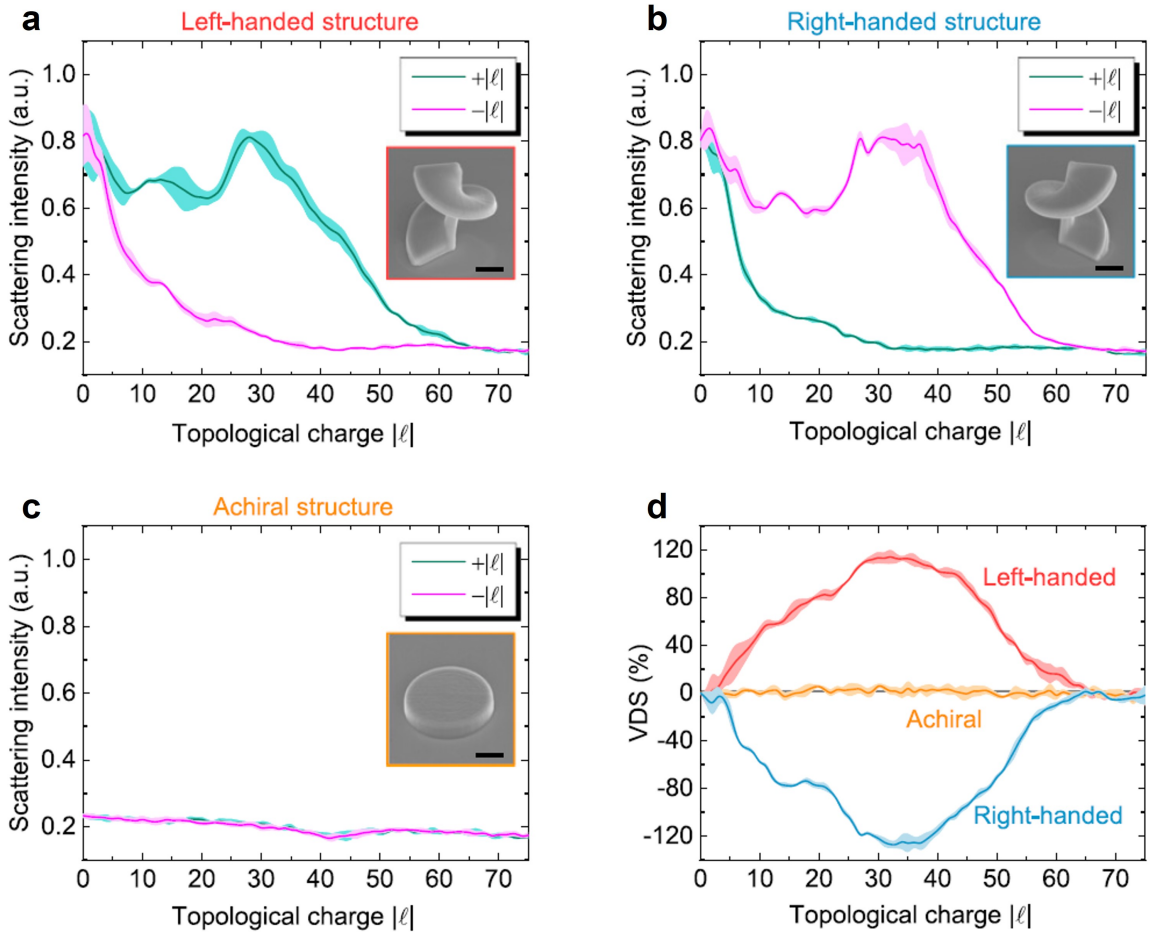

Figure 2.18: Helical dichroism with spatial match between the beam and the structure. (a,b,c) Scattering intensity for varying values of positive (cyan) and negative (magenta) topological charges for (a) left-handed, (b) right-handed and (c) achiral structures. (d) Helical dichroism obtained from subfigures (a,b,c). The scale bar is 5 μm. Figure taken from [103].

In the case of non-paraxial beams, the interaction of OAM with chiral media is more subtle because tightly-focused beams have a considerable electric field in the propagation direction (longitudinal fields). Therefore, the OAM in tightly-focused beams can engage in chiral interactions *via* different mechanisms. The first one includes E2 excitation due to the azimuthal gradient in the same way as for paraxial light beams, and then non-paraxial beams can interact through the effects due to longitudinal fields.[13] The latter do not require some degree of order or anisotropic samples, so a helical dichroism can be observed even when the sample is isotropic.[100] Examples of studies where dichroism effects have been attributed to longitudinal fields can be found in the study conducted by Zambrana-Puyalto.[105] In this study, a CD was observed for non-chiral

samples by realizing that, as we will see in Chapter 5, circularly-polarized LG beams with antiparallel ($\sigma = \mp 1$, $l = \pm 1$) and parallel ($\sigma = \pm 1$, $l = \pm 1$) combinations of SAM and OAM ($l = 1$) beams are not mirror images of each other in the non-paraxial regime due to longitudinal fields.[106, 107] Other studies exploiting this idea by using spherical (non-chiral) nanoparticles have been observed under the non-paraxial regime.[108] Additionally, as a consequence of the longitudinal fields, tightly-focused OAM develops optical chirality density even when the incoming beam before focusing possesses no spin at all.[109–111] Therefore, if a chiral nanostructure is positioned in a region with positive or negative optical chirality density, a helical dichroism can be observed also through E1M1 interactions, as observed by Wozniak *et al.*[112]

2.5 Conclusions

The fundamental aspects about angular momentum of light and Laguerre-Gaussian beams have been introduced to the reader. In addition, some of the applications of angular momentum beams that are relevant to understand the results in this thesis have been discussed; these are optical spanners (relevant for Chapters 3 and 4) and optical activity (relevant for Chapter 5).

Chapter 3

Numerical simulations of optical angular momentum transfer to 2D materials

3.1 Introduction

With the recent advancements in technology and increasing computational power that the scientific community has witnessed in the last few decades, numerical methods have become an essential part of many research areas such as nanophotonics. Numerical simulations are required in certain areas of physics for a variety of reasons. In the first instance because, for certain mathematical problems, no solution can be found analytically, and therefore numerical methods were developed to find approximate solutions to such problems.[113] Secondly, numerical simulations can predict what the properties of a system may look like prior to fabrication, saving cost, materials and fabrication time.[114, 115] Last, but not least, numerical methods are crucial in cases where some information cannot be found experimentally, and therefore they provide means to gain a deeper understanding of the system under study.[116–118]

Numerical simulations in this chapter have been performed to establish the foundations of angular momentum transfer between a light beam and 2D materials, and

predict angular momentum as the origin for the observed wrinkling in the experiments involving 2D materials in Chapter 4.

In the first part of this chapter (§ 3.2), continuity equations are derived to express the conservation of linear and angular momenta inside a dielectric medium. From the continuity equations, expressions for the electromagnetic linear momentum flux and angular momentum flux densities inside the dielectric medium are obtained, which can be subsequently used to calculate the forces and torques.

In the second part of this chapter (§ 3.3), Laguerre-Gaussian beams are implemented into a numerical method software, which employs the finite-element method to find approximate solutions to Maxwell's equations in complex systems. Subsequently, the expected torque and forces imparted by the LG beam onto the 2D materials used in the experiments of Chapter 4 are derived. Finally, laser heating simulations are performed to rule out the possibility of laser heating to be the cause of the experimental observations with angular momentum beams in the next chapters.

3.1.1 Finite-element method

Numerical methods are frequently used in different areas of physics to solve partial differential equations (PDEs) numerically. For many real-life problems that are governed by PDEs this is a necessity, as no analytical solution exists, hence an approximate solution must be found. Examples of PDEs that are solved by numerical methods include Maxwell's equations (§ 2.1) in nanomaterials, and these are the PDEs solved in this thesis using numerical methods.

Different numerical methods to solve PDEs exist, among which finite-different method and finite-element method are the most commonly used. The simulations performed in this thesis were done using a commercially-available numerical simulation package (COMSOL Multiphysics, v. 6.2). COMSOL uses the finite-element method (FEM) to find approximate solutions for PDEs in a variety of fields, therefore the focus will be on how FEM works.

In FEM, PDEs are solved numerically by dividing the geometry of the structure that needs to be solved into different elements, and the PDEs are solved at the nodes of the elements. The solution is then approximated over the entire geometry using a linear combination of basis functions. For example, let $f(x)$ be the function to be obtained from the model. Then f can be approximated as a linear combination of basis functions

$$f(x) \approx \sum_i f_i(x_i)\psi_i(x_i), \tag{3.1}$$

where i denotes a node subindex, ψ_i is a basis function at that node and f_i are coefficients that represent the function at that node. As a simple example to illustrate this, consider a one-dimensional problem. Let $\sin(x)$ be the function that we are trying to find an approximation for, and consider the hat function $\psi_i(x)$, which is 1 at a particular node and 0 at adjacent nodes.[119]

$$\psi_i(x) = \begin{cases} \frac{x-x_{i-1}}{x_i-x_{i-1}}, & \text{if } x_{i-1} \leq x < x_i, \\ 1 - \frac{x-x_i}{x_{i+1}-x_i}, & \text{if } x_i \leq x < x_{i+1}, \\ 0, & \text{elsewhere.} \end{cases} \tag{3.2}$$

A linear combination of $\sin(x_i)\psi_i(x_i)$ can be used to approximate the true $\sin(x)$ function, as depicted in Figure 3.1a. In Figure 3.1b, a larger number of basis functions are used, leading to a better approximation.

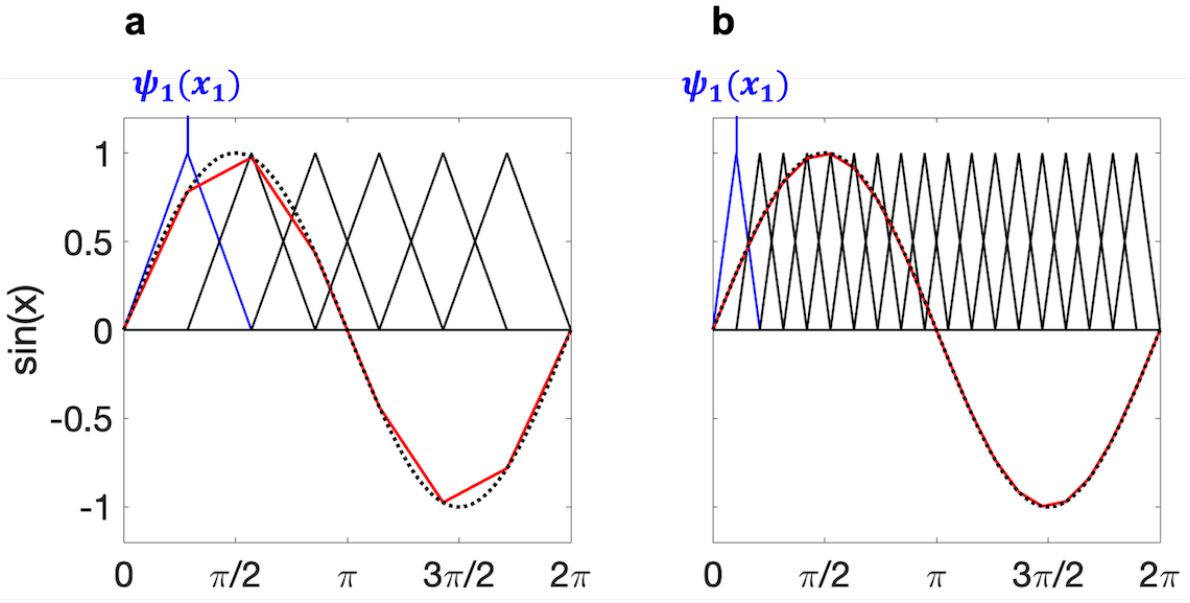

Figure 3.1: Approximation of the $\sin(x)$ function (red line) and the true $\sin(x)$ function (dashed black line) using a linear combination of (a) 6 basis functions and (b) 18 basis functions. In both (a) and (b), the basis function used is a hat function, and the basis function at the node x_1 is depicted in blue.

In 1D problems, the elements can be line segments, such as the ones used in Figure 3.1. For 3D problems, the model to be solved is divided using 3D elements. This process is called meshing. The elements used in the meshing of 3D structures include prisms, hexahedra, pyramids and tetrahedra, as shown in Figure 3.2. For 2D surfaces, triangular and rectangular elements are used.

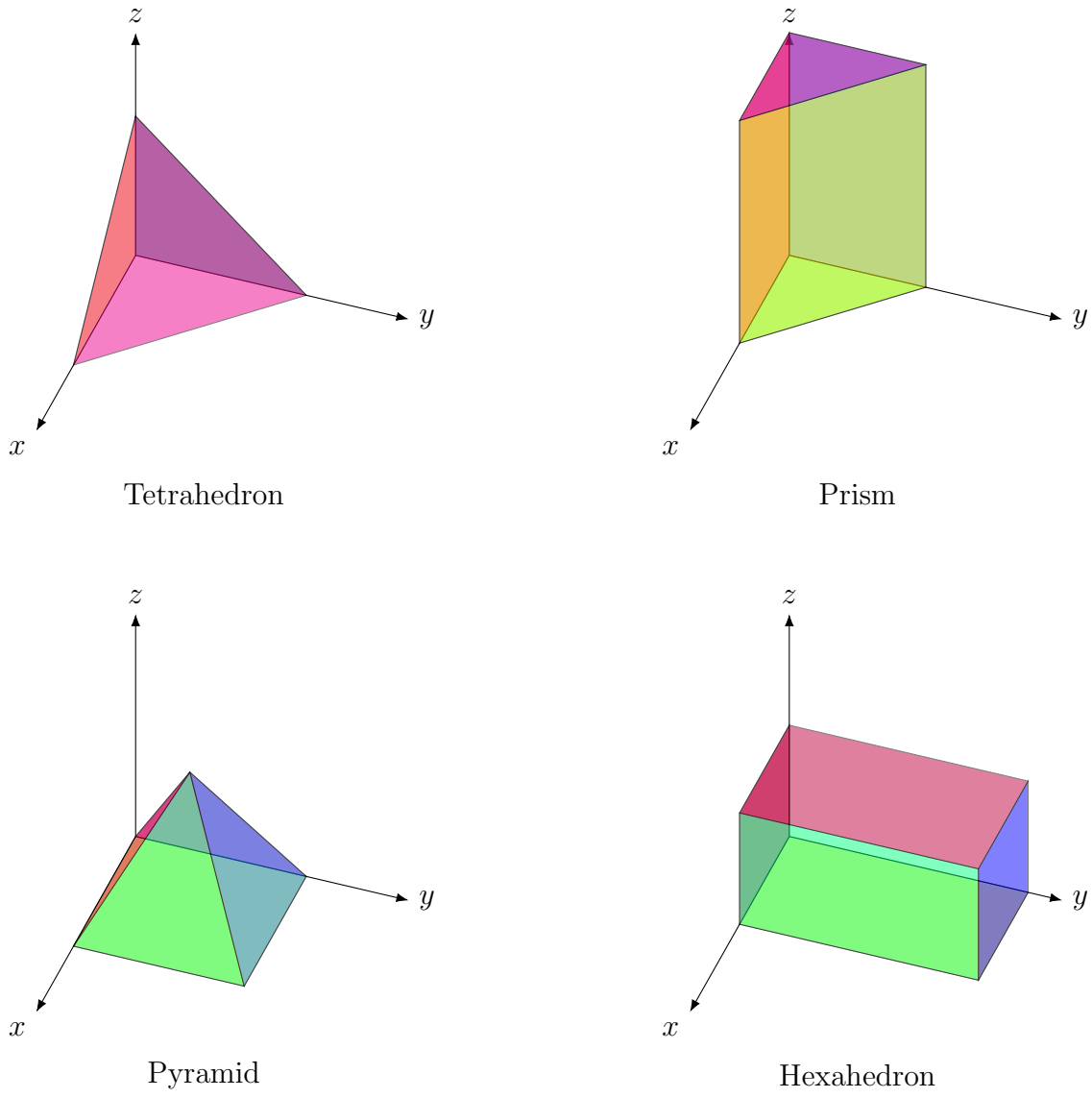

Figure 3.2: Elements used in meshing of a 3D structure in FEM.

An example of a meshing process in COMSOL is shown in Figure 3.3. As it can be seen, areas of interest or smaller areas (in this case, a spherical silicon nanoparticle) are meshed with finer elements. Maxwell's equations are solved at the nodes of the elements, and a combination of basis functions is used to approximate the solution over the entire structure. Smaller elements will lead to a more accurate solution, but the computational cost increases accordingly, therefore a balance between the number of elements and computational time must be found while ensuring accurate results.

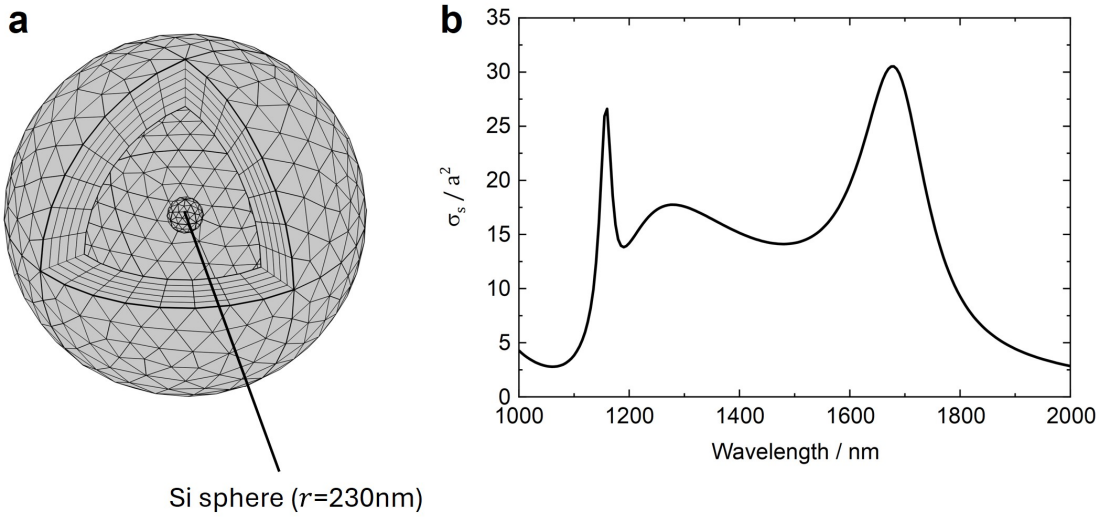

Figure 3.3: Simulation example using COMSOL. (a) 3D meshing process for a Si spherical nanoparticle, with the radius of the particle indicated in parentheses. (b) Simulated scattering cross section, σ_s, for a range of wavelengths, in agreement with reference [120].

3.2 Derivation of electromagnetic forces and torques inside a medium

In this section, expressions for the electromagnetic forces and torques in dielectric media are derived. The mathematical derivation included in this section was done by Neel Mackinnon, Stephen Barnett and Jörg Götte.

3.2.1 Momentum flux density

The local continuity of momentum within a dielectric medium is used to derive an expression for the electromagnetic momentum flux tensor inside the medium. In order to move forward, it is convenient to use the tensor notation instead of the vector notation. Thus, the i-th component of the vector product $\mathbf{A} \times \mathbf{B}$ becomes $(\mathbf{A} \times \mathbf{B})_i = \varepsilon_{ijk} A_j B_k$, where ε_{ijk} is the permutation symbol explained in § 2.3.1. The divergence of a vector field $\mathbf{A}$ becomes $\nabla \cdot \mathbf{A} = \nabla_i A_i = \frac{\partial A_x}{\partial x} + \frac{\partial A_y}{\partial y} + \frac{\partial A_z}{\partial z}$. The the i-th component of the curl of a vector field $\nabla \times \mathbf{A}$ is written as $(\nabla \times \mathbf{A})_i = \varepsilon_{ijk} \nabla_j A_k$.[56]

The conservation of the i-th component of electromagnetic momentum inside the medium can be expressed using the continuity equation

$$\frac{\partial g_i}{\partial t} + f_i = -\nabla_j T_{ij}, \tag{3.3}$$

where g_i is the momentum density, f_i is the Lorentz force density and T_{ij} is the momentum flux tensor, also known as Maxwell stress tensor (the ij-th component of T_{ij} is the flux of the i component of momentum in the j direction). If we now write down expressions for the momentum density $\mathbf{g}$, and the Lorentz force density, $\mathbf{f}$, in a dielectric medium, it is possible to obtain an expression for T_{ij} from the requirement that the continuity equation 3.3 is satisfied.

In free space, the momentum density of an electromagnetic field is undoubtedly given by the Poynting vector divided by the speed of light squared, $\mathbf{g} = \frac{1}{c^2}\mathbf{E} \times \mathbf{H}$.[19] Inside a dielectric medium, however, the definition of electromagnetic momentum density is more subtle and it is still a subject of debate nowadays. Different formulations exist and both are supported by experimental evidence.[121, 122] Precisely, the momentum inside a medium can be expressed using the Minkowski formulation[123]

$$\mathbf{g} = \mathbf{D} \times \mathbf{B}, \tag{3.4}$$

or using the Abraham formulation[124]

$$\mathbf{g} = \frac{1}{c^2}\mathbf{E} \times \mathbf{H}. \tag{3.5}$$

In this derivation we use the Abraham formulation, and take the momentum density of light inside the medium to be $\mathbf{g} = \frac{1}{c^2}\mathbf{E} \times \mathbf{H}$.

In a dielectric medium, the Lorentz force density can be written as

$$\mathbf{f} = (\mathbf{P} \cdot \nabla)\mathbf{E} + \frac{\partial \mathbf{P}}{\partial t} \times \mathbf{B}, \tag{3.6}$$

where $\mathbf{P}$ is the polarisation density[1].[125]

Substituting in the expressions for momentum density and Lorentz force density, the continuity equation 3.3 becomes

$$\frac{1}{c^2}\frac{\partial}{\partial t}(\varepsilon_{ijk}E_jH_k) + P_j\nabla_jE_i + \varepsilon_{ijk}\dot{P}_jB_k = -\nabla_jT_{ij}, \tag{3.7}$$

where a dot above a symbol indicates a time derivative. Assuming that the material is non-magnetic, it follows that $\mathbf{H} = \frac{1}{\mu_0}\mathbf{B}$, so the left-hand side of equation 3.7 can be rewritten as

$$\varepsilon_0(\varepsilon_{ijk}\dot{E}_jB_k + \varepsilon_{ijk}E_j\dot{B}_k) + P_j\nabla_jE_i + \varepsilon_{ijk}\dot{P}_jB_k. \tag{3.8}$$

We then use the definition of the displacement field in a dielectric medium, $\mathbf{D} = \varepsilon_0\mathbf{E} + \mathbf{P}$, to remove the polarisation field $\mathbf{P}$ from the expression above.

$$\varepsilon_0(\varepsilon_{ijk}\dot{E}_jB_k + \varepsilon_{ijk}E_j\dot{B}_k) + P_j\nabla_jE_i + \varepsilon_{ijk}\dot{P}_jB_k$$

$$= \varepsilon_0(\varepsilon_{ijk}\dot{E}_jB_k + \varepsilon_{ijk}E_j\dot{B}_k) + (D_j - \varepsilon_0E_j)\nabla_jE_i + \varepsilon_{ijk}(\dot{D}_j - \varepsilon_0\dot{E}_j)B_k$$

$$= \varepsilon_0\varepsilon_{ijk}E_j\dot{B}_k + (D_j - \varepsilon_0E_j)\nabla_jE_i + \varepsilon_{ijk}\dot{D}_jB_k. \tag{3.9}$$

We now make use of Maxwell's equations $\nabla\times\mathbf{E} = -\dot{\mathbf{B}}$ and $\nabla\times\mathbf{H} = \dot{\mathbf{D}} = \frac{1}{\mu_0}\nabla\times\mathbf{B}$ (where again it is assumed that the medium is non-magnetic) to write

$$\varepsilon_0\varepsilon_{ijk}E_j\dot{B}_k + (D_j - \varepsilon_0E_j)\nabla_jE_i + \varepsilon_{ijk}\dot{D}_jB_k$$

[1]Note that this expression treats the material as a collection of electric dipoles specified by P, and the electric part of the Lorentz force is taken as force on the centre of each dipole. An alternative approach would be to consider the Lorentz force on each individual charge, rather than each dipole. The distinction between the two approaches is relevant to the torque calculation that follows.

$$= -\varepsilon_0 \varepsilon_{ijk} E_j \varepsilon_{klm} \nabla_l E_m + (D_j - \varepsilon_0 E_j) \nabla_j E_i + \frac{1}{\mu_0} \varepsilon_{ijk} B_k \varepsilon_{jlm} \nabla_l B_m. \tag{3.10}$$

Finally, we use the identity $\varepsilon_{abc}\varepsilon_{ade} = \delta_{bd}\delta_{ce} - \delta_{be}\delta_{cd}$, where δ_{ij} is the Kronecker delta function[56] to write

$$-\varepsilon_0 \varepsilon_{ijk} E_j \varepsilon_{klm} \nabla_l E_m + (D_j - \varepsilon_0 E_j) \nabla_j E_i + \frac{1}{\mu_0} \varepsilon_{ijk} B_k \varepsilon_{jlm} \nabla_l B_m$$

$$= -\varepsilon_0 (\delta_{il}\delta_{jm} - \delta_{im}\delta_{jl}) E_j \nabla_l E_m + (D_j - \varepsilon_0 E_j) \nabla_j E_i + \frac{1}{\mu_0} (\delta_{lk}\delta_{im} - \delta_{km}\delta_{il}) B_k \nabla_l B_m$$

$$= -\varepsilon_0 E_j \nabla_i E_j + D_j \nabla_j E_i + \frac{1}{\mu_0} B_k \nabla_k B_i - \frac{1}{\mu_0} B_k \nabla_i B_k. \tag{3.11}$$

Our task is now to write the expression 3.11 as the divergence of a second-rank tensor. It is possible to show that this is accomplished if the momentum flux density is given by

$$T_{ij} = -E_i D_j - \frac{1}{\mu_0} B_i B_j + \frac{1}{2} \left(\varepsilon_0 E_k E_k + \frac{1}{\mu_0} B_k B_k \right) \delta_{ij}, \tag{3.12}$$

since $-\nabla_j T_{ij}$ becomes

$$-\nabla_j T_{ij} = -\nabla_j \left[-E_i D_j - \frac{1}{\mu_0} B_i B_j + \frac{1}{2} \left(\varepsilon_0 E_k E_k + \frac{1}{\mu_0} B_k B_k \right) \delta_{ij} \right]$$

$$= D_j \nabla_j E_i + E_i \nabla_j D_j + \frac{1}{\mu_0} B_i \nabla_j B_j + \frac{1}{\mu_0} B_j \nabla_j B_i - \varepsilon_0 E_k \nabla_i E_k - \frac{1}{\mu_0} B_k \nabla_i B_k. \tag{3.13}$$

Assuming there are no free charges, we can use Maxwell's equations $\nabla \cdot \mathbf{D} = 0$ and $\nabla \cdot \mathbf{B} = 0$, so the equality of the expressions 3.12 and 3.13 immediately follows.

3.2.2 Angular momentum flux density

Using the expression of the momentum flux tensor, we can derive an expression for the angular momentum continuity equation inside the medium. Recall that angular momentum $\mathbf{L}$ is defined as the cross product of the position vector $\mathbf{r}$ with the linear momentum $\mathbf{p}$

$$\mathbf{L} = \mathbf{r} \times \mathbf{p}. \tag{3.14}$$

Similarly, we can define the angular momentum flux density as the cross product of the position vector with the momentum flux tensor.[27] The i-th component of the angular momentum flux in the l direction is

$$M_{li} = \varepsilon_{ijk} r_j T_{kl}. \tag{3.15}$$

Using the expression derived for the momentum flux tensor T_{ij} in equation 3.12, the angular momentum flux density in the medium is given by

$$M_{li} = \varepsilon_{ijk} r_j T_{kl} = \varepsilon_{ijk} r_j \left[\frac{1}{2} \delta_{kl} \left(\varepsilon_0 E_m E_m + \frac{1}{\mu_0} B_m B_m \right) - \varepsilon_0 E_k D_l - \mu_0^{-1} B_k B_l \right]. \tag{3.16}$$

To obtain a continuity equation for the angular momentum of light, we begin by taking the cross product of the position vector $\mathbf{r}$ and the linear momentum continuity equation 3.3, so it is possible to write

$$\frac{1}{c^2} \varepsilon_{ijk} r_j \frac{\partial}{\partial t} (\mathbf{E} \times \mathbf{H})_k + \varepsilon_{ijk} r_j P_m \nabla_m E_k + \varepsilon_{ijk} r_j \varepsilon_{klm} \dot{P}_l B_m = -\varepsilon_{ijk} r_j \nabla_l T_{kl}. \tag{3.17}$$

The first term in equation 3.17 represents the time derivative of the angular momentum density $\frac{1}{c^2} \mathbf{r} \times (\mathbf{E} \times \mathbf{H})$. The second two terms are $\mathbf{r} \times \mathbf{f}$, where $\mathbf{f}$ is the Lorentz force density given in equation 3.6, and so these two terms correspond to a torque density.

However, this is not the total torque density. The force density was defined as the force acting on the centre of each electric dipole, and therefore the torque density derived from this does not include the torque on each individual dipole about its own centre. We might expect an extra torque, with a form like $\boldsymbol{\tau}_{\text{orienting}} = \mathbf{P} \times \mathbf{E}$, which would act to orient each dipole to align with the electric field.

Finally, we note that the term on the right-hand side is not quite equal to the divergence of the angular momentum flux density. The divergence of M is equal to the divergence of the cross product of r and T, but so far the right-hand side of equation 3.17 is the cross product of r with the divergence of T. We can see that the divergence of M will have an extra contribution

$$\nabla_l M_{li} = \nabla_l(\varepsilon_{ijk} r_j T_{kl}) = \varepsilon_{ijk} T_{kl} \nabla_l(r_j) + \varepsilon_{ijk} r_j \nabla_l(T_{kl}) \tag{3.18}$$

due to the product rule when the divergence is taken. The expression $\varepsilon_{ijk} T_{kl} \nabla_l(r_j)$ becomes

$$\varepsilon_{ijk} T_{kl} \nabla_l(r_j) = \varepsilon_{ijk} T_{kl} \delta_{lj}$$

$$= \varepsilon_{ijk} \delta_{lj} \left(-E_k D_l - \frac{1}{\mu_0} B_k B_l + \frac{1}{2} \left(\varepsilon_0 E_m E_m + \frac{1}{\mu_0} B_m B_m \right) \delta_{kl} \right)$$

$$= \varepsilon_{ijk} \left(-E_k D_j - \frac{1}{\mu_0} B_k B_j + \frac{1}{2} \left(\varepsilon_0 E_m E_m + \frac{1}{\mu_0} B_m B_m \right) \delta_{kj} \right). \tag{3.19}$$

Because $\varepsilon_{ijk} \delta_{kj} = 0$, the part involving E^2 and B^2 vanishes, and because ε_{ijk} is antisymmetric, the contraction with the symmetric tensor $B_k B_j$ also vanishes. We can then use $\mathbf{D} = \varepsilon_0 \mathbf{E} + \mathbf{P}$ to write

$$\varepsilon_{ijk} T_{kl} \nabla_l(r_j) = -\varepsilon_{ijk} E_k (\varepsilon_0 E_j + P_j) = -\varepsilon_{ijk} E_k P_j, \tag{3.20}$$

where we have again used the antisymmetry of ε_{ijk} to write $\varepsilon_{ijk}E_kE_j = 0$. Equation 3.18 therefore becomes

$$\nabla_l M_{li} = \varepsilon_{ijk} r_j \nabla_l (T_{kl}) - (\mathbf{P} \times \mathbf{E})_i. \tag{3.21}$$

We can therefore see that if we add $(\mathbf{P} \times \mathbf{E})_i$ to both sides of equation 3.17, we obtain the continuity equation

$$\frac{1}{c^2}\varepsilon_{ijk} r_j \frac{\partial}{\partial t}(\mathbf{E} \times \mathbf{H})_k + \varepsilon_{ijk} r_j P_m \nabla_m E_k + \varepsilon_{ijk} r_j \varepsilon_{klm} \dot{P}_l B_m + \varepsilon_{ijk} P_j E_k = -\nabla_l M_{li}. \tag{3.22}$$

Equation 3.22 is the continuity equation for angular momentum inside the medium: the divergence of the angular momentum flux density on the right-hand side is equated to the local rate of change of angular momentum on the left. This rate of change is given by the time derivative of the optical angular momentum density and a torque density (both the torque due to the Lorentz force density $\mathbf{f} = (\mathbf{P} \cdot \nabla)\mathbf{E} + \frac{\partial \mathbf{P}}{\partial t} \times \mathbf{B}$, and also the torque on each dipole about its own centre, $\mathbf{P} \times \mathbf{E}$).

3.2.3 Time-averaged forces and torques

Recall that the continuity equation for linear momentum of light is given by

$$\frac{1}{c^2}\frac{\partial}{\partial t}(\varepsilon_{ijk} E_j H_k) + P_j \nabla_j E_i + \varepsilon_{ijk} \dot{P}_j B_k = -\nabla_j T_{ij}, \tag{3.23}$$

where T_{ij} is the momentum flux density given in equation 3.12. If an experiment is performed with a continuous source of monochromatic light, then it is possible to time-average the continuity equation over a cycle. Under this averaging, the term corresponding to the time derivative of the Poynting vector vanishes, and we are therefore able to equate the divergence of the momentum flux density with the force on the dielectric

$$P_j \nabla_j E_i + \varepsilon_{ijk} \dot{P}_j B_k = -\nabla_j T_{ij}. \tag{3.24}$$

To find the force on a volume in terms of the surface integral of the momentum flux density through the surface enclosing the volume, we can, using the divergence theorem,[19] rewrite this expression as

$$\iiint_V [\text{Force}]_i \, dV = -\oiint_S T_{ij} n_j dS, \tag{3.25}$$

where n_j is a unit vector in the direction of the surface element dS. Therefore, the force imparted by the beam at an interface can be calculated by considering the surface integral of T_{ij} over a surface enclosing the interface; this could, for example, be the difference in momentum fluxes through a plane just before the interface and one just after.

Similarly, a net torque can be obtained from the surface integral of the angular momentum flux density in the same way as a force can be obtained from the linear momentum. If a beam is propagating in the z direction normal to an interface, then the torque about this propagation direction will be given by the difference in the fluxes of the z component of angular momentum through two planes on either side of the interface. The relevant component of the angular momentum flux density tensor, to be evaluated on either side of the interface, is

$$M_{zz} = \varepsilon_{zjk} r_j T_{kz} = \varepsilon_{zjk} r_j \left[-E_k D_z - \frac{1}{\mu_0} B_k B_z + \frac{1}{2} \left(\varepsilon_0 E_m E_m + \frac{1}{\mu_0} B_m B_m \right) \delta_{kz} \right]$$

$$= y(E_x D_z + \mu_0^{-1} B_x B_z) - x(E_y D_z + \mu_0^{-1} B_y B_z), \tag{3.26}$$

where we have made use of the fact that $\varepsilon_{azz} = 0$. This quantity is, in essence, the cross product of the position vector $\mathbf{r}$ and the momentum flux density.

We now compute the cycle-average of 3.26 for monochromatic fields. We begin by expressing the real electric and magnetic field components E_i and B_j in terms of complex fields $\mathcal{E}_j$ and $\mathcal{B}_j$

$$E_i = \mathrm{Re}(\mathcal{E}_i) = \mathrm{Re}(\tilde{E}_i e^{-i\omega t}), \tag{3.27}$$

$$B_j = \mathrm{Re}(\mathcal{B}_j) = \mathrm{Re}(\tilde{B}_j e^{-i\omega t}), \tag{3.28}$$

with complex amplitudes $\tilde{E}_i$ and $\tilde{B}_j$. Maxwell's equations in the medium in the absence of sources are

$$\nabla \cdot \mathbf{D} = 0, \tag{3.29}$$

$$\nabla \cdot \mathbf{B} = 0, \tag{3.30}$$

$$\nabla \times \mathbf{E} + \frac{\partial \mathbf{B}}{\partial t} = 0, \tag{3.31}$$

$$\nabla \times \mathbf{H} - \frac{\partial \mathbf{D}}{\partial t} = 0. \tag{3.32}$$

Note $\mathbf{D} = \varepsilon \mathbf{E}$ and $\mathbf{B} = \mu \mathbf{H}$. In terms of the complex fields, Maxwell's equations become

$$\nabla \cdot \boldsymbol{\mathcal{D}} = 0, \tag{3.33}$$

$$\nabla \cdot \boldsymbol{\mathcal{B}} = 0, \tag{3.34}$$

$$\nabla \times \boldsymbol{\mathcal{E}} - i\omega \boldsymbol{\mathcal{B}} = 0, \tag{3.35}$$

$$\nabla \times \boldsymbol{\mathcal{H}} + i\omega \boldsymbol{\mathcal{D}} = 0. \tag{3.36}$$

From the last two equations, using tensor notation we obtain

$$\tilde{B}_j = \frac{1}{i\omega} \varepsilon_{jkl} \frac{\partial}{\partial r_k} \tilde{E}_l, \tag{3.37}$$

$$\tilde{D}_i = -\frac{1}{i\omega} \varepsilon_{ikl} \frac{\partial}{\partial r_k} \tilde{H}_l, \tag{3.38}$$

with the complex conjugates of these expressions given by

$$\tilde{B}_j^* = -\frac{1}{i\omega} \varepsilon_{jkl} \frac{\partial}{\partial r_k} \tilde{E}_l^*, \tag{3.39}$$

$$\tilde{D}_i^* = -\frac{1}{-i\omega} \varepsilon_{ikl} \frac{\partial}{\partial r_k} \tilde{H}_l^*. \tag{3.40}$$

Therefore, it follows that

$$\tilde{B}_z^* = -\frac{1}{i\omega} \varepsilon_{312} \frac{\partial}{\partial x} \tilde{E}_y^* - \frac{1}{i\omega} \varepsilon_{321} \frac{\partial}{\partial y} \tilde{E}_x^* = -\frac{1}{i\omega} \frac{\partial}{\partial x} \tilde{E}_y^* + \frac{1}{i\omega} \frac{\partial}{\partial y} \tilde{E}_x^*, \tag{3.41}$$

$$\tilde{D}_z^* = -\frac{1}{-i\omega} \varepsilon_{312} \frac{\partial}{\partial x} \tilde{H}_y^* - \frac{1}{-i\omega} \varepsilon_{321} \frac{\partial}{\partial y} \tilde{H}_x^* = \frac{1}{i\omega} \frac{\partial}{\partial x} \tilde{H}_y^* - \frac{1}{i\omega} \frac{\partial}{\partial y} \tilde{H}_x^*. \tag{3.42}$$

Taking the time-averaged angular momentum flux density and substituting expressions for $\tilde{D}_z^*$ and $\tilde{B}_z^*$ to remove all the z components we obtain

$$\bar{M}_{zz} = \frac{1}{2}\,\mathrm{Re}\left[y(\tilde{E}_x\tilde{D}_z^* + \mu_0^{-1}\tilde{B}_x\tilde{B}_z^*) - x(\tilde{E}_y\tilde{D}_z^* + \mu_0^{-1}\tilde{B}_y\tilde{B}_z^*)\right]$$

$$= \frac{1}{2}\,\mathrm{Re}\left[(y\tilde{E}_x - x\tilde{E}_y)\tilde{D}_z^* + \mu_0^{-1}(y\tilde{B}_x - x\tilde{B}_y)\tilde{B}_z^*)\right]$$

$$= \frac{1}{2}\,\mathrm{Re}\left[(y\tilde{E}_x - x\tilde{E}_y)\frac{1}{i\omega}\left(\frac{\partial}{\partial x}\tilde{H}_y^* - \frac{\partial}{\partial y}\tilde{H}_x^*\right) + \mu_0^{-1}(y\tilde{B}_x - x\tilde{B}_y)\frac{1}{i\omega}\left(\frac{\partial}{\partial y}\tilde{E}_x^* - \frac{\partial}{\partial x}\tilde{E}_y^*\right)\right]$$

$$= \frac{1}{2\omega}\,\mathrm{Re}\left\{-i\left[(y\tilde{E}_x - x\tilde{E}_y)\left(\frac{\partial}{\partial x}\tilde{H}_y^* - \frac{\partial}{\partial y}\tilde{H}_x^*\right) + \mu_0^{-1}(y\tilde{B}_x - x\tilde{B}_y)\left(\frac{\partial}{\partial y}\tilde{E}_x^* - \frac{\partial}{\partial x}\tilde{E}_y^*\right)\right]\right\}. \tag{3.43}$$

As we have assumed that the medium is not magnetic, $\mathbf{H} = \mu_0^{-1}\mathbf{B}$, and since $\mu_0^{-1} = \epsilon_0 c^2$ we can rewrite equation 3.43 as

$$\bar{M}_{zz} = \frac{\varepsilon_0 c^2}{2\omega}\,\mathrm{Re}\left\{-i\left[(y\tilde{E}_x - x\tilde{E}_y)\left(\frac{\partial}{\partial x}\tilde{B}_y^* - \frac{\partial}{\partial y}\tilde{B}_x^*\right) + (y\tilde{B}_x - x\tilde{B}_y)\left(\frac{\partial}{\partial y}\tilde{E}_x^* - \frac{\partial}{\partial x}\tilde{E}_y^*\right)\right]\right\}. \tag{3.44}$$

The angular momentum (AM) flux is then obtained from the surface integral of the angular momentum flux density $\bar{M}_{zz}$

$$\text{AM flux}_{zz} = \iint_S \bar{M}_{zz}dS =$$

$$\frac{\varepsilon_0 c^2}{2\omega}\,\mathrm{Re}\left\{-i\iint\left[(y\tilde{E}_x - x\tilde{E}_y)\left(\frac{\partial}{\partial x}\tilde{B}_y^* - \frac{\partial}{\partial y}\tilde{B}_x^*\right) + (y\tilde{B}_x - x\tilde{B}_y)\left(\frac{\partial}{\partial y}\tilde{E}_x^* - \frac{\partial}{\partial x}\tilde{E}_y^*\right)\right]\right\}. \tag{3.45}$$

For a linearly-polarised beam (*i.e.* no spin angular momentum), the AM flux equals the OAM flux.

3.3 Results and discussion

3.3.1 Implementation of Laguerre-Gaussian beams in vacuum

As part of this thesis, a model was developed in a numerical method solver to simulate the interaction of Laguerre-Gaussian beams with nanomaterials. Numerical simulations of Laguerre-Gaussian beams were done using a commercial numerical simulation software (COMSOL Multiphysics, version 6.2). COMSOL uses the finite-element method (see § 3.1.1) to solve differential equations numerically, in this case Maxwell's equations.

The simulations were done using the electromagnetic wave frequency domain and two first-order scattering boundary conditions at the input and output surfaces of the simulated domain, respectively. The scattering boundary conditions are non-reflecting when the incident radiation is at normal incidence to the boundary, which is the case for simple systems containing thin films. In the case of problems involving complex systems and strong scattering where some radiation is at a non-normal incidence to the boundary, perfectly-matched layers are preferred instead, such as in the simulations of Chapter 5.

The polarization of the beam was linear unless otherwise specified. The LG beam was implemented in COMSOL using the expression for a Laguerre-Gaussian beam, which in cylindrical coordinates takes the form

$$E_{l,p}(\rho,\phi,z) = C_{l,p}E_0\frac{w_0}{w(z)}e^{-\frac{\rho^2}{w^2(z)}}e^{il\phi}\left(\frac{\rho\sqrt{2}}{w(z)}\right)^{|l|}L_p^{|l|}\left(\frac{2\rho^2}{w^2(z)}\right)e^{-ikz-\frac{ik\rho^2}{2R(z)}+i\psi_{l,p}(z)}, \quad (3.46)$$

where p is the radial mode and l the topological charge. In our case, $p = 0$. The other beam parameters are defined as[5, 21]

$$\text{Normalization constant: } C_{l,p} = \sqrt{\frac{2p!}{\pi(p+|l|)!}} \quad (3.47)$$

$$\text{Beam width: } w(z) = w_0\sqrt{1+\frac{z^2}{z_R^2}};\ \text{beam waist: } w_0 \tag{3.48}$$

$$\text{Generalized Laguerre polynomial: } L_p^{|l|}(x) = \frac{e^x}{p!}x^{-|l|}\frac{d^p}{dx^p}(e^{-x}x^{p+|l|});\ L_0^{|l|} = 1 \tag{3.49}$$

$$\text{Wave front curvature: } R(z) = z\left(1+\frac{z_R^2}{z^2}\right) \tag{3.50}$$

$$\text{Rayleigh range: } z_R = \frac{1}{2}w_0^2 k;\ k = k_0 n \tag{3.51}$$

$$\text{Gouy phase: } \psi_{l,p}(z) = (|l|+2p+1)\arctan\left(\frac{z}{z_R}\right). \tag{3.52}$$

The intensity of the beam was defined as the power per unit area

$$I_0 = \frac{P}{A}, \tag{3.53}$$

where P is the incident power and A is the area of the surface through which the beam is travelling. From I_0 it is possible to calculate the electric field of the beam E_0 *via*[19]

$$E_0 = \sqrt{\frac{2I_0}{c\varepsilon_0}}. \tag{3.54}$$

In the first instance, the LG beam was implemented in free space, and a few checks were carried out to ensure that the simulated beam agreed with the theory. As expected from the expression of the LG beam in 3.46, the simulated electric field intensity ring increases in size with the topological charge l and the phase front is helical, with the number of helices in the phase front corresponding to the topological charge (Figure 3.4).

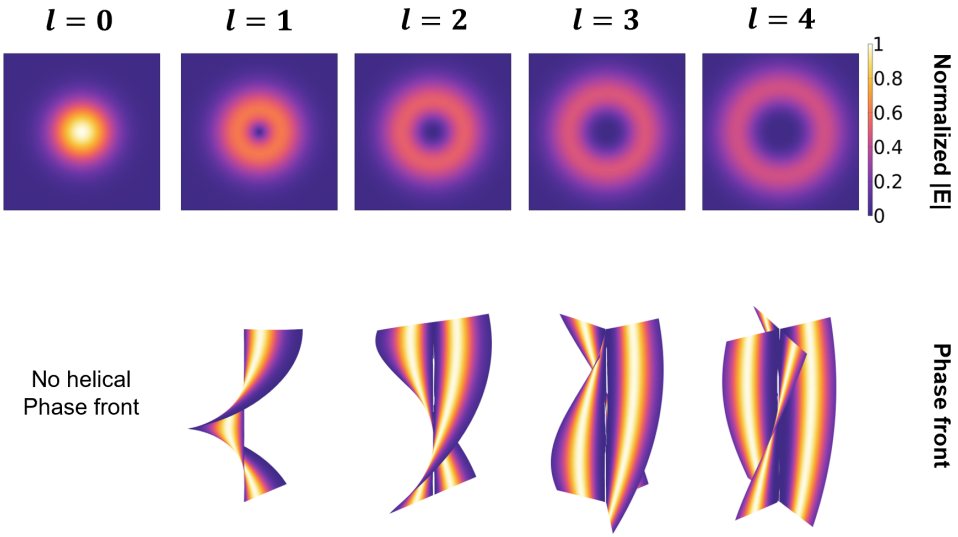

Figure 3.4: Simulated electric field intensity and phase front of LG beams as a function of the topological charge. The electric field has been normalized to the maximum intensity of the Gaussian ($l = 0$) beam.

Furthermore, changing the sign of the topological charge reversed the handedness of the phase fronts, as depicted in Figure 3.5.

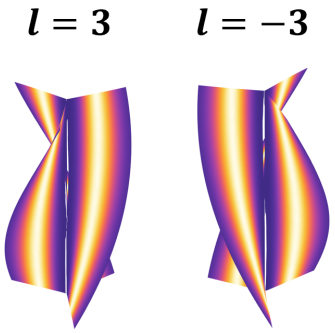

Figure 3.5: Simulated phase fronts for LG beams of opposite handedness, $l = 3$ and $l = -3$.

It was checked that the simulated intensity of the beam agreed with that predicted from the theory. The beam radius where the maximum intensity is observed, r_{max}, should depend on l and w_0 as[33]

$$r_{max} = \sqrt{\frac{z_R|l|}{k}} = \frac{\sqrt{2}w_0}{2}\sqrt{|l|}, \tag{3.55}$$

where we have made use of $z_R = \frac{1}{2}kw_0^2$. Additionally, the maximum intensity (Appendix C) is

$$I_{max}(r_{max}) = \frac{2}{\pi|l|!} A e^{-|l|} \sqrt{|l|}^{2|l|}, \tag{3.56}$$

where A is an amplitude constant.

A horizontal line of the simulated intensity extracted across the centre of the beam is shown in Figure 3.6a. From this, the radius of maximum intensity and maximum intensity was extracted (Figure 3.6b-c), which agrees well with the theoretical radius and intensity expected from equations 3.55 and 3.56, respectively.

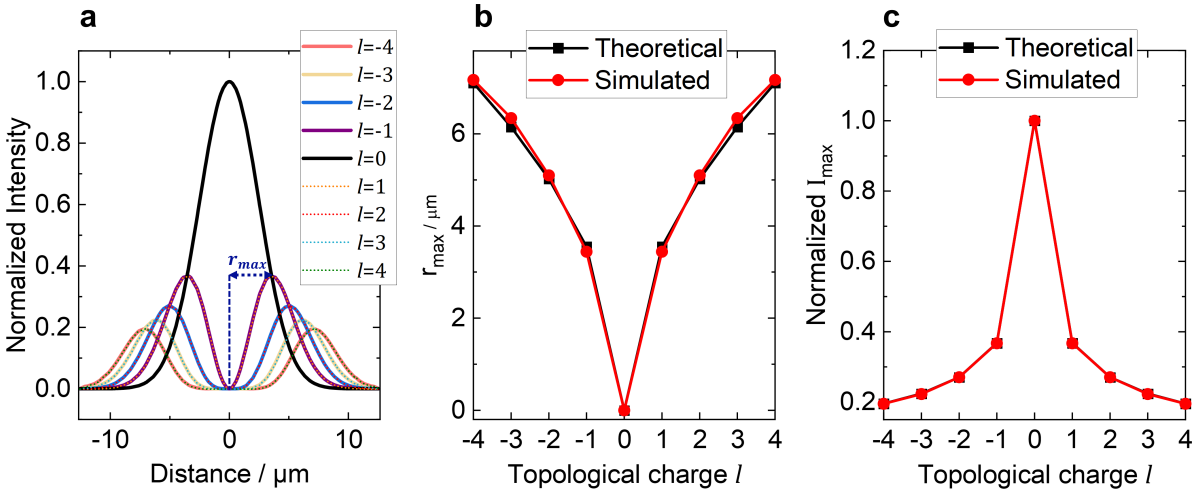

Figure 3.6: (a) Simulated intensity of different LG beams as a function of topological charge. (b) Radius of maximum intensity (r_{max}) (red) obtained from panel (a), compared to the theoretical radius (black) from equation 3.55. (c) Maximum intensity (I_{max}) (red) obtained from panel (a), compared to the theoretical maximum intensity (black) from equation 3.56. In panels (a) and (c), The intensity has been normalized to the maximum intensity of the Gaussian ($l = 0$) beam.

Furthermore, if a Gaussian beam were to be transformed into an LG beam, the intensity of the beam (power per unit area) through a surface perpendicular to the beam propagation should remain constant due to the energy conservation law. Note that for LG beams, the electric field intensity increases as a function of topological charge as $\left(\frac{\rho\sqrt{2}}{w(z)}\right)^{|l|}$, therefore the normalization constant $C_{l,p} = \sqrt{\frac{2p!}{\pi(p+|l|)!}}$ is included to ensure energy conservation. This constant is derived from the normalization condition

$$\iint |E_{l,p}|^2 dxdy = 1. \tag{3.57}$$

To verify that energy is conserved in the beam, the surface integral of the electric field intensity squared $|E|^2$ in the transverse plane was calculated and compared for different topological charges. As shown in Figure 3.7a, the obtained values remained constant for different topological charges. Failing to include the normalization constant leads to violation of energy conservation law and incorrect results, as shown in Figure 3.7b. This in turn will lead to incorrect results of all the properties that depend on the incident power *e.g.* OAM flux. Therefore, it is important to include the normalization constant in the simulations when different topological charges or powers are used.

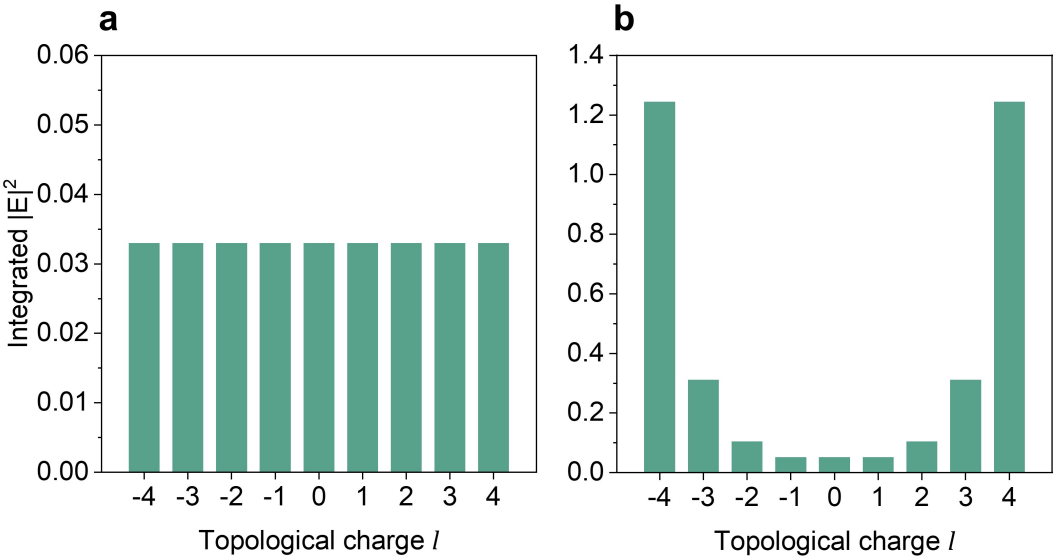

Figure 3.7: Surface integral of $|E|^2$ in the transverse plane as a function of the topological charge with (a) and (b) without normalization constant $C_{l,p}$. In (a) the energy is conserved, whereas in (b) the integrated intensity increases exponentially with l.

Recall from § 3.2 that the momentum flux density T_{ij} is given by

$$T_{ij} = -E_i D_j - \frac{1}{\mu_0} B_i B_j + \frac{1}{2}\left(\varepsilon_0 E_k E_k + \frac{1}{\mu_0} B_k B_k\right)\delta_{ij}. \tag{3.58}$$

As the beam propagates in the z direction, the momentum flux density is

$$T_{iz} = -E_i D_z - \frac{1}{\mu_0} B_i B_z + \frac{1}{2}\left(\varepsilon_0 E_k E_k + \frac{1}{\mu_0} B_k B_k\right)\delta_{iz}, \tag{3.59}$$

and the time average of the individual components is given by

$$\bar{T}_{xz} = -\frac{1}{2}\,\mathrm{Re}\left\{E_x D_z^* + \frac{1}{\mu_0} B_x B_z^*\right\}, \tag{3.60}$$

$$\bar{T}_{yz} = -\frac{1}{2}\,\mathrm{Re}\left\{E_y D_z^* + \frac{1}{\mu_0} B_y B_z^*\right\}, \tag{3.61}$$

$$\bar{T}_{zz} = -\frac{1}{2}\,\mathrm{Re}\left\{E_z D_z^* + \frac{1}{\mu_0} B_z B_z^*\right\} + \frac{1}{4}\left(\varepsilon_0 |E|^2 + \frac{1}{\mu_0}|B|^2\right). \tag{3.62}$$

Looking at the transverse plane (x and y components), the simulations show that the momentum flux density is rotationally symmetric and changes handedness upon changing the sign of the topological charge (Figure 3.8). Recall from § 3.2 that one obtains the time-averaged OAM flux density $\bar{M}_{zz}$ by taking the cross product of position vector $\mathbf{r}$ and momentum flux density. $\bar{M}_{zz}$ is given by

$$\begin{aligned}\bar{M}_{zz} = \frac{\varepsilon_0 c^2}{2\omega}\,\mathrm{Re}\Bigg\{ -i\Bigg[&\frac{1}{2}B_x^*\left(y\frac{\partial}{\partial x} - x\frac{\partial}{\partial y}\right)E_y + \frac{1}{2}E_x\left(y\frac{\partial}{\partial x} - x\frac{\partial}{\partial y}\right)B_y^* \\ &+ \frac{1}{2}B_y^*\left(x\frac{\partial}{\partial y} - y\frac{\partial}{\partial x}\right)E_x + \frac{1}{2}E_y\left(x\frac{\partial}{\partial y} - y\frac{\partial}{\partial x}\right)B_x^*\Bigg]\Bigg\}.\end{aligned} \tag{3.63}$$

The simulations show that $\bar{M}_{zz}$ also changes handedness upon changing the sign of the topological charge (Figure 3.8). As expected, only the LG beams have transverse components of the momentum flux density due to the azimuthally-varying phase, and possess OAM flux density. The simulated Gaussian ($l = 0$) beams have no momentum flux in the transverse plane, and therefore no orbital angular momentum flux density.

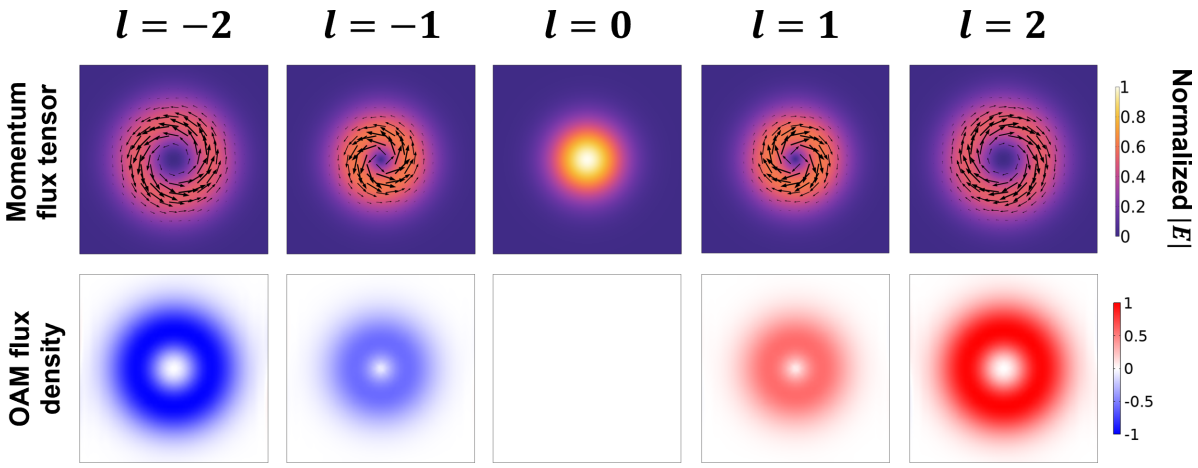

Figure 3.8: Top row: simulated time-averaged x and y components of the momentum flux density, superimposed on the electric field intensity (normalized for the Gaussian beam $l = 0$). Bottom row: simulated time-averaged OAM flux density $\bar{M}_{zz}$, normalized to the maximum of $l = 1$ beam. Both quantities are plotted in the transverse xy plane.

As the OAM of a Laguerre-Gaussian beam amounts to $l\hbar$ per photon, the OAM should depend linearly on l. To verify this, the OAM flux was calculated in the simulations by integrating the OAM flux density $\bar{M}_{zz}$ through the xy-plane[27]

$$\text{OAM flux} = \iint \bar{M}_{zz} dx dy. \tag{3.64}$$

The OAM flux can then be calculated in air at any plane normal to the beam propagation. As shown in Figure 3.9a, the OAM flux was found to follow a linear relationship for increasing topological charge, which agrees with the fact that orbital angular momentum per photon is $l\hbar$. The OAM flux is positive for $l > 0$, and negative for $l < 0$, as the OAM changes sign upon reversing the handedness of phase fronts. Finally, it was checked that the OAM flux also increased linearly with power, as the OAM of the beam should be linearly dependent on the number of photons that carry OAM, shown in Figure 3.9b.

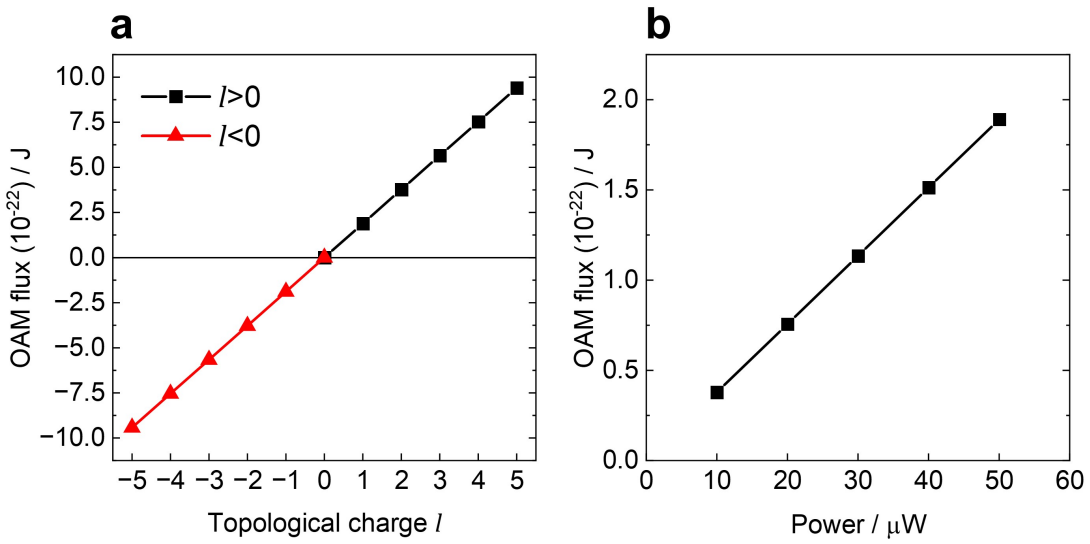

Figure 3.9: Simulated OAM flux of Laguerre-Gaussian beams in free space as a function of (a) topological charge (excitation power: $50\mu W$) and (b) excitation power ($l = 1$). Adapted from [126].

It was found that special care must be taken deciding the size of the simulated domain. Recall that the size of the LG beam increases for increasing topological charge, so the simulated domain must be large enough to fit all the LG beams used. An example is shown below, where an $l = 4$ beam is simulated in a geometry which is too small for the beam size. As it can be seen for increasing topological charge (Figure 3.10a) the angular momentum flux deviates from linear relationship as the intensity profile of the beam does not fit entirely in the simulation geometry (Figure 3.10b). This can be solved by using a simulation geometry that is large enough to fit the beam for all topological charges used (Figure 3.10c-d).

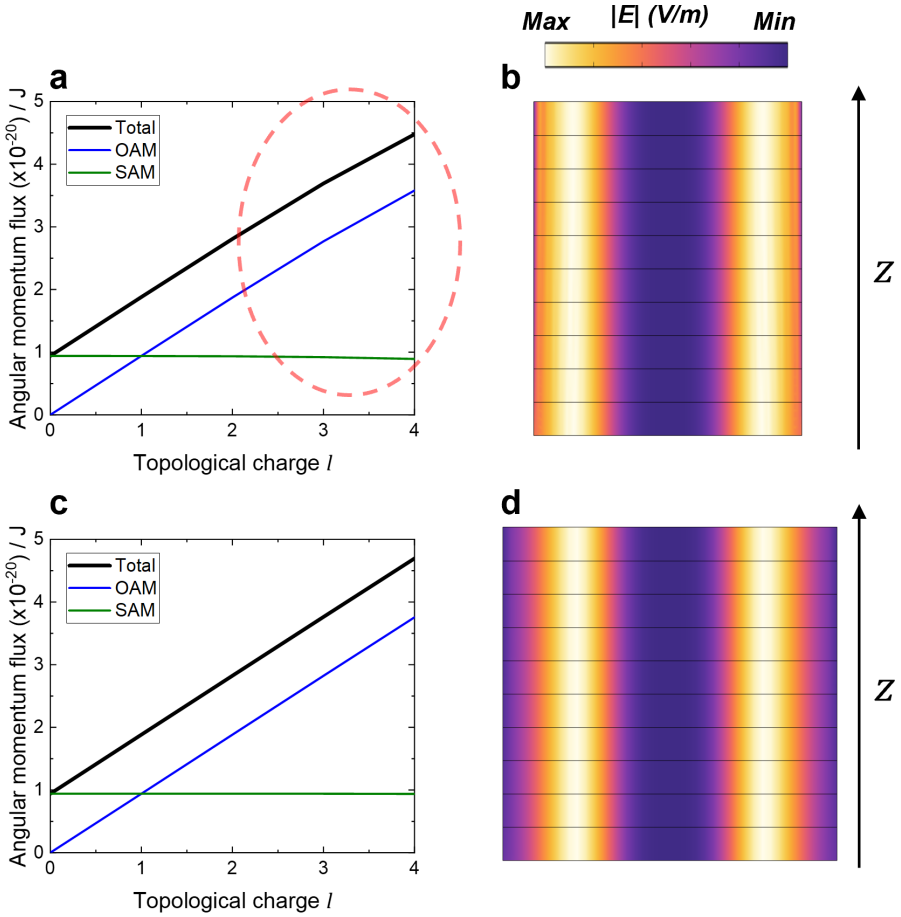

Figure 3.10: Effects of simulation geometry size. (a,b) Angular momentum flux (a) and electric field intensity of $l = 4$ beam (b) in a case where the simulation geometry is too small. The flux deviates from a linear relationship at large topological charge (red dashed oval marked in (a)). (c,d) Angular momentum flux (c) and electric field intensity of a $l = 4$ beam (d) in a case where the simulation geometry size is appropriate. The flux follows a linear relationship for all topological charges as expected.

3.3.2 Optical forces and torques in monolayer WS_2 and graphene

The purpose of this section is to demonstrate that angular momentum is transferred to monolayer WS_2 and monolayer graphene to validate the morphological changes observed experimentally in Chapter 4.

A monolayer of material was modelled in COMSOL with a thickness of 2 nm due to constraints in the minimum element size used for the meshing of the monolayer. The simulation was built using 3 different domains: air, 2D material (WS_2 or graphene) and the corresponding substrate used in the experiments of Chapter 4. The real and

imaginary refractive indices for monolayer WS_2 and monolayer graphene were taken from references [127] and [128], respectively. The simulations containing the WS_2 layer were performed using two substrates, Al_2O_3 and SiO_2. The simulations containing the graphene layer were done using the substrate SiO_2. The real and imaginary parts of the refractive index of Al_2O_3 and SiO_2 were taken from [129] and [130], respectively.

Careful consideration was taken when specifying the wave vector, as the simulation goes through different media. For simulations in different media, the phase defined as

$$\phi(\mathbf{r}) = \mathbf{k} \cdot \mathbf{r} \tag{3.65}$$

was set as a variable, and the wave vector $\mathbf{k}$ changes depending on the the refractive index of the medium. As the Rayleigh range also depends on the wave number, this was also set as a variable, where $k = k_0 n$ is the wave number in the medium and the Rayleigh range is now given by

$$z_R = \frac{1}{2} w_0^2 k = \frac{1}{2} w_0^2 k_0 n. \tag{3.66}$$

As explained in § 2.3.1, quantities such as energy, linear momentum and angular momentum are conserved, and therefore can be transferred from a light beam to a material. In the general sense, we can understand the origin of the torque acting on the 2D materials from Newton's second law of motion, which states that the force acting is given by the rate of change of linear momentum. Equivalently, the torque arises from the rate of change of angular momentum.

As derived in § 3.2, the conservation of the i-th component of EM momentum inside a medium can be expressed using the continuity equation

$$\frac{\partial g_i}{\partial t} + f_i = -\nabla_j T_{ij}, \tag{3.67}$$

where g_i is the momentum density, f_i is the Lorenz force density and T_{ij} is the momen-

tum flux tensor. The experiments performed in Chapter 4 employ a continuous-wave laser and hence the term $\partial g_i/\partial t$ vanishes when averaged over time; therefore, the change in the momentum of the EM field within the material is fully determined by the momentum flux density, that is, the flow of the optical momentum density through the medium.

To map out the forces acting in the 2D materials, the time-averaged components of the optical momentum flux density were plotted at the interface. As shown in Figure 3.11a, most of the momentum flux density is in the direction of propagation in all cases studied (Gaussian $l = 0$, and LG beams $l = 2$ and $l = 4$). This would be equivalent to a physical force generated on the 2D material by an AFM tip in contact mode.[131] Most importantly, in the case of the LG beam, there is substantial momentum flux density in the transverse plane (x and y components) which generates an in-plane force, Figure 3.11b. This azimuthal momentum or in-plane force is not present in the linearly-polarized Gaussian beam, and therefore the simulations predict that no wrinkling of the 2D materials can be produced with linearly-polarized Gaussian beams.

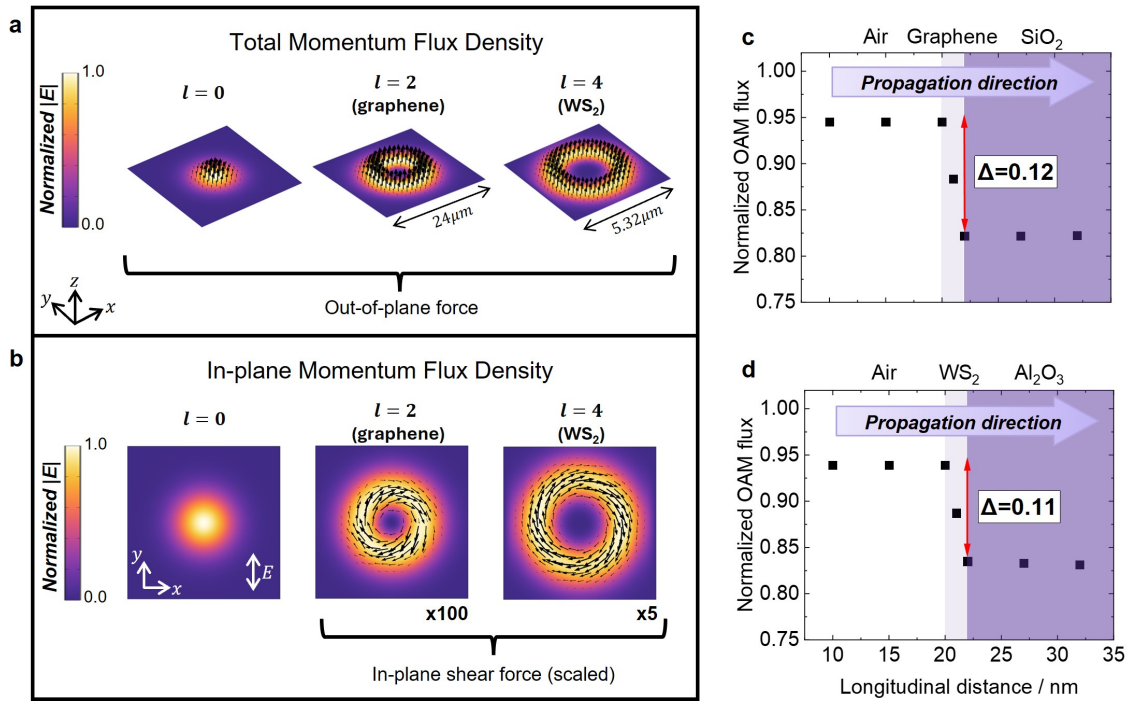

Figure 3.11: Simulated momentum flux density and OAM transfer to graphene and monolayer WS_2. (a,b) Total (a) and in-plane (b) momentum flux densities for $l = 0$, $l = 2$ and $l = 4$ beams at the focal plane, superimposed on the normalized electric field intensity. The in-plane momentum flux densities in (b) have been scaled to match the range of the total momentum flux densities in (a). (c,d) Simulated OAM flux as an LG beam propagates through air, 2D material and substrate, normalized by the OAM flux of the beam in air. Graphene and SiO_2 substrate is shown in (c), and monolayer WS_2 and Al_2O_3 substrate in (d). In all cases, the simulated beam is linearly-polarized. Figure taken from reference [126].

The LG beam acting on the 2D material can also be understood in terms of the angular momentum transfer, which generates a torque, in an analogous fashion to the azimuthal linear momentum generating an in-plane force. The torque is given by the angular momentum flux, and the torque experienced by the 2D material is given by the difference in flux before and after the 2D material. The OAM flux as the beam propagates through the different media is shown in Figure 3.11c,d, and it can be seen that the OAM flux decreases by $\approx 11 - 12\%$ after leaving the 2D material, hence $\approx 11 - 12\%$ of the OAM flux is transferred to the monolayer. Note that for WS_2, only that on Al_2O_3 is shown, although using the different substrate used SiO_2 produced similar results, Figure 3.12.

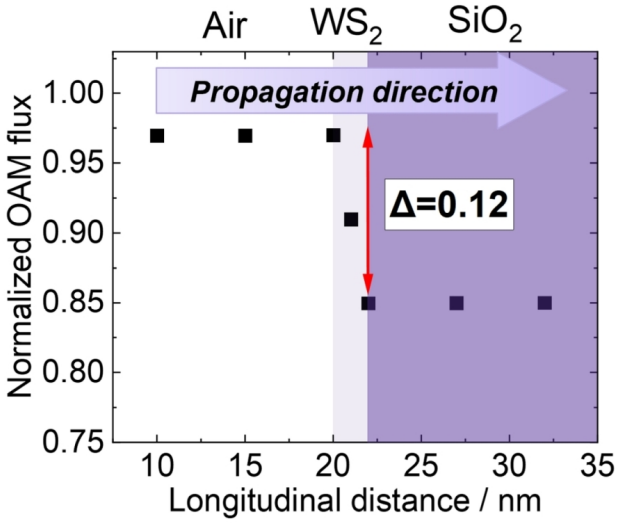

Figure 3.12: Normalized OAM flux as a function of longitudinal distance as the beam propagates across air, WS_2 and SiO_2 substrate. Figure taken from reference [126].

In the case of graphene, where the excitation wavelength used is 405 nm, $l = 2$ and excitation power is 500 μW, it is calculated that the magnitude of the torque would be

$$\Gamma_z = \frac{Pl}{\omega} \times 0.12 = \frac{Pl\lambda}{c2\pi} \times 0.12 = 2.6 \times 10^{-20} \text{ N m}. \tag{3.68}$$

This value is comparable but slightly smaller than the bending rigidity of graphene ($1.3 - 2.3 \times 10^{-19}$ N m),[132, 133] which predicts that no new wrinkles can be generated in the 2D material for this power and topological charge. However, as it will be shown in Chapter 4, this torque is sufficient to enhance the amplitude of pre-existing wrinkles. Similarly, in the case of WS_2, where the excitation wavelength used is 532 nm, $l = 4$ and excitation power is 100 μW, it is calculated that the magnitude of the torque would be

$$\Gamma_z = \frac{Pl}{\omega} \times 0.12 = \frac{Pl\lambda}{c2\pi} \times 0.12 = 1.4 \times 10^{-20} \text{ N m}. \tag{3.69}$$

It must me mentioned that the calculated magnitude of the torque reported here is for a 2 nm thick monolayer. A thickness of 2 nm had to be used due to out-of-memory errors while trying to mesh a layer thinner than 2 nm. In reality, however, the true

thickness of a graphene layer is ∼0.34 nm.[134, 135] Similarly, the true thickness of monolayer WS_2 is ∼0.8 nm,[136] so the changes in the OAM flux across the monolayer are expected to be smaller than the values reported here.

The results presented so far have employed linearly-polarized beams, which carry no SAM. Numerical simulations were also performed for different combinations of SAM ($\sigma = -1, 0, 1$) and OAM ($l = +2$), giving a total AM of $j = +1, +2, +3$. Furthermore, simulations were performed for the different combinations of SAM ($\sigma = -1, 0, +1$) and a Gaussian beam carrying no OAM ($l = 0$), giving total AM of $j = -1, 0, +1$.

Using the same methodology as for Figure 3.11a,b, numerical simulations of the in-plane momentum flux density were performed for these beams to visualize the in-plane forces exerted by the light, as depicted in Figure 3.13. The simulations reveal that the torque generated by the OAM + SAM beams increases with j due to an increased distance from the central axis, and predict that the same-sign combination of SAM and OAM will give the largest torque. In contrast, simulations for the Gaussian beam carrying SAM only show torques produced within the illuminated area but without a central singularity, unlike the OAM beam.

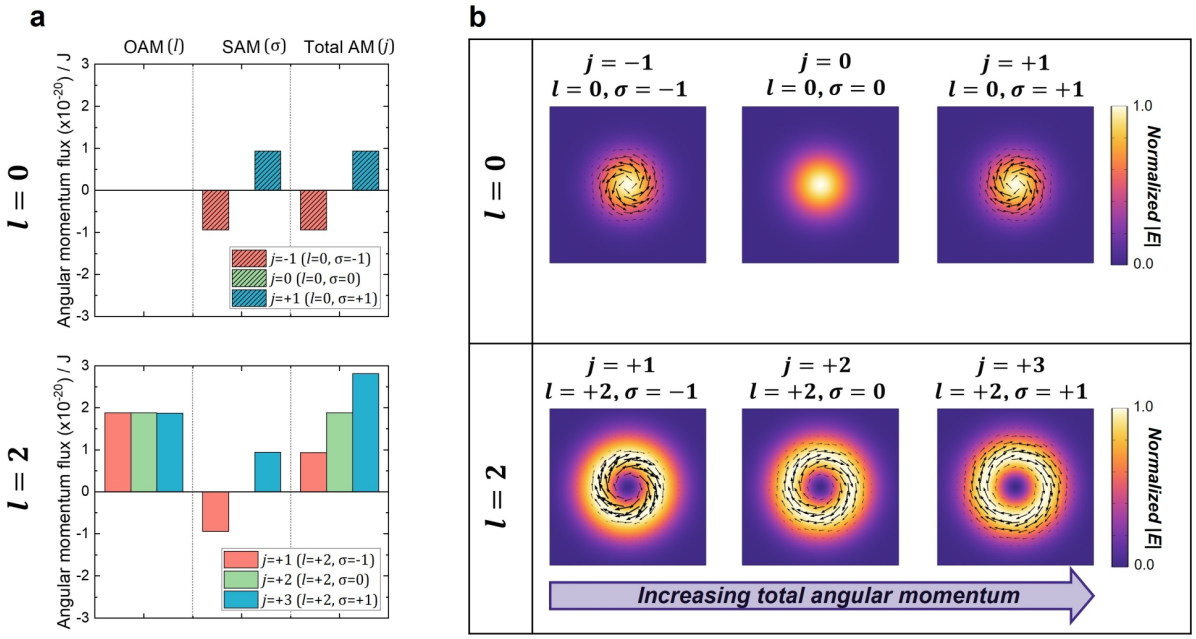

Figure 3.13: Numerical simulations of beams possessing some combination of OAM and SAM. (a) Simulated angular momentum fluxes (OAM, SAM, total AM) for $l = 0$ beams (top row) and $l = 2$ beams (bottom row) combined with SAM. (b) Simulated in-plane momentum flux density of $l = 0$ (top row) and $l = 2$ (bottom row) beams combined with SAM, superimposed on the normalized electric field intensity. Arrows indicating linear momentum flux density are plotted on the same scale. Figure adapted from reference [126].

3.3.3 Laser heating in monolayer WS_2 and graphene

Simulations in COMSOL were also performed to rule out the possibility that the experimental results arise from laser heating. To simulate the laser heating of Laguerre-Gaussian beams, the heat transfer module was used, coupled to the electromagnetic wave frequency domain *via* electromagnetic heating. In the heat transfer module, a temperature boundary condition was used at the input (air) surface with a fixed temperature of 293.15 K. The electromagnetic power loss density was used as a heat source, which results from coupling the electromagnetic waves and heat transfer modules. The heat transfer coefficient was set to 5 $W/(m^2 \cdot K)$ and the thermal parameters used across the different media can be seen in Table 3.1.[137–139] Note that the heat capacity at constant pressure (C_p) of graphene at room temperature is ~700,[137] whereas the value used in Table 3.1 ($C_p = 2100$) is the upper limit of heat capacity of graphene, normally seen at higher temperatures.[137]

	Heat capacity (J/(kg·K))	**Thermal conductivity (W/(m·K))**
Air	1000	0.02623
Graphene	2100	4000
WS_2	192.2	32
SiO_2	703	1.3
Al_2O_3	880	12

Table 3.1: Heating parameters across different media used in the laser heating simulations.

The simulated electric field intensity and temperature rises for the case of graphene and monolayer WS_2 are shown in Figures 3.14 and 3.15, respectively. The results show that, locally, electric field in LG beams is distributed over a larger area. Recall the normalization condition

$$\iint |E_{p,l}|^2 dxdy = 1, \tag{3.70}$$

which ensures energy conservation for different LG beams. Since the intensity ring of LG beams increases as a function of the topological charge, as seen in the term $\left(\frac{\rho\sqrt{2}}{w(z)}\right)^{|l|}$, the intensity must be distributed over a larger area. Locally, the intensity of LG beams is weaker and therefore LG beams induce smaller temperature rises compared to Gaussian beams, as observed in in Figures 3.14 and 3.15. By comparing a result obtained with a Gaussian and LG beam, this rules out the possibility that the changes observed in the experiments in the next chapters are due to laser heating.

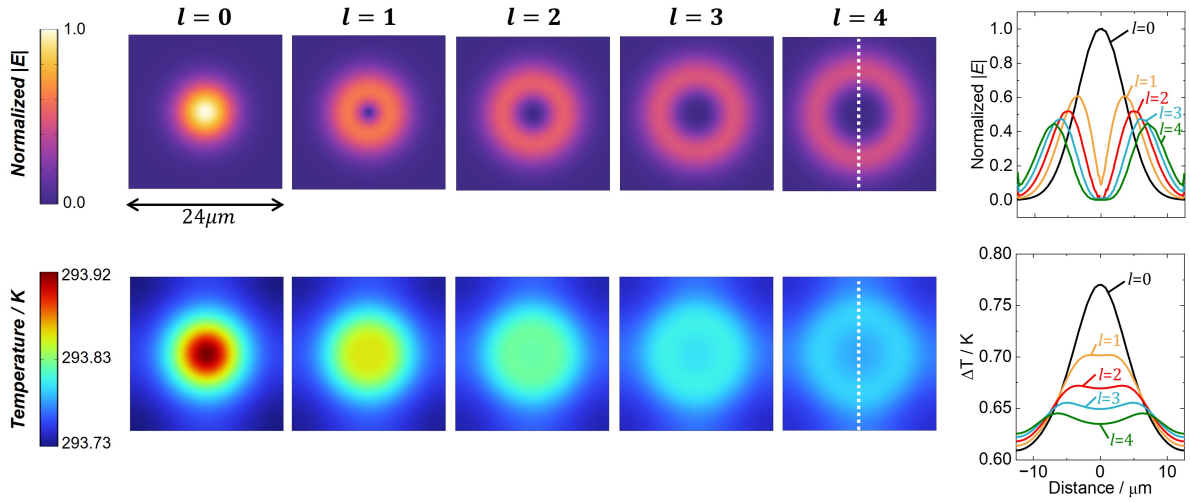

Figure 3.14: Simulated electric field intensity and temperature for beams of varying topological charge at the graphene-SiO_2 interface ($w_0 = 12.4\lambda$, power: 1 mW). A cut line (white line) of the electric field intensity and temperature rise with respect to the initial temperature $T_0 = 293.15\ K$ is displayed on the right hand side.

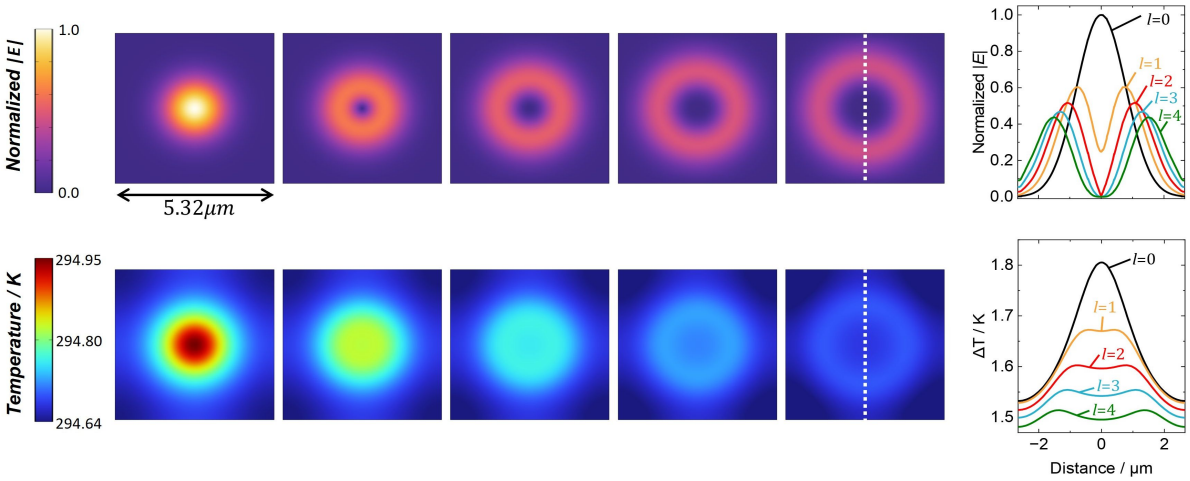

Figure 3.15: Simulated electric field intensity and temperature for beams of varying topological charge at the WS_2-Al_2O_3 interface ($w_0 = 2\lambda$, power: 200 μW). A cut line (white line) of the electric field intensity and temperature rise with respect to the initial temperature $T_0 = 293.15\ K$ is displayed on the right hand side.

3.4 Conclusions

To conclude this chapter, expressions to calculate optical forces and torques have been derived in dielectric media. Additionally, Laguerre-Gaussian beams have been implemented in a numerical method solver, and the characteristics of the simulated beams in air agree well with what it is predicted by the theory.

The simulations have been then used to predict that some angular momentum is transferred to the 2D materials used in the experiments in Chapter 4. The simulations predict that the in-plane forces experienced by the 2D materials arise due to the azimuthally-dependent linear momentum flux density in LG beams. The torque acting on the 2D materials has been calculated from the change in the OAM flux as the beam propagates through the absorbing medium. Overall, a theoretical and simulation framework of the LG beams acting on the 2D materials has been established. With this in mind, the experimental control of the morphology and properties of 2D materials with LG beams is achieved in Chapter 4.

Furthermore, the simulations rule out the possibility that the observed changes due to LG beams compared to Gaussian beams in the next chapters originate from laser heating.

Chapter 3: Summary

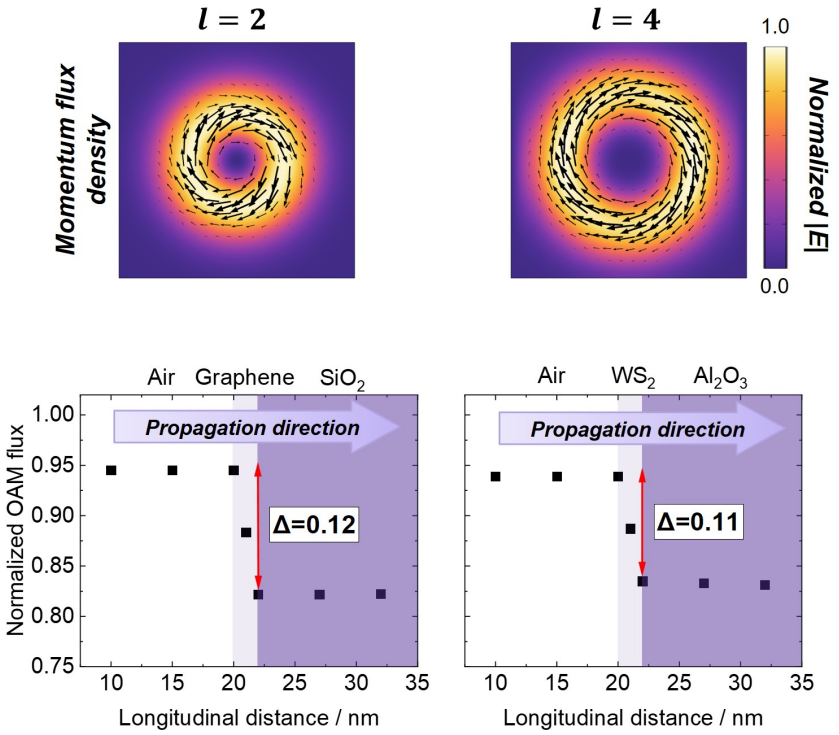

Figure 3.16: Chapter 3 concept figure.

Key findings:

- Expressions for optical forces and torques have been derived for dielectric media.
- Laguerre-Gaussian beams have been implemented in a numerical simulation software.
- The transverse momentum flux density of Laguerre-Gaussian beams generates an in-plane force.
- The torques acting on 2D materials have been calculated from the change in the OAM flux across the medium.

Chapter 4

Controlling the morphology and properties of 2D monolayers with optical angular momentum

4.1 Introduction

Two-dimensional (2D) materials[140] are single- or a few-layer materials that have emerged as a particularly interesting class of materials since the isolation and characterisation of graphene in 2004.[141] 2D materials have caused great attention in the scientific community in the last two decades particularly due to the fact that their properties strongly differ from those of their 3D counterparts, which has opened the way to new and otherwise inaccessible scientific inventions in the area of nanomaterials. Typically, the 3D counterpart is a layered material, and new properties arise when the number of layers is scaled down to one or several layers (that is, a few nanometers in thickness). For example, compared to graphite, the 3D counterpart of graphene, monolayer graphene has much larger conductivity[142] and larger tensile strength, making it the strongest material on Earth.[143] In addition, electrons behave as massless relativistic (Dirac) fermions, which gives rise to 'unusual' properties characteristic of such particles.[144] After graphene, other 2D materials were isolated and new properties dif-

ferent from those of graphene were found. For example, transition metal dichalcogenides (TMDCs), specifically monolayer MoS_2 in the first instance. When the number of layers is reduced to the monolayer regime, MoS_2 becomes a direct band-gap semiconductor and it exhibits strong photoluminescence,[145] finding applications in optoelectronic devices.[146–148] Additionally, the isolation and characterisation of monolayer MoS_2 gave rise to a new research area called valleytronics, which aims at using a new degree of freedom based on band maxima to store information.[149–151] These exotic properties arise on transitioning from the 3D bulk to the monolayer regime.[152]

In addition to the number of layers, the properties of 2D materials can be tuned by applying strain to the sample, which gives access to even newer and more exotic properties without the need of any chemical modifications.[153] As strain is applied to the material to tune and tailor the properties, this research area is known as strain engineering. Strain engineering of 2D materials can be used to enhance device performance for a desired application. For instance, carrier mobilities are enhanced in monolayer TMDCs transistors,[154, 155] or in multilayer TMDCs, where the emission is inherently weak, strong emission can be achieved with the application of strain.[156, 157] Nevertheless, the methods that have been proposed so far to induce strain can be irreversible, as it is often the case when the sample is chemically modified to apply strain.[158] Additionally, they may possess no spatial control on where the strain is applied to in the sample and they often use complicated physical manipulators to apply strain, increasing the complexity of the process and manufacturing costs. Therefore, a simpler, spatially-selective and reversible method to generate strain is desired.

As we saw in Chapter 3, numerical simulations establish that angular momentum transfer to the 2D material can be understood due to the azimuthally-varying linear momentum (which generates an in-plane force), or due to a change in the orbital angular momentum of the beam as it propagates through the medium. Even though 2D materials are incredibly strong, with graphene having the largest tensile strength ever measured,[143] 2D materials are extremely flexible, and out-of-plane deformations like wrinkling are easy to produce. In fact, wrinkles and rumples are formed naturally af-

ter the fabrication process, but they can also be produced by applying minimal forces ($< 10^{-12}$ N) to the sample.[159, 160]

In this chapter, we propose a novel method to wrinkle 2D materials by employing light beams which carry orbital angular momentum. This is a simple method which exploits the angular momentum transfer between a light beam and the absorbing material, with the resulting torque inducing wrinkling of the monolayer at the illuminated area. This is illustrated with two commonly used 2D materials, namely monolayer graphene and monolayer WS_2. The method is both non-contact, reversible, spatially-selective and it frees strain engineering from the fabrication of complicated and bulky mechanical manipulators.

4.1.1 Monolayer graphene and WS_2

Monolayer graphene, or simply graphene, is a one-atom thick 2D material composed of carbon atoms arranged in a hexagonal lattice, as shown in Figure 4.1. Commonly, graphene is obtained from the 3D bulk layered material graphite *via* exfoliation methods, as the individual layers in the bulk are held together by weak van der Waals forces; or it is frequently grown by chemical vapour deposition (CVD).[161]

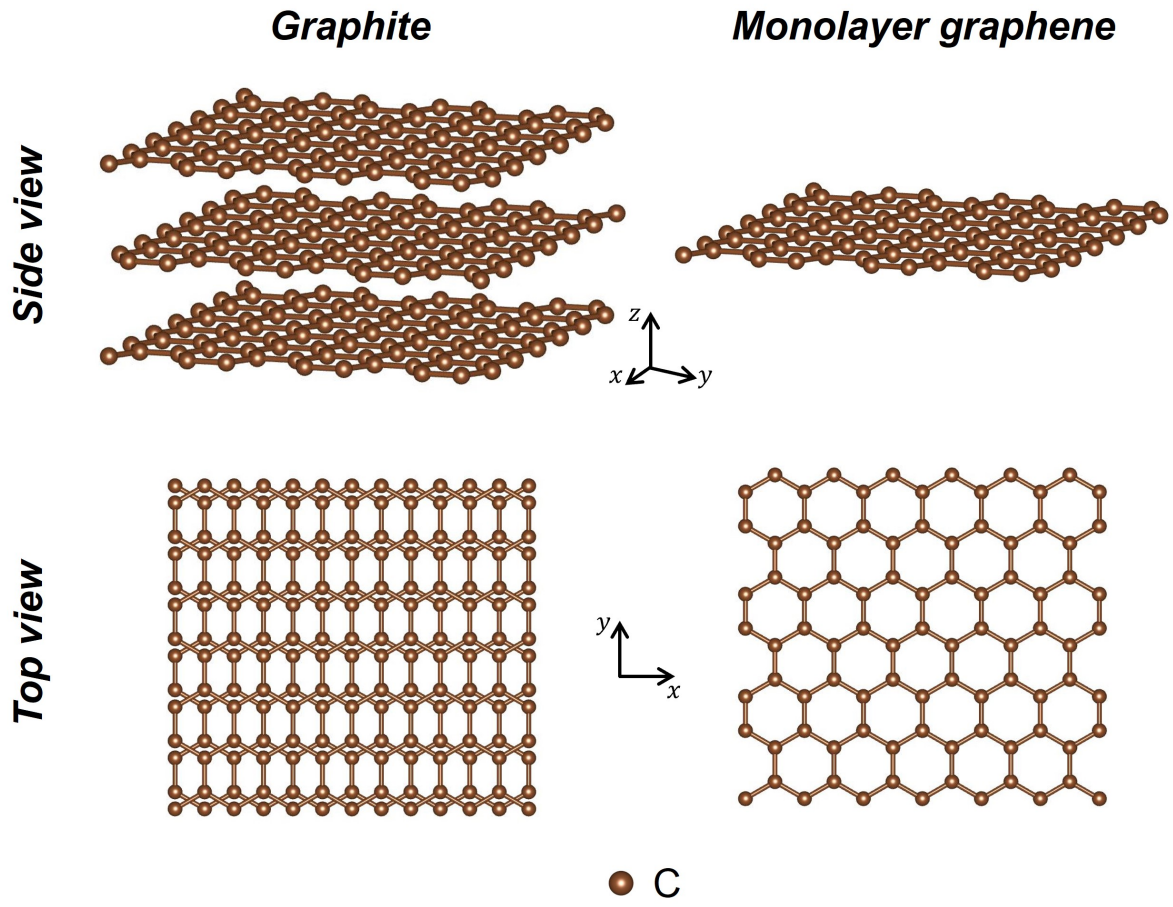

Figure 4.1: Top and side views of graphite and monolayer graphene. Carbon (C) atoms (shown in brown) are covalently bonded in a hexagonal lattice to form 2D layers. An individual 2D layer in graphite corresponds to monolayer graphene. This figure has been produced using Vesta software.[162]

Similar to graphite, TMDCs form layered structures and they have emerged as particularly interesting two-dimensional materials due to their remarkable difference in physical and electronic properties when comparing bulk materials and monolayers. As shown in Figure 4.2, the thermodynamically stable phase is trigonal prismatic and each layer in the bulk is composed of a transition metal atom (*e.g.* W, Mo) coordinated to two layers of chalcogen atoms (*e.g.* S, Se).[163, 164] The layers are held together by weak van der Waals forces, so two-dimensional flakes can be easily prepared by exfoliation from the bulk material.[163, 165] In a similar manner to graphene, TMDCs are also frequently prepared by CVD.[166]

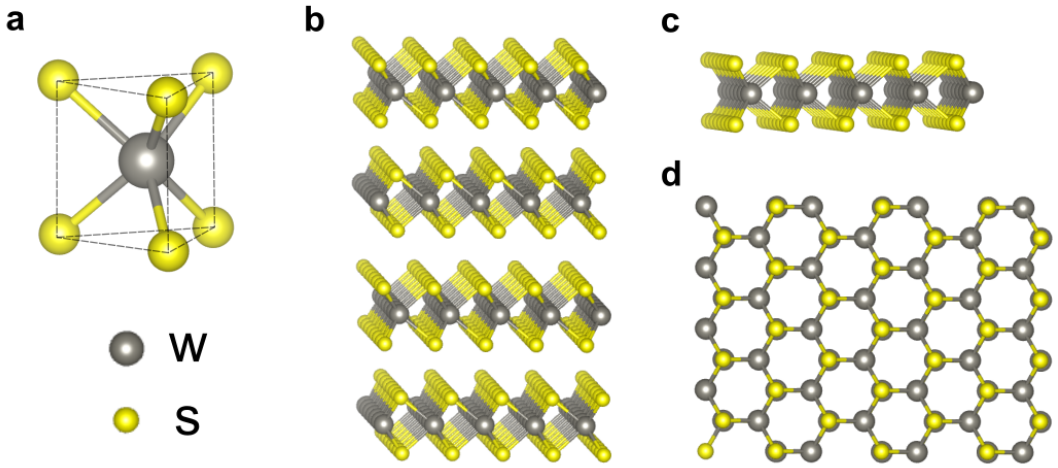

Figure 4.2: The crystal structure of a TMDC, WS_2. (a) Coordination geometry of the trigonal prismatic phase. (b) Side view of the bulk material, showing a layered structure of four layers with inversion symmetry. (c) Side view of a monolayer, with broken inversion symmetry. (d) Top view. Tungsten (W) and sulphur (S) atoms are shown in grey and yellow, respectively. This figure has been produced using Vesta software.[162]

Graphene is considered a zero-gap semiconductor, or a semimetal.[167] The interest in graphene over the last decades arises due to its outstanding mechanical,[143], thermal[168] and electronic properties,[140, 144, 169] making it suitable for applications such as biosensors,[170, 171] composite materials[172, 173] and field effect transistors.[174, 175] In comparison, some TMDCs, such as WS_2 and MoS_2, are semiconductors and have a band gap, and thus they are also photoluminescent due to exciton (electron-hole pair) recombination upon photon excitation.[176–178] Interestingly, the band gap can be tuned depending on the number of layers. Thus, the bulk material and several-layer TMDCs exhibit an indirect band gap, as the optical transition occurs at two different points in momentum space[179] (Figure 4.3a) and therefore photoluminescence is weak.[156, 180] The band gap becomes direct (momentum-allowed, Figure 4.3b) on going to the monolayer regime, which enhances photoluminescence by several orders of magnitude and shifts the energy transition to higher energies (Figure 4.3c).[180–184]

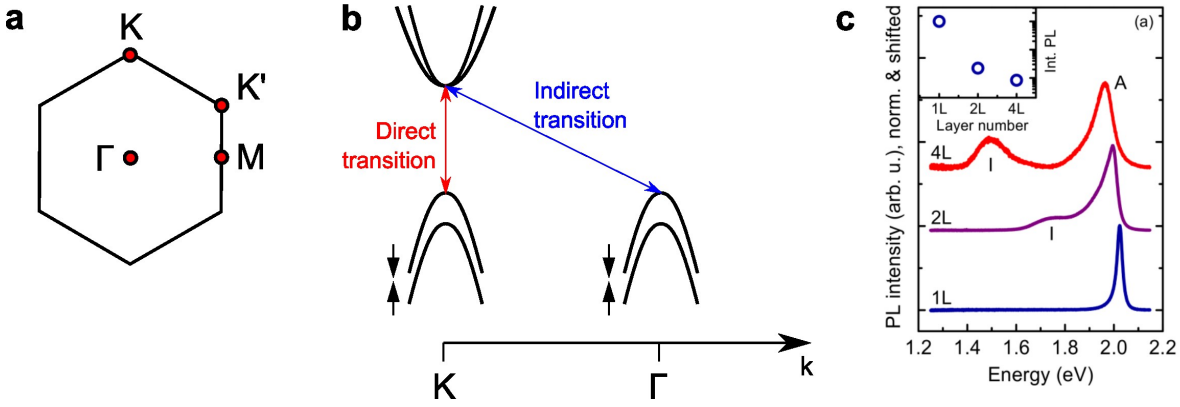

Figure 4.3: Optical properties of TMDCs. (a) First Brillouin zone showing the high-symmetry points K, K', Γ and M. (b) Diagram showing direct (red) and indirect (blue) transitions in momentum (k) space. Note that the valence band is primarily made of d-orbitals and thus it is split due to spin-orbit coupling.[184] (c) Layer-dependent photoluminescence in WS_2 (taken from reference [185]).

The highly tunable band gap of TMDCs has opened up new applications in optoelectronic devices, such as photodetectors that can detect different wavelengths depending on the number of layers in the TMDC.[148] Another reason why TMDCs have attracted the attention of the scientific community is due to the rich exciton physics that can be found in these materials.[186] For example, the introduction of defects creates localized excitons (*e.g.* at edges) which can be used as single quantum emitters.[187–189] Due to the layered structure of TMDCs, interlayer excitons in TMDC heterostructures can be formed, providing different means to tune the band gap properties for optoelectronic devices.[190, 191] TMDCs also find applications as valleytronic devices due to valley-selective polarization and spin-valley coupling,[192], which could be used for information storage devices.

4.1.2 Strain engineering of 2D materials

The properties of 2D materials can be tuned by applying different types of strain to the sample. Strain engineering encompasses wrinkle formation,[193–195] stretching,[196] bending[159, 197, 198] or compression.[199] Traditionally, this has been done utilizing micromanipulators, which are devices that allow to either mechanically stretch, compress or bend the sample.[199] In the case of wrinkle formation, the strain can be

generated by pre-stretching the substrate, depositing the 2D material and releasing to generate the wrinkles.[193]

In TMDCs, it has been observed that the band gap is very sensitive to the different types of strain, such as uniaxial compression and elongation,[156, 200–202] uniaxial strain by bending,[196] biaxial strain,[198] wrinkling[193, 195, 203] and others.[204] As 2D materials have a large tensile strength,[159, 160] stretching or compressing the material requires strong forces (Figure 4.4a). However, as it can be seen in the examples of Figure 4.4b,c, 2D materials are flexible and out-of-plane deformations can be produced with minimal forces. In all the three examples of strain applied, strain generates a red shift of the band gap in addition to a direct-to-indirect band gap transition,[202, 204] although out-of-plane deformations are much more facile to produce.

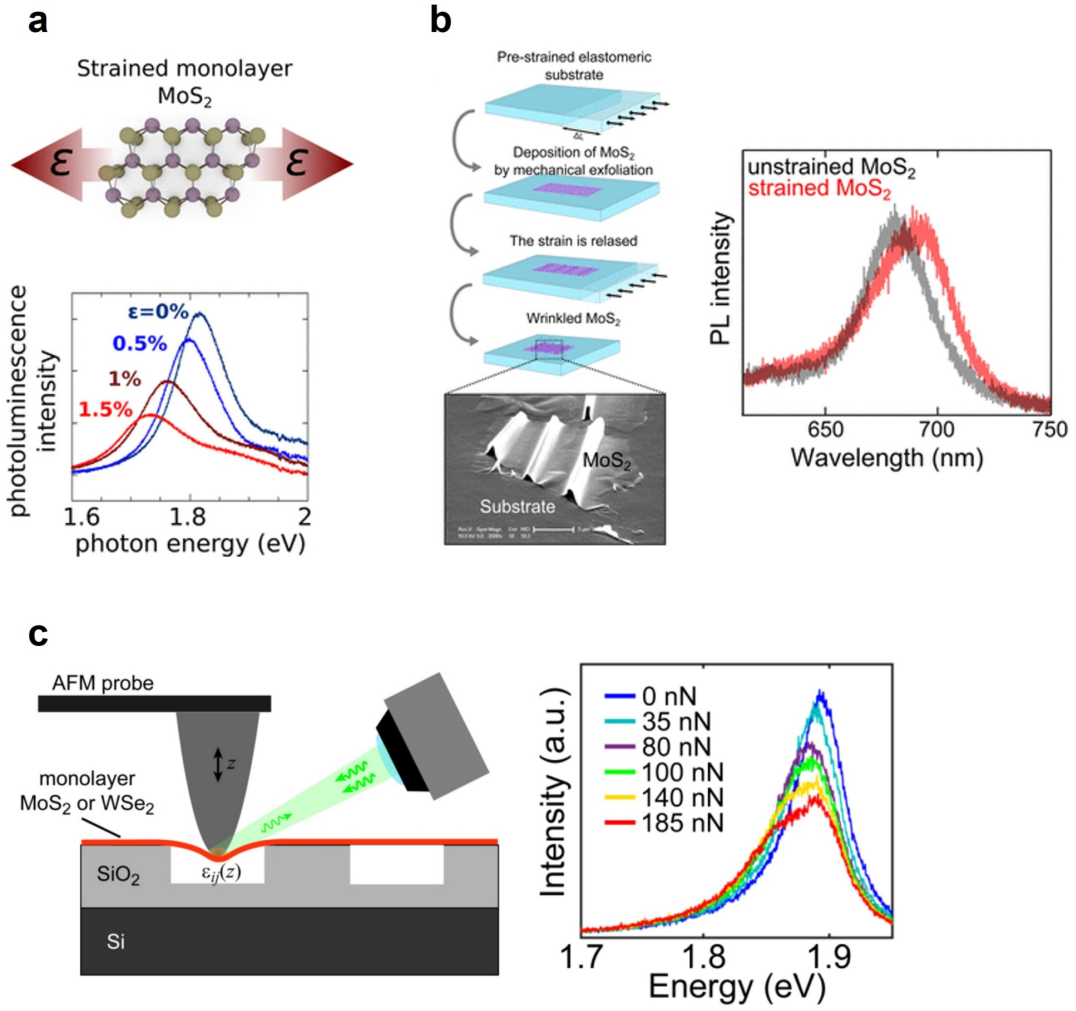

Figure 4.4: Examples of strain engineering in TMDCs. (a) Uniaxial tensile strain applied in monolayer MoS_2. Taken from reference [196]. (b) Wrinkle formation in monolayer MoS_2. Taken from reference [193]. (c) Out-of-plane deformation in MoS_2 using an AFM tip. Taken from reference [131]. In all cases, a red shift in the PL and shoulder at smaller energies is observed.

In the case of graphene, the electrical properties are highly dependent on the presence of out-of-plane deformations in the sample, with wrinkles and rumples reducing the conductance.[205, 206] Furthermore, new properties, such as band gap opening, have been predicted with other types of strain, such as uniaxial tensile strain[207] and shear strain.[208] The effects of strain on graphene can be extensively studied using Raman spectroscopy,[209] as discussed in more detail in § 4.2.5.

In this chapter, a new non-contact method for wrinkling 2D materials is developed. This method simply exploits the orbital angular momentum transfer between a light beam and an absorbing medium. Not only does this method expand on the research

that has been undertaken so far in the optical manipulation of matter (§ 2.3.2), but it also provides a non-contact and reversible means to tune the properties of 2D materials. This is exemplified by controlling the conductance of monolayer graphene, and photoluminescence in monolayer WS_2, and wrinkle enhancement is verified by Raman spectroscopy and AFM.

4.2 Experimental details

4.2.1 Samples

The effects of angular momentum transfer on monolayer graphene were investigated using conductance measurements, Raman spectroscopy and AFM. Conductance measurements and Raman spectroscopy were performed using a commercially available graphene field effect transistor (GFET, from Graphenea). A field effect transistor is an electrical device consisting of a semiconductor channel and three electrodes (the source, the drain and the gate electrodes), which are used to control the flow of current through the channel. In a GFET, the channel is monolayer graphene, and being a monolayer means that the current running through the graphene channel is extremely sensitive to the environment. For example, the conductance across the channel changes when different molecules are adsorbed, making the detection of single molecules possible.[210, 211] In the GFET used in this work, the monolayer graphene is grown by CVD and transferred onto a 90 nm SiO_2/Si substrate. The active component of the GFET is a 90 μm$\times$ 90 μm monolayer graphene, as depicted in Figure 4.5.

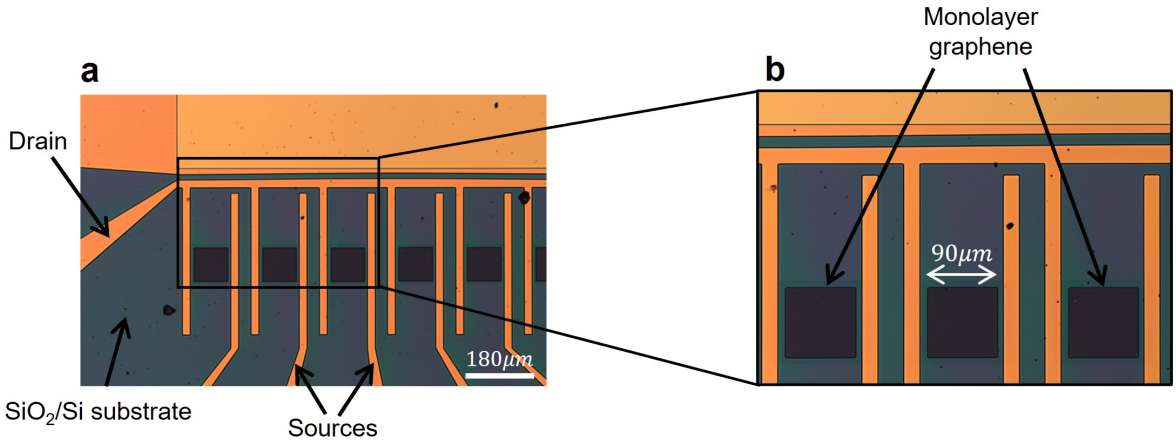

Figure 4.5: (a) Optical microscopy image of the GFET used in this work, showing external drain and individual source electrodes. (b) Optical microscopy image of the GFET taken with higher magnification. Taken from reference [126].

For AFM measurements of graphene, an equivalent CVD-grown 1 cm×1 cm full-coverage monolayer graphene sample (also obtained from Graphenea) was used. This was done due to experimental constraints of the AFM tip not being able to reach the cavity where the monolayer graphene was in the GFET.

In the case of monolayer WS_2, the effect of orbital angular momentum was investigated using a 1 cm×1 cm CVD-grown full-coverage monolayer WS_2 on Al_2O_3 (Ossila) and exfoliated monolayer WS_2 flakes on SiO_2/Si (2D semiconductors). The exfoliated flakes were prepared *via* chemical exfoliation from the bulk material onto a 90 nm thick thermal oxide. As shown in the optical microscopy images of Figure 4.6, chemical exfoliation from the bulk leads to flakes of different sizes and shapes, with lateral dimensions approximately spanning 5-40 μm. Exfoliation also results in flakes with varying thicknesses, which appear with a different optical contrast under the optical microscope. The monolayer flakes were easily identified with photoluminescence spectroscopy as they exhibit strong photoluminescence in the red region.[181]

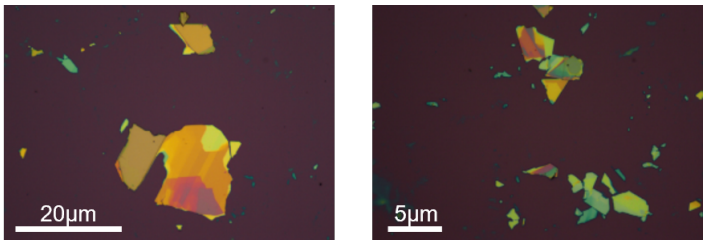

Figure 4.6: Optical microscopy images of exfoliated WS_2 flakes on SiO_2/Si. The exfoliation process results in flakes with random shapes, sizes and thicknesses.

4.2.2 Generation of angular momentum beams

Beams carrying spin angular momentum were generated using a quarter-wave ($\lambda/4$) plate. $\lambda/4$ plates are made of birefringent materials, and therefore their refractive index is different for vertical and horizontal directions. If the light is polarized along the axis with lower refractive index it will travel faster (fast axis) than the light polarized along the axis with higher refractive index (slow axis).[28] In the example shown in Figure 4.7, unpolarized light goes through a linear polarizer and becomes linearly polarized, with the electric field oscillating in the polarization direction of the polarizer. The linearly-polarized light then can go through a $\lambda/4$ plate where the fast axis is aligned at $+45$ or -45 degrees from the polarization direction, which results in left or right-handed circularly-polarized light.

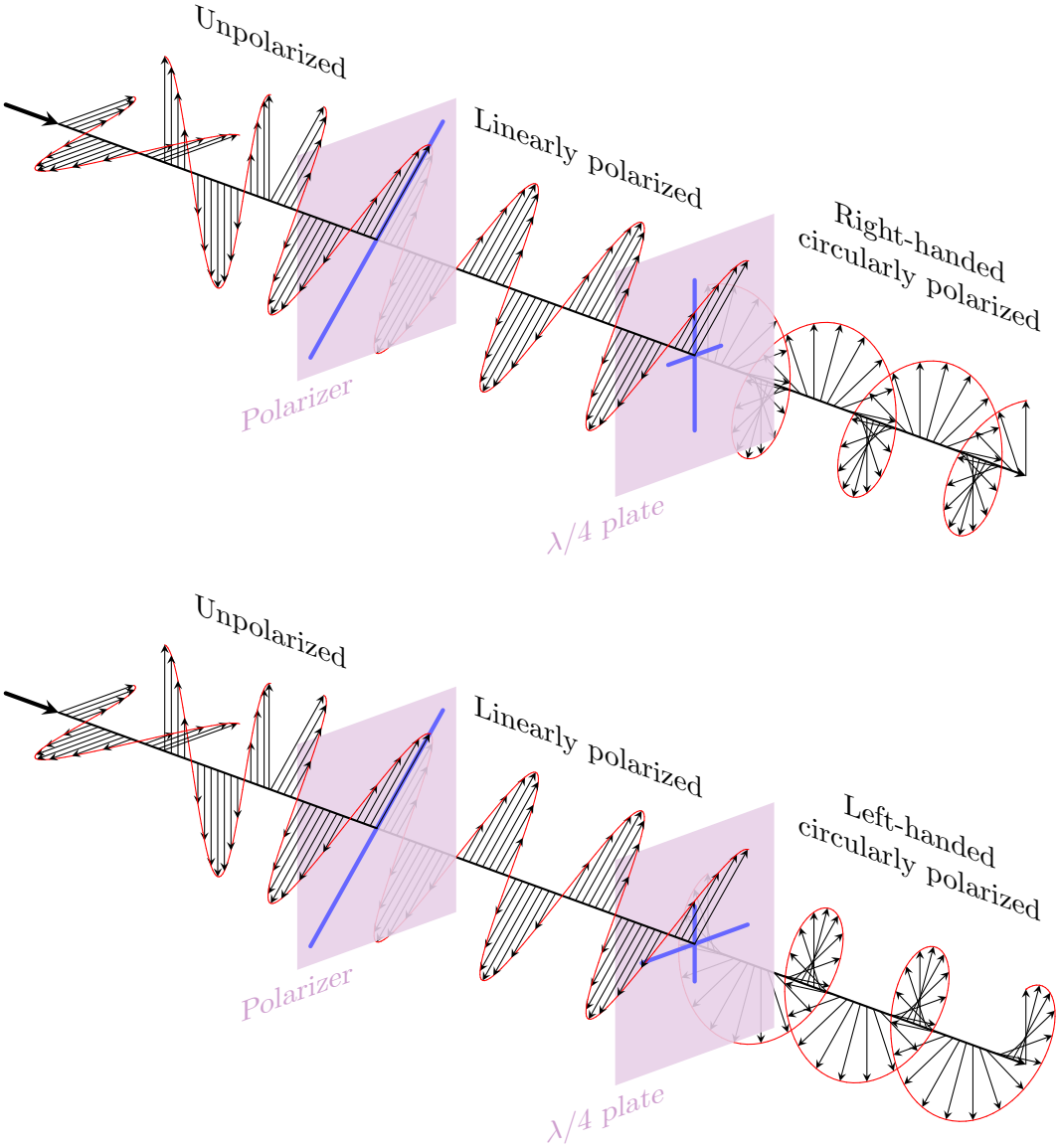

Figure 4.7: Unpolarized light becomes linearly polarized along the polarization axis of the polarizer (blue line). Circularly-polarized light is generated with a $\lambda/4$ plate whose fast axis is aligned at $+45$ or -45 degrees with respect to the polarization direction. In the $\lambda/4$ plate, the fast and slow axes are indicated with a longer and shorter blue vertical lines, respectively.

LG beams carrying orbital angular momentum were generated using spiral phase plates. A spiral phase plate is a spiral-like piece of glass whose thickness increases with the azimuthal angle ϕ, in a continuous or step-wise manner, as shown in Figure 4.8a.[212, 213] It can be mounted in a lens mount which can be then easily inserted along the optical axis, depicted in Figure 4.8b.

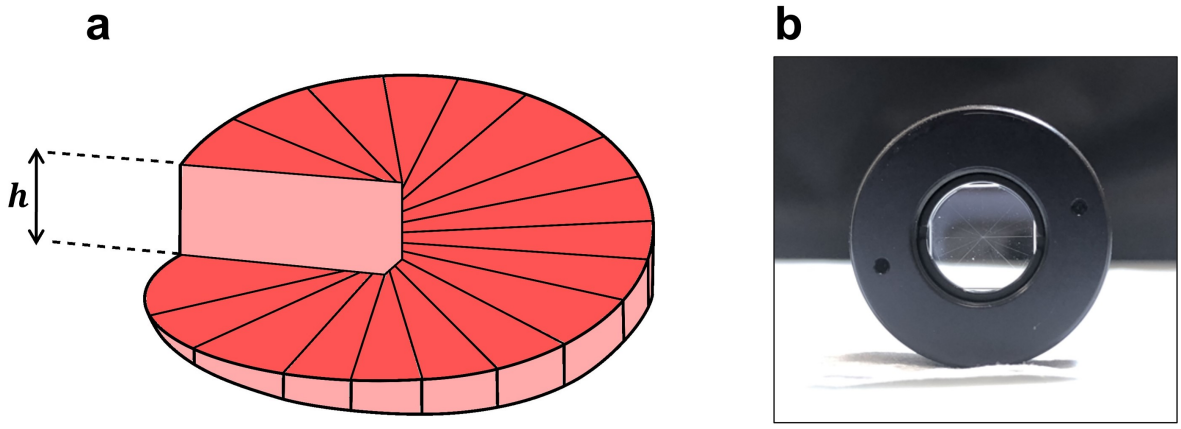

Figure 4.8: (a) Diagram of a spiral phase plate, showing that after $2\pi l$ cycles, the step height of the plate is h. The diagram is shown for a spiral phase plate with $l = 1$. (b) Spiral phase plate ($\lambda_{exc} = 532$nm, $l = 4$) from Vortex Photonics, mounted in a lens mount.

Rays travelling through the thicker portion of the plate will experience a larger phase delay than those travelling through the thinner portion, and thus the phase of the beam becomes azimuthally dependent. Let h be the difference in height between the thinnest ($\phi = 0$) and thickest ($\phi = 2\pi$) portions of the spiral phase plate, Figure 4.8. Then, the thickness of the plate around the azimuth should depend on the azimuthal angle ϕ as[21]

$$t(\phi) = \frac{h\phi}{2\pi}, \tag{4.1}$$

and the phase delay experienced by the beam after going through the spiral phase plate is[213]

$$\psi(\phi) = \frac{(n_1 - n_2)h}{\lambda}\phi, \tag{4.2}$$

where n_1 and n_2 are the refractive indexes of the spiral phase plate and air, respectively, and λ is the wavelength in free space. As shown in equation 4.2, the phase delay is proportional to the azimuthal angle ϕ and height difference h. The topological charge

of the plate is given by[213]

$$l = \frac{h(n_1 - n_2)}{\lambda}. \tag{4.3}$$

If the spiral phase plate is manufactured in such a way that equation 4.3 holds, the LG beam acquires a topological charge of l. Substituting equation 4.3 into equation 4.2, it is clear that the additive phase delay around the plate is $2\pi l$. The handedness of the beam is changed by reversing the orientation of the spiral phase plate.

As seen in equations 4.2 and 4.3, the spiral phase plate design is different depending on the wavelength and topological charges used. The fact that spiral phase plates are wavelength-dependent can be a disadvantage in applications where tuning the wavelength is required (for example, in Chapter 5, where Q-plates were used instead for this reason). In this chapter, angular momentum transfer was studied at a particular wavelength. Recall that one of the methods to transfer angular momentum to a material requires photon absorption (see § 2.3.2 for more details). The imaginary refractive index k (extinction coefficient) is related to the absorption within the material *via* the absorption coefficient $\alpha = 2\omega k/c$, with the beam intensity decreasing as a function of the absorption coefficient as[28]

$$I(z) = I_0 e^{-\alpha z}. \tag{4.4}$$

The excitation wavelength (λ_{exc}) was chosen depending on the availability of spiral phase plates, lasers and absorption characteristics of the material. Different spiral phase plates were used for the illumination of monolayer graphene and monolayer WS_2, operating at $l = 2$ ($\lambda_{exc} = 405$ nm) and $l = 4$ ($\lambda_{exc} = 532$ nm), respectively (Vortex photonics). Figure 4.9 shows the real and imaginary refractive indices of monolayer graphene and monolayer WS_2 in comparison to the excitation wavelength. The extinction coefficients k of monolayer graphene and WS_2 at the excitation wavelengths have value of 1.13 at 405 nm[127] and 0.9 at 532 nm,[128] respectively. Therefore, absorption

and subsequently angular momentum transfer are expected at these wavelengths, as validated by the simulations in Chapter 3.

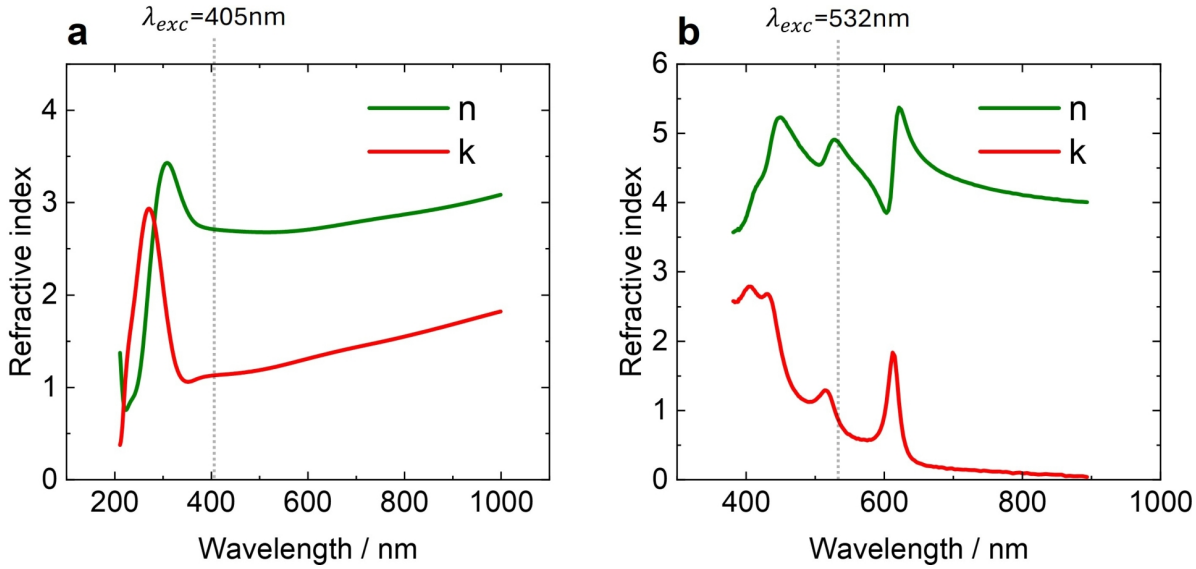

Figure 4.9: Real (n) and imaginary (k) refractive indices of (a) monolayer graphene and (b) monolayer WS_2. The values have been taken from references [127] and [128], respectively. The excitation wavelengths (λ_{exc}) are shown with a dashed vertical line.

In the illumination of both graphene and WS_2, the spiral phase plate was placed in an xy mount to align its centre with the optical axis of the beam, as beams going off centre can distort the optical vortex.[214] Centering of the beam was achieved by tuning the xy mount until the position of the optical vortex was in the middle of the beam and the beam visually looked as symmetric as possible. Some images of the LG beams are shown in Figure 4.10.

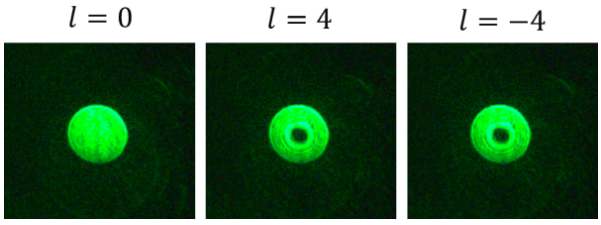

Figure 4.10: Images of a Gaussian beam (l= 0), and OAM beams (l= 4 and l= −4) after inserting the spiral phase plate for the 532 nm laser.

In the case of graphene, spin-orbital effects were also investigated, where the beam had both spin and orbital angular momentum. Here, the relative sign of SAM and OAM had to be determined as it dictates the total angular momentum content of the beam. In

the case of circularly-polarized light carrying SAM, it has been established that (looking towards the source) left-circularly polarized light has SAM of $+\hbar$ and right-circularly polarized light has an SAM of $-\hbar$, and this is determined by the relative orientation between the linear polarizer and the $\lambda/4$ plate (Figure 4.11).[28]

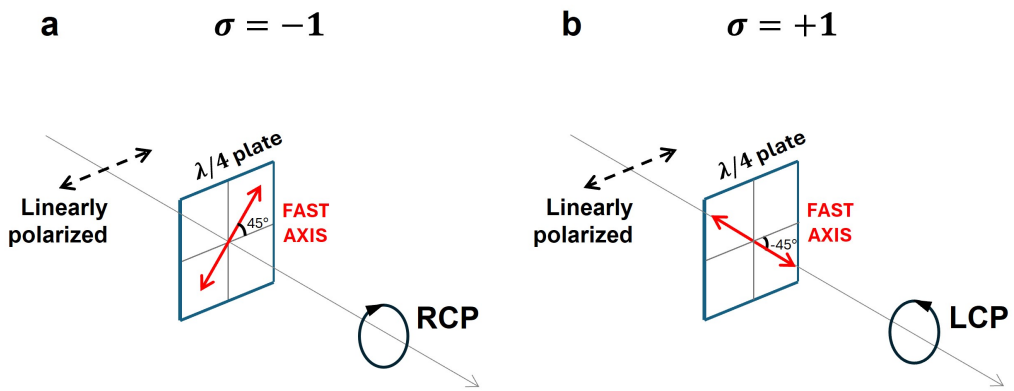

Figure 4.11: (a,b) Schematic showing the sign convention for SAM of (a) $-\hbar$ and (b) $+\hbar$. The fast axis of the quarter wave plate is indicated with a red arrow, and the propagation axis is shown with a grey arrow.

The sign of OAM in the LG beam generated by the spiral phase plate was obtained using the diffraction by a knife edge technique.[215] The beam was diffracted by an object having a sharp edge and the diffraction image was recorded with a camera. As shown in Figure 4.12, a forked diffraction pattern is obtained, as expected for beams carrying OAM.[216] The number of components in the fork is given by $|l| + 1$.[216, 217] Figure 4.12 shows 3 components, which agrees with the topological charge of $l = 2$ used in this work.[218] Most importantly, the fork points in the opposite direction when the orientation of the plate is reversed, from which the sign of OAM can be determined.[218] Additionally, it was observed that changing the polarization of the beam did not alter the pattern, as expected for a spiral phase plate.

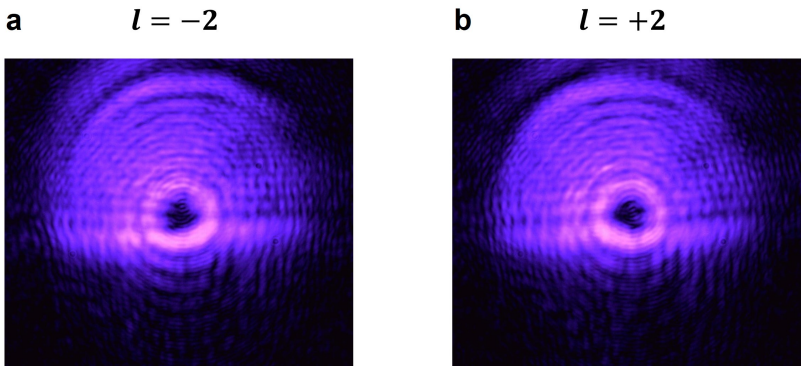

Figure 4.12: (a,b) Experimental images of a $l = 2$ beam diffracted by a knife edge technique[215] having a topological charge of (a) $l = -2$ and (b) $l = +2$. The transition from (a) to (b) was done simply by reversing the orientation of the spiral phase plate.

4.2.3 Building an optical set-up

As part of this thesis, an optical set-up was built from scratch in order to illuminate monolayer graphene with beams carrying angular momentum. A schematic of the set-up used for the illumination of graphene is shown in Figure 4.13. A 405 nm laser beam (Laser Arx, MDL-III-405-100) was used as the excitation source. The beam was cleaned and expanded to 5 mm diameter using a beam expander and spatial filter comprised of a first lens ($f_1 = 50$ mm), a pinhole (100 μm) and a second lens ($f_2 = 150$ mm). The beam was expanded in order to minimize possible misalignments which affect the quality of the vortex.[214]

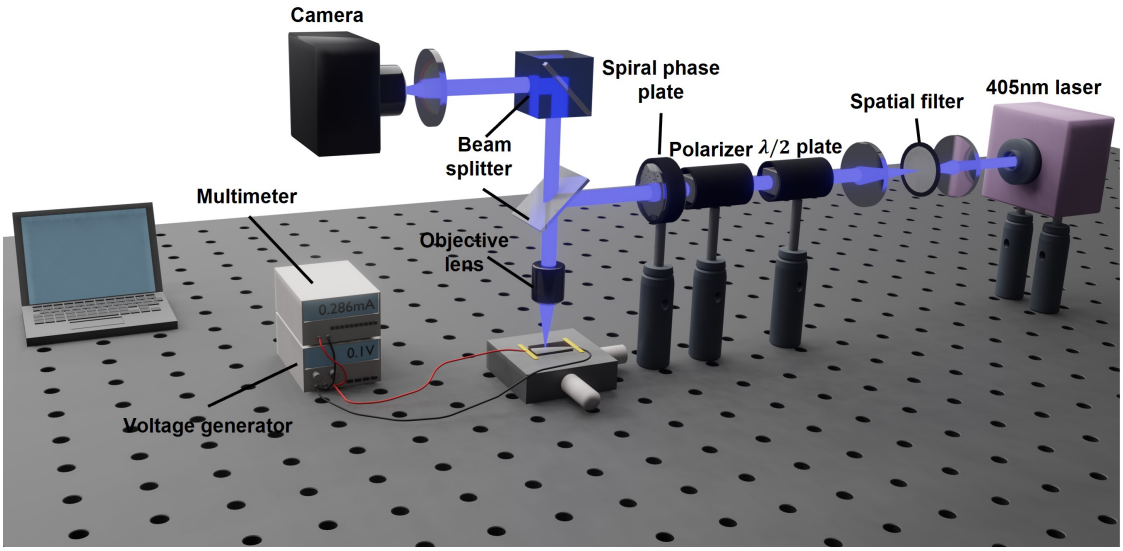

Figure 4.13: Schematic of the set-up that was built for the illumination of graphene in this chapter. Figure obtained from reference [126].

A $\lambda/2$ plate and a Glan-Thomson polarizer were used to control the excitation power. The polarizer was aligned with a another polarizer. By changing the angle between the two polarizers, the beam intensity can be plotted according to Malus' law, $I = I_0 \cos^2\theta$, where θ is the angle between the two polarizers. It was checked that minimum power was obtained at a relative angle of $\theta = 90°$, Figure 4.14.

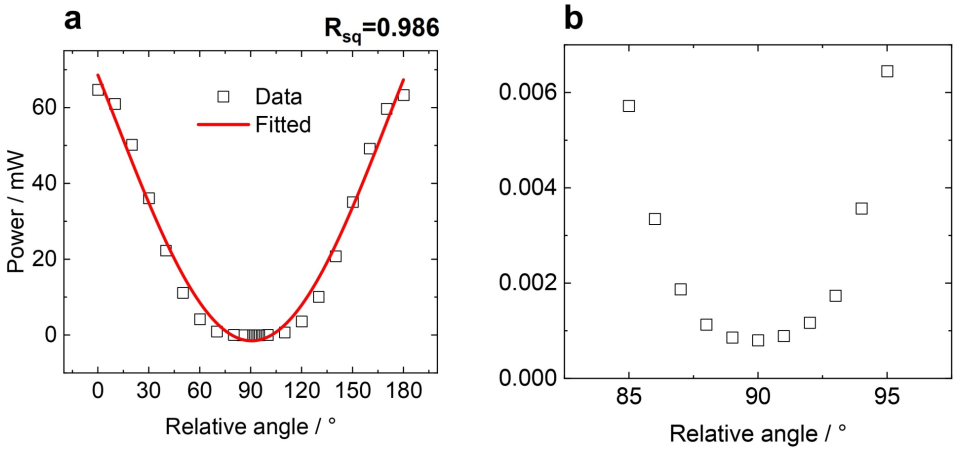

Figure 4.14: Power measured as a function between two linear polarizers for (a) relative angles between 0 and 90 degrees and (b) angles in the vicinity of 90 degrees. In (a), the data (open squares) have been fitted to the intensity function $I = I_0 \cos^2\theta + y_0$, where θ is the relative angle between the polarizers and the R-squared parameter (R_{sq}) is indicated at the top right corner.

A spiral phase plate was placed along the optical axis to generate the LG beam

(Vortex photonics, $l = 2$, 405 nm). The plate was placed in an xy mount to allow proper alignment of the centre of the spiral phase plate with respect to the optical axis. After this, the beam was coupled to a home-built microscope system containing a 50:50 beam splitter and a 10X objective (NA=0.25) to direct the beam towards the sample. The excitation power of the beam was measured between this beam splitter and the objective lens.

A broadband light source (Thorlabs, SLS203F/M, not shown in the schematic of Figure 4.13) was implemented to visualize the sample while it is illuminated with the laser beam. For this, the white light was focused with a $f = 200$ mm achromatic lens into the back aperture of the objective lens, which makes the beam collimated for an even illumination of the sample. The back reflected light was collected using the same objective lens and projected onto a camera (Thorlabs, CS165CU1/M) with a $f = 100$ mm lens to visualize the sample. The precise position of this lens was adjusted by placing the lens in a slotted tube (Thorlabs, SM1L10C) to easily adjust its position. Perfect focusing and positioning of the lens was achieved by adding an objective wheel (Thorlabs, OT1) with 10X, 60X and 100X objectives attached. Then, the light was focused onto the sample with 100X by moving the sample stage in the z direction until an image was observed; the objective was then changed to 10X and the position of the lens was adjusted until the image was visible again. This refocusing process was repeated until changing from 100X to 10X no longer changed the focus and until an image was observed in both cases without further tuning the position of the lens or the height of the sample stage. Some examples of the optical microscopy images achieved with 10X and 100X objectives are shown in Figure 4.15. The images show a plasmonic array that contains periodic shuriken-shaped nanoindentations.

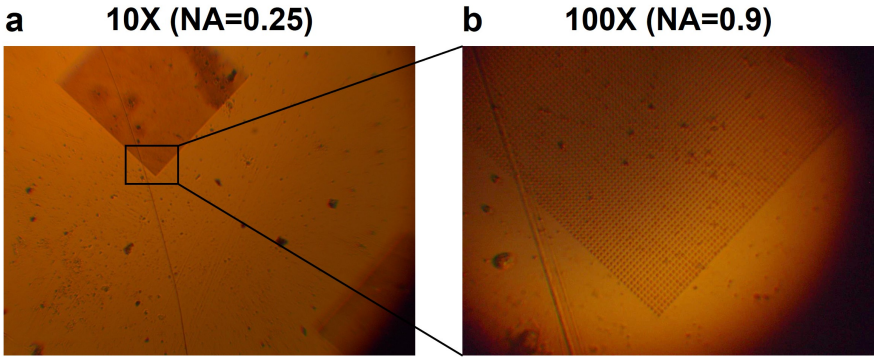

Figure 4.15: Optical microscopy of shuriken-shaped nanoindentations achieved with the home-built microscope system. (a) With 10X objective. (b) With 100X objective.

4.2.4 Conductance measurements

Conductance measurements were taken from monolayer graphene in the GFET to illustrate how shear strain generated by LG beams can be used to reconfigure the response of 2D material-based electronic devices.

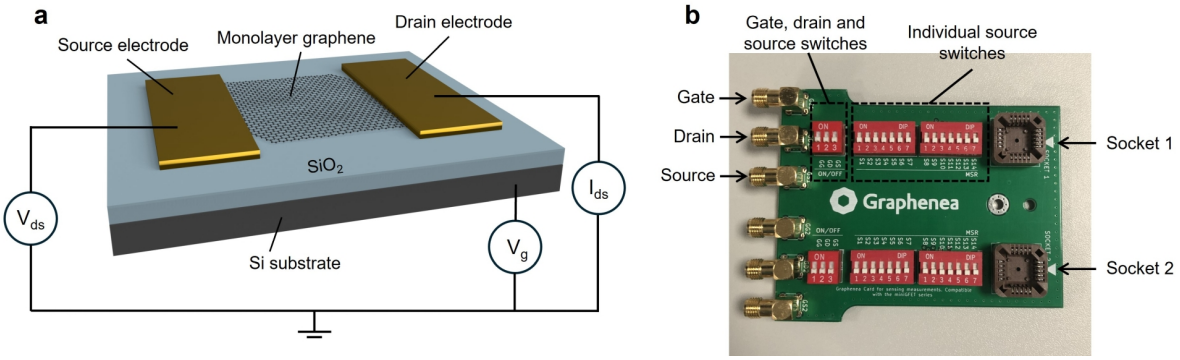

Figure 4.16: (a) Schematic showing the electrical connections in the GFET. V_{ds}: drain-source voltage. V_g: gate voltage. I_{ds}: drain-source current. (b) Image of the physical card (Graphenea) into which the GFET is incorporated for the conductance measurements.

The conductance was obtained from the collection of I-V curves in the GFET; that is, the current between the drain and the source (I_{ds}) was measured as a function of the voltage applied between the drain and the source (V_{ds}), before and after illumination (Figure 4.16a). The gate voltage (V_g) was set to 0 in all the measurements. The GFET was directly incorporated into a physical card (Graphenea) containing external switches for each individual source corresponding to different individual graphene

channels (Figure 4.16b).

A DC power supply (Rapid HY3005-3) was used in order to apply the voltage between the drain and the source. A multimeter (True RMS digital multimeter DM-441B) was used to measure the current between the drain and the source. The current and voltage are related using Ohm's law, given by

$$I_{ds} = \frac{1}{R} V_{ds}, \tag{4.5}$$

where R is the resistance. The conductance is simply obtained from the inverse of the resistance, $1/R$, which corresponds to the slope of equation 4.5. The error in the conductance was obtained from the standard error of linear fits of the I-V characteristics. An example of a linear fit is shown in Figure 4.17a. The conductance (slope) obtained from the linear fit is 1504±4 $\mu\Omega^{-1}$.

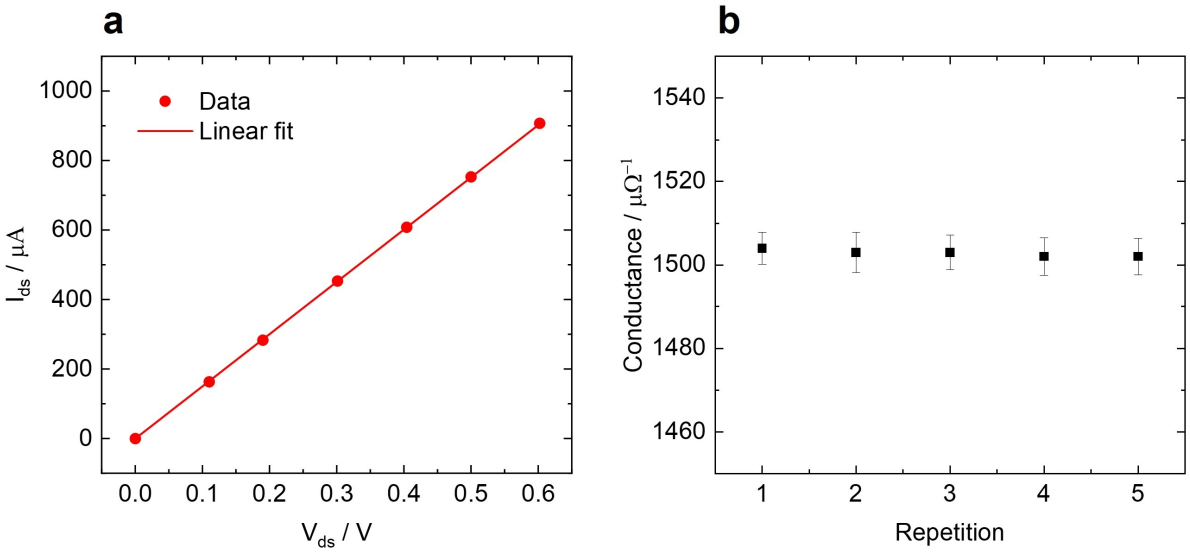

Figure 4.17: (a) Example of the I-V characteristics of a GFET (red circles) fitted to a linear fit (red line). The R-squared parameter of the fit is >0.999. (b) Extracted conductance from the linear fit after consecutive measurements, showing no variation in the conductance after the application of voltage.

The maximum drain-source voltage applied was 0.6 V to prevent heating in the GFET. The I-V curves were repeated five times prior to illumination to verify that no heating was produced in the GFET, and the conductance was extracted each time. An example of this procedure is shown Figure 4.17b, showing that the conductance

remained constant over the five repetitions.

4.2.5 Raman spectroscopy and mapping

Raman spectroscopy is a useful characterization technique based on scattering, different from photoluminescence spectroscopy which is based on absorption (§ 4.2.7). If the scattering is elastic and the energy of the photon does not change, the scattering process is called Rayleigh scattering. In the case where the photon energy changes, the scattering is called inelastic or Raman scattering. Raman scattering is an inherently weak process, as the scattering process is dominated by Rayleigh scattering and only one in $10^6 - 10^8$ photons is Raman scattered.[219] In Raman scattering, shown schematically in Figure 4.18a, the incoming photon with energy $\hbar\omega_1$ changes its energy to $\hbar\omega_2$, where ω_1 and ω_2 are the angular frequencies of the incoming and outgoing photons, respectively, and $\omega_1 \neq \omega_2$. Raman scattering can be of two types: Stokes and anti-Stokes scattering. Stokes scattering occurs if some of the energy is transferred from the photon to a vibrational state of the sample ($\omega_2 < \omega_1$). Instead, anti-Stokes scattering occurs when the sample transfers some energy to the photon ($\omega_2 > \omega_1$).[219] In this way, it is possible to obtain a spectrum, called Raman spectrum, which contains features derived from the vibrational states of the sample, and therefore Raman spectra are characteristic of each material.[220] Generally, Stokes scattering is much more intense than anti-Stokes scattering, therefore Raman spectra are frequently reported using the Stokes scattering.[219]

As graphene does not have a band gap, no information can be obtained from photoluminescence spectroscopy, which is frequently used for 2D semiconductors such as monolayer WS_2. Instead, Raman spectroscopy is widely used to study the properties of graphene, and it is used to gain a wide range of information about the sample.[221]

In this chapter, Raman spectroscopy and mapping was used to characterize the properties of monolayer graphene before and after illumination with LG beams. Raman mapping of the GFET (Graphenea) was done using a commercially-available Raman

spectroscopy set-up (LabRAM HR Evolution) employing a laser excitation wavelength of 532 nm (excitation power: 500 μW) and 50X objective (NA=0.5). The Raman mapping was started approximately 5 minutes after LG beam illumination and it took an overall time of 2 hours to be completed.

Raman spectra are reported in wavenumbers ($\tilde{\nu} = 1/\lambda$, in cm^{-1} units) with respect to Rayleigh scattering, thus 0 cm^{-1} corresponds to the Rayleigh scattering at the laser excitation (532 nm in this case). An example of a Raman spectrum collected from the monolayer graphene in the GFET is shown Figure 4.18b. The spectrum contains mainly two peaks, commonly referred to as G- (1590 cm-1) and 2D- (2685 cm-1) bands.[222] A lot of information about the characteristics of graphene can be obtained from these two bands, such as the number of layers,[223, 224] adherence to the substrate,[225] electron and hole doping, [226] strain effects[227, 228] and others.[221, 229] Another peak, known as the D-band, can appear at 1350 cm^{-1} due to the presence of defects or disorder in the sample. Disorder in graphene may be due to physical modifications that reduce the translation symmetry, such as the formation of wrinkles.[222, 229, 230]

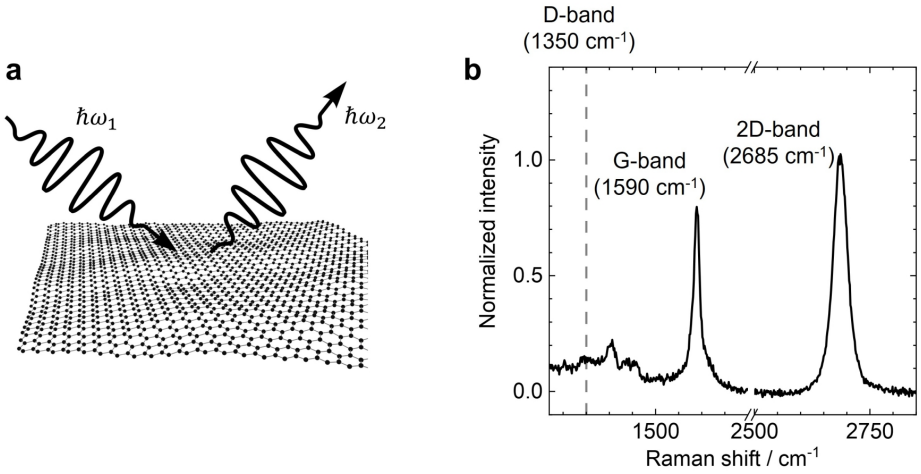

Figure 4.18: (a) Schematic of inelastic Raman scattering process in a monolayer graphene sample. ω_1 and ω_2 are the angular frequencies of the incoming and outgoing photons, respectively. (b) Example of a Raman spectrum taken from the monolayer graphene in the GFET.

Raman mapping in the GFET was done to monitor the changes at the areas illuminated with beams carrying angular momentum in comparison to the non-illuminated areas. Raman mapping consists of collecting a Raman spectrum point by point across

the sample, and several features, such as the position of the G- and 2D-bands, can be plotted as a two-dimensional image to visualize the differences in the Raman scattering across the sample. The Raman mapping conducted here was performed using a 12×12 grid across the 90 μm× 90 μm monolayer graphene, and the obtained two-dimensional image was smoothed in the x and y directions. An example of the raw and smoothed data for the G- and 2D-band positions is shown in Figure 4.19.

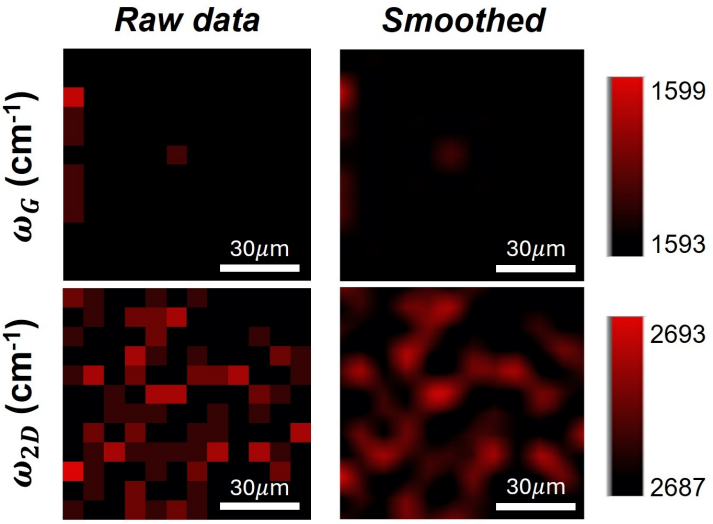

Figure 4.19: Raw and smoothed images for the position of the G- (ω_G) and 2D- (ω_{2D}) bands in a GFET.

4.2.6 Atomic force microscopy

Atomic force miscroscopy (AFM) was used to study the effects angular momentum transfer from a light beam to monolayer graphene. AFM is a useful technique to study the morphological characteristics of samples. The technique uses a cantilever with a sharp silicon or silicon nitride tip at the end; the tip usually has a radius of several nanometers. A laser is focused on the cantilever and the reflected light is detected in a photo detector. When the tip is scanned across the surface of the sample it will oscillate up and down, causing the reflected laser beam to deflect. The laser deflection is detected in the photo detector and a map of the height of the surface can be generated. This process is shown schematically in Figure 4.20.

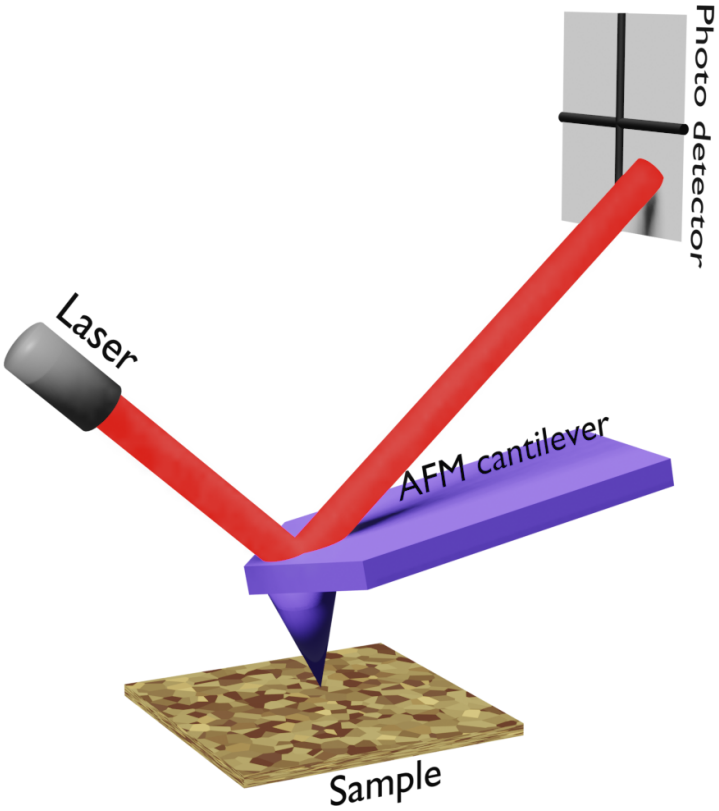

Figure 4.20: Schematic of an AFM set-up. A laser beam is focused on a cantilever and the reflected beam is detected in a photodetector. The laser deflection will change as the tip goes across the surface, therefore providing information about the height and roughness of the sample.

As opposed to similar surface characterization techniques, such as scanning tunneling microscopy, AFM does not require conductive samples and it is based on force interactions between the tip and the sample, and not based on the tunneling current between the tip and the surface. Therefore, AFM creates a map of the height distribution of the sample, rather than local density of states.[231]

In addition to getting an image of what the physical dimensions of the sample look like, height profiles and roughness parameters can be obtained. An example of how AFM can be useful is given in Figure 4.21. In this example, a CVD-grown MoS_2 flake was transferred onto shuriken-shaped nanoindentations. From the image, it is possible to see the periodic nanoindentations, obtain information about the lateral distances, periodicity and depth of the nanoindentations, and the size of the MoS_2 flake. It is also possible to see that some parts of the flake have sunk inside the nanoindentations, whereas other parts of the flake are suspended over them.

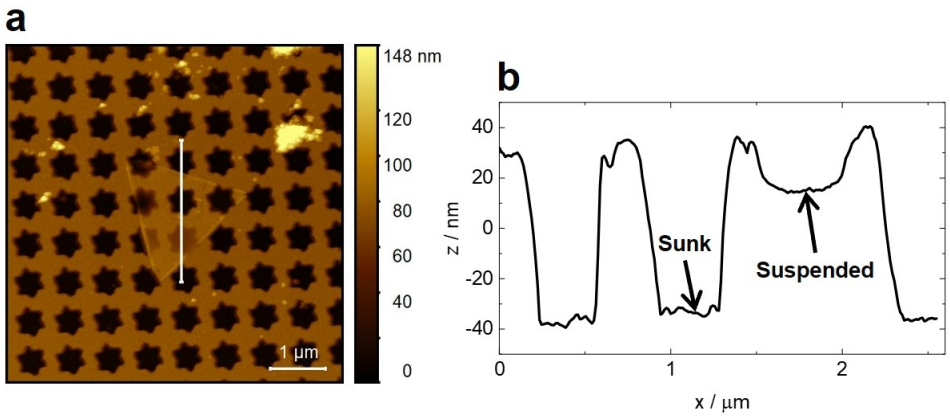

Figure 4.21: AFM example. (a) AFM image of a MoS_2 flake transferred onto shuriken nanoindentations. (b) Extracted height profile across the white line shown in (a), showing that some parts of the flake sunk inside one of nanoindentations and others are suspended over.

There are several modes that are routinely used in AFM, including contact mode and tapping mode. In contact mode, the tip is in contact with the surface; however, this can damage sensitive samples. AFM measurements in this thesis were performed using peak-force tapping mode and a Dimension Icon Atomic Force Microscope System with ScanAsyst equipped with a silicon tip (ScanAsyst-Air-HPI). It was not possible to do AFM directly in the GFET, as the tip was not able to reach the surface of the GFET due to experimental constraints. Instead, AFM was done on a commercially available (1 cm×1 cm) monolayer graphene sample also grown by CVD and transferred onto 90 nm SiO_2/Si substrate (Graphenea). A scan size of 10 μm, a scan rate of 0.3 Hz and 512 samples/line were used for all the AFM images collected.

All the AFM images in this thesis were processed using Gwyddion software to obtain the roughness and the waviness of the surface of monolayer graphene, which represent high-frequency and low-frequency height variations from a mean value, respectively. The obtained values were compared before and after illuminating the sample with the LG beams. To calculate the roughness, it is assumed that the mean value of the heights is 0 *i.e.*

$$\overline{z} = \frac{\sum_{j=1}^{N} z_j}{N} = 0, \tag{4.6}$$

where z_j is the height at the j-th position. If we define the height deviation at the j-th position to be $r_j = z_j - \overline{z}$, the assumption in 4.6 implies that $r_j = z_j$, and the roughness at the j-th position is given by $|r_j| = |z_j|$. Across all the AFM images, the roughness was parametrized with the root-mean-square roughness parameter R_{RMS}, which is given by

$$R_{RMS} = \sqrt{\frac{1}{N}\sum_{j=1}^{N} z_j^2}. \tag{4.7}$$

The root-mean-square waviness W_{RMS} is the low-frequency variation of R_{RMS}.

Figure 4.22 shows examples of AFM images taken from monolayer graphene. The images show intrinsic wrinkles which appear to have a height $\approx$ 2 nm, in agreement with previous studies.[232, 233] In this work, the error in R_{RMS} was estimated from the standard error in R_{RMS} of the same area of monolayer graphene imaged with two different tips, as depicted in Figure 4.22. This gave an error of $\sigma/\sqrt{2} = 0.14$ nm, where σ is the standard deviation in the R_{RMS} values between the two images.

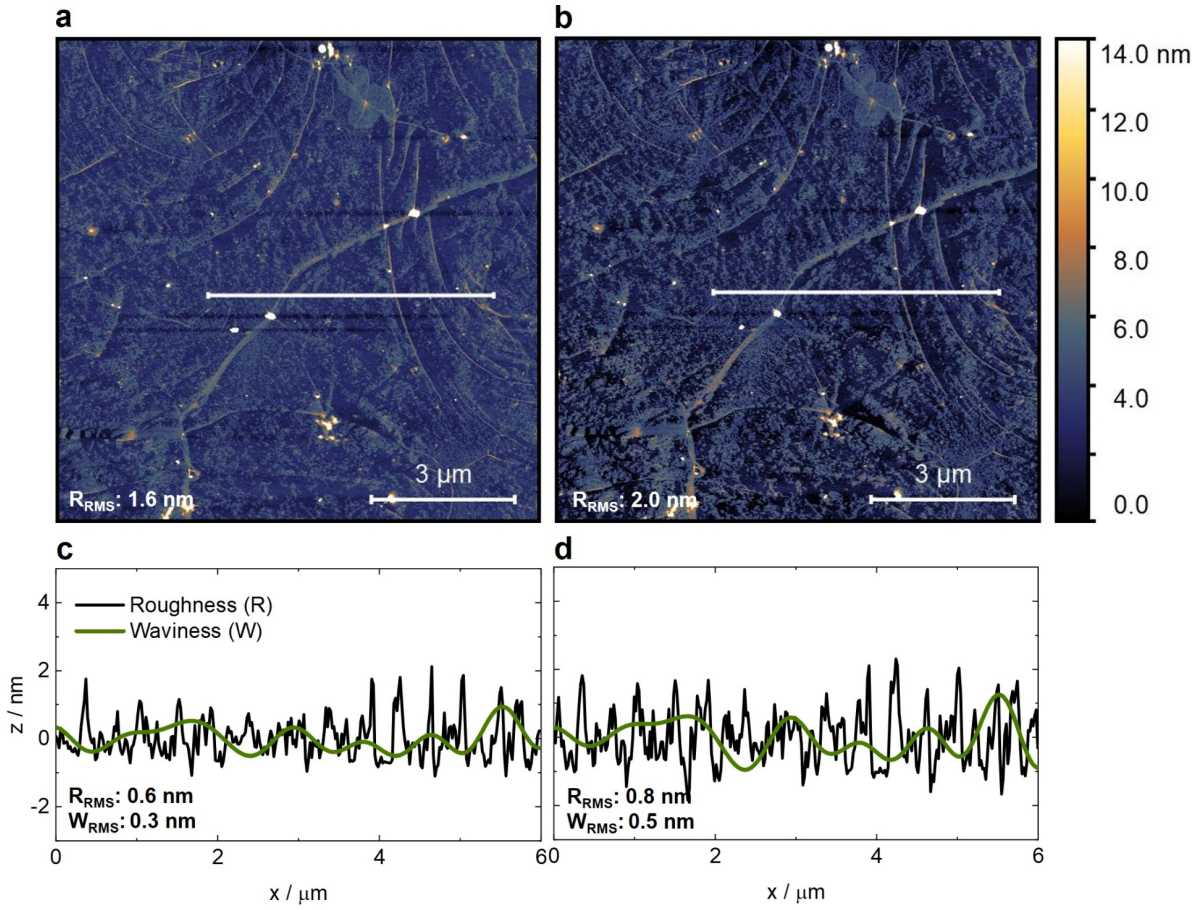

Figure 4.22: (a,b) AFM image of monolayer graphene taken with tip 1 (a) and tip 2 (b). The R_{RMS} of the imaged area shown in the bottom left corner. (c,d) Roughness and waviness profiles across the white cut line in (a) and (b), respectively. R_{RMS} and W_{RMS} are shown in the bottom left corner.

After the monolayer graphene sample was illuminated with a Gaussian ($l = 0$) or a LG ($l = 2$) beam for 2 hours, the AFM scan was started approximately 30 minutes after the illumination stopped and it took an overall time of 30 minutes to be completed.

4.2.7 Photoluminescence spectroscopy

As mentioned in the introduction of this chapter, monolayer WS_2 is a direct-band gap semiconductor and hence it exhibits strong photoluminescence (PL).[145] Therefore, PL spectroscopy is frequently used to characterise the properties of monolayer WS_2.[234, 235] In different studies across the literature, it has been observed that out-of-plane deformations, such as wrinkles, lead to a red shift of the photoluminescence in spectra.[160, 193, 196, 198, 202, 203, 236] Therefore, PL spectroscopy was used to

monitor the wrinkling of the monolayer by the LG beam.

PL spectroscopy is an absorption-based technique and it is commonly used to study the emission and electronic structure of molecules. The emission of a photon by a molecule is called luminescence. After a photon is absorbed, different processes can occur, as depicted in the Jablonski diagram in Figure 4.23. During the absorption, an electron is excited from the ground state to an excited electronic state ($S_0 \rightarrow S_1$ transition). The electron can then undergo vibrational relaxation, where some of the energy is transferred into vibrational modes, and it decays back to the ground state. The decay back to the ground state can be radiative, where a photon is emitted, or non-radiative, without emission, for example, the energy is loss as heat. For the radiative emission, if the decay involves singlet to singlet states, the process is called photoluminescence. Occasionally, it can happen that the electron undergoes a transition from the excited singlet state to a triplet state before decaying back to the ground electronic state. This process, due to being forbidden, is much slower and is known as phosphorescence.

Due to the vibrational relaxation process, the emitted photon has a lower energy than the absorbed photon. This difference in energy is called Stokes shift.

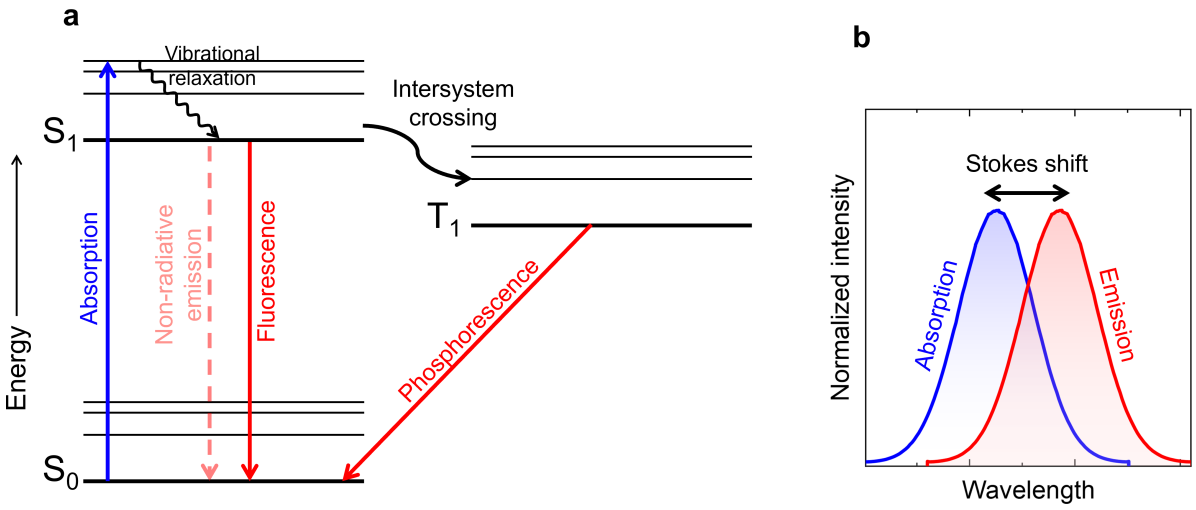

Figure 4.23: (a) Jablonski diagram showing all the processes that can occur after the absorption of a photon in a molecule. S_0 and S_1 denote ground and excited electronic singlet states, respectively, and T_1 excited triplet state. (b) Schematic of absorption and emission spectra, showing the difference in wavelength as the Stokes shift.

In the case of 2D semiconductors, which are the main concern of this thesis re-

garding PL spectroscopy, the energy levels are not discrete. Instead, the energy levels form continuous bands known as valence and conduction bands and the photoluminescence is mediated by excitons (electron-hole pairs). When the photon is absorbed by the sample, the energy of the photon can transfer an electron from the valence to the conduction band, forming an exciton. Due to exciton recombination, photoluminescence can occur. Frequently, neutral exciton (electron-hole pair) and negative trions (2 electrons-hole pair) are observed,[237] as depicted in Figure 4.24. Trions can occur because the substrate can act as a doping centre, favouring the formation of charged excitons like trions.[238] Therefore, it is frequently observed that the PL spectra of monolayer WS_2 have components associated with a neutral (X^0) and trionic (T) excitonic states. Negative trions (2 electrons-hole pair) are common.[237] Positive trions (electron-2 holes pair) have been observed[239] but are less common.

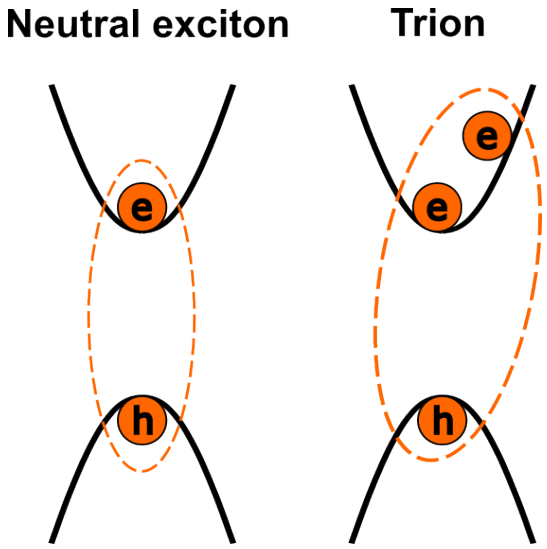

Figure 4.24: Common bound excitons found in 2D semiconductors, such as monolayer TMDCs. e and h denote electrons and holes, respectively.

Photoluminescence spectroscopy of monolayer WS_2 was collected using a home-built set-up equipped with a DPSS 532 nm laser diode (DJ532-40, Thorlabs). The laser beam was collimated using a lens and two polarizers were used to control the excitation power according to Malus' law. A spiral phase plate ($l = 4$, $\lambda_{exc} = 532$ nm, Vortex Photonics) was used to generate LG beams. The beam was directed towards the sample using a 50:50 beam splitter and an objective lens. The excitation power was measured between

this beam splitter and the objective lens. For the CVD-grown sample, the spectra were collected with an excitation power of 100μW and 60X objective (NA=0.9). For the exfoliated monolayer WS_2 flakes, an excitation power of 10μW and a 100X objective (NA=0.9) were used.

A 10:90 beam splitter was used to direct 10% of the light towards a camera (Thorlabs, CS165CU1/M), where the sample can be visualized, and 90% of the signal towards an optical fibre which carries the photoluminescence signal to the CCD/camera (Newton CCD, Andor Technology). A 30mm lens focuses the light into the camera, and another 30mm lens focuses the light into the optical fibre. A schematic of the set-up is shown in Figure 4.25.

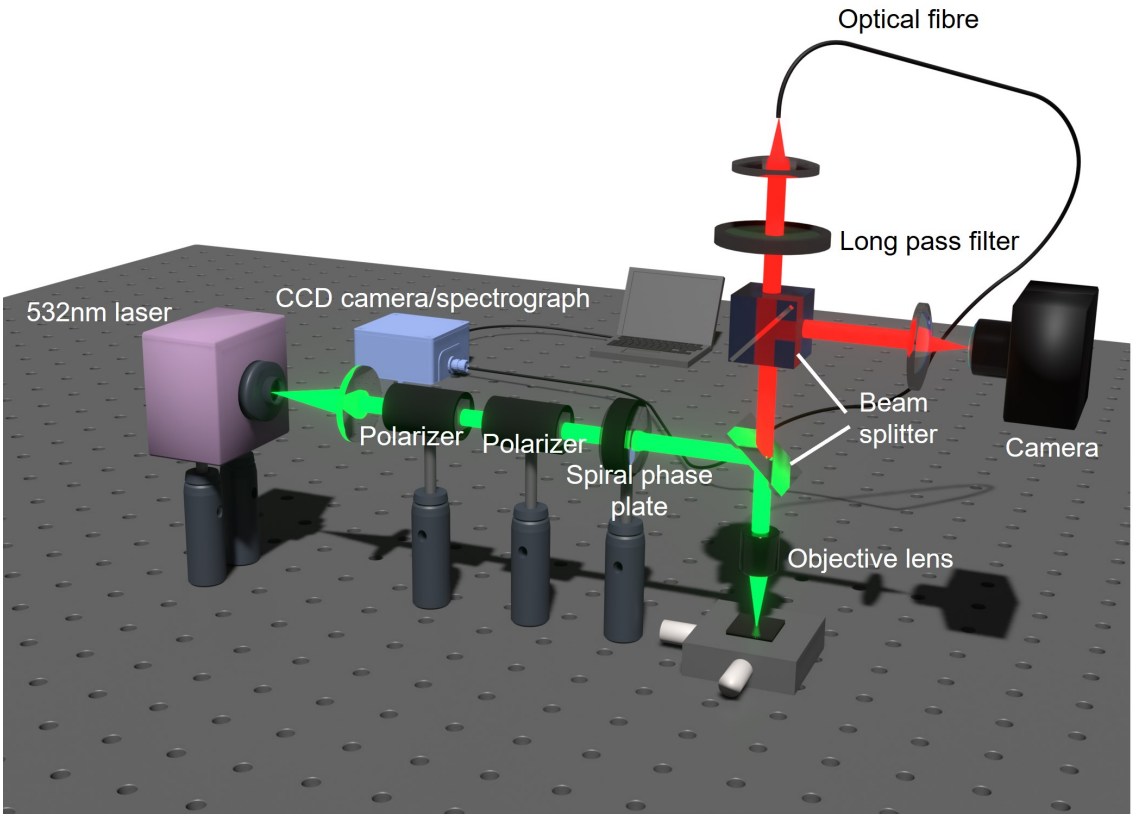

Figure 4.25: Schematic of the PL set-up used to collect the PL emission of monolayer WS_2. CCD: charge-coupled device.

The effects of sample heating in the PL of monolayer WS_2 were also studied. Heating of monolayer WS_2 was done using a heating table (Linkam Scientific CO 102) from 20 °C to 50 °C in steps of 10 °C. At each temperature, the sample was left to stabilize for 1

hour before collecting the PL emission.

The PL spectra were deconvoluted into individual components by fitting the PL emission using two Gaussian functions, each corresponding to the emission of the neutral exciton X^0 and trion T in the monolayer. This was done in OriginLab using the Gaussian function

$$y = y_0 + \frac{A}{w\sqrt{\pi/2}} e^{\frac{-2(x-x_0)^2}{w^2}}, \tag{4.8}$$

where y_0 is an offset parameter, w is the width, A the area and x_0 the peak centre. During the fitting process, y_0 was set to 0 and A was restricted to positive values ($A > 0$).

4.3 Results and discussion

4.3.1 Monolayer graphene

The monolayer graphene in the GFET was illuminated for 2 hours with either a Gaussian ($l = 0$) or LG beam ($l = 2$). The effects of the orbital angular momentum on monolayer graphene were first investigated *via* conductance measurements through the collection of I-V curves. Illumination with both Gaussian ($l = 0$) and LG beams ($l = 2$) led to a reduction of the conductance, as shown by the reduction of the slope of the I-V curve; however, the reduction induced by LG beams was significantly larger, as shown in Figure 4.26.

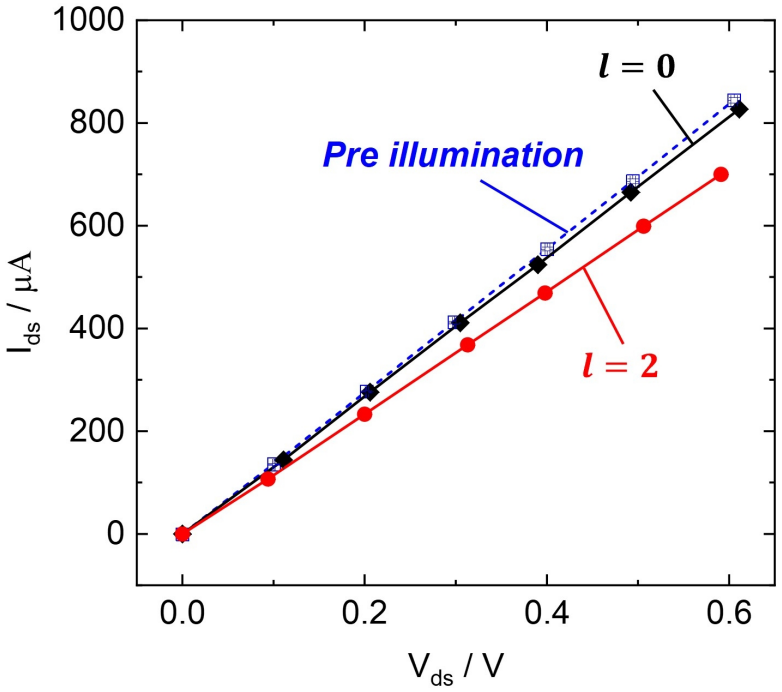

Figure 4.26: I-V characteristics after monolayer graphene is illuminated with $l = 0$ beam (black) and $l = 2$ beam (red) compared to prior illumination (blue). Power: 500μW. Figure taken from reference [126].

To aid comparison, the conductance was normalized to the conductance value prior to illumination. It was seen that, specifically, the conductance dropped to 97% of its initial value with $l = 0$ beam and 85% with the LG beam at an excitation power of 500 μW. The same experiment was also done at different excitation powers, and it was observed that the conductance drop scales for increasing excitation powers, as shown in Figure 4.27. This agrees with the theory and simulations of Chapter 3, as the magnitude of optical forces and torques are proportional to the number of photons that carry momenta. Note that the larger decrease in conductance for the LG beam cannot be produced due to laser heating. Laser heating was ruled out in Chapter 3. Specifically, we saw that LG beams have lower power density than Gaussian beams, producing lower temperature rises.

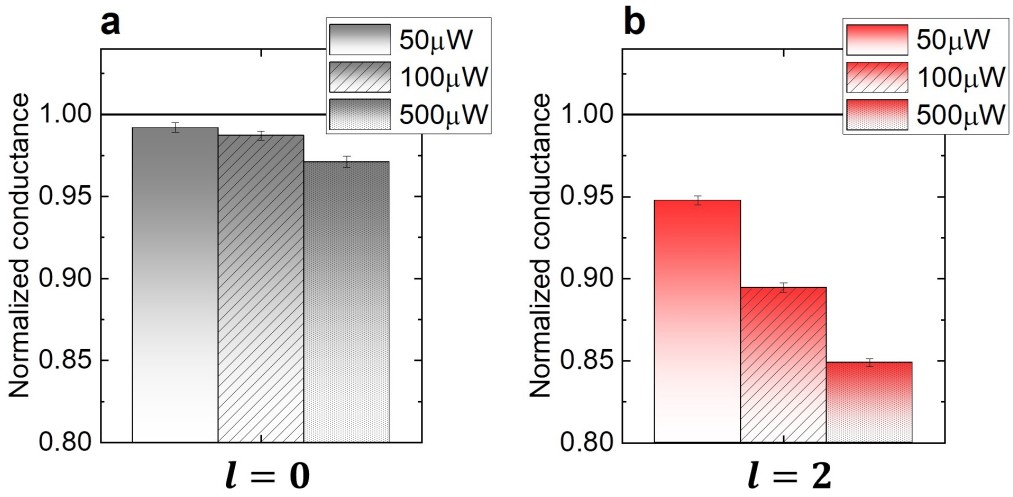

Figure 4.27: Conductance reduction observed in monolayer graphene after illuminating with (a) $l = 0$ beams and (b) $l = 2$ beams at different excitation powers.

Once the laser illumination was switched off, relaxation of the conductance back to its initial value occurred over several hours (Figure 4.28). For both Gaussian and LG illumination and for all laser powers used, the conductance returned to $> 90\%$ of its pre-illumination value within six hours (Figure 4.28), whereas complete relaxation to the pre-illuminated conductance took up to > 48 hours.

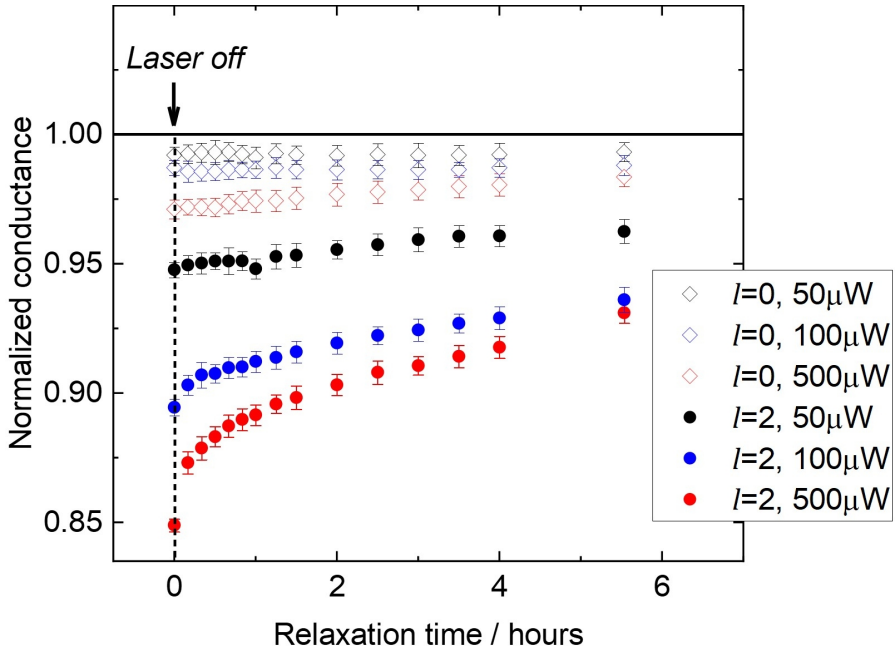

Figure 4.28: Relaxation of the conductance as a function of time (hours) once the laser beam is switched off after illuminating monolayer graphene with $l = 0$ (unfilled diamonds) and $l = 2$ beams (filled circles) at an excitation power of 50μW (black), 100μW (blue) and 500μW (red). In all cases, the conductance has been normalized to the value prior to illumination (black horizontal line at 1). Figure taken from reference [126].

As the reduction of conductance is much larger for LG beams, and it increases with excitation power, it is clear that the effect is coming from the torque imparted by the LG beam. The hypothesis now is that the reduction in conductance may be due to the fact that the LG beam is causing wrinkling of material, as it has been reported previously that the conductance of monolayer graphene is reduced as a function of out-of-plane bending[206] and wrinkles.[205, 240]

It is noted that the relaxation curves of Figure 4.28 could not be fitted to a single exponential function

$$f_1(x) = A_1 e^{\frac{-x}{t_1}} + y_0, \tag{4.9}$$

as this led to a poor R-squared parameter of 0.95 (Figure 4.29a). Instead, the data fitted well to a double exponential function

$$f_2(x) = A_1 e^{\frac{-x}{t_1}} + A_2 e^{\frac{-x}{t_2}} + y_0, \tag{4.10}$$

leading to a much better R-squared parameter of 0.999 (Figure 4.29b). These fittings indicate a bimodal relaxation process in monolayer graphene, characterized by a rapid relaxation phase ($t_1 = 0.15 \pm 0.02$ hours) and slow phase ($t_2 = 6.94 \pm 0.33$ hours) for the excitation power of 500μW. The slower phase may be associated with wrinkles that are "pinned" to defects in the underlying substrate, as it has been previously observed that the activation barrier for wrinkle relaxation for such pinned wrinkles is higher in comparison with those that are formed in regions of the substrate that are free of defects.[241] Therefore, the pinned wrinkles will relax slower than the wrinkles which appear in defect-free regions, giving rise to the double exponential relaxation process observed in Figure 4.29b.

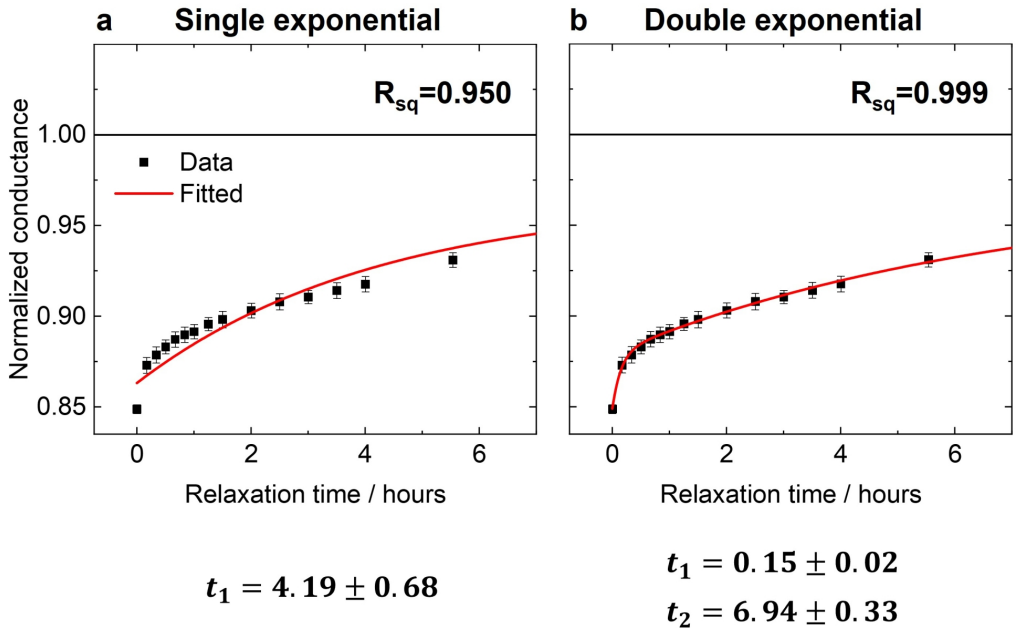

Figure 4.29: Exponential curve fitting of the conductance relaxation for $l = 2$ and 500μW power with (a) single exponential function (equation 4.9) and (b) double exponential function (equation 4.10). The R-squared parameter (R_{sq}) is indicated at the top right corner.

Raman spectroscopy and AFM were used in order to prove that the reduction in conductance is due to physical deformations caused by the orbital angular momentum of the beam. Recall that the Raman spectrum of contains primarily two bands, the G- (1590 cm^{-1}) and 2D- (2685 cm^{-1}) bands.[222] For a flat monolayer graphene sample, which is well-ordered, the G-band is less intense than the 2D-band,[223, 230] as it is observed in this work before the sample is illuminated by the LG beam. Raman mapping of the 90 μm$\times$ 90 μm monolayer graphene of the GFET was collected using the G-band wavelength. As shown in Figure 4.30a, some spatial heterogeneity was observed before illumination with the LG beam. As illustrated in Figure 4.30b, Raman maps collected after LG beam illumination show a blue shift at the illuminated area, which has been attributed to strain in the sample in previous studies.[242] Importantly, however, is that the G/2D intensity ratio increases at the illuminated area, as well as showing the appearance of the D-band ($\sim$1350 cm^{-1}). These two observations combined have been attributed to the appearance of wrinkles in monolayer graphene in previous studies,[223, 230, 243] and they are consistent with the conductance measurements done in this work, as wrinkles are also known to decrease the electrical conductivity of graphene.[205, 240]

Additionally, it can be noticed that both the G-band and 2D-bands are blue shifted. This is not related to the appearance of wrinkles, instead it may indicate doping effects. This could be investigated further by studying the relative blue shifts between the G- and 2D-bands.[244]

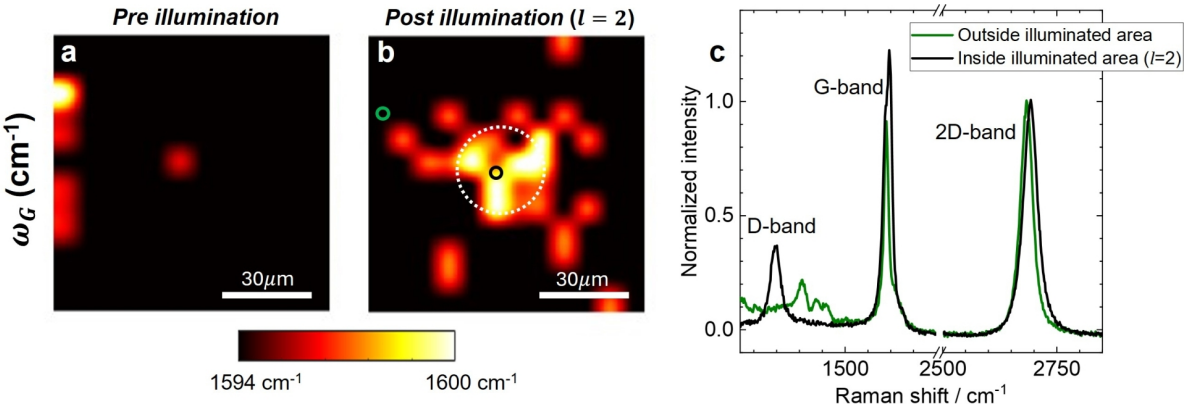

Figure 4.30: Effects of LG beam illumination in Raman scattering from monolayer graphene. (a,b) Raman mapping of the G-band before (a) and after (b) illumination with an LG ($l = 2$) beam. The approximate position of the illuminated area is indicated with a white dotted circle. (c) Raman spectra of illuminated (black) and non-illuminated areas collected at the positions depicted with a black and green circles in (b), respectively. Figure taken from reference [126].

It was observed that the Raman spectrum of the monolayer graphene relaxed back to that corresponding to a flat, ordered state of graphene after a relaxation period of 48 hours. As depicted in Figure 4.31, the D-band was almost indistinguishable and the G/2D ratio returned to the original value of less than 1.

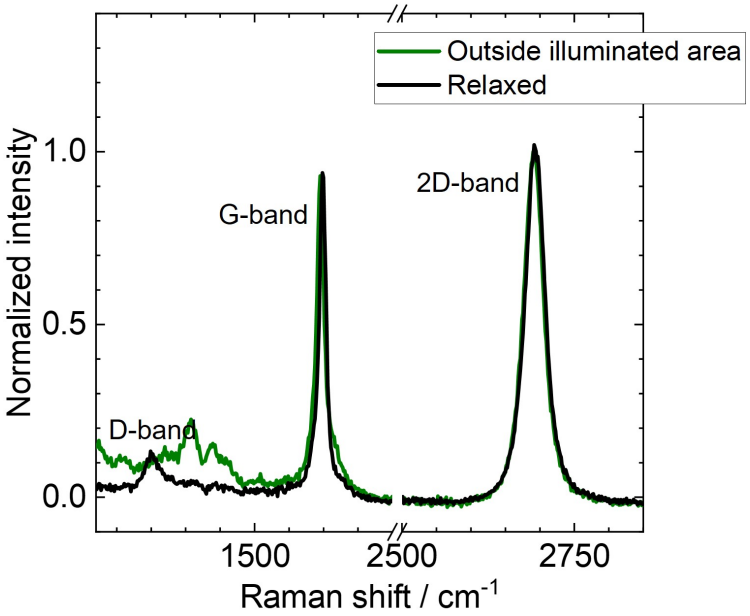

Figure 4.31: Raman spectra at the illuminated area with an LG beam after a relaxation period of 48 hours (black) compared to that outside the illuminated area (green). Figure taken from reference [126].

For reference, the same experiment was conducted by illuminating the monolayer graphene in the GFET with a Gaussian ($l = 0$) beam, which carries no orbital angular momentum. In contrast to the observations with LG beams, illumination with the Gaussian beam had no significant effect on the Raman scattering, as shown in Figure 4.32. The Raman maps showed no evidence of an increase in the G/2D ratio, or a significant appearance of the D-band at the illuminated area, indicating no evidence for wrinkling of the film with a Gaussian beam.

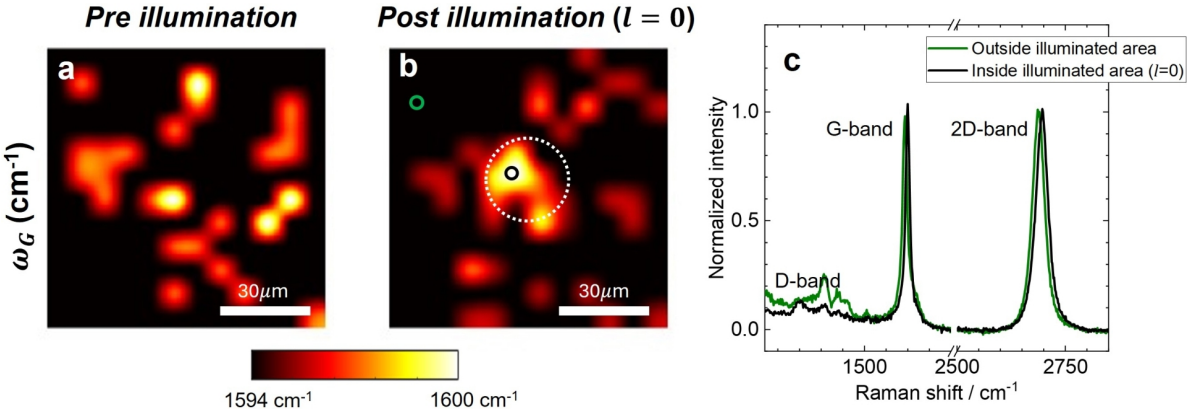

Figure 4.32: Effects of Gaussian beam illumination in Raman scattering of monolayer graphene. (a,b) Raman mapping of the G-band before (a) and after (b) illumination with a Gaussian ($l = 0$) beam. The approximate position of the illuminated area is indicated with a white dotted circle. (c) Raman spectra of illuminated (black) and non-illuminated areas collected at the positions depicted with a black and green circles in (b), respectively. Taken from reference [126].

AFM was then used to understand the morphological changes in monolayer graphene after illumination with LG beams and prove the enhancement of intrinsic wrinkles in the sample. The AFM images collected before illuminating showed the presence of intrinsic wrinkles, which are well-established in the literature to be caused by the fabrication technique, CVD.[232, 233, 245] AFM collected after illumination with LG beams show that the LG beam caused the pre-existing wrinkles to increase in height, causing the overall root-mean-square roughness, R_{RMS}, of the whole image to increase. No notable new wrinkles can be seen in the image, so the increase in roughness is solely dictated by the enhancement of pre-existing wrinkles. This is shown in two examples of areas illuminated with LG beams (Figures 4.33 and 4.34). In particular, the R_{RMS} parameter increases by 267% and 275% in Figure 4.33 and 4.34, respectively. By tracing a 1D horizontal line of the roughness in both examples, it is clear that the size of the wrinkles has increased.

The same experiment was repeated illuminating monolayer graphene with a Gaussian beam which carries no orbital angular momentum. In contrast to the observations with LG beams, illumination with a conventional Gaussian beam had no significant effect on the pre-existing wrinkles. As shown in Figures 4.35 and 4.36, no significant increase in the amplitude of the wrinkles or the morphology of the surface was found

in the illuminated areas. Therefore, AFM shows that LG beams are capable to amplify the existing wrinkles compared to a conventional Gaussian beam.

Since the topological charge of the spiral phase plate is fixed, it was not possible to vary the applied torque by varying the topological charge. However, it is possible to vary the applied torque by changing the relative sign between SAM and OAM, which changes the total angular momentum content of the beam. In the next experiments, the effects of spin-orbital interaction were investigated by using beams carrying some combination of SAM and OAM, and again the morphological changes were probed with AFM. In many experiments across the literature, it has been demonstrated that SAM and OAM can be added together or be subtracted, increasing and decreasing the resulting torque accordingly (see § 2.3.2 about optical spanners). Therefore, we used beams carrying both orbital angular momentum (OAM, $l = +2$) and different values of spin angular momentum (SAM, $\sigma = -1,\ 0,\ +1$), resulting in total angular momentum $j = l + \sigma$ values of $+1$ ($l = +2,\ \sigma = -1$), $+2$ ($l = +2,\ \sigma = 0$), and $+3$ ($l = +2,\ \sigma = +1$). In these experiments, the relative signs of OAM and SAM had to be determined (see § 4.2.2). Additionally, circularly-polarized Gaussian beams ($l = 0$), which only carry spin angular momentum ($\sigma = \pm 1$, $j = \pm 1$), were also investigated.

The relative ability of these beams to increase the wrinkles in monolayer graphene was again monitored with AFM. No change in surface roughness or amplitude of the pre-existing wrinkles was found for total angular momentum of $j = \pm 1$, in both circularly-polarized Gaussian beams ($\sigma = \pm 1,\ l = 0$) and antiparallel combination of SAM and OAM in circularly-polarized LG beam ($\sigma = -1,\ l = +2$). However, the AFM images clearly show a correlation between an increase in the roughness parameter R_{RMS} and the total angular momentum j (Figures 4.37 and 4.38), which indicates that the wrinkles are enhanced more when SAM and OAM have the same sign, and therefore the magnitude of the effect scales with the total angular momentum of the beam.

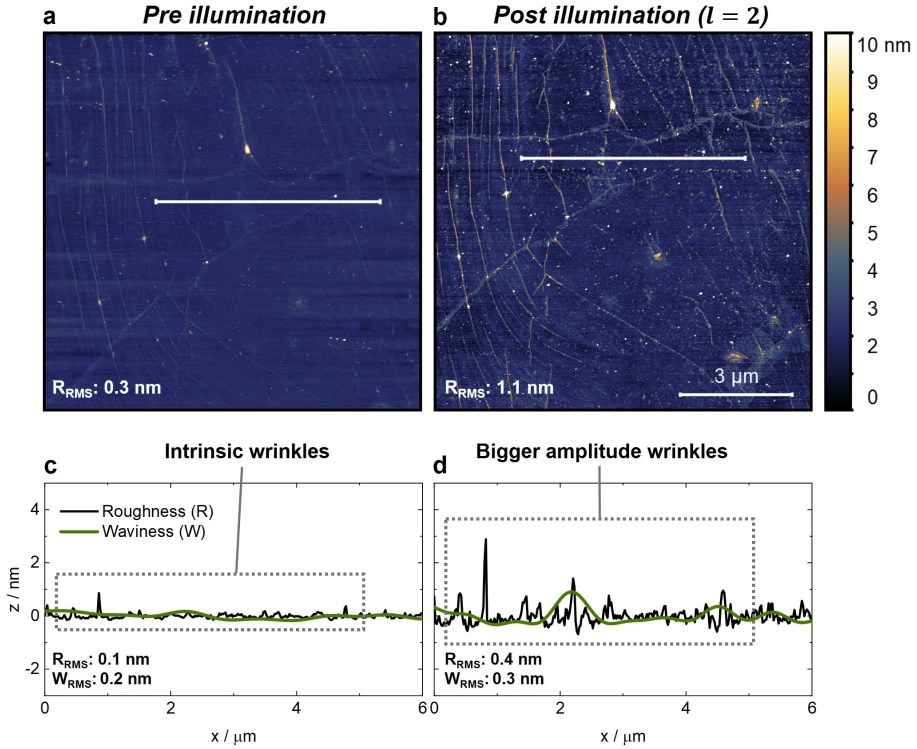

Figure 4.33: (a,b) AFM scan before (a) and after (b) linearly-polarized LG beam ($l = 2$) illumination, with the R_{RMS} of the imaged area shown in the bottom left corner. (c,d) Roughness and waviness profiles across the white cut line in (a) and (b), respectively. R_{RMS} and W_{RMS} are shown in the bottom left corner. Taken from reference [126].

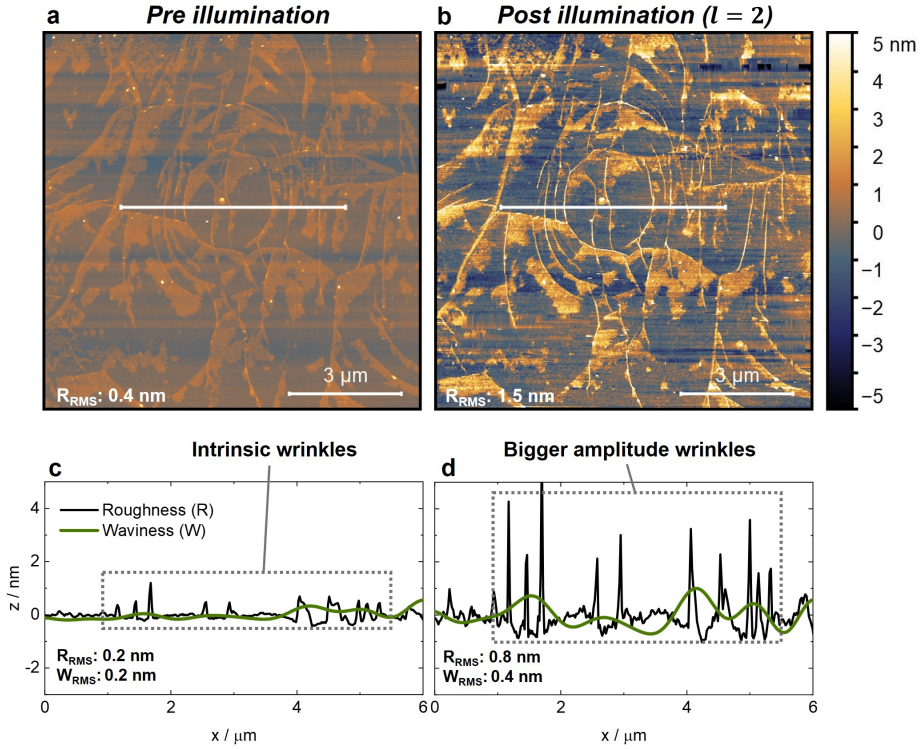

Figure 4.34: (a,b) AFM scan before (a) and after (b) linearly-polarized LG beam ($l = 2$) illumination, with the R_{RMS} of the imaged area shown in the bottom left corner. (c,d) Roughness and waviness profiles across the white cut line in (a) and (b), respectively. R_{RMS} and W_{RMS} are shown in the bottom left corner. Taken from reference [126].

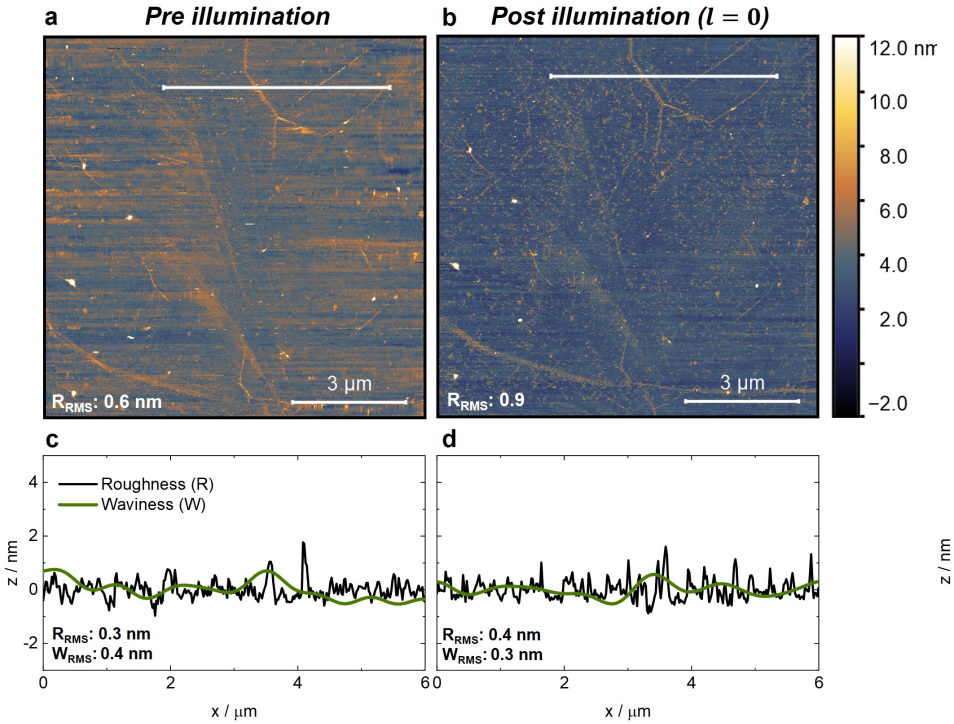

Figure 4.35: (a,b) AFM scan before (a) and after (b) linbearly-polarized Gaussian ($l = 0$) illumination, with the R_{RMS} of the imaged area shown in the bottom left corner. (c,d) Roughness and waviness profiles across the white cut line in (a) and (b), respectively. R_{RMS} and W_{RMS} are shown in the bottom left corner. Taken from reference [126].

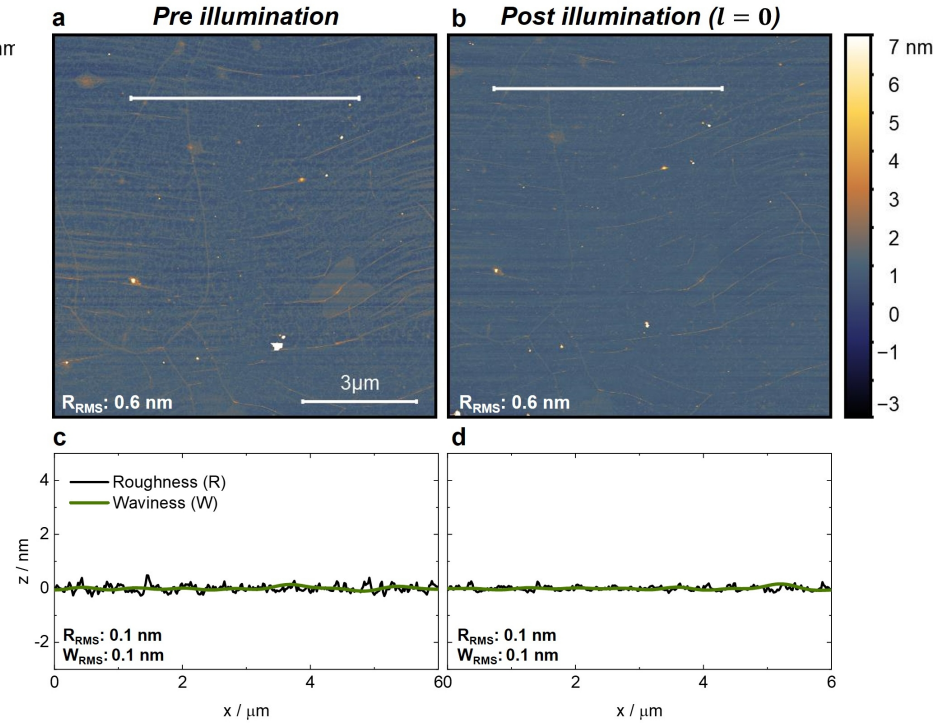

Figure 4.36: (a,b) AFM scan before (a) and after (b) linearly-polarized Gaussian ($l = 0$), with the R_{RMS} of the imaged area shown in the bottom left corner. (c,d) Roughness and waviness profiles across the white cut line in (a) and (b), respectively. R_{RMS} and W_{RMS} are shown in the bottom left corner. Taken from reference [126].

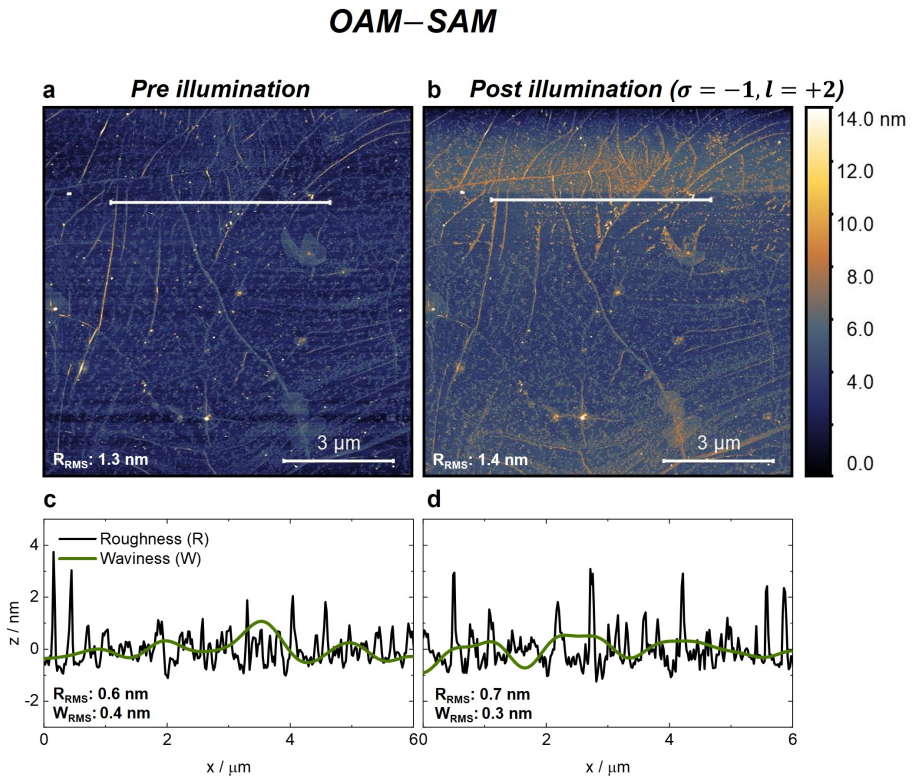

Figure 4.37: (a,b) AFM scan before (a) and after (b) circularly-polarized LG beam ($\sigma = -1$, $l = 2$) illumination, with the R_{RMS} of the imaged area shown in the bottom left corner. (c,d) Roughness and waviness profiles across the white cut line in (a) and (b), respectively. R_{RMS} and W_{RMS} are shown in the bottom left corner.

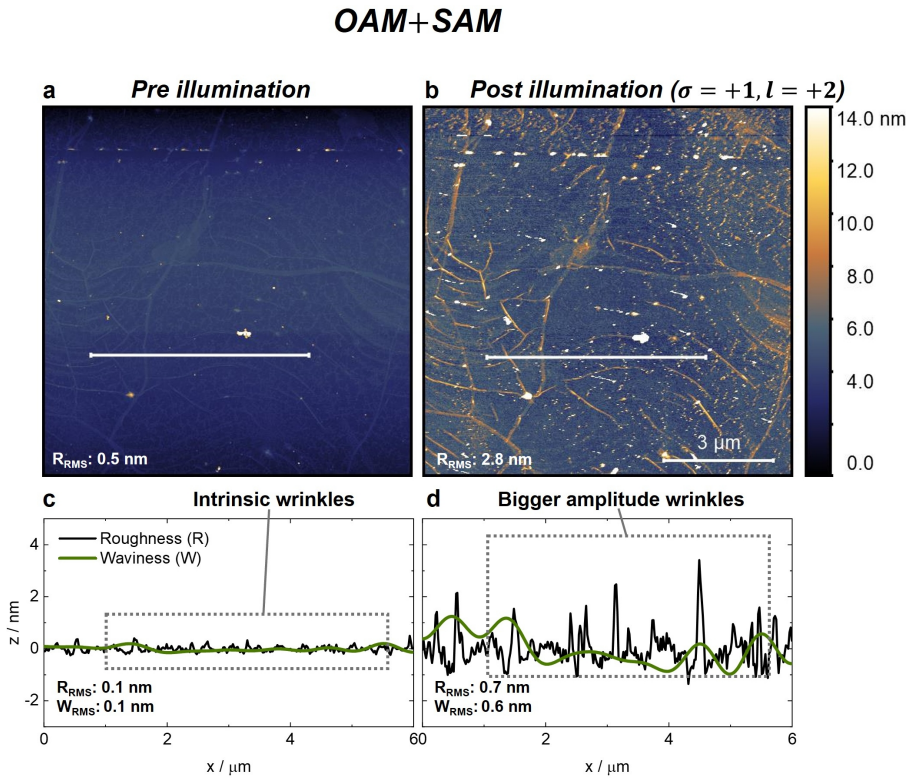

Figure 4.38: (a,b) AFM scan before (a) and after (b) circularly-polarized LG beam ($\sigma = +1$, $l = 2$) illumination, with the R_{RMS} of the imaged area shown in the bottom left corner. (c,d) Roughness and waviness profiles across the white cut line in (a) and (b), respectively. R_{RMS} and W_{RMS} are shown in the bottom left corner.

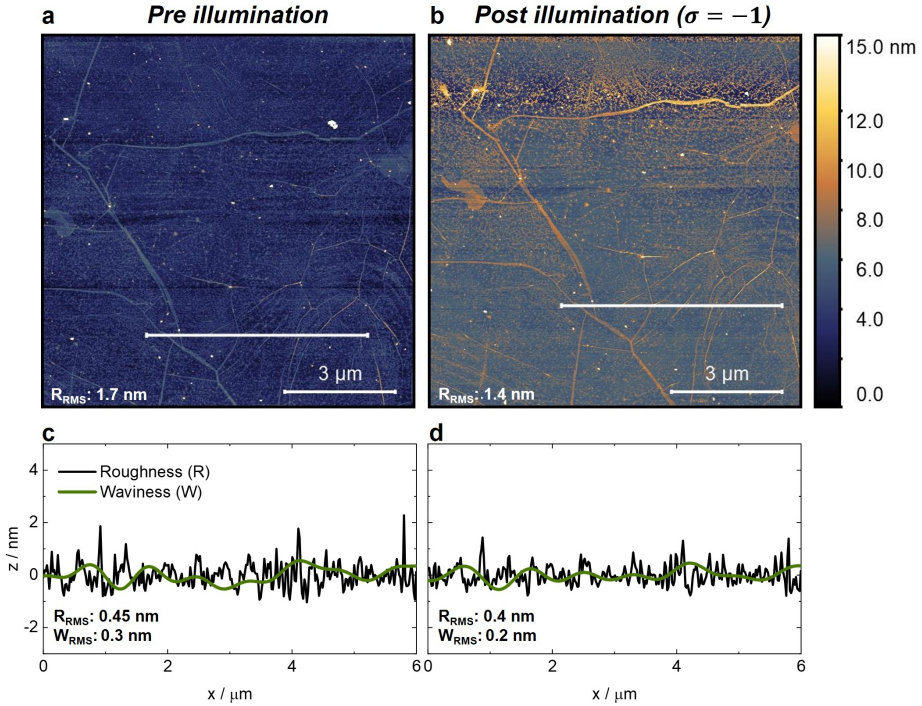

Figure 4.39: (a,b) AFM scan before (a) and after (b) circularly-polarized Gaussian ($\sigma = -1$, $l = 0$) illumination, with the R_{RMS} of the imaged area shown in the bottom left corner. (c,d) Roughness and waviness profiles across the white cut line in (a) and (b), respectively. R_{RMS} and W_{RMS} are shown in the bottom left corner.

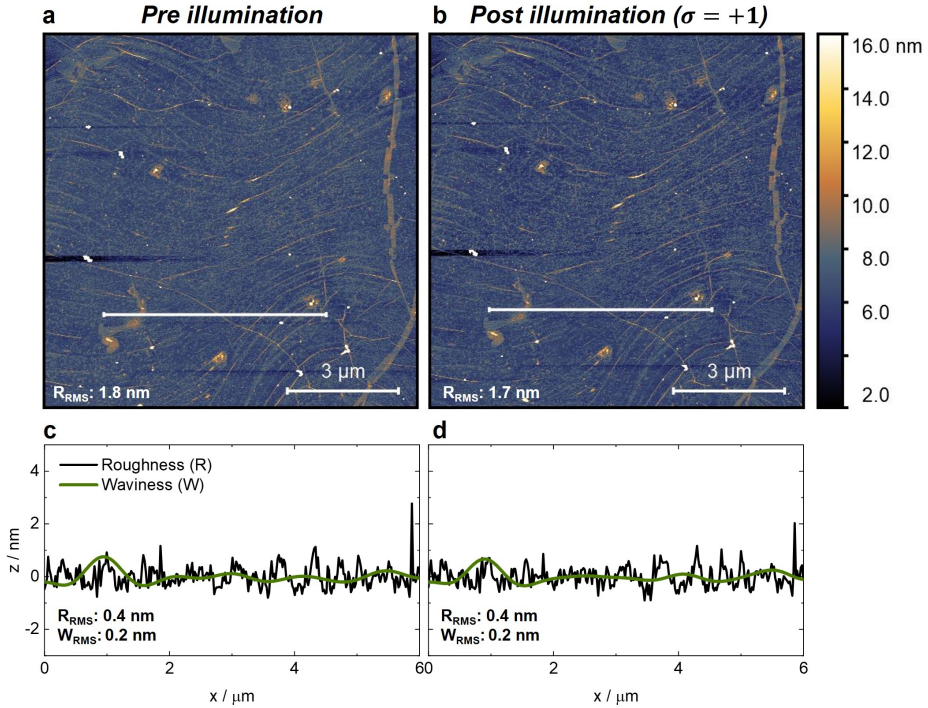

Figure 4.40: (a,b) AFM scan before (a) and after (b) circularly-polarized Gaussian ($\sigma = +1$, $l = 0$) illumination, with the R_{RMS} of the imaged area shown in the bottom left corner. (c,d) Roughness and waviness profiles across the white cut line in (a) and (b), respectively. R_{RMS} and W_{RMS} are shown in the bottom left corner.

To conclude from the AFM images, it has been demonstrated that the magnitude of the morphological changes, that is, the increase in amplitude of the pre-existing wrinkles in monolayer graphene, is correlated to the total amount of angular momentum and torque generated by angular momentum beams. A summary of the change in R_{RMS} for all the beams used, in comparison with the angular momentum fluxes predicted by the simulations from Chapter 3, can be seen in Figure 4.41. The figure shows that no change in R_{RMS} is produced with linearly or circularly-polarized Gaussian beams, all of which carry no orbital angular momentum. In contrast, the change in roughness correlates with the increase in total angular momentum for linearly and circularly-polarized LG beams.

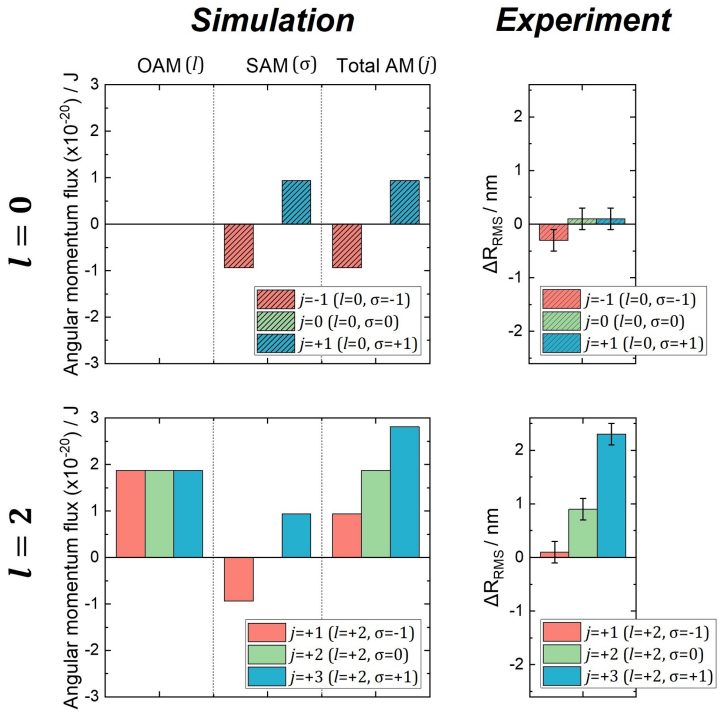

Figure 4.41: Simulated angular momentum fluxes obtained in Chapter 3 and experimental root-mean-square roughness variation, ΔR_{RMS}, after illuminating monolayer graphene with beams carrying different amounts of angular momentum j. Top row: Gaussian ($l = 0$) beams. Bottom row: LG ($l = 2$) beams. Adapted from reference [126].

In summary, the results from Raman spectroscopy and AFM demonstrate that beams carrying orbital angular momentum increase the size of pre-existing wrinkles, and rationalise the decrease in the conductance of the GFET, as wrinkles decrease the conductance.[205, 240]

4.3.2 Monolayer WS_2

Wrinkling of 2D materials by orbital angular momentum beams was further illustrated *via* photoluminescence spectroscopy of another common 2D material, monolayer WS_2.

CVD-grown full coverage monolayer WS_2 on sapphire (Al_2O_3) showed strong red photoluminescence upon excitation with 532 nm laser (Figure 4.42a). The peak due to PL emission from monolayer WS_2 is found at about 2.01 eV (Figure 4.42b). The peak is asymmetric and peak deconvolution shows that the spectrum is composed of a neutral exciton (X^0) and a broader trion (T) component at an energy lower than the neutral exciton (Figure 4.42c). Some other peaks are observed below 1.9 eV, with an intense peak at 1.78 eV dominating the spectrum. These are attributed to the PL from the sapphire substrate.[246]

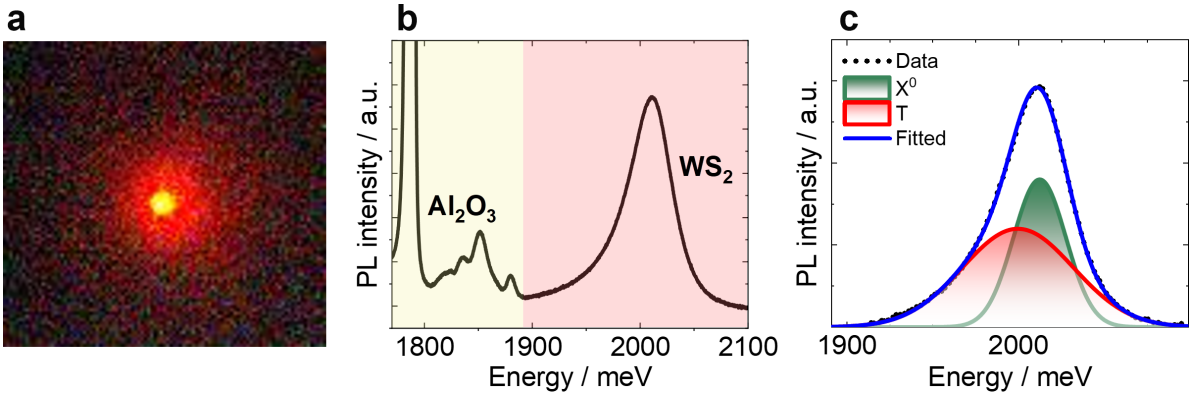

Figure 4.42: PL spectrum of CVD-grown monolayer WS_2 on Al_2O_3 substrate. (a) Image taken with a camera of the red photoluminescence emitted upon exciting monolayer WS_2 with a 532 nm laser. (b) Example of PL spectrum showing the characteristic emission of monolayer WS_2 (red square) and sapphire Al_2O_3 substrate (yellow square). (c) Fitted PL spectrum of monolayer WS_2 with two Gaussian components corresponding to the neutral exciton X^0 (green) and trion T (red) emissions.

In the first instance, the effects of OAM in the CVD-grown monolayer are presented. The induction of wrinkles in WS_2 was inferred from differences in PL spectra collected during illumination with LG and Gaussian beams. The sample was illuminated with a Gaussian beam ($l = 0$), LG beam ($l = 4$) and Gaussian beam ($l = 0$) after having applied OAM to the sample. As a reference, two consecutive spectra were collected

with a Gaussian beam to make sure that the sample was not changing over time before applying any OAM. As seen from Figure 4.43a, no change is observed in the two consecutive spectra collected with a Gaussian beam, which indicates that the emission is not changing over time. In Figure 4.43b it can be observed that OAM causes a red shift of the PL spectrum. Illuminating the sample with a Gaussian beam after OAM is applied showed that, qualitatively, the peak returned almost to the original position, but some red shift still remains in the sample (Figure 4.43c).

The spectra were fitted with two Gaussian components to quantitatively determine the shift, and it was found that OAM decreases the energy position of the neutral exciton X_0 by 6.09 meV. Once the effect of OAM stops, the energy positions increases by 4.56 meV, so the peak returns to 75% of the original position (Figure 4.43g). The same effect was observed for the trion peak but to a smaller extent (Figure 4.43h). Upon addition of OAM, the energy position of the trion peak decreases by 2.57 meV and increases by 0.95 meV after OAM is removed. Furthermore, it is noted that upon addition of OAM, the T/X^0 ratio increases from 0.87 to 0.92, indicating that the trion emission has been enhanced with OAM. After removing OAM, the T/X^0 ratio decreases back to 0.85. This has been marked with horizontal lines to guide the eye in the changes of the relative emission of the neutral exciton and trion emission, where it is clearly observed that the trion and neutral exciton emissions are enhanced and reduced, respectively, upon addition of OAM (Figure 4.43d-f).

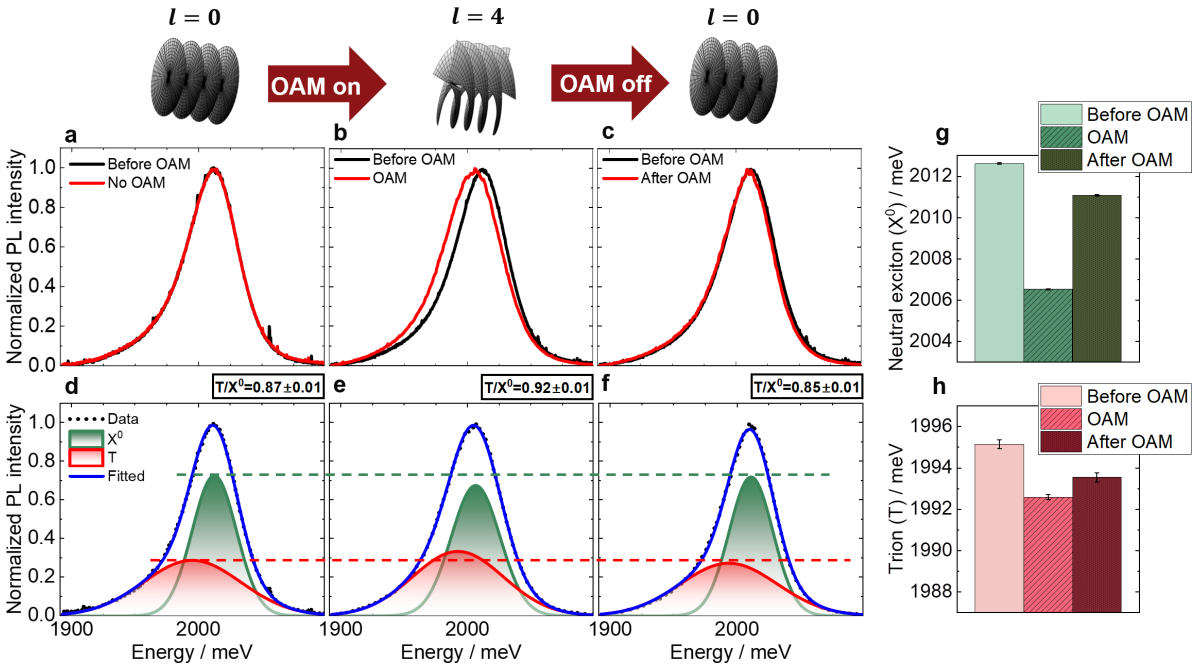

Figure 4.43: Effects of OAM in the PL spectrum of CVD-grown monolayer WS_2 upon illumination with LG beams. (a) Reference spectra with no OAM (red) and before OAM is introduced (black). (b) Spectrum collected with OAM $l = 4$ (red) compared to the spectrum before OAM (black). (c) Spectrum collected with a Gaussian beam after OAM (red) and before OAM (black). (d-f) Gaussian fits for the red spectra shown in (a-c), respectively. The green and red horizontal lines show changes in neutral exciton (X^0) and trion (T) emissions, respectively, and the T/X^0 intensity ratio is indicated at the top right corner of each panel. (g,h) Obtained energies from the fittings shown in panels (d-f) for the neutral exciton X^0 (g) and trion T (h) before, during and after illumination with LG beams. Figure taken from reference [126].

The experiment was repeated across multiple sample positions, and it was found that the magnitude of the red shift varied depending on sample positions. Some examples where a small red shift was observed are shown in Figures 4.44 and 4.45. Close inspection reveals that, in both cases, the PL spectrum collected under OAM light illumination is shifting towards the red, and the red shift is partially removed once the beam is switched back to a Gaussian beam. The red shift with OAM can be clearly visualized by taking the spectral difference. In Figures 4.44g and 4.45g, it can be seen that with no OAM, the difference between two consecutive spectra is flat as no changes in the sample are occurring with a Gaussian beam. A bisignate shape is observed in the PL difference spectra when the sample is illuminated with an OAM beam. The peak occurs at low energy and the dip at higher energy, indicating that the OAM beam is red shifting the PL emission. After OAM, a smaller bisignate shape is still observed in

the difference spectrum of Figures 4.44g and 4.45g, indicating that the change imparted on the sample by the OAM beam partially remained in the material in agreement with the sample position where a larger shift was observed (Figure 4.43).

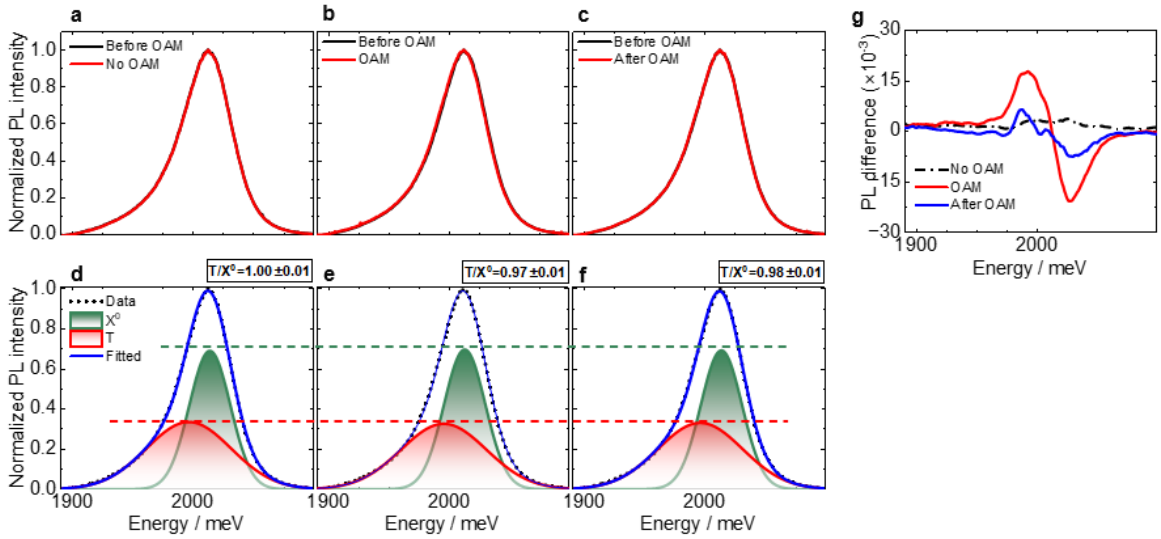

Figure 4.44: OAM-induced red shift in other sample positions in CVD-grown monolayer WS_2. (a) Reference spectra with no OAM (red) and before OAM is introduced (black). (b) Spectrum collected with OAM $l = 4$ (red) compared to the spectrum before OAM (black). (c) Spectrum collected with a Gaussian beam after OAM (red) and before OAM (black). (d-f) Gaussian fits for the red spectra shown in (a-c), respectively. The green and red horizontal lines show changes in neutral exciton (X^0) and trion (T) emissions, respectively, and the T/X^0 intensity ratio is indicated at the top right corner of each panel. (g) Difference spectra for panels (a-c).

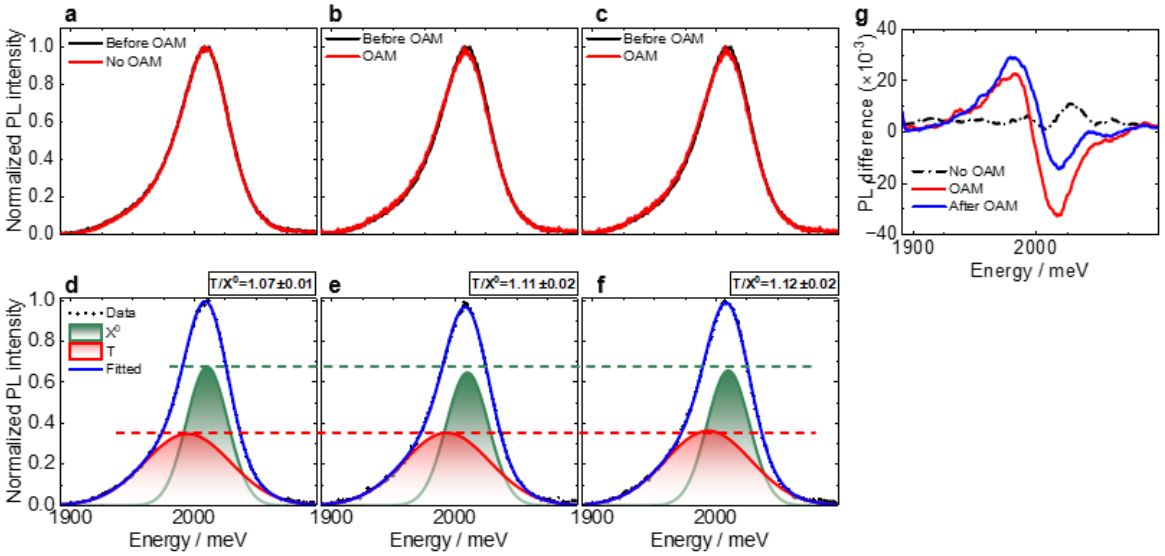

Figure 4.45: OAM-induced red shift in other sample positions in CVD-grown monolayer WS_2. (a) Reference spectra with no OAM (red) and before OAM is introduced (black). (b) Spectrum collected with OAM $l = 4$ (red) compared to the spectrum before OAM (black). (c) Spectrum collected with a Gaussian beam after OAM (red) and before OAM (black). (d-f) Gaussian fits for the red spectra shown in (a-c), respectively. The green and red horizontal lines show changes in neutral exciton (X^0) and trion (T) emissions, respectively, and the T/X^0 intensity ratio is indicated at the top right corner of each panel. (g) Difference spectra for panels (a-c).

Some other sample positions showed no changes upon illumination with OAM. An example of these is shown in Figure 4.46. Close inspection reveals that no change can be seen in the PL spectrum upon addition of the OAM beam. Fitting the spectra with two components and plotting the energy position of the neutral exciton X^0 and T also shows no significant changes (Figure 4.46g-h).

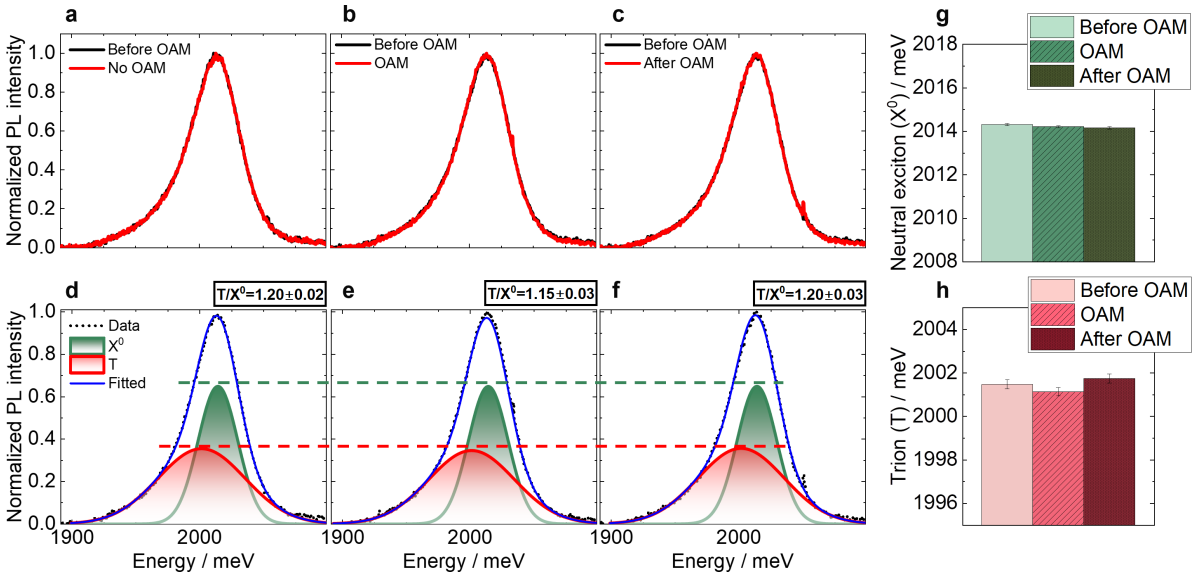

Figure 4.46: OAM-induced red shift in other sample positions in CVD-grown monolayer WS_2. (a) Reference spectra with no OAM (red) and before OAM is introduced (black). (b) Spectrum collected with OAM $l = 4$ (red) compared to the spectrum before OAM (black). (c) Spectrum collected with a Gaussian beam after OAM (red) and before OAM (black). (d-f) Gaussian fits for the red spectra shown in (a-c), respectively. The green and red horizontal lines show changes in neutral exciton (X^0) and trion (T) emissions, respectively, and the T/X^0 intensity ratio is indicated at the top right corner of each panel. (g) (h) Changes in the energies for the neutral exciton X^0 and trion T, respectively, obtained from the fittings shown in subfigures (d-f).

To rationalize why the magnitude of the red shift changes observed depended on the spot, the sample heterogeneity was considered. It can be seen from the fitted spectra that the energy positions and the full width half maximum (FWHM) vary across different sample positions. In particular, the energy position of the neutral exciton (X^0) falls within the range $2010.4 - 2014.3$ meV, and that of the trion (T) is $1994.5 - 2001.5$ meV. The obtained ranges for the FWHM of X^0 and T are $31.0 - 35.0$ meV and $68.3 - 76.8$, respectively (Figure 4.47).

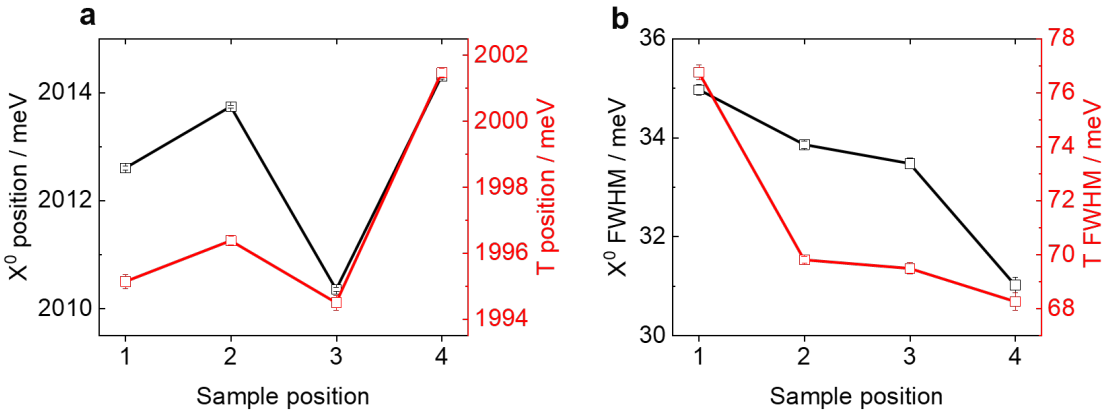

Figure 4.47: Sample heterogeneity in CVD-grown monolayer WS_2. (a) Energy positions (meV) of the neutral exciton and trion across different sample positions. (b) FWHM of the neutral exciton and trion across different sample positions.

It was found that the red shift caused by the OAM beam is correlated to the T/X^0 ratio of the illuminated sample position, as depicted in Figure 4.48. Particularly, the positions within the sample with the smallest T/X^0 ratio (0.87 ± 0.01) lead to a largest shift with OAM. Positions with an initially high T/X^0 ratio (1.20 ± 0.02) do not experience any shift at all. In summary, if the trion emission of the illuminated spot is low, it is easier to distort the sample with the OAM beam.

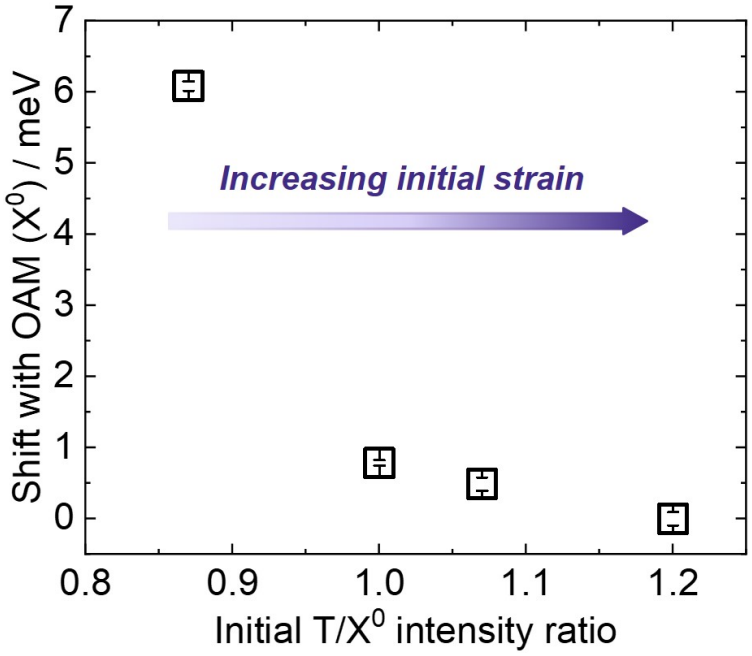

Figure 4.48: Shift caused by OAM in the neutral exciton (X^0) energy position as a function of the initial T/X^0 intensity ratio in CVD-grown monolayer WS_2. Figure taken from reference [126].

It may be argued that the differences that we see are due to a change in the power density on converting a Gaussian to an LG beam. However, power-dependent measurements using a Gaussian beam showed no change in the PL spectrum. As shown in Figure 4.49, energy position of X^0, T and T/X^0 intensity ratio remained unaffected for different excitation powers, in agreement with what it has been reported in the literature for as-grown monolayer WS_2 on a sapphire substrate.[234].

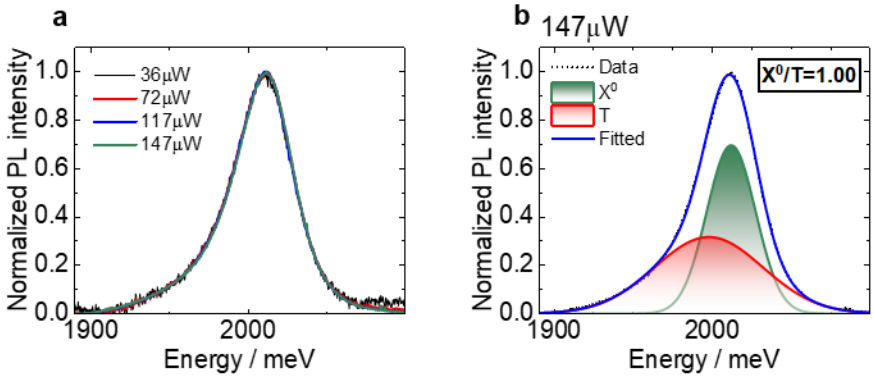

Figure 4.49: (a) Power-dependent PL spectrum of CVD-grown monolayer WS2. (b) Fitted spectrum of subfigure (a).

From Figure 4.49 it can be concluded that the red shift and increase in the T/X^0 intensity ratio in the PL spectrum of CVD-grown monolayer WS_2 cannot be attributed to a change in the power density of the beam, and hence it is due to the OAM of the LG beam. The results presented here agree with the increase of wrinkle amplitude, as a red shift and trion emission enhancement has been observed due to out-of-plane deformations in monolayer TMDCs.[131] The magnitude of the change correlates with the initial trion emission of the sample. In particular, sample positions with initial low trion emission are found to be more sensitive to the OAM in comparison with positions with an initial high trion emission. This suggests that, as trion emission is enhanced by out-of-plane deformations in CVD-grown monolayers,[131] the areas of the sample which have an initial high trion emission have a larger wrinkle density, and therefore it is more difficult to induce changes in the wrinkles. In an analogous manner, the areas of the sample with a low trion emission have wrinkles with smaller amplitude and they are easier to distort with the OAM beam.

The same experiments were also performed using exfoliated monolayer WS_2 flakes on SiO_2/Si. In this section, due to the long exposure time (3s) and low power used (10μW), a large amount of γ-rays appeared in the spectrum. A MATLAB code was developed (Appendix B) to remove the γ-rays without modifying the spectrum. An example of how the γ-ray removal procedure operates is shown in Figure 4.50.

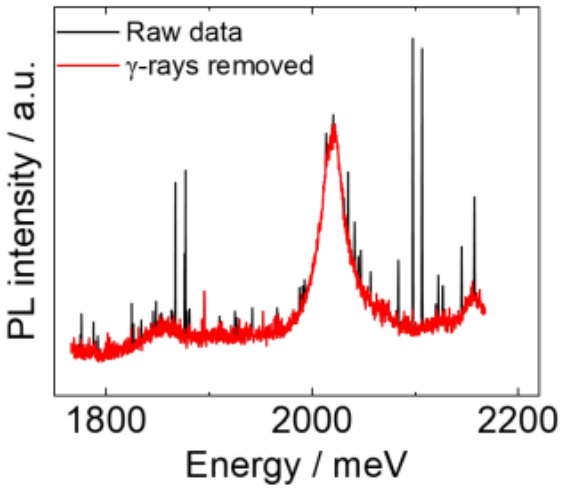

Figure 4.50: Example of γ-ray removal from the spectrum using the MATLAB code developed in Appendix B.

A red shift and enhanced trion emission was observed although, in a way similar to the CVD-grown sample, the magnitude of the effect varied across different flakes. The most prominent change observed is shown in Figure 4.51. As a reference, two consecutive spectra were collected with a Gaussian beam to make sure that the sample was not changing over time before applying any OAM. As seen from Figure 4.51a, no change is observed with a Gaussian beam. In Figure 4.51b it can be observed that OAM causes a red shift and increase in the trion emission in the lower energy side of the spectrum. Illuminating the sample with a Gaussian beam 10 minutes after OAM is applied showed that, qualitatively, the red shift and enhanced trion emission remained in the sample (Figure 4.51c), but the PL returns to almost the original state after 2 hours, although some of the red shift still remains in the sample (Figure 4.51d).

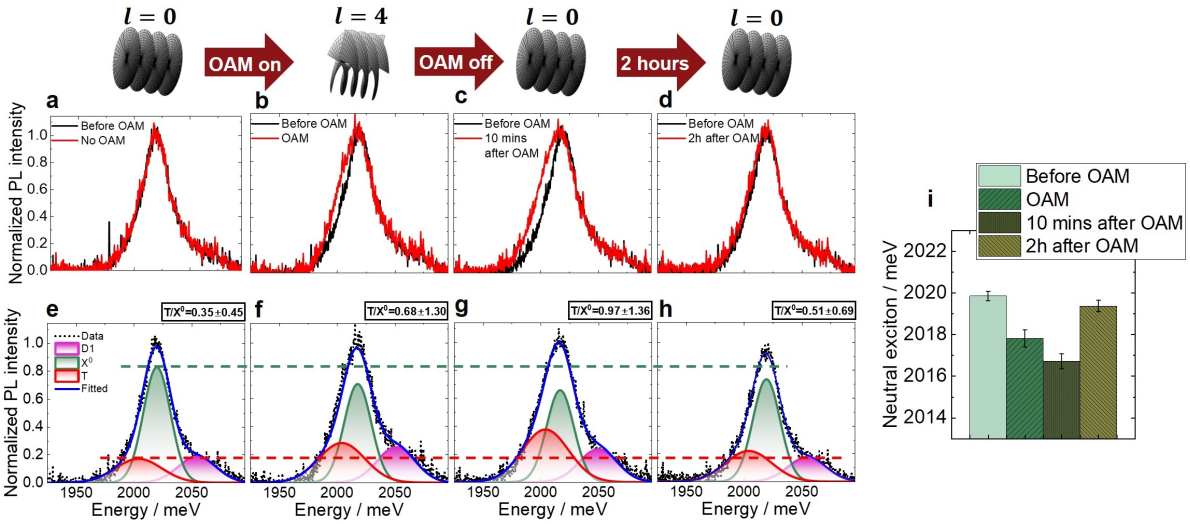

Figure 4.51: Effects of OAM in the PL spectrum of exfoliated WS_2 flakes upon illumination with LG beams. (a) Reference spectra with no OAM (red) and before OAM is introduced (black). (b) Spectrum collected with OAM $l = 4$ (red) compared to the spectrum before OAM (black). (c,d) Spectrum collected with a Gaussian beam 10 minutes (c) and 2 hours (d) after OAM (red), compared to before OAM (black). (e-h) Gaussian fits for the red spectra shown in (a-d), respectively. The green and red horizontal lines show changes in neutral exciton (X^0) and trion (T) emissions, respectively, and the T/X^0 intensity ratio is indicated at the top right corner of each panel (j) Changes in the energy of the neutral exciton X^0 obtained from the fittings shown in subfigures (e-h). Figure taken from reference [126].

The magnitude of the effect due to OAM varied across different flakes. Another example where a red shift was observed is presented in Figure 4.52.

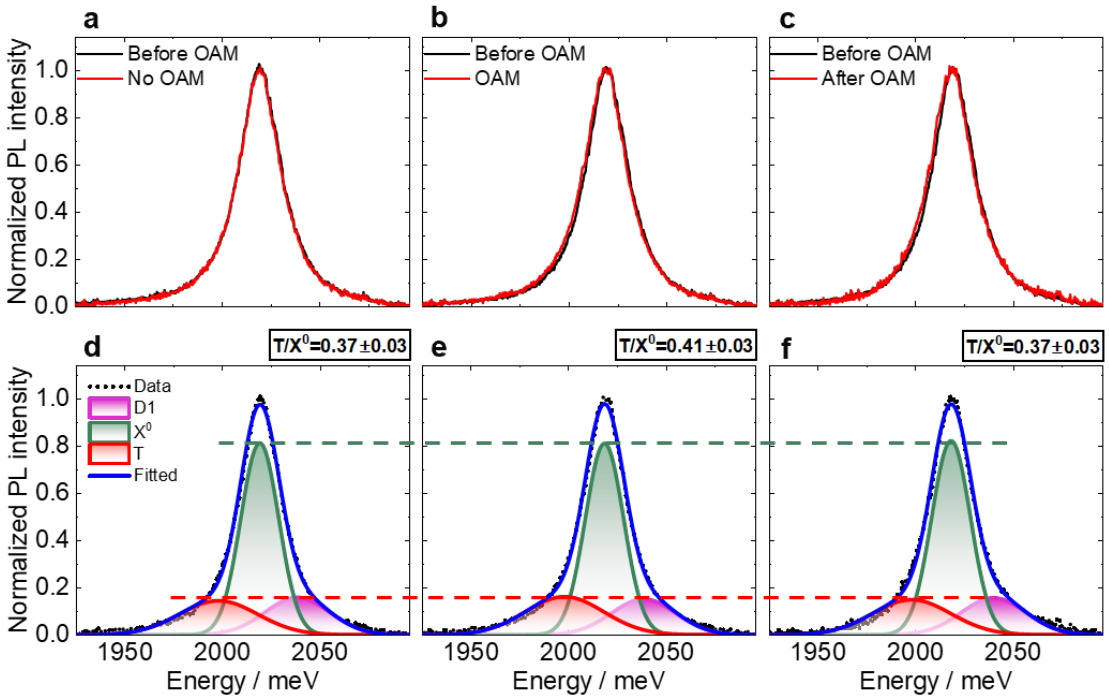

Figure 4.52: OAM-induced red shift in another exfoliated monolayer WS_2 flake. (a) Reference spectra with no OAM (red) and before OAM is introduced (black). (b) Spectrum collected with OAM $l = 4$ (red) compared to the spectrum before OAM (black). (c) Spectrum collected with a Gaussian beam after OAM (red) and compared to before OAM (black). (d-f) Gaussian fits for the red spectra shown in (a-c), respectively. The green and red horizontal lines show changes in neutral exciton (X^0) and trion (T) emissions, respectively, and the T/X^0 intensity ratio is indicated at the top right corner of each panel.

Note that the experiment was also repeated with opposite topological charge ($l = -4$), and the same result was obtained, as shown in Figure 4.53.

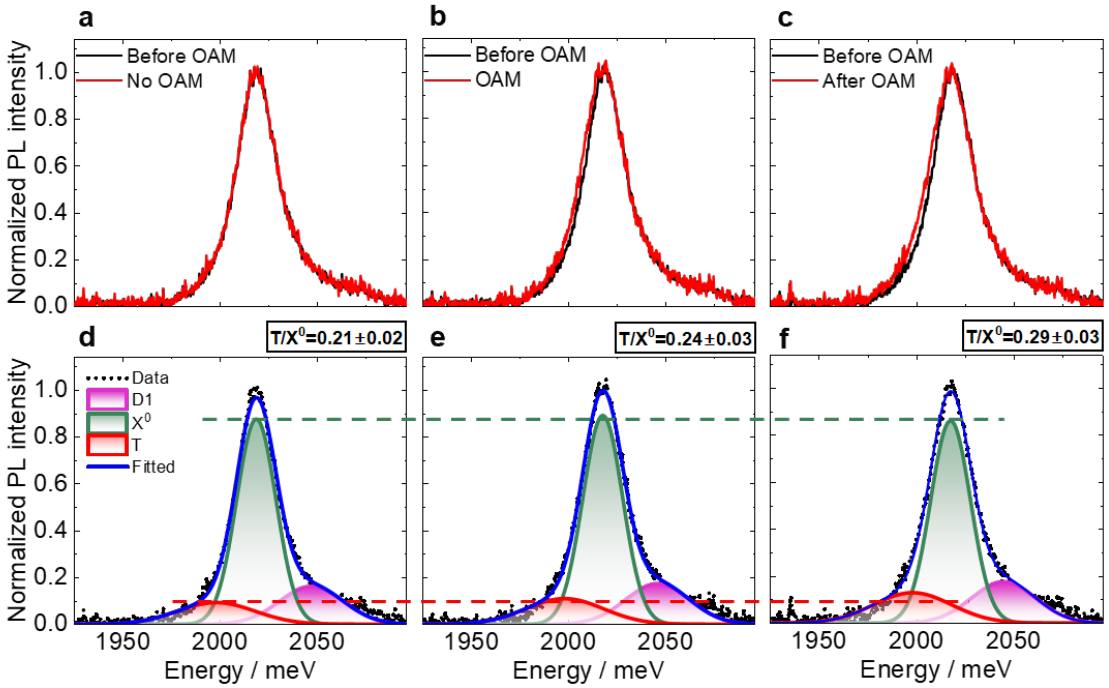

Figure 4.53: OAM-induced red shift in another exfoliated monolayer WS_2 flake collected with opposite topological charge ($l = -4$). (a) Reference spectra with no OAM (red) and before OAM is introduced (black). (b) Spectrum collected with OAM $l = -4$ (red) compared to the spectrum before OAM (black). (c) Spectrum collected with a Gaussian beam after OAM (red) and compared to before OAM (black). (d-f) Gaussian fits for the red spectra shown in (a-c), respectively. The green and red horizontal lines show changes in neutral exciton (X^0) and trion (T) emissions, respectively, and the T/X^0 intensity ratio is indicated at the top right corner of each panel. Figure taken from reference [126].

Finally, there were some flakes where the spectrum did not shift at all with OAM (Figure 4.54).

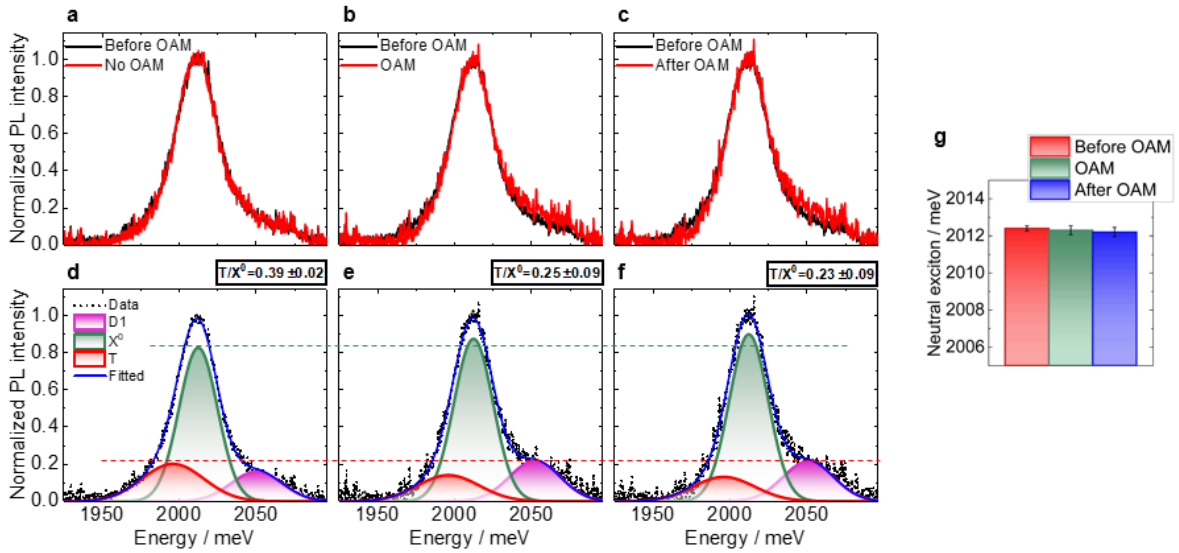

Figure 4.54: OAM-induced effects in another exfoliated monolayer WS_2 flake. (a) Reference spectra with no OAM (red) and before OAM is introduced (black). (b) Spectrum collected with OAM $l = 4$ (red) compared to the spectrum before OAM (black). (c) Spectrum collected with a Gaussian beam after OAM (red) and compared to before OAM (black). (d-f) Gaussian fits for the red spectra shown in (a-c), respectively. The green and red horizontal lines show changes in neutral exciton (X^0) and trion (T) emissions, respectively, and the T/X^0 intensity ratio is indicated at the top right corner of each panel.

From the data obtained across different flakes, it can be deduced that the shift with OAM correlates with the initial position of the neutral exciton X^0. In particular, flakes where the initial position of the neutral exciton was high experienced a larger red shift with OAM compared to the flakes where the intial position of the X^0 was low (Figure 4.55).

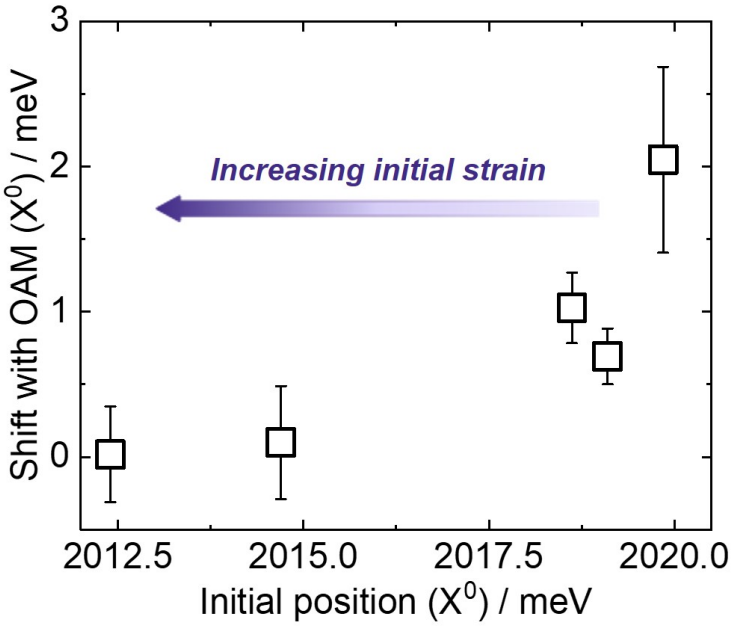

Figure 4.55: Shift caused by OAM in the neutral exciton (X^0) energy position of different exfoliated monolayer WS_2 flakes as a function of the initial position of the neutral exciton X^0. Figure taken from reference [126].

To rationalize this observation, the power-dependent PL of exfoliated flakes is discussed. As opposed to CVD-grown monolayer WS_2, it was found that exfoliated monolayer flakes have low trion emission at low power and large trion emission at high power (Figure 4.56), in agreement with the literature.[247] The measurements with OAM were done at low power, hence suggesting that the strain levels are controlled by the position of the band gap, as demonstrated by Figure 4.55. This agrees with previous studies where strain release occurred after transferring a grown sample to a different substrate, with low strain levels being manifested with an increase of the energy position.[234]

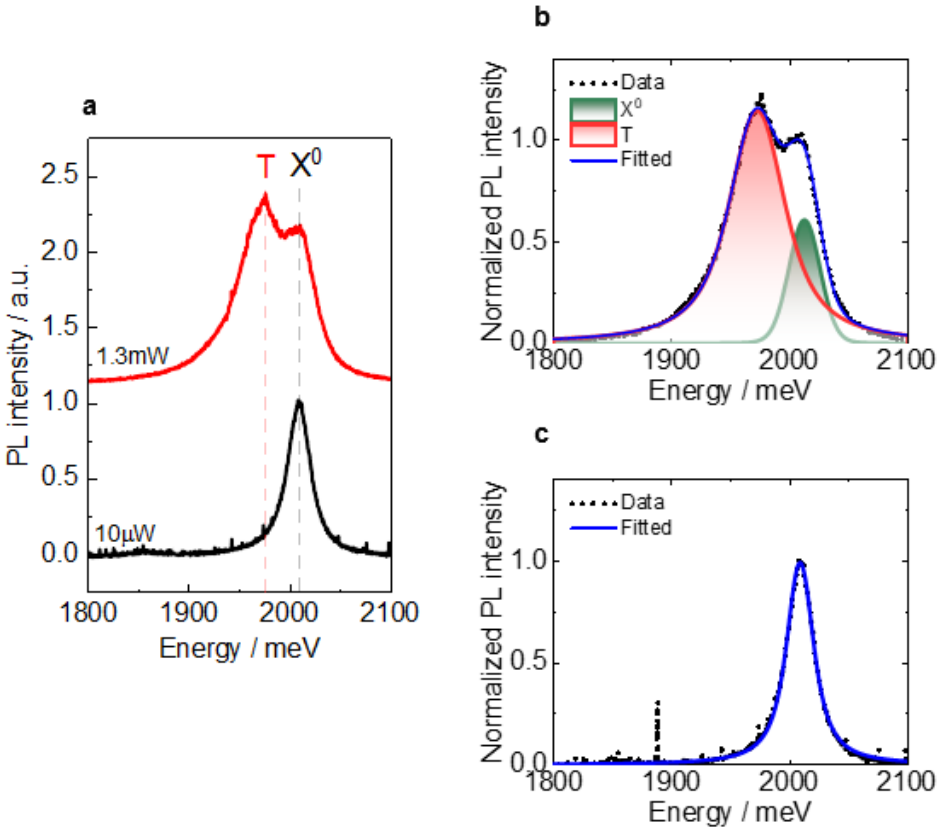

Figure 4.56: (a) Power-dependent PL spectrum of exfoliated monolayer WS_2 flakes. (b) Fitted spectrum at high power. (c) Fitted spectrum at low power. At low power (10μW), the spectrum is dominated by the neutral exciton. Increasing the power density results in an enhanced trion emission, in agreement with previous studies.[247]

Due to the power-dependency of Figure 4.56, the red-shift and trion enhancement due to OAM cannot be produced by a change in the power density on converting a Gaussian to an LG beam. As demonstrated in the simulations of Chapter 3, LG beams have lower power density, and according to Figure 4.56 this would produce lower trion emission, which does not agree with OAM inducing an enhancement of the trion emission.

To strengthen the argument of OAM being the cause of the red shift and trion enhancement one must rule out the possibility that the mechanical effects are due to laser heating. Laser heating was already ruled out in Chapter 3, as LG beams have lower power density and therefore they induce lower temperature rises compared to Gaussian beams. For completeness, temperature-dependent PL spectra were measured in both the CVD-grown and exfoliated samples. Heating the sample caused different

spectral changes to those produced by an LG beam. In particular, the overall PL spectrum in the CVD-grown sample red shifted (Figure 4.57a) but the neutral exciton and trion red shifted at the same rate with increasing temperature (Figure 4.57b). This is in contrast with our observations with OAM, where there was a greater shift for the neutral exciton. In addition, the T/X^0 intensity ratio did not vary over a temperature of up to 30 degrees (Figure 4.57c). The same reasoning applies for the exfoliated monolayer flake (Figure 4.57d-f).

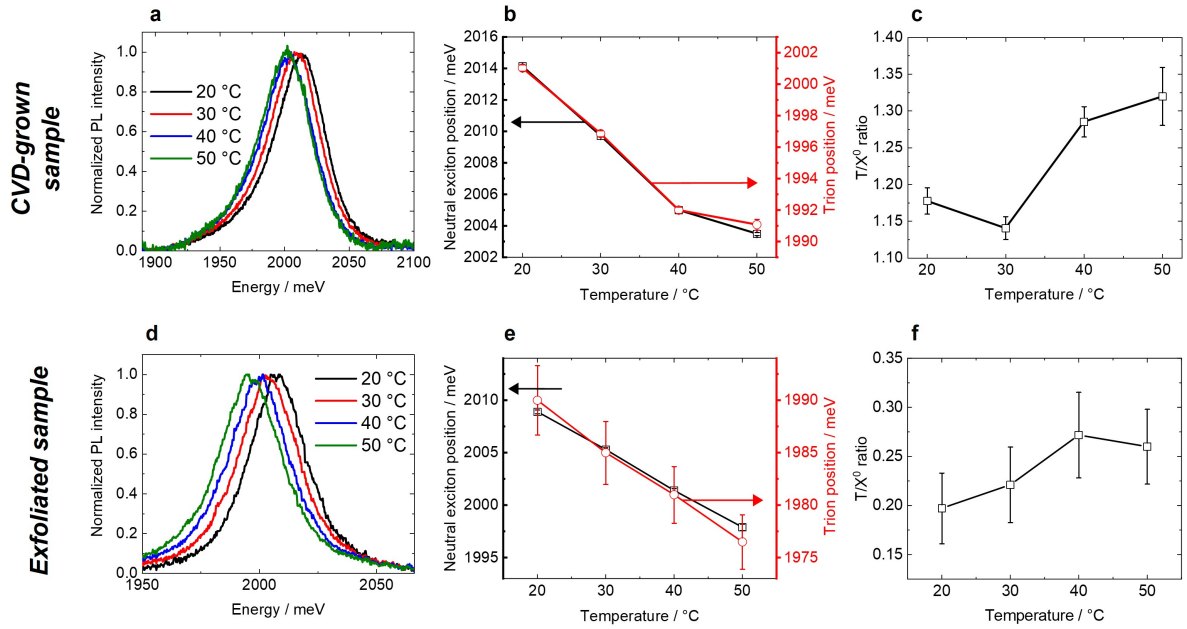

Figure 4.57: (a-c) Temperature-dependent PL in CVD-grown monolayer WS_2. (a) PL spectrum. (b) Energy positions of neutral exciton (black) and trion (red). (c) T/X^0 intensity ratio. (d-f) Temperature-dependent PL in exfoliated monolayer WS_2. (d) PL spectrum. (e) Energy positions of neutral exciton (black) and trion (red). (f) T/X^0 intensity ratio. Figure taken from reference [126].

To summarize this section, the red shift and trion enhancement observed upon illumination with OAM is attributed to the torque imparted by the beam on the material, which locally is causing the material to strain. As in the case of graphene, the PL data supports the induction of wrinkles in 2D monolayers. Note that, due to the faster relaxation times compared to graphene, it was not possible to monitor the wrinkles with AFM.

Finally, it is noted that the relaxation times to return to the original state are different for the two different monolayers WS_2 studied. This is likely to be due to monolayer-

substrate interactions, as frictional forces have been proved to strongly correlate to the properties of the substrate upon which the 2D material is grown/deposited.[241] The longer relaxation times in silicon correlate with its larger friction coefficient (≈0.4)[248] in comparison with sapphire substrate (≈0.2).[249]

4.4 Conclusions

Strain engineering has emerged in recent years as a means to tune the properties of 2D materials by applying strain to the sample. Even though 2D materials have a large Young's modulus,[250] making graphene the strongest material ever found,[143] out-of-plane deformations such as wrinkles require minimal forces[159, 160] and are formed intrinsically even after material fabrication.[232, 233, 245]

In this chapter, a novel, non-contact and all-optical method exploiting the small optical forces generated by a laser beam is used to induce out-of-plane deformations in 2D materials. The method is based on angular momentum transfer between a light beam and an absorbing medium. This has been exemplified using two well-known examples of 2D materials, namely monolayer graphene and monolayer WS_2. Spatial and dynamic control of their properties at the illuminated areas has been achieved; in particular, control of the conductance in graphene and band gap in WS_2 has been accomplished. From AFM it has been inferred that the changes are attributed to an increase in the amplitude of pre-existing wrinkles in the monolayer. Therefore, another possible application where optical angular momentum can act as an optical spanner has been developed here, and the work in this chapter has established the foundations for optical strain engineering of 2D materials. The method is limited by sample heterogeneity and monolayer-substrate interactions, although this is predicted to improve with the rapid developments in spatial homogeneity in the growth of 2D materials.[251]

Looking forward, other applications of optical strain engineering can be envisaged. For example, in the twist angle of 2D bilayers, which strongly affects their properties and it is a topic of growing interest.[252–256] Furthermore, other momentum distributions,

such as Hermite-Gaussian modes, could be explored for strain photopatterning.

Chapter 4: Summary

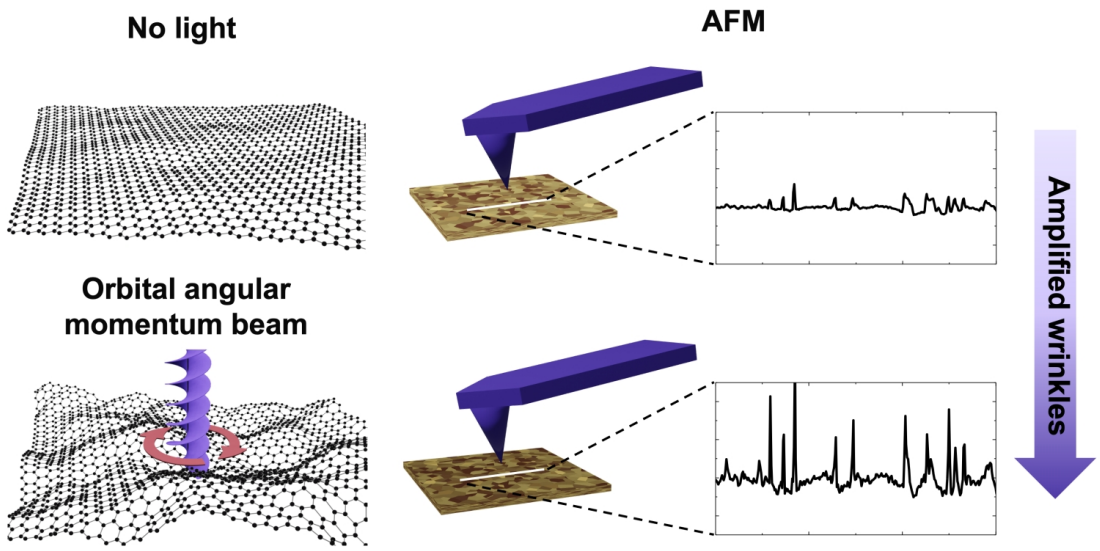

Figure 4.58: Chapter 4 concept figure. Taken from reference [126].

Key findings:

- Wrinkles are amplified with optical orbital angular momentum.
- Optical and electronic properties are tuned by the morphological changes caused by angular momentum.
- A non-contact, all-optical and reversible mechanism has been developed to tune the morphology and properties of 2D materials.

Chapter 5

Dynamic optical activity control in chiral metamaterials with optical angular momentum

5.1 Introduction

Chirality, the property of lacking mirror symmetry, is a defining feature of both physical structures and light.[82] While chiral objects derive their handedness from geometric asymmetry, light with angular momentum exhibits chirality through helical polarization and/or phase front structure. Light beams which combine spin angular momentum (SAM) and orbital angular momentum (OAM) expand the toolkit for manipulating chiral light-matter interactions. Unlike circularly-polarized light, which carries a fixed SAM of $\pm\hbar$ per photon,[29, 257] OAM encodes any integer multiples of $\pm l\hbar$ angular momentum per photon[5] in addition to their SAM, introducing new ways to control and engineer interactions at the nanoscale.[90, 104, 258–260]

Circular dichroism (CD), a hallmark of optical activity, describes the differential absorption of left- and right-handed circularly polarized light by a material.[82] CD can be used to investigate and detect chiral material such as protein secondary structure,[261, 262] DNA,[263, 264] molecular aggregates[265] and others.[266, 267] Chiral interactions

originate from the coupling of an electric dipole (E1) with either a magnetic dipole (M1) or an electric quadrupole (E2), giving rise to either E1M1 interactions or E1E2 interactions. The first type of interactions are more common, as the latter average to 0 for isotropic (randomly-oriented) samples and therefore require some degree of anisotropy to be observed.[86, 87]

Traditionally, optical activity has been dictated by the intrinsic symmetry and geometry of a system and it is limited to optically active modes. Higher-order modes, which are non-dipolar and optically dark, do not independently contribute to optical activity under standard excitation conditions. While these modes have been exploited in static systems through structural engineering and design,[268–271] their dynamic manipulation remains largely unexplored.

This chapter demonstrates how light beams carrying different combinations of SAM and OAM can be used to control optically active bright and dark modes, providing a mechanism for dynamically engineering optical activity. The main idea behind this work is based on the fact that Laguerre-Gaussian beams and their associated OAM can directly excite higher-order dark modes, such as electric quadrupoles, due to their superior field gradient compared to Gaussian beams.[90, 99] Dynamic manipulation of optical activity is achieved by selectively exciting higher-order modes which can couple to optically active modes, modulating the chiroptical response thereby. The effect is investigated *via* numerical simulations and experimental dichroisms measurements across the entire visible range in chiral shuriken-shaped metamaterials, under both the weakly- and tightly-focused regimes.

5.1.1 Chiral metamaterials

Metamaterials are a periodic arrangement of nanostructures of a specific shape with a unit cell typically smaller than the wavelength of light. When light impinges on metamaterials new properties that go beyond those of the constituent unit cells arise, somewhat related to the famous Aristotles' quote *'The whole is greater than the*

sum of its parts'. Unusual properties that have been achieved using metamaterials include electromagnetically-induced transparency (EIT)[272, 273] and negative refractive index,[274–277] and therefore they find applications in slow-light devices,[278, 279] refractive index sensing[280, 281] and biosensing.[116, 282] Some examples of metamaterials are depicted in Figure 5.1.

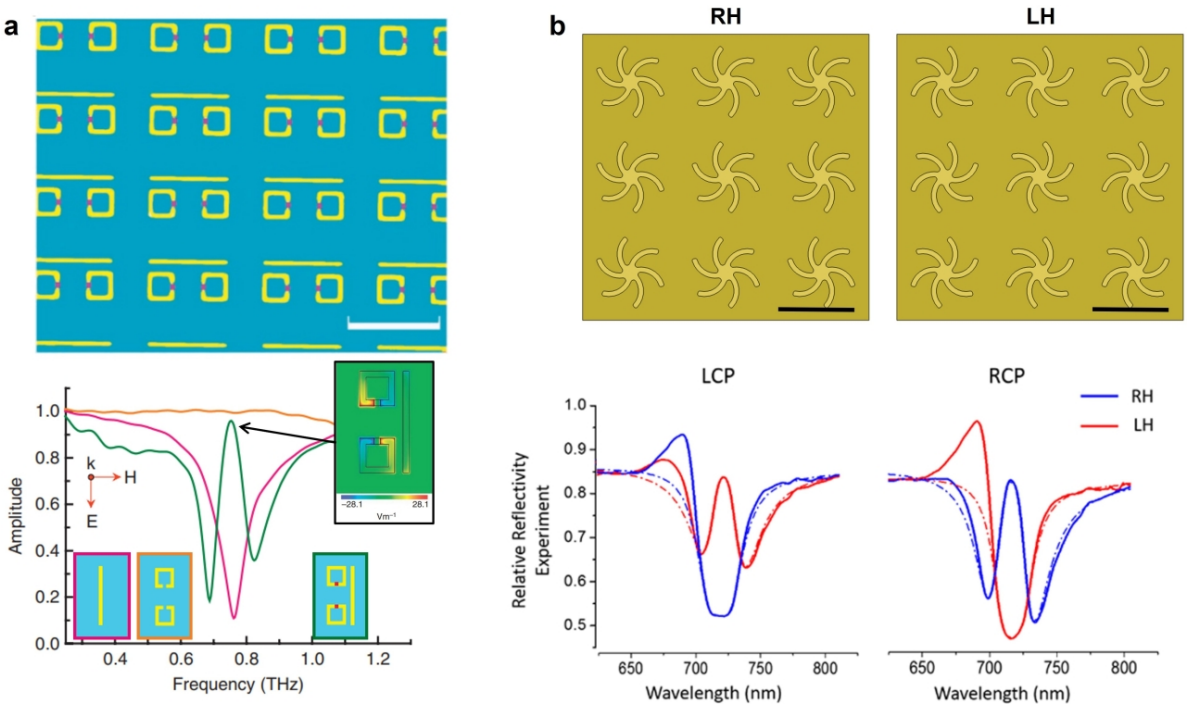

Figure 5.1: (a) Example of a metamaterial (scale bar: 100 μm). Each unit cell is composed of a cut wire (bright mode) and split-ring resonators (dark mode) and their corresponding transmission spectra are shown in pink and orange, respectively. The bright mode interacts with the light (dip in transmission spectrum), whereas the dark mode does not. When both resonators are placed together the transmission spectrum shows an electromagnetically-induced transparency (EIT) window (green), as the bright mode radiation is suppressed by the near-field coupling to the dark mode (electric quadrupole shown in the black square). Figure adapted from reference [272]. (b) Chiral plasmonic (gold-made) shuriken metamaterials used in this work (scale bar: 1 μm) The reflectivity, collected in water, shows the equivalent of EIT in plasmonic metamaterials: plasmonic-induced reflectance (PIR). In this case, a spin-dependent (LCP or RCP) PIR is observed for LH (red) and RH (blue) structures. Reflectivity taken from reference [283].

EIT is a phenomenon that was initially observed in atoms and it arises because of destructive interference between two excitation pathways.[284, 285] In metamaterials EIT arises because of near-field coupling between bright and dark modes.[272, 286] A bright mode is a mode that can be excited directly by the light, for example an electric dipole, and a bright mode resonator is a structure that supports a bright mode, for

example the cut wire shown in Figure 5.1a. A dark mode is a mode that cannot be excited directly by the light under ordinary conditions, for example an electric quadrupole. Equivalently, a dark mode resonator is a structure that supports a dark mode, for example the split-ring resonator in Figure 5.1a. As shown in Figure 5.1a, if both resonators exist independently of each other one finds that only the bright mode can be excited. When both resonators are placed together, the bright mode can excite the dark mode *via* near-field coupling, destructive interference occurs so the radiation from the bright mode is suppressed, resulting in a transparency window (EIT). Classical models based on coupled oscillators are frequently used to obtain information about the system.[272, 283, 287]

Figure 5.1b shows the chiral shuriken-shaped metamaterials used in this work. As shown in the reflectance spectra, chiral shuriken metamaterials support the equivalent of EIT in plasmonics, that is, plasmonic-induced reflectance (PIR). The shurikens are chiral as each unit cell contains a shuriken structure that can be left- or right-handed. Owing to its chirality, helicity-dependent PIR has been observed,[283] as depicted in Figure 5.1b.

The chirality in chiral metamaterials can arise because of different reasons. One of them is because the unit cell itself is chiral, as in the example of Figure 5.1b and gammadion structures,[116, 288] which are chiral planar metamaterials, or metamaterials composed of 3D helical structures.[289, 290] Another method is to arrange achiral components in a chiral fashion, for example twisted nanorods,[291, 292] Moiré chiral metamaterials[293] and others.[294] All these chiral metamaterials have in common that they are able to enhance the electric field by several orders of magnitude[295] and create superchiral hot spots,[296] which can greatly enhance the sensitivity towards the detection of chiral media.[116, 297] Even though a large amount of studies have been carried out regarding the interaction between circularly-polarized light and metamaterials,[283, 298, 299] there are not many studies regarding how the orbital angular momentum of light can interact with metamaterials. Arikawa *et al.* studied the effects of optical angular momentum in periodic plasmonic and non-chiral disks and proved the excitation of

different multipolar modes with varying SAM and OAM combinations, which changes the total angular momentum.[300] Liu *et al.* have achieved a large helical dichroism in chiral twisted metamaterials for varying topological charges and fixed wavelength.[301] Furthermore, they established that the HD can be largely modulated with the structural design.[301]

In the present chapter, we achieve dynamic tuning of the chiroptical response of shuriken metamaterials without the need of structural design. The work investigates the interaction between different combinations of SAM and OAM and chiral shuriken metamaterials over the visible range. The effect is studied under both the weakly- and tightly-focused regimes and this work establishes OAM as a potential route to dynamically modify the optical activity of the shuriken structures.

5.2 Experimental methods

5.2.1 Sample fabrication and characterization

Chiral shuriken-shaped nanoindentations were fabricated at the University of Glasgow using an injection moulding technique as described in detail by Gadegaard *et al.*[302] An injection moulding machine (ENGEL) was used to fabricate the nanoindentations first in a polycarbonate substrate.[303] The nanoindentations have a depth of 80 nm and form part of a periodic array with a periodicity of 720 nm.

Once the nanoindentations were produced and prior to gold evaporation, the substrate slides were cleaned with IPA and dried with N_2. After this, a 100 nm of gold were evaporated onto the clean slides using a commercial e-beam evaporator (Plassys MEB550S) at a rate of 0.3 nm/s. While the evaporation process takes place, the gold takes the shape of the nanoindentations. More details about the plasmonic behaviour of these chiral shuriken-shaped nanoindentations can be found in Karimullah *et al.*[303]

After fabrication, the shuriken-shaped nanoindentations were characterized with AFM (see § 4.2.6 in Chapter 4 for more details about the technique). The AFM was

performed using a Dimension Icon Atomic Force Microscopy System in ScanAsyst mode and equipped with a silicon tip (ScanAsyst-Air-HPI). The images were processed using Gwyddion software. The nanoindentations can be left- (LH) or right-handed (RH) and have a depth of ≈ 80 nm, as shown in the AFM images of Figure 5.2.

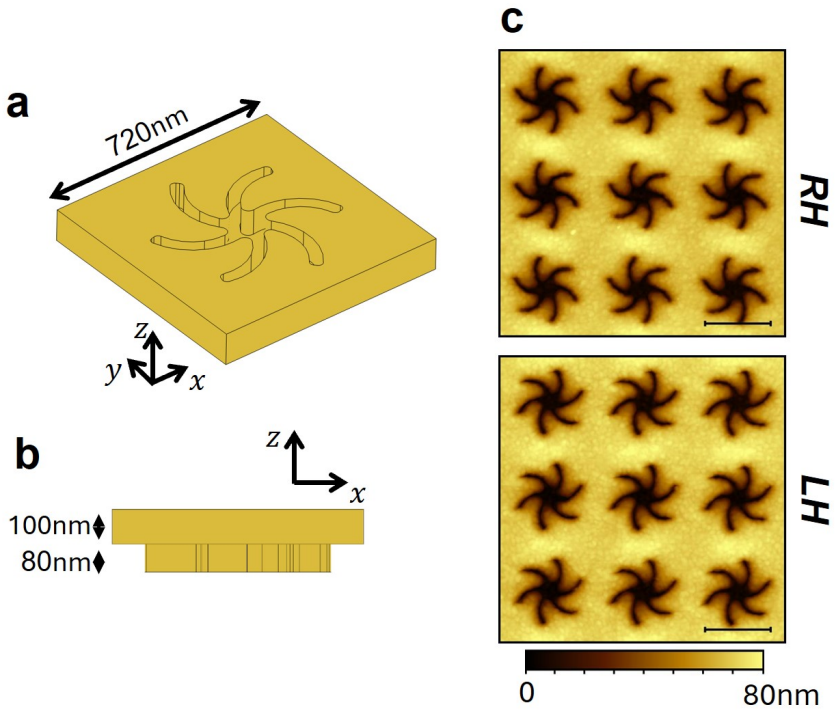

Figure 5.2: Chiral shuriken-shaped nanoindentations after 100 nm of gold are deposited on a polycarbonate substrate. (a) Schematic of a unit cell. (b) Side view of the unit cell in (a). (c) AFM images of the left-handed (LH) and right-handed (RH) nanoindentations (scale bar: 500nm).

5.2.2 Optical-rotatory dispersion measurements

ORD measurements were performed at the University of Glasgow using a home-built polarization microscope system equipped with a 500-9000 nm stabilized light source (Thorlabs, SLS203F/M). In this case, the beam is Gaussian ($l = 0$) and is linearly-polarized ($\sigma = 0$). The beam is focused on the sample using a 10X objective (NA=0.3) and the spectra are measured in a reflection geometry using a spectrometer (Ocean optics USB4000). The intensity of the reflected light is measured at four different angles with respect to the input polarization using an analyzer and the ORD spectrum

in degrees can be calculated as

$$\theta(\lambda) = \frac{1}{2}\tan^{-1}\left(\frac{I_{45} - I_{135}}{I_0 - I_{90}}\right), \tag{5.1}$$

where I_0, I_{45}, I_{90} and I_{135} are the reflected intensities at 0°, 45°, 90° and 135° with respect to the input polarization (Stokes angles).[94]

5.2.3 Generation of angular momentum beams

Beams carrying angular momentum were generated with different combinations of SAM and OAM across the visible range (500-800 nm) in order to measure the dichroism spectra (§ 5.2.4). SAM in this chapter was generated using a photoelastic modulator (PEM). The PEM induces a periodic phase modulation in the beam given by

$$\delta = \delta_0 \sin \Omega t, \tag{5.2}$$

where δ_0 is the amplitude of phase modulation and Ω the modulation frequency. The modulation frequency is about 50 kHz, so CPL beams are modulated at high frequency. This is in contrast with quarter wave plates, the method used to generate SAM in Chapter 4.

The method to generate LG beams carrying OAM in this chapter involves the use of a Q-plate. Recall that the transfer of spin angular momentum alone, that is, without orbital angular momentum transfer, occurs when the medium is anisotropic *e.g.* birefringent, for example, in a quarter wave plate.[29] In contrast, the transfer of orbital angular momentum independently of spin occurs when the medium is inhomogeneous isotropic and transparent, such as spiral phase plates[212] or cylindrical lenses.[43] In 2006, it was discovered that circularly-polarized light can undergo spin-to-orbital conversion after passing through a medium that is both anisotropic and inhomogeneous.[304] Such a device is referred to as Q-plate and it is made of nematic liquid crystals.[305]

The underlying principle is that, if we started from a left-circularly polarized beam, described by the Jones vector $[1,\ +i]$, the electric field vectors for the incoming and outgoing beams, $\mathbf{E_{in}}$ and $\mathbf{E_{out}}$, respectively, are expressed as[304]

$$\mathbf{E_{in}} = E_0 \begin{bmatrix} 1 \\ +i \end{bmatrix}, \tag{5.3}$$

$$\mathbf{E_{out}} = E_0 e^{i2Q\phi} e^{i2\alpha_0} \begin{bmatrix} 1 \\ -i \end{bmatrix}, \tag{5.4}$$

where the outgoing beam now has changed spin from $\hbar$ to $-\hbar$ and is now right-circularly polarized with Jones vector $[1,\ -i]$. Furthermore, we can see that the beam has now acquired an azimuthal phase of $2Q\phi$, and therefore has an orbital angular momentum of $2Q\hbar$ per photon.[304] Similarly, if the incoming beam is right-circularly polarized, then the outgoing beam acquires an orbital angular momentum of $-2Q\hbar$ and it becomes left-circularly-polarized with SAM of $+\hbar$. The incoming and outgoing electric field vectors are therefore given by

$$\mathbf{E_{in}} = E_0 \begin{bmatrix} 1 \\ -i \end{bmatrix}, \tag{5.5}$$

$$\mathbf{E_{out}} = E_0 e^{-i2Q\phi} e^{-i2\alpha_0} \begin{bmatrix} 1 \\ +i \end{bmatrix}. \tag{5.6}$$

Q is a number representing the order of the Q-plate. If $Q = 1$, the outgoing beams have a topological charge of $l = \pm 2$, where total angular momentum conversion has taken place. In this thesis, a Q-plate made of a liquid crystal and $Q = 1/2$ (ARCoptix, Inc.) was used, so the outgoing beam has a topological charge of $l = \pm 1$ and the remaining angular momentum is transferred to the Q-plate itself, in a similar manner to Beth's

experiment.[29] Therefore, the outgoing beam after the Q-plate has an antiparallel combination of SAM and OAM ($\sigma = \mp 1$, $l = \pm 1$) and a total AM of 0.

The Q-plate is electrically driven, so it can be turned on and off and the voltage can be adjusted to produce OAM in a wide range of wavelengths.[306, 307] This is a major advantage compared to the use of spiral phase plates to generate LG beams in Chapter 4, as the same spiral phase plate cannot be used for different wavelengths. Instead, the use of a Q-plate allows to collect dichroism measurements for all the wavelengths and different combinations of SAM and OAM, depending on whether the Q-plate is on or off. Similar to the spiral phase plate case in Chapter 4, the Q-plate was mounted in a xy mount to align the centre of the Q-plate with the optical axis in order to obtain an optical vortex that is as symmetric as possible.

The dichroism experiments were conducted under weak (NA=0.3) and also tight (NA=0.95) focusing in air. It is of crucial importance to know how large the beam spot size is compared to the structure size, so the beam profiles for the $l = 0$ and $l = 1$ beams for the low NA case are shown in Figure 5.3. The Gaussian beam intensity was fitted to the intensity function[126]

$$I(\rho) = |E(\rho)|^2 = Ae^{-\frac{2(\rho-\rho_0)^2}{w_0^2}}, \tag{5.7}$$

where A is an amplitude term, ρ the radial position, ρ_0 the peak centre and w_0 the beam waist. From this fitting, a beam waist of $w_0 = 2.153 \pm 0.016$ μm was obtained, as indicated in Figure 5.3d.

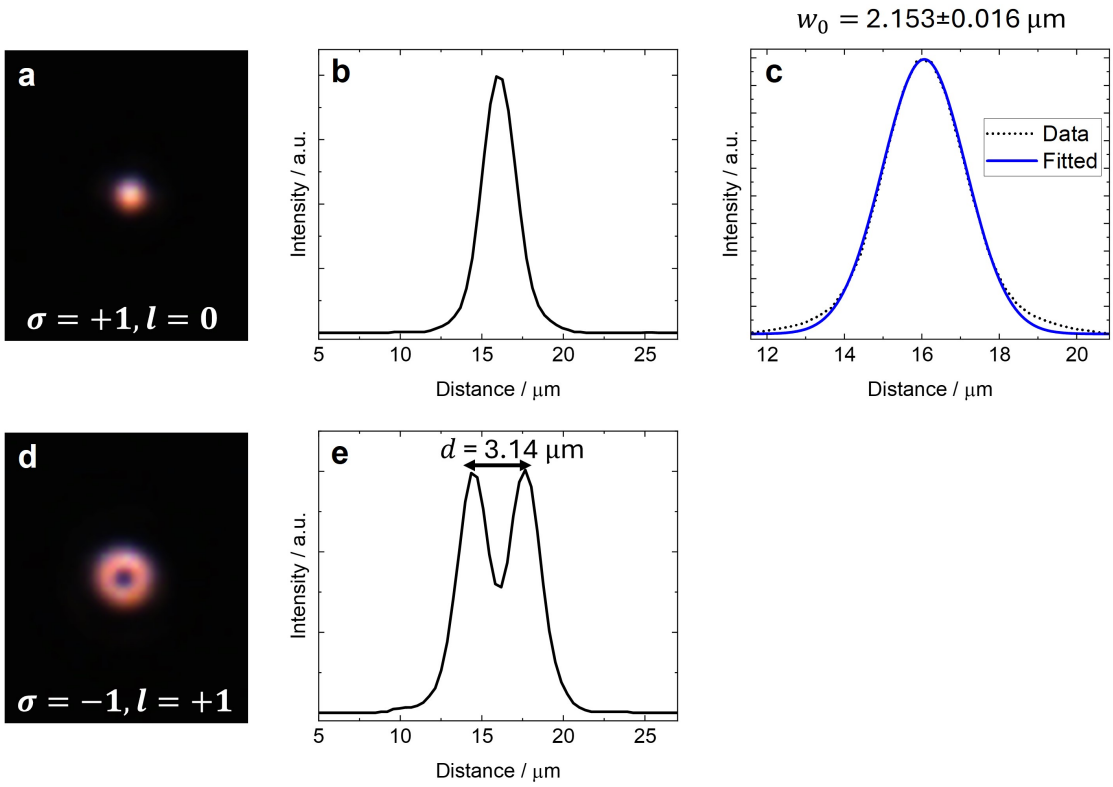

Figure 5.3: Beam profiles for weakly-focused beams (NA=0.3) at $\lambda = 600$ nm. (a) Image of the Gaussian $\sigma = +1$, $l = 0$ beam. (b) 1D plot across (a). (c) Gaussian fit of (b), from which the beam waist value indicated above is obtained. (d) Image of the LG $\sigma = +1$, $l = 0$ beam. (e) 1D plot across (d), with the peak-to-peak distance d indicated above.

Figure 5.4 shows the beam profiles for circularly-polarized $l = 0$ and $l = 1$ beams for high NA. The extracted beam waist from the Gaussian fitting is $w_0 = 647 \pm 5$ nm, as indicated in Figure 5.4d. This implies that $w_0 \approx \lambda$ and therefore the tightly-focused beams are non-paraxial.

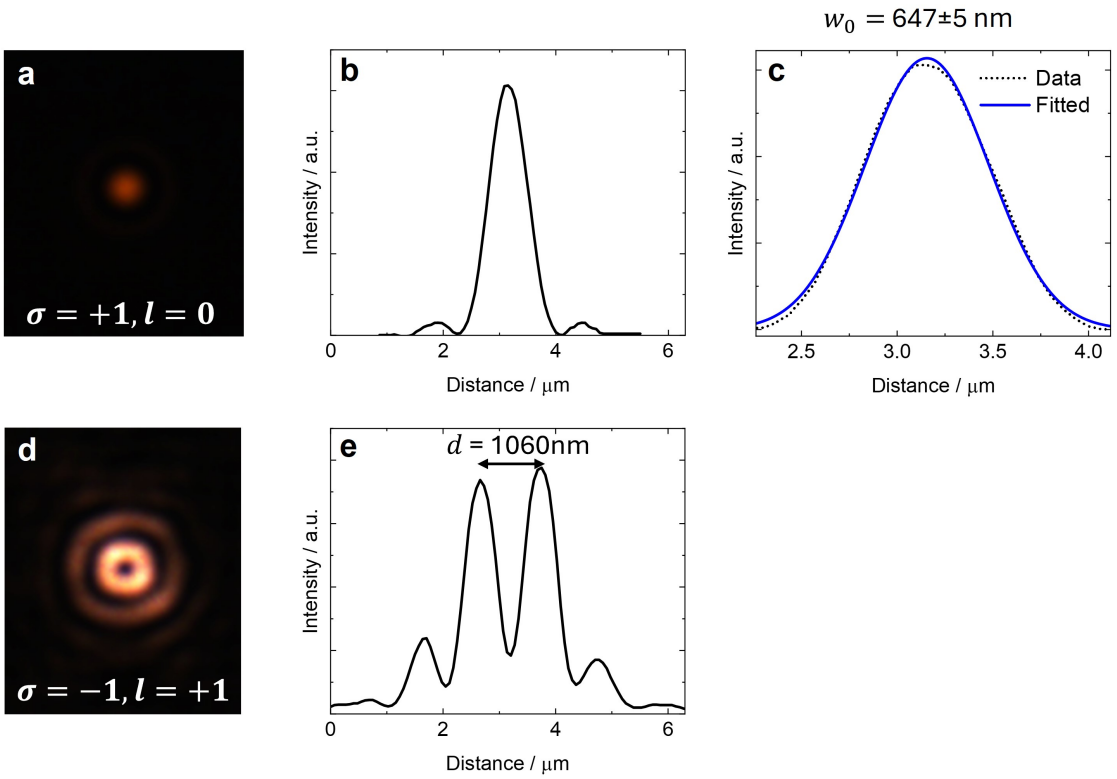

Figure 5.4: Beam profiles for tightly-focused beams (NA=0.95) at $\lambda = 600$ nm. (a) Image of the Gaussian $\sigma = +1$, $l = 0$ beam. (b) 1D plot across (a). (c) Gaussian fit of (b), from which the beam waist value indicated above is obtained. (d) Image of the LG $\sigma = +1$, $l = 0$ beam. (e) 1D plot across (d), with the peak-to-peak distance d indicated above.

In order to visualize how large the beam is in comparison with the structures for weak and tight focusing, AFM images with a red circle representing the beam diameter (taken to be $2w_0$) are presented in Figure 5.5. The Gaussian beam spot has a diameter spanning approximately 6 lattice spacings after weak focusing. In the tightly-focused beam, the Gaussian beam has a diameter spanning slightly less than 2 lattice spacings.

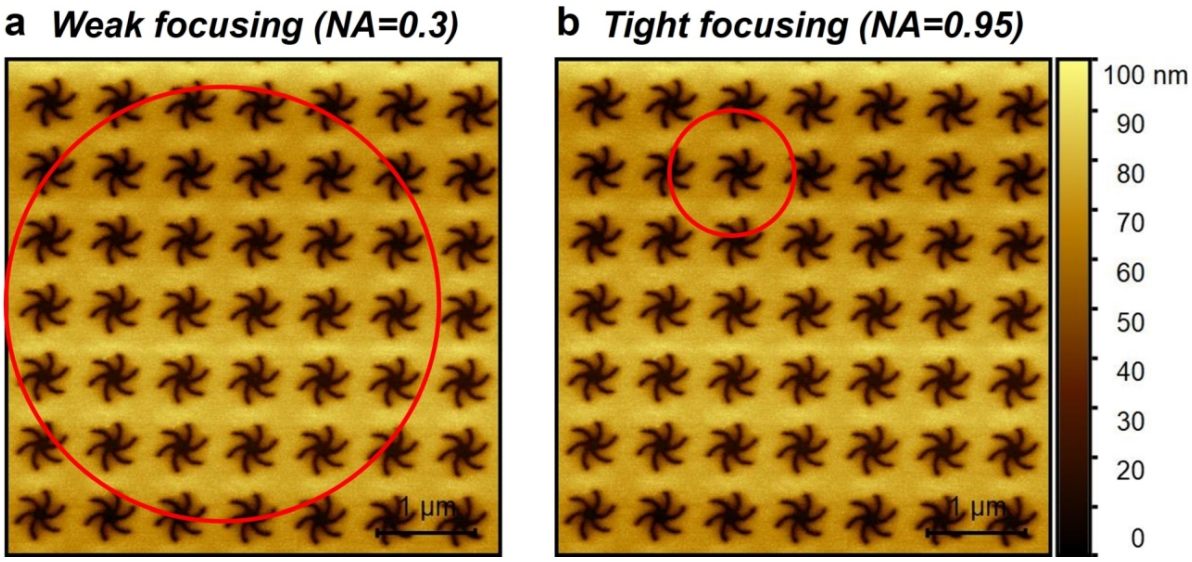

Figure 5.5: AFM images of the periodic shuriken nanoindentations with the beam diameter of the Gaussian beam (defined as $2w_0$) for weak and tight focusing indicated as a red circle.

5.2.4 Dichroism measurements

Dichroism measurements were performed at Hokkaido University using a home-built set-up which was built by Shun Hashiyada and Yoshito Tanaka.[218] The set-up collects the dichroism using various combinations of SAM and OAM across the visible range, as depicted in Figure 5.6. The set-up employs a collimated white light laser (Superk EVO EUL-10, NKT Photonics), which operates in the wavelength range 425-2250 nm and has a maximum power of 0.3 W. A monochromator (SpectraPro HRS-300, Princeton Instruments) is then used to choose a specific wavelength. After the monochromator, the beam passes through a beam expander and spatial filter comprised of a first lens (f_1 =50 mm), a pinhole (50 μm) and a second lens (f_2 =200 mm).

The beam passes through a linear polarizer so it becomes linearly-polarized. Circularly-polarized light is then generated using a PEM (II/FS50, HINDS Instruments, Inc.). A Q-plate (ARCoptix, Inc.) that operates in the wavelength range of 400-1700 nm was then used to generate the LG beam *via* spin-orbit conversion, as explained in more detail in § 5.2.3. The modulated CPL beam enters the Q-plate and SAM is converted into OAM,[304] so the beam leaving the Q-plate now has OAM and SAM which are

antiparallel ($\sigma = \mp 1, l = \pm 1$).

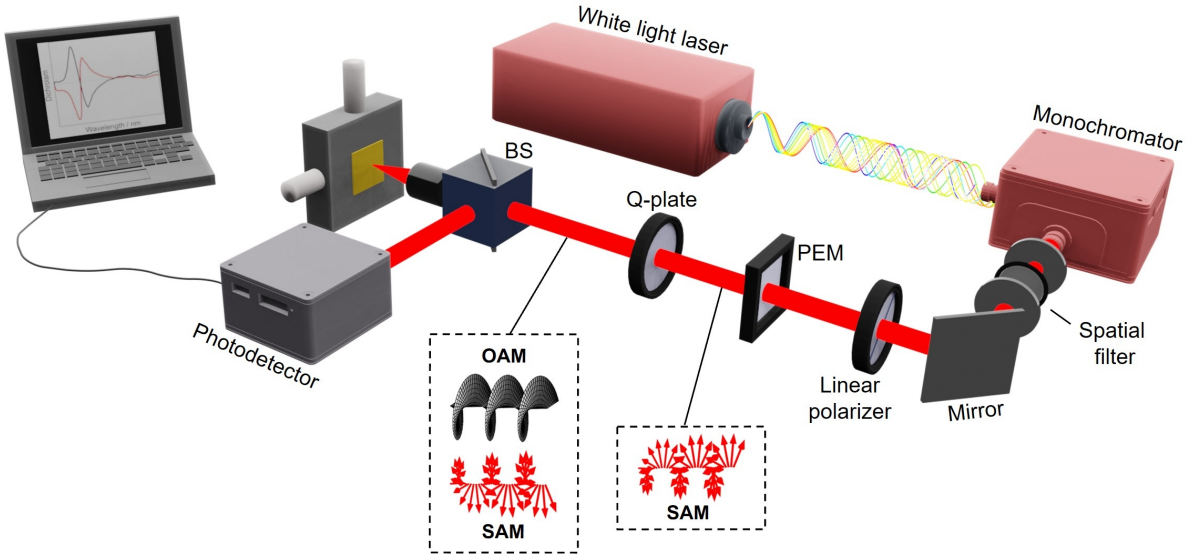

Figure 5.6: Experimental set-up used to achieve variable angular momentum modulation across the visible range. PEM: photoelastic modulator; BS: beam splitter.

In the case where helical dichroism was collected, a linear polarizer was added after the Q-plate to remove the spin contribution and leave the OAM unaffected, so the beam is now a linearly-polarized LG beam ($\sigma = 0, l = \pm 1$).

The beam is then focused onto the sample, which is positioned on a piezo stage (Angstrom Technology Inc.). After reflecting off the sample, the beam is focused into a photomultiplier tube (H10723-20, Hamamatsu Photonics K. K.) using an achromatic lens (f =180 mm). The detected signal, I_{det}, has $n\Omega$ components (where n is an integer) due to the modulation $\delta = \delta_0 \sin \Omega t$ and it is given by[308]

$$I_{det} = I(0) + I(\Omega) \sin(\Omega t) + I(2\Omega) \sin(2\Omega t) + ... \tag{5.8}$$

In our case, we only detect the 0th and 1st harmonic (1Ω) components of the detected signal,[218] so the detected signal is given by

$$I_{det} = I(0) + I(\Omega) \sin(\Omega t), \tag{5.9}$$

where

$$I(0) = I_0(T_+^2 + T_-^2)\{1 + J_0(\delta_0)\sin(2\phi)\} \quad \text{(DC signal)} \tag{5.10}$$

and

$$I(\Omega) = I_0(T_+^2 - T_-^2)J_1(\delta_0) \quad \text{(AC signal).} \tag{5.11}$$

J_n is an n-th order Bessel function of the first kind and $I_0 = (\varepsilon/8\pi)E^2$. In simple terms, the AC signal contains information about the chirality of the sample, and the DC signal contains information about the total signal of the sample.

As it can be seen, the DC signal is proportional to the sum of the intensities of the detected LH and RH beams, whereas the AC signal is proportional to the difference between the detected intensities of LH and RH beams, and therefore contains the chiral response by the sample.

As shown in Figure 5.7, the 0-th order Bessel function $J_0(\delta_0)$ is 0 when $\delta_0 = 2.405$.

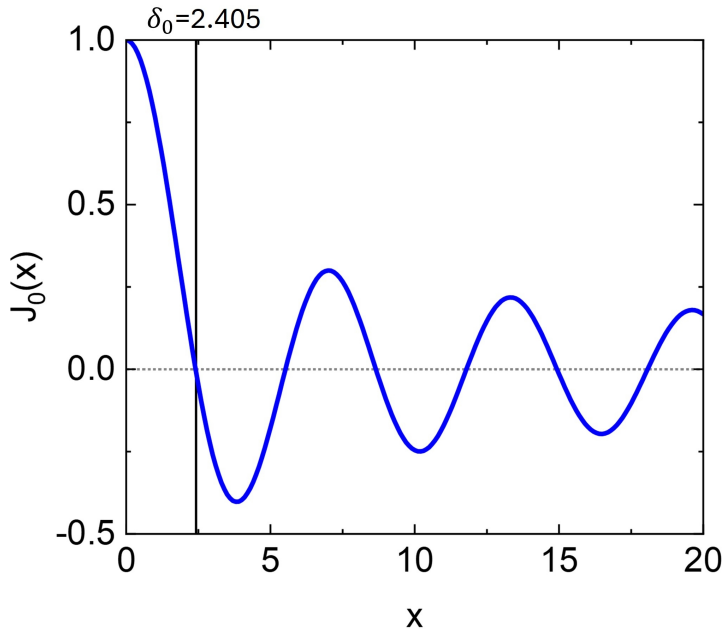

Figure 5.7: Bessel function of 0-th order, $J_0(x)$. $J_0(\delta_0) = 0$ for $\delta_0 = 2.405$.

Therefore, by choosing $\delta_0 = 2.405$ the sample dichroism can be expressed as

$$\text{Dichroism} = \frac{T_+^2 - T_-^2}{T_+^2 + T_-^2} = \frac{AC_{\text{Sample}}}{J_1(\delta_0)DC_{\text{Sample}}}. \tag{5.12}$$

As PEM modulates the signal at high frequency (50kHz), the AC and DC signals can be detected using a lock-in amplifier (NF corporation, LI5655). The dichroism was then calculated using equation 5.12.

The extinction (sum of absorption and scattering) is also obtained from AC and DC signals and it is given by

$$\text{Extinction} = -log_{10}\left(\frac{DC_{\text{Sample}}}{DC_{\text{Background}}}\right), \tag{5.13}$$

where $DC_{\text{Background}}$ is the DC signal of plain gold (outside the chiral nanoindentations).

As the monochromator is used to choose any wavelength, a CD, a helical dichroism spectrum or a dichroism spectrum with different amounts of SAM and OAM can be obtained over the visible range by measuring the chiral response at each wavelength. This process is dynamic, as the Q-plate can be turned on and off to choose the desired angular momentum.

5.3 Computational methods

Numerical simulations were performed in this chapter using COMSOL Multiphysics (version 6.2) and the electromagnetic wave frequency domain. COMSOL uses the FEM method, as outlined in § 3.1.1, to find approximate solutions to Maxwell's equations.

The incoming beam in the experiments is a focused beam with a either NA= 0.3 or NA=0.95. To implement the focused beam, expressions for all the focused fields were derived, as explained in detail in the next section (§ 5.4.1). The simulations were performed with the different combinations of SAM and OAM: circularly-polarized Gaussian beam ($\sigma \pm 1$, l=0), which carries SAM only; linearly-polarized LG beam (σ=0, $l = \pm 1$), which carries OAM only; circularly-polarized LG beam ($\sigma \pm 1$, $l = \mp 1$), where

SAM and OAM are antiparallel. For completeness, the circularly-polarized LG beam with parallel combination of SAM and OAM was also simulated ($\sigma \pm 1$, $l = \pm 1$). All the varying combinations of SAM and OAM are summarized in Table 5.1.

	Polarization	Intensity profile	SAM	OAM	Total AM
Case 1	Circular	Laguerre-Gaussian	$\pm\hbar$	$\mp\hbar$	0
Case 2	Circular	Gaussian	$\pm\hbar$	0	$\pm\hbar$
Case 3	Linear	Laguerre-Gaussian	0	$\pm\hbar$	$\pm\hbar$
Case 4	Circular	Laguerre-Gaussian	$\pm\hbar$	$\pm\hbar$	$\pm 2\hbar$

Table 5.1: The different beams which have been simulated in this chapter.

As shown in Figure 5.8, the beam propagates in the negative z direction and it is focused on a single gold shuriken-shaped nanoindentation placed on a polycarbonate substrate. The surface of the gold is placed at $z = 0$. The refractive indices of gold and polycarbonate were taken from references [309] and [310]. The size of the mesh elements in the gold span the range 0.44-25 nm. The simulated domain is a sphere of radius 500 nm + $\lambda/2$ and it is surrounded by a perfectly-matched layer (PML) of thickness $\lambda/2$, where λ is the wavelength of the incident light.

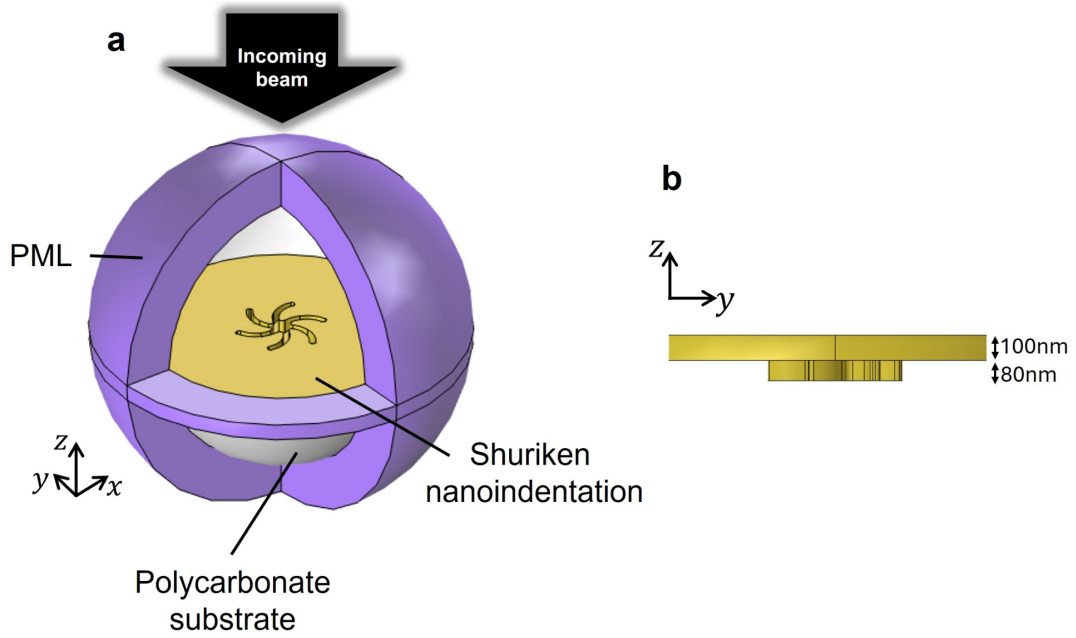

Figure 5.8: (a) Simulation model containing a gold shuriken-shaped nanoindentation. The nanoindentations can be right- or left-handed (only the right-handed one is shown). Above the gold there is an air domain and below the polycarbonate substrate. PML: perfectly-matched layers. (b) Side view of the gold layer.

In the simulations with focused LG beams it was not possible to include a periodic structure due to the large computational time for each wavelength. However, another set of simulations were performed using ports and plane waves, where in this case it was possible to include the periodicity of the structure. In this set of simulations, the structure was evenly illuminated everywhere and the beam includes no information on the transverse characteristics, so OAM could not be included here. Instead, these simulations were only used to understand what the effect of the periodic array is in the optical characteristics of the shuriken for SAM only. The model used for these simulations is shown in Figure 5.9. The model includes two PML layers above and below the input and output ports, respectively. To account for the periodicity of the structure, the width of the gold layer was set to the periodicity of the structure (720 nm) and periodic boundary conditions (Floquet periodicity) were applied in the x and y directions.

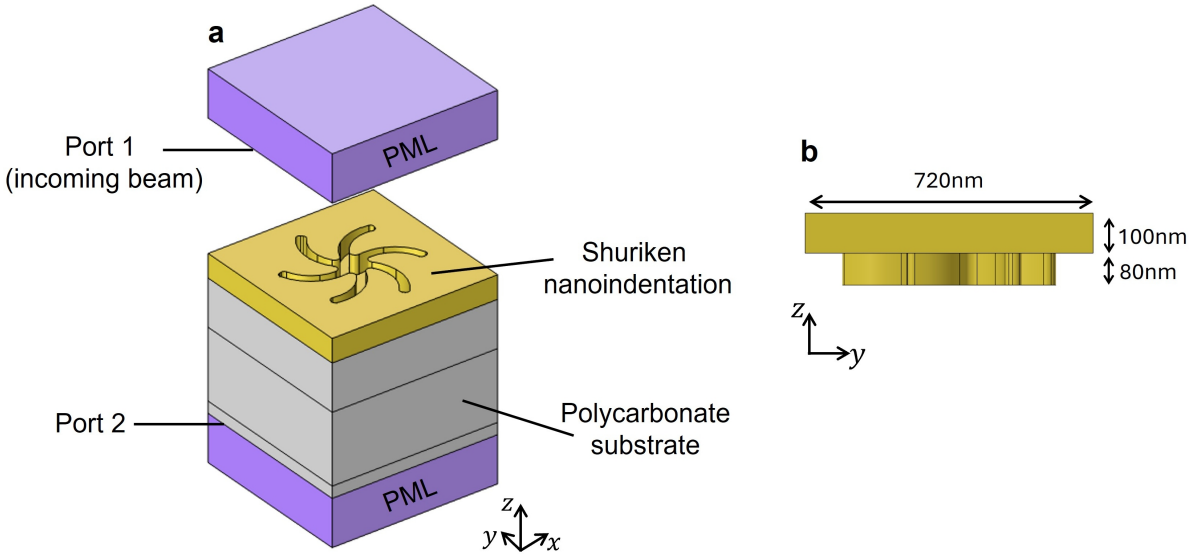

Figure 5.9: (a) Simulation model in the case of periodic structures. PML (perfectly-matched layers) are placed above and below the input and output ports, respectively. The model includes Floquet periodicity in the x and y directions. (b) Side view of the gold layer.

The scattering A_{sc} and absorption cross sections A_{abs} were extracted from the simulations using the expressions[291]

$$A_{sc} = \frac{1}{I_0} \iint_S \mathbf{S_{sc}} \cdot \hat{\mathbf{n}} \, dS, \tag{5.14}$$

$$A_{abs} = \frac{1}{I_0} \iiint_V Q \; dV. \tag{5.15}$$

I_0 is the intensity of the incident beam, $\mathbf{S_{sc}}$ the Poynting vector of the scattered light, S a closed surface enclosing the gold layer, $\hat{\mathbf{n}}$ an outward unit vector normal to the surface S, Q the power loss density in the gold layer and V the volume of the gold layer. The extinction cross section A_{ext} is the sum of the scattering and absorption cross sections

$$A_{ext} = A_{sc} + A_{abs}. \tag{5.16}$$

The g-factor was calculated using the expression[82]

$$g\text{-factor} = 2\frac{A_{ext}^{\sigma=+1} - A_{ext}^{\sigma=-1}}{A_{ext}^{\sigma=+1} + A_{ext}^{\sigma=-1}}. \tag{5.17}$$

5.4 Results and discussion

5.4.1 Simulated focused beams in free space

The expression that was used to implement Laguerre-Gaussian beams in Chapter 3 is a solution of the paraxial wave equation and it is assumes that the electric field oscillates mainly in the transverse direction. Nevertheless, the paraxial expression does not account for the electric longitudinal fields (E_z) when the beam is tightly focused.

In this chapter, the effects of optical angular momentum were studied for both weak and tight focusing, therefore longitudinal fields cannot be neglected. In this section, expressions for all the focused fields used in this chapter are derived.

The focused fields were derived following the diffraction theory developed by Richards and Wolf in reference [311]. This theory is used to describe the electric field of a light beam after it is focused by a lens. As schematically shown in Figure 5.10, the electric

field vector will experience a rotation by an angle θ when the beam is refracted by the lens and the beam will focus at a distance f, where f is the focal length of the lens. The maximum angle by which the electric field can be rotated is given by θ_{max}, which can be derived from the numerical aperture NA of the objective as[28]

$$\mathrm{NA} = n \sin(\theta_{max}), \tag{5.18}$$

where n is the refractive index of the medium after the objective lens.

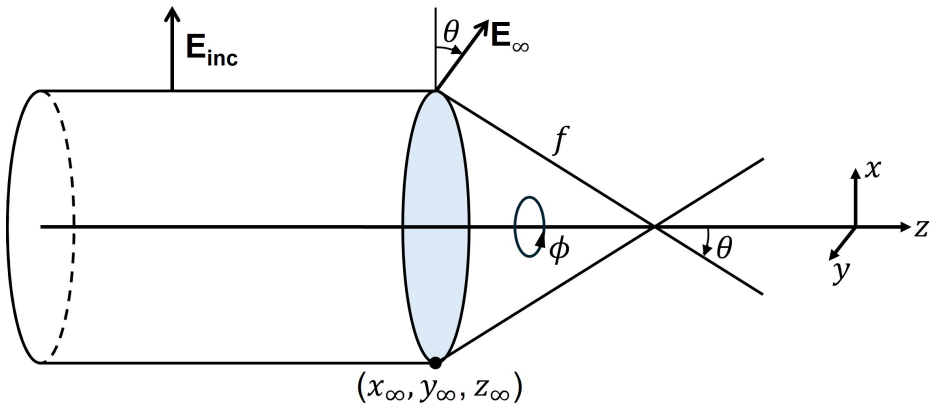

Figure 5.10: Electric field transformation by lens focusing. The lens is represented by a blue surface. In this example, the incoming electric field $\mathbf{E}_{\mathbf{inc}}$ points along the x direction, and it is rotated by an angle θ by the lens to give $\mathbf{E}_\infty$. The lens has a focal length of f, which defines the radius of the cone of the focused field. An arbitrary point on the lens surface is marked as $(x_\infty, y_\infty, z_\infty)$.

The rotation of the electric field experienced at the lens can be expressed as a function of the incident electric field as[22]

$$\mathbf{E}_\infty = \left[[\mathbf{E_{inc}} \cdot \hat{\boldsymbol{\phi}}]\hat{\boldsymbol{\phi}} + [\mathbf{E_{inc}} \cdot \hat{\boldsymbol{\rho}}]\hat{\boldsymbol{\theta}} \right] \sqrt{\frac{n_1}{n_2}} (\cos\theta)^{1/2}, \tag{5.19}$$

where $\mathbf{E}_\infty$ is the refracted electric field at the lens surface. $[\mathbf{E_{inc}} \cdot \hat{\boldsymbol{\phi}}]\hat{\boldsymbol{\phi}}$ is the component of the incident field corresponding to s-polarization and $[\mathbf{E_{inc}} \cdot \hat{\boldsymbol{\rho}}]\hat{\boldsymbol{\theta}}$ that corresponding to p-polarization. $\hat{\boldsymbol{\rho}}$, $\hat{\boldsymbol{\phi}}$ and $\hat{\boldsymbol{\theta}}$ are unit vectors, related to the Cartesian unit vectors as[22]

$$\hat{\boldsymbol{\rho}} = \cos\phi\hat{\mathbf{x}} + \sin\phi\hat{\mathbf{y}}, \tag{5.20}$$

$$\hat{\boldsymbol{\phi}} = -\sin\phi\hat{\mathbf{x}} + \cos\phi\hat{\mathbf{y}}, \tag{5.21}$$

$$\hat{\boldsymbol{\theta}} = \cos\theta\cos\phi\hat{\mathbf{x}} + \cos\theta\sin\phi\hat{\mathbf{y}} - \sin\theta\hat{\mathbf{z}}, \tag{5.22}$$

where $\hat{\mathbf{x}}$, $\hat{\mathbf{y}}$ and $\hat{\mathbf{z}}$ are Cartesian unit vectors in the x, y and z directions, respectively. Then the rotation of the incident electric field vector $\mathbf{E_{inc}}$ after refraction by the lens can be written in Cartesian coordinates as[22]

$$\begin{aligned}\mathbf{E}_\infty = &\left[\mathbf{E_{inc}}(\theta,\phi)\cdot\begin{pmatrix}-\sin\phi\\ \cos\phi\\ 0\end{pmatrix}\right]\begin{pmatrix}-\sin\phi\\ \cos\phi\\ 0\end{pmatrix}\sqrt{\frac{n_1}{n_2}}(\cos\theta)^{1/2}\\ &+\left[\mathbf{E_{inc}}(\theta,\phi)\cdot\begin{pmatrix}\cos\phi\\ \sin\phi\\ 0\end{pmatrix}\right]\begin{pmatrix}\cos\theta\cos\phi\\ \cos\theta\sin\phi\\ -\sin\theta\end{pmatrix}\sqrt{\frac{n_1}{n_2}}(\cos\theta)^{1/2}.\end{aligned} \tag{5.23}$$

For now, we can focus on a polarized beam in the x direction, so $\mathbf{E_{inc}}$ is given by

$$\mathbf{E_{inc}} = |\mathbf{E_{inc}}|\hat{\mathbf{x}} = |\mathbf{E_{inc}}|\begin{bmatrix}1\\ 0\\ 0\end{bmatrix}. \tag{5.24}$$

After vector multiplication in expression 5.23, the x-polarized beam becomes

$$\begin{aligned}\mathbf{E}_\infty(\theta,\phi) =& |\mathbf{E_{inc}}|\sqrt{\frac{n_1}{n_2}}(\cos\theta)^{1/2}[\cos\phi\hat{\boldsymbol{\theta}} - \sin\phi\hat{\boldsymbol{\phi}}] \\ =& |\mathbf{E_{inc}}|\sqrt{\frac{n_1}{n_2}}(\cos\theta)^{1/2}\begin{bmatrix}\cos^2\phi\cos\theta + \sin^2\phi \\ -(1-\cos\theta)\sin\phi\cos\phi \\ -\sin\theta\cos\phi\end{bmatrix} \\ =& |\mathbf{E_{inc}}|\sqrt{\frac{n_1}{n_2}}(\cos\theta)^{1/2}\frac{1}{2}\begin{bmatrix}(1+\cos\theta) - (1-\cos\theta)\cos(2\phi) \\ -(1-\cos\theta)\sin(2\phi) \\ -2\sin\theta\cos\phi\end{bmatrix}.\end{aligned} \tag{5.25}$$

To obtain the final expression in equation 5.25, the trigonometric identities $\sin^2\phi = 1-\cos^2\phi$, $\cos(2\phi) = 2\cos^2\phi - 1$ and $\sin(2\phi) = 2\sin\phi\cos\phi$ have been used. In equation 5.25, $\mathbf{E}_\infty(\theta,\phi)$ is the electric field vector at the lens surface when the incident beam is x-polarized, as a function of the spherical coordinates angles θ and ϕ. n_1 and n_2 are the refractive indices before and after the lens. $|\mathbf{E_{inc}}|$ is the electric field amplitude of the beam that is focused by the lens.[22]

Similarly, it is possible to derive an equivalent expression for an y-polarized beam, so the incident electric field vector is given by

$$\mathbf{E_{inc}} = |\mathbf{E_{inc}}|\hat{\mathbf{y}} = |\mathbf{E_{inc}}|\begin{bmatrix}0\\1\\0\end{bmatrix}. \tag{5.26}$$

After vector multiplication in equation 5.23, the y-polarized beam becomes

$$\begin{aligned}\mathbf{E}_\infty(\theta,\phi) =& |\mathbf{E_{inc}}|\sqrt{\frac{n_1}{n_2}}(\cos\theta)^{1/2}[\sin\phi\hat{\boldsymbol{\theta}} + \cos\phi\hat{\boldsymbol{\phi}}] \\ =& |\mathbf{E_{inc}}|\sqrt{\frac{n_1}{n_2}}(\cos\theta)^{1/2}\begin{bmatrix} -(1-\cos\theta)\sin\phi\cos\phi \\ \sin^2\phi\cos\theta + \cos^2\phi \\ -\sin\theta\sin\phi \end{bmatrix} \\ =& |\mathbf{E_{inc}}|\sqrt{\frac{n_1}{n_2}}(\cos\theta)^{1/2}\frac{1}{2}\begin{bmatrix} -(1-\cos\theta)\sin(2\phi) \\ (1+\cos\theta) + (1-\cos\theta)\cos(2\phi) \\ -2\sin\theta\sin\phi \end{bmatrix}.\end{aligned} \tag{5.27}$$

To obtain the final expression in equation 5.27, the trigonometric identities $\cos^2\phi = 1 - \sin^2\phi$, $\cos(2\phi) = 1 - 2\sin^2\phi$ and $\sin(2\phi) = 2\sin\phi\cos\phi$ have been used.

Using $x = \rho\cos\varphi$, $y = \rho\sin\varphi$ to express the transverse components of the electric field at the focal point, the electric field near the focus is given by[22]

$$\mathbf{E_f}(\rho,\varphi,z) = -\frac{ikfe^{-ikf}}{2\pi}\int_0^{\theta_{max}}\int_0^{2\pi}\mathbf{E}_\infty(\theta,\phi)e^{ikz\cos\theta}e^{ik\rho\sin\theta\cos(\phi-\varphi)}\sin\theta\ d\phi\ d\theta. \tag{5.28}$$

Equation 5.28 allows to calculate the electric field at the focus for an arbitrary beam that is focused using a lens with focal length f and numerical aperture NA$= n\sin(\theta_{max})$, for $0 < \theta_{max} < \pi/2$.[22] In order to compute equation 5.28, it is necessary to know the the electric field amplitude $|\mathbf{E_{inc}}|$ that forms part of $\mathbf{E}_\infty(\theta,\phi)$. For example, if the incident beam is a Gaussian beam, then $|\mathbf{E_{inc}}|$ is given by[22]

$$|\mathbf{E_{Gaussian}}| = E_0 e^{-(x_\infty^2+y_\infty^2)/w_0^2}, \tag{5.29}$$

where w_0 is the beam waist. The Cartesian coordinates (x_∞, y_∞, z_∞) can be written in spherical coordinates (f, θ, ϕ) as[22]

$$x_\infty = f \sin\theta \cos\phi, \tag{5.30}$$

$$y_\infty = f \sin\theta \sin\phi, \tag{5.31}$$

$$z_\infty = f \cos\theta. \tag{5.32}$$

Note that now the radius is given by f, the focal length of the lens, as this defines the radius of the cone after lens focusing (see Figure 5.10). This transforms expression 5.29 to

$$|\mathbf{E_{Gaussian}}| = E_0 e^{-(f^2 \sin^2\theta \cos^2\phi + f^2 \sin^2\theta \sin^2\phi)/w_0^2} = E_0 e^{-f^2 \sin^2\theta/w_0^2} = E_0 f_w(\theta), \tag{5.33}$$

as $\cos^2\phi + \sin^2\phi = 1$. The exponential term in equation 5.33 is called the apodization function[22]

$$f_w(\theta) = e^{-f^2 \sin^2\theta/w_0^2}. \tag{5.34}$$

Additionally, we can make use of the expressions

$$\int_0^{2\pi} \cos(n\phi) e^{ix\cos(\phi-\varphi)} d\phi = 2\pi(i^n) J_n(x) \cos(n\varphi), \tag{5.35}$$

$$\int_0^{2\pi} \sin(n\phi) e^{ix\cos(\phi-\varphi)} d\phi = 2\pi(i^n) J_n(x) \sin(n\varphi), \tag{5.36}$$

to compute the integral over ϕ in equation 5.28,[311] where $J_n(x)$ is a n-th order Bessel function. Finally, we can compute the integral over θ in expression 5.28. Typically, the following abbreviations for the integrals over θ are used in the literature.[22, 311]

$$I_{00}(\rho,z) = \int_0^{\theta_{max}} f_w(\theta)(\cos\theta)^{1/2}\sin\theta(1+\cos\theta)\ J_0(k\rho\sin\theta)\ e^{ikz\cos\theta}\ d\theta, \tag{5.37}$$

$$I_{01}(\rho,z) = \int_0^{\theta_{max}} f_w(\theta)(\cos\theta)^{1/2}\sin^2\theta\ J_1(k\rho\sin\theta)\ e^{ikz\cos\theta}\ d\theta, \tag{5.38}$$

$$I_{02}(\rho,z) = \int_0^{\theta_{max}} f_w(\theta)(\cos\theta)^{1/2}\sin\theta(1-\cos\theta)\ J_2(k\rho\sin\theta)\ e^{ikz\cos\theta}\ d\theta, \tag{5.39}$$

$$I_{10}(\rho,z) = \int_0^{\theta_{max}} f_w(\theta)(\cos\theta)^{1/2}\sin^3\theta\ J_0(k\rho\sin\theta)\ e^{ikz\cos\theta}\ d\theta, \tag{5.40}$$

$$I_{11}(\rho,z) = \int_0^{\theta_{max}} f_w(\theta)(\cos\theta)^{1/2}\sin^2\theta(1+3\cos\theta)\ J_1(k\rho\sin\theta)\ e^{ikz\cos\theta}\ d\theta, \tag{5.41}$$

$$I_{12}(\rho,z) = \int_0^{\theta_{max}} f_w(\theta)(\cos\theta)^{1/2}\sin^2\theta(1-\cos\theta)\ J_1(k\rho\sin\theta)\ e^{ikz\cos\theta}\ d\theta, \tag{5.42}$$

$$I_{13}(\rho,z) = \int_0^{\theta_{max}} f_w(\theta)(\cos\theta)^{1/2}\sin^3\theta\ J_2(k\rho\sin\theta)\ e^{ikz\cos\theta}\ d\theta, \tag{5.43}$$

$$I_{14}(\rho,z) = \int_0^{\theta_{max}} f_w(\theta)(\cos\theta)^{1/2}\sin^2\theta(1-\cos\theta)\ J_3(k\rho\sin\theta)\ e^{ikz\cos\theta}\ d\theta. \tag{5.44}$$

The term $f_w(\theta)$ is the apodization function given in 5.34. Using these abbreviations it is possible to write an expression for the focused fields. First, we can do this for the x-polarized Gaussian beam. By inserting equation 5.25 with the Gaussian beam amplitude into equation 5.28, the x-polarized Gaussian beam after focusing is given by

$$\begin{aligned}
\mathbf{E_f}(\rho,\varphi,z) =& \mathbf{E}^{\text{x-polarized}}_{\text{Gaussian}} \\
=& -\frac{ikfe^{-ikf}}{2\pi}E_0\sqrt{\frac{n_1}{n_2}}\int_0^{\theta_{max}}\int_0^{2\pi} f_w(\theta)(\cos\theta)^{1/2}\sin\theta \\
& \frac{1}{2}\begin{bmatrix}(1+\cos\theta)-(1-\cos\theta)\cos(2\phi)\\ -(1-\cos\theta)\sin(2\phi)\\ -2\sin\theta\cos\phi\end{bmatrix} e^{ikz\cos\theta}e^{ik\rho\sin\theta\cos(\phi-\varphi)}\ d\phi\ d\theta \\
=& -\frac{1}{2}\frac{ikfe^{-ikf}}{2\pi}E_0\sqrt{\frac{n_1}{n_2}}\int_0^{\theta_{max}} f_w(\theta)(\cos\theta)^{1/2}\sin\theta \\
& \begin{bmatrix}(1+\cos\theta)2\pi J_0(k\rho\sin\theta)-(1-\cos\theta)2\pi i^2 J_2(k\rho\sin\theta)\cos(2\varphi)\\ -(1-\cos\theta)2\pi i^2 J_2(k\rho\sin\theta)\sin(2\varphi)\\ -2(2\pi i J_1(k\rho\sin\theta)\cos\varphi)\sin\theta\end{bmatrix} e^{ikz\cos\theta}d\theta,
\end{aligned} \tag{5.45}$$

which can be abbreviated to

$$\mathbf{E}^{x\text{-polarized}}_{\text{Gaussian}}(\rho,\varphi,z) = -\frac{ikf}{2}\sqrt{\frac{n_1}{n_2}}E_0 e^{-ikf}\begin{bmatrix} I_{00}+I_{02}\cos(2\varphi) \\ I_{02}\sin(2\varphi) \\ -2iI_{01}\cos(\varphi)\end{bmatrix}, \tag{5.46}$$

which agrees with the expression derived in [22]. Here the same procedure is used to derive the y-polarized Gaussian beam. By inserting equation 5.27 with the Gaussian beam amplitude into equation 5.28, the y-polarized focused Gaussian beam is obtained to be

$$\begin{aligned}\mathbf{E_f}(\rho,\varphi,z) =& \mathbf{E}^{y\text{-polarized}}_{\text{Gaussian}} \\ =& -\frac{ikfe^{-ikf}}{2\pi}E_0\sqrt{\frac{n_1}{n_2}}\int_0^{\theta_{max}}\int_0^{2\pi} f_w(\theta)(\cos\theta)^{1/2}\sin\theta \\ & \frac{1}{2}\begin{bmatrix} -(1-\cos\theta)\sin(2\phi) \\ (1+\cos\theta)+(1-\cos\theta)\cos(2\phi) \\ -2\sin\theta\sin\phi\end{bmatrix} e^{ikz\cos\theta}e^{ik\rho\sin\theta\cos(\phi-\varphi)}\,d\phi\,d\theta \\ =& -\frac{1}{2}\frac{ikfe^{-ikf}}{2\pi}E_0\sqrt{\frac{n_1}{n_2}}\int_0^{\theta_{max}} f_w(\theta)(\cos\theta)^{1/2}\sin\theta \\ & \begin{bmatrix} -(1-\cos\theta)2\pi i^2 J_2(k\rho\sin\theta)\sin(2\varphi) \\ (1+\cos\theta)2\pi J_0(k\rho\sin\theta)+(1-\cos\theta)2\pi i^2 J_2(k\rho\sin\theta)\cos(2\varphi) \\ -2(2\pi i J_1(k\rho\sin\theta)\sin\varphi)\sin\theta\end{bmatrix} e^{ikz\cos\theta}d\theta,\end{aligned} \tag{5.47}$$

which can be abbreviated to

$$\mathbf{E}^{y\text{-polarized}}_{\text{Gaussian}}(\rho,\varphi,z) = -\frac{ikf}{2}\sqrt{\frac{n_1}{n_2}}E_0 e^{-ikf}\begin{bmatrix} I_{02}\sin(2\varphi) \\ I_{00}-I_{02}\cos(2\varphi) \\ -2iI_{01}\sin(\varphi)\end{bmatrix}. \tag{5.48}$$

To obtain a circularly-polarized beam, recall from § 2.2.1 that a circularly-polarized

beam is obtained by adding the x and y components and shifting the y component by $\pi/2$. A shift of $-\pi/2$ in the y component is the same as multiplying the y component by i, giving rise to left-circular polarization; similarly, a shift of $\pi/2$ in the y component is the same as multiplying the y component by $-i$, giving rise to right-circular polarization. Therefore, we can write

$$\mathbf{E}^{\sigma=\pm\mathbf{1}} = \frac{1}{\sqrt{2}}(\mathbf{E_x} \pm i\mathbf{E_y}), \tag{5.49}$$

where + and − correspond to left- and right-circularly polarized beam. Therefore, the focused circularly-polarized beam is obtained to be

$$\begin{aligned}\mathbf{E}^{\sigma=\pm1}_{\mathbf{Gaussian}}(\rho,\varphi,z) &= -\frac{1}{\sqrt{2}}\frac{ikf}{2}\sqrt{\frac{n_1}{n_2}}E_0 e^{-ikf}\begin{bmatrix} I_{00}+I_{02}\cos(2\varphi)\pm iI_{02}\sin(2\varphi) \\ I_{02}\sin(2\varphi)\pm i(I_{00}-I_{02}\cos(2\varphi)) \\ -2iI_{01}\cos(\varphi)\pm i(-2iI_{01}\sin(\varphi))\end{bmatrix} \\ &= -\frac{1}{\sqrt{2}}\frac{ikf}{2}\sqrt{\frac{n_1}{n_2}}E_0 e^{-ikf}\begin{bmatrix} I_{00}+I_{02}e^{\pm i2\varphi} \\ \pm iI_{00}\mp iI_{02}e^{\pm i2\varphi} \\ -2iI_{01}e^{\pm i\varphi}\end{bmatrix},\end{aligned} \tag{5.50}$$

where Euler's formula $e^{ix} = \cos x + i\sin x$ has been used. Now it is possible to write equation 5.50 in terms of individual SAM and OAM contributions of the circularly-polarized focused field.

$$\mathbf{E}^{\sigma=\pm1}_{\mathbf{Gaussian}}(\rho,\varphi,z) = -\frac{1}{\sqrt{2}}\frac{ikf}{2}\sqrt{\frac{n_1}{n_2}}E_0 e^{-ikf}\begin{bmatrix} I_{00}+I_{02}e^{\pm i2\varphi} \\ \pm iI_{00}\mp iI_{02}e^{\pm i2\varphi} \\ -2iI_{01}e^{\pm i\varphi}\end{bmatrix}$$

$$= -\frac{1}{\sqrt{2}}\frac{ikf}{2}\sqrt{\frac{n_1}{n_2}}E_0 e^{-ikf}\left(I_{00}\begin{bmatrix}1\\ \pm i\\ 0\end{bmatrix} + I_{01}e^{\pm i\varphi}\begin{bmatrix}0\\ 0\\ -2i\end{bmatrix} + I_{02}e^{\pm i2\varphi}\begin{bmatrix}1\\ \mp i\\ 0\end{bmatrix}\right). \tag{5.51}$$

Equation 5.51 represents the focused electric field for the circularly-polarized Gaussian beam. The first term represents the SAM only contribution ($\sigma = \pm 1$, $l = 0$), which dominates for weak focusing. The second and third terms constitute the OAM only contribution ($\sigma = 0$, $l = \pm 1$) and SAM-OAM ($\sigma = \mp 1$, $l = \pm 2$) terms, respectively, as a result of spin-orbit conversion after focusing, and they become important for tight focusing. Importantly, all the individual terms have a total angular momentum of $l + \sigma = \pm 1$, indicating that total angular momentum is conserved.

To derive the expressions for Laguerre-Gaussian beams of topological charge l, we can make use of the fact that Laguerre-Gaussian (LG) modes can be expressed using a combination of Hermite-Gaussian (HG) modes. The electric field amplitude of the incident field of the HG_{10} and HG_{01} modes are[22]

$$|\mathbf{E_{HG_{10}}}| = E_0(2x_\infty/w_0)e^{-(x_\infty^2+y_\infty^2)/w_0^2} = (2E_0 f/w_0)\sin\theta\cos\phi e^{-f^2\sin^2\theta/w_0^2}, \tag{5.52}$$

$$|\mathbf{E_{HG_{01}}}| = E_0(2y_\infty/w_0)e^{-(x_\infty^2+y_\infty^2)/w_0^2} = (2E_0 f/w_0)\sin\theta\sin\phi e^{-f^2\sin^2\theta/w_0^2}. \tag{5.53}$$

With the same procedure as the one applied for the x-polarized Gaussian beam, the x-polarized HG_{10} mode becomes

$$
\begin{aligned}
\mathbf{E_f}(\rho,\varphi,z) =& \mathbf{E}^{\textbf{x-polarized}}_{\mathbf{HG}_{10}}(\rho,\varphi,z) \\
=& -\frac{i2kf^2e^{-ikf}}{2\pi w_0}E_0\sqrt{\frac{n_1}{n_2}}\int_0^{\theta_{max}}\int_0^{2\pi} f_w(\theta)(\cos\theta)^{1/2}\sin^2\theta\cos\phi \\
& \frac{1}{2}\begin{bmatrix}(1+\cos\theta)-(1-\cos\theta)\cos(2\phi)\\ -(1-\cos\theta)\sin(2\phi)\\ -2\sin\theta\cos\phi\end{bmatrix} e^{ikz\cos\theta}e^{ik\rho\sin\theta\cos(\phi-\varphi)}\,d\phi\,d\theta \\
=& -\frac{ikf^2e^{-ikf}}{2\pi w_0}E_0\sqrt{\frac{n_1}{n_2}}\int_0^{\theta_{max}} f_w(\theta)(\cos\theta)^{1/2}\sin^2\theta \\
& \begin{bmatrix}\pi i[(1+3\cos\theta)J_1(k\rho\sin\theta))\cos\varphi+(1-\cos\theta)J_3(k\rho\sin\theta)\cos(3\varphi)]\\ \pi i[(1-\cos\theta)J_3(k\rho\sin\theta))\sin(3\varphi)-(1-\cos\theta)J_1(k\rho\sin\theta)\sin(\varphi)]\\ 2\pi[(-\sin\theta)J_0(k\rho\sin\theta)+\sin\theta J_2(k\rho\sin\theta)\cos(2\varphi)]\end{bmatrix} e^{ikz\cos\theta}d\theta.
\end{aligned}
\tag{5.54}
$$

Note that the following trigonometric identities $\cos(3\phi) = 4\cos^3\phi - 3\cos\phi$, $\sin(3\phi) = 3\sin\phi - 4\sin^3\phi$ and $\cos(2\phi) = 2\cos^2\phi - 1$ to simplify some of the terms that appear in the x, y and z components, respectively:

$$
\cos 2\phi\cos\phi = (2\cos^2\phi - 1)\cos\phi = 2\cos^3\phi - \cos\phi = \frac{\cos(3\phi)+\cos\phi}{2}, \tag{5.55}
$$

$$
2\sin\phi - 2\sin^3\phi = \frac{\sin(3\phi)-\sin\phi}{2}, \tag{5.56}
$$

$$
\cos^2\phi = \frac{\cos(2\phi)+1}{2}. \tag{5.57}
$$

Equation 5.54 can be abbreviated to

$$\mathbf{E}^{\mathbf{x\text{-}polarized}}_{\mathbf{HG}_{10}}(\rho,\varphi,z) = -\frac{ikf^2}{2w_0}\sqrt{\frac{n_1}{n_2}}E_0 e^{-ikf}\begin{bmatrix} iI_{11}\cos(\varphi) + iI_{14}\cos(3\varphi) \\ iI_{14}\sin(3\varphi) - iI_{12}\sin(\varphi) \\ -2I_{10} + 2I_{13}\cos(2\varphi) \end{bmatrix}, \tag{5.58}$$

which agrees with the expression derived by Novotny.[22] Applying the same procedure to the x-polarized HG_{01} mode one obtains

$$\begin{aligned}
\mathbf{E_f}(\rho,\varphi,z) =& \mathbf{E}^{\mathbf{x\text{-}polarized}}_{\mathbf{HG}_{01}}(\rho,\varphi,z) \\
=& -\frac{i2kf^2e^{-ikf}}{2\pi w_0}E_0\sqrt{\frac{n_1}{n_2}}\int_0^{\theta_{max}}\int_0^{2\pi} f_w(\theta)(\cos\theta)^{1/2}\sin^2\theta\sin\phi \\
& \frac{1}{2}\begin{bmatrix} (1+\cos\theta) - (1-\cos\theta)\cos(2\phi) \\ -(1-\cos\theta)\sin(2\phi) \\ -2\sin\theta\cos\phi \end{bmatrix} e^{ikz\cos\theta}e^{ik\rho\sin\theta\cos(\phi-\varphi)}\, d\phi\, d\theta \\
=& -\frac{ikf^2e^{-ikf}}{2\pi w_0}E_0\sqrt{\frac{n_1}{n_2}}\int_0^{\theta_{max}} f_w(\theta)(\cos\theta)^{1/2}\sin^2\theta \\
& \begin{bmatrix} \pi i[(3+\cos\theta)J_1(k\rho\sin\theta))\sin\varphi + (1-\cos\theta)J_3(k\rho\sin\theta)\sin(3\varphi)] \\ \pi i[-(1-\cos\theta)J_3(k\rho\sin\theta))\cos(3\varphi) - (1-\cos\theta)J_1(k\rho\sin\theta)\cos(\varphi)] \\ 2\pi\sin\theta J_2(k\rho\sin\theta)\sin(2\varphi) \end{bmatrix} e^{ikz\cos\theta}d\theta,
\end{aligned} \tag{5.59}$$

Note that the following trigonometric identities $\sin(3\phi) = 3\sin\phi - 4\sin^3\phi$, $\cos(3\phi) = 4\cos^3\phi - 3\cos\phi$ and $\sin(2\phi) = 2\sin\phi\cos\phi$ to simplify some of the terms that appear in the x, y and z components, respectively:

$$\cos 2\phi\sin\phi = (2\cos^2\phi - 1)\sin\phi = \sin\phi - 2\sin^3\phi = \frac{\sin(3\phi) - \sin\phi}{2}, \tag{5.60}$$

$$\sin 2\phi\sin\phi = 2\sin^2\phi\cos\phi = 2\cos\phi - 2\cos^3\phi = -\frac{\cos(3\phi) - \cos\phi}{2}, \tag{5.61}$$

$$2\sin\phi\cos\phi = \sin 2\phi. \tag{5.62}$$

Equation 5.59 can be abbreviated to

$$\mathbf{E}^{\textbf{x-polarized}}_{\mathbf{HG}_{01}}(\rho,\varphi,z) = -\frac{ikf^2}{2w_0}\sqrt{\frac{n_1}{n_2}}E_0 e^{-ikf}\begin{bmatrix} i(I_{11}+2I_{12})\sin\varphi + iI_{14}\sin(3\varphi) \\ -iI_{12}\cos\varphi - iI_{14}\cos(3\varphi) \\ 2I_{13}\sin(2\varphi) \end{bmatrix}. \tag{5.63}$$

Now it is possible to do the same for the y-polarized Hermite-Gaussian modes. For the y-polarized HG_{10} mode it is obtained

$$\begin{aligned}
\mathbf{E_f}(\rho,\varphi,z) =& \mathbf{E}^{\textbf{y-polarized}}_{\mathbf{HG}_{10}}(\rho,\varphi,z) \\
=& -\frac{i2kf^2e^{-ikf}}{2\pi w_0}E_0\sqrt{\frac{n_1}{n_2}}\int_0^{\theta_{max}}\int_0^{2\pi} f_w(\theta)(\cos\theta)^{1/2}\sin^2\theta\cos\phi \\
& \frac{1}{2}\begin{bmatrix} -(1-\cos\theta)\sin(2\phi) \\ (1+\cos\theta)+(1-\cos\theta)\cos(2\phi) \\ -2\sin\theta\sin\phi \end{bmatrix} e^{ikz\cos\theta}e^{ik\rho\sin\theta\cos(\phi-\varphi)}\, d\phi\, d\theta \\
=& -\frac{ikf^2e^{-ikf}}{2\pi w_0}E_0\sqrt{\frac{n_1}{n_2}}\int_0^{\theta_{max}} f_w(\theta)(\cos\theta)^{1/2}\sin^2\theta \\
& \begin{bmatrix} \pi i[(1-\cos\theta)J_3(k\rho\sin\theta))\sin(3\varphi) - (1-\cos\theta)J_1(k\rho\sin\theta)\sin(\varphi)] \\ \pi i[(3+\cos\theta)J_1(k\rho\sin\theta))\cos(\varphi) - (1-\cos\theta)J_3(k\rho\sin\theta)\cos(3\varphi)] \\ 2\pi\sin\theta J_2(k\rho\sin\theta)\sin(2\varphi) \end{bmatrix} e^{ikz\cos\theta}d\theta,
\end{aligned} \tag{5.64}$$

which abbreviates to

$$\mathbf{E}^{\textbf{y-polarized}}_{\mathbf{HG}_{10}}(\rho,\varphi,z) = -\frac{ikf^2}{2w_0}\sqrt{\frac{n_1}{n_2}}E_0 e^{-ikf}\begin{bmatrix} iI_{14}\sin(3\varphi) - iI_{12}\sin\varphi \\ i(I_{11}+2I_{12})\cos\varphi - iI_{14}\cos(3\varphi) \\ 2I_{13}\sin(2\varphi) \end{bmatrix}. \tag{5.65}$$

Similarly,

$$
\begin{aligned}
\mathbf{E_f}(\rho,\varphi,z) =& \mathbf{E}^{\textbf{y-polarized}}_{\mathbf{HG}_{01}}(\rho,\varphi,z) \\
=& -\frac{i2kf^2e^{-ikf}}{2\pi w_0}E_0\sqrt{\frac{n_1}{n_2}}\int_0^{\theta_{max}}\int_0^{2\pi} f_w(\theta)(\cos\theta)^{1/2}\sin^2\theta\sin\phi \\
& \frac{1}{2}\begin{bmatrix} -(1-\cos\theta)\sin(2\phi) \\ (1+\cos\theta)+(1-\cos\theta)\cos(2\phi) \\ -2\sin\theta\sin\phi \end{bmatrix} e^{ikz\cos\theta}e^{ik\rho\sin\theta\cos(\phi-\varphi)}\ d\phi\ d\theta \\
=& -\frac{ikf^2e^{-ikf}}{2\pi w_0}E_0\sqrt{\frac{n_1}{n_2}}\int_0^{\theta_{max}} f_w(\theta)(\cos\theta)^{1/2}\sin^2\theta \\
& \begin{bmatrix} \pi i[-(1-\cos\theta)J_3(k\rho\sin\theta))\cos(3\varphi)-(1-\cos\theta)J_1(k\rho\sin\theta)\cos(\varphi)] \\ \pi i[(1+3\cos\theta)J_1(k\rho\sin\theta))\sin(\varphi)-(1-\cos\theta)J_3(k\rho\sin\theta)\sin(3\varphi)] \\ 2\pi\sin\theta[J_0(k\rho\sin\theta)+i^2J_2(k\rho\sin\theta)\cos(2\varphi)] \end{bmatrix} e^{ikz\cos\theta}d\theta,
\end{aligned}
\tag{5.66}
$$

which abbreviates to

$$
\mathbf{E}^{\textbf{y-polarized}}_{\mathbf{HG}_{01}}(\rho,\varphi,z) = -\frac{ikf^2}{2w_0}\sqrt{\frac{n_1}{n_2}}E_0e^{-ikf}\begin{bmatrix} -iI_{14}\cos(3\varphi)-iI_{12}\cos\varphi \\ iI_{11}\sin\varphi-iI_{14}\sin(3\varphi) \\ -2I_{10}-2I_{13}\cos(2\varphi) \end{bmatrix}. \tag{5.67}
$$

Now we have all the necessary expression to calculate the expressions for the LG beams. A linearly-polarized (x-polarized) LG beam of topological charge $l=\pm1$ is then obtained by adding expressions 5.58 and 5.63 with a $\pi/2$ phase difference[5, 43]

$$
\mathrm{LG}^{\textbf{x-polarized}}_{l=\pm1} = \frac{1}{\sqrt{2}}(\mathrm{HG}_{10}\hat{\mathbf{x}} \pm i\mathrm{HG}_{01}\hat{\mathbf{x}}), \tag{5.68}
$$

where $+$ corresponds to positive topological charge and $-$ to negative topological charge, respectively, and where we have assumed that the radial index $p=0$. Therefore, the final expression becomes

$$\mathbf{E}_{\mathrm{LG}_{l=\pm1}^{\text{x-polarized}}} \propto \begin{bmatrix} iI_{11}\cos(\varphi) + iI_{14}\cos(3\varphi) \\ iI_{14}\sin(3\varphi) - iI_{12}\sin(\varphi) \\ -2I_{10} + 2I_{13}\cos(2\varphi) \end{bmatrix} \pm i \begin{bmatrix} i(I_{11}+2I_{12})\sin\varphi + iI_{14}\sin(3\varphi) \\ -iI_{12}\cos\varphi - iI_{14}\cos(3\varphi) \\ 2I_{13}\sin(2\varphi) \end{bmatrix}$$
$$= iI_{11}e^{\pm i\varphi}\begin{bmatrix}1\\0\\0\end{bmatrix} + iI_{14}e^{\pm i3\varphi}\begin{bmatrix}1\\\mp i\\0\end{bmatrix} + iI_{12}\sin\varphi\begin{bmatrix}\pm i\\0\\0\end{bmatrix}$$
$$+ iI_{12}e^{\mp i\varphi}\begin{bmatrix}0\\\mp i\\0\end{bmatrix} + 2I_{13}e^{\pm i2\varphi}\begin{bmatrix}0\\0\\1\end{bmatrix} - 2I_{10}\begin{bmatrix}0\\0\\1\end{bmatrix}. \tag{5.69}$$

Expressions for circularly-polarized LG beams of topological charge $l = \pm 1$ were derived by Shun Hashiyada by appropriately combining the HG modes. In the first instance, the circularly-polarized LG beam with antiparallel combination of SAM and OAM can be obtained from radial and azimuthal vector beams, which are given by[22, 312, 313]

$$\mathrm{RP} = \frac{1}{\sqrt{2}}(\mathrm{HG}_{10}\hat{\mathbf{x}} + \mathrm{HG}_{01}\hat{\mathbf{y}}), \tag{5.70}$$

and

$$\mathrm{AP} = \frac{1}{\sqrt{2}}(-\mathrm{HG}_{01}\hat{\mathbf{x}} + \mathrm{HG}_{10}\hat{\mathbf{y}}), \tag{5.71}$$

where RP and AP denote radial and azimuthal polarizations, respectively, as depicted in Figure 5.11.

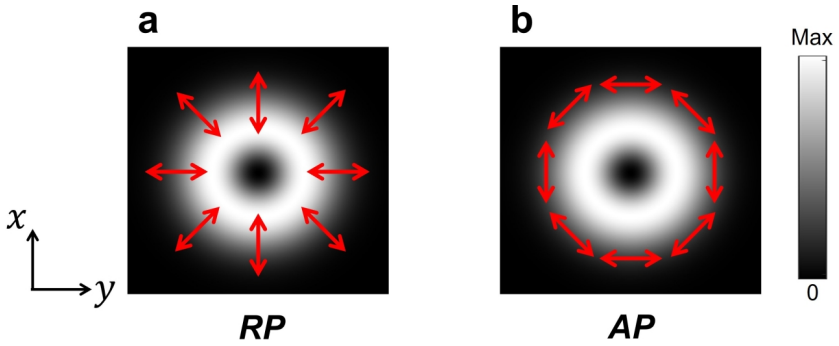

Figure 5.11: Examples of common vector beams, where the polarization varies in the transverse plane. (a) Radially-polarized beam. (b) Azimuthally-polarized beam. The red arrows denote the polarization direction.

Therefore, it is obtained that

$$\mathrm{LG}_{l=\pm 1}^{\sigma=\mp 1} = \mathrm{RP} \mp i\mathrm{AP} = \frac{1}{\sqrt{2}}\left[(\mathrm{HG}_{10}\hat{\mathbf{x}} \pm i\mathrm{HG}_{01}\hat{\mathbf{x}}) + (\mathrm{HG}_{01}\hat{\mathbf{y}} \mp i\mathrm{HG}_{10}\hat{\mathbf{y}})\right], \tag{5.72}$$

so the final expression becomes

$$
\begin{aligned}
\mathbf{E}_{\mathrm{LG}_{l=\pm1}^{\sigma=\mp1}} \propto & \begin{bmatrix} iI_{11}\cos(\varphi)+iI_{14}\cos(3\varphi) \\ iI_{14}\sin(3\varphi)-iI_{12}\sin(\varphi) \\ -2I_{10}+2I_{13}\cos(2\varphi) \end{bmatrix} \pm i \begin{bmatrix} i(I_{11}+2I_{12})\sin\varphi+iI_{14}\sin(3\varphi) \\ -iI_{12}\cos\varphi-iI_{14}\cos(3\varphi) \\ 2I_{13}\sin(2\varphi) \end{bmatrix} \\
& + \begin{bmatrix} -iI_{14}\cos(3\varphi)-iI_{12}\cos\varphi \\ iI_{11}\sin\varphi-iI_{14}\sin(3\varphi) \\ -2I_{10}-2I_{13}\cos(2\varphi) \end{bmatrix} \pm i \begin{bmatrix} iI_{12}\sin\varphi-iI_{14}\sin(3\varphi) \\ -i(I_{11}+2I_{12})\cos\varphi+iI_{14}\cos(3\varphi) \\ -2I_{13}\sin(2\varphi) \end{bmatrix} \\
= & \begin{bmatrix} i(I_{11}-I_{12})\cos\varphi \\ i(I_{11}-I_{12})\sin\varphi \\ -4I_{10} \end{bmatrix} \pm i \begin{bmatrix} i(I_{11}+3I_{12})\sin\varphi \\ -i(I_{11}+3I_{12})\cos\varphi \\ 0 \end{bmatrix} \\
= & \frac{i\{(1\pm1)I_{11}-(1\mp3)I_{12}\}}{2} e^{+i\varphi} \begin{bmatrix} 1 \\ -i \\ 0 \end{bmatrix} + \frac{i\{(1\mp1)I_{11}-(1\pm3)I_{12}\}}{2} e^{-i\varphi} \begin{bmatrix} 1 \\ +i \\ 0 \end{bmatrix} \\
& - 4I_{10} \begin{bmatrix} 0 \\ 0 \\ 1 \end{bmatrix}.
\end{aligned}
\tag{5.73}
$$

The first two terms in equation 5.73 represent the antiparallel combination of SAM and OAM ($\sigma = \mp1$, $l = \pm1$), whereas the third term contains the no SAM and OAM contribution after focusing due to spin-orbit conversion. The total angular momentum of each term is 0, indicating that total angular momentum is conserved.

Circularly-polarized LG beams with parallel combination of SAM ($\sigma = \pm1$) and OAM ($l = \pm1$) can be obtained with the following combination of HG modes

$$
\mathrm{LG}_{l=\pm1}^{\sigma=\pm1} = \frac{1}{\sqrt{2}} \left[(\mathrm{HG}_{10}\hat{\mathbf{x}} \pm i\mathrm{HG}_{01}\hat{\mathbf{x}}) - (\mathrm{HG}_{01}\hat{\mathbf{y}} \mp i\mathrm{HG}_{10}\hat{\mathbf{y}}) \right], \tag{5.74}
$$

so the final expression becomes

$$
\begin{aligned}
\mathbf{E}_{\mathrm{LG}_{l=\pm1}^{\sigma=\pm1}} \propto & \begin{bmatrix} iI_{11}\cos(\varphi) + iI_{14}\cos(3\varphi) \\ iI_{14}\sin(3\varphi) - iI_{12}\sin(\varphi) \\ -2I_{10} + 2I_{13}\cos(2\varphi) \end{bmatrix} \pm i \begin{bmatrix} i(I_{11}+2I_{12})\sin\varphi + iI_{14}\sin(3\varphi) \\ -iI_{12}\cos\varphi - iI_{14}\cos(3\varphi) \\ 2I_{13}\sin(2\varphi) \end{bmatrix} \\
& - \begin{bmatrix} -iI_{14}\cos(3\varphi) - iI_{12}\cos\varphi \\ iI_{11}\sin\varphi - iI_{14}\sin(3\varphi) \\ -2I_{10} - 2I_{13}\cos(2\varphi) \end{bmatrix} \mp i \begin{bmatrix} iI_{12}\sin\varphi - iI_{14}\sin(3\varphi) \\ -i(I_{11}+2I_{12})\cos\varphi + iI_{14}\cos(3\varphi) \\ -2I_{13}\sin(2\varphi) \end{bmatrix} \\
= & \begin{bmatrix} i(I_{11}+I_{12})\cos\varphi + 2iI_{14}\cos(3\varphi) \\ -i(I_{11}+I_{12})\cos\varphi + 2iI_{14}\sin(3\varphi) \\ 4I_{13}\cos(2\varphi) \end{bmatrix} \pm i \begin{bmatrix} i(I_{11}+I_{12})\sin\varphi + 2iI_{14}\sin(3\varphi) \\ i(I_{11}+I_{12})\cos\varphi - 2iI_{14}\cos(3\varphi) \\ 4I_{13}\sin(2\varphi) \end{bmatrix} \\
= & i(I_{11}+I_{12})e^{\pm i\varphi} \begin{bmatrix} 1 \\ \pm i \\ 0 \end{bmatrix} + 2iI_{I_{14}}e^{\pm i3\varphi} \begin{bmatrix} 1 \\ \mp i \\ 0 \end{bmatrix} + 4I_{13}e^{\pm i2\varphi} \begin{bmatrix} 0 \\ 0 \\ 1 \end{bmatrix}.
\end{aligned}
\tag{5.75}
$$

The first term in equation 5.75 contains the parallel combination of SAM and OAM ($\sigma = \pm1$, $l = \pm1$), whereas the second and third are due to spin-orbit conversion after focusing and include a contribution due to antiparallel SAM and OAM ($\sigma = \mp1$, $l = \pm3$) and OAM only ($l = \pm2$), respectively. Again, it can be seen that the total angular momentum is conserved, amounting to $l + \sigma = \pm2$ for all the terms.

Using the equations presented in this section, the electric field of the focused fields for all the combinations of SAM and OAM were implemented into COMSOL by Shun Hashiyada. This was done using the NA and focal length f of the objective lenses used in the experiments.

The simulated results for the weakly- and tightly-focused beams in air can be seen in Figure 5.12. The simulations of the beam in air agree with the expected behaviour that focusing has in the beam intensity. The simulations show that some intensity is present at the centre of the vortex (on-axis intensity) in the case of circularly-polarized LG beam with antiparallel combination of SAM and OAM ($\sigma = \pm1$, $l = \mp1$) and

linearly-polarized LG beam ($\sigma = 0$, $l = \mp 1$), but no on-axis intensity is seen in the circularly-polarized LG beam with parallel combination of SAM and OAM ($\sigma = \pm 1$, $l = \pm 1$). This agrees with previous theoretical and experimental studies.[106, 107] As this on-axis intensity arises from longitudinal fields,[106, 107] it increases for higher levels of focusing and it is more prominent for the tightly-focused beam. Additionally, it can be seen that the intensity of the linearly-polarized LG beam is not evenly distributed and the intensity is elongated in the polarization direction (the x axis), in agreement with previous studies.[314]

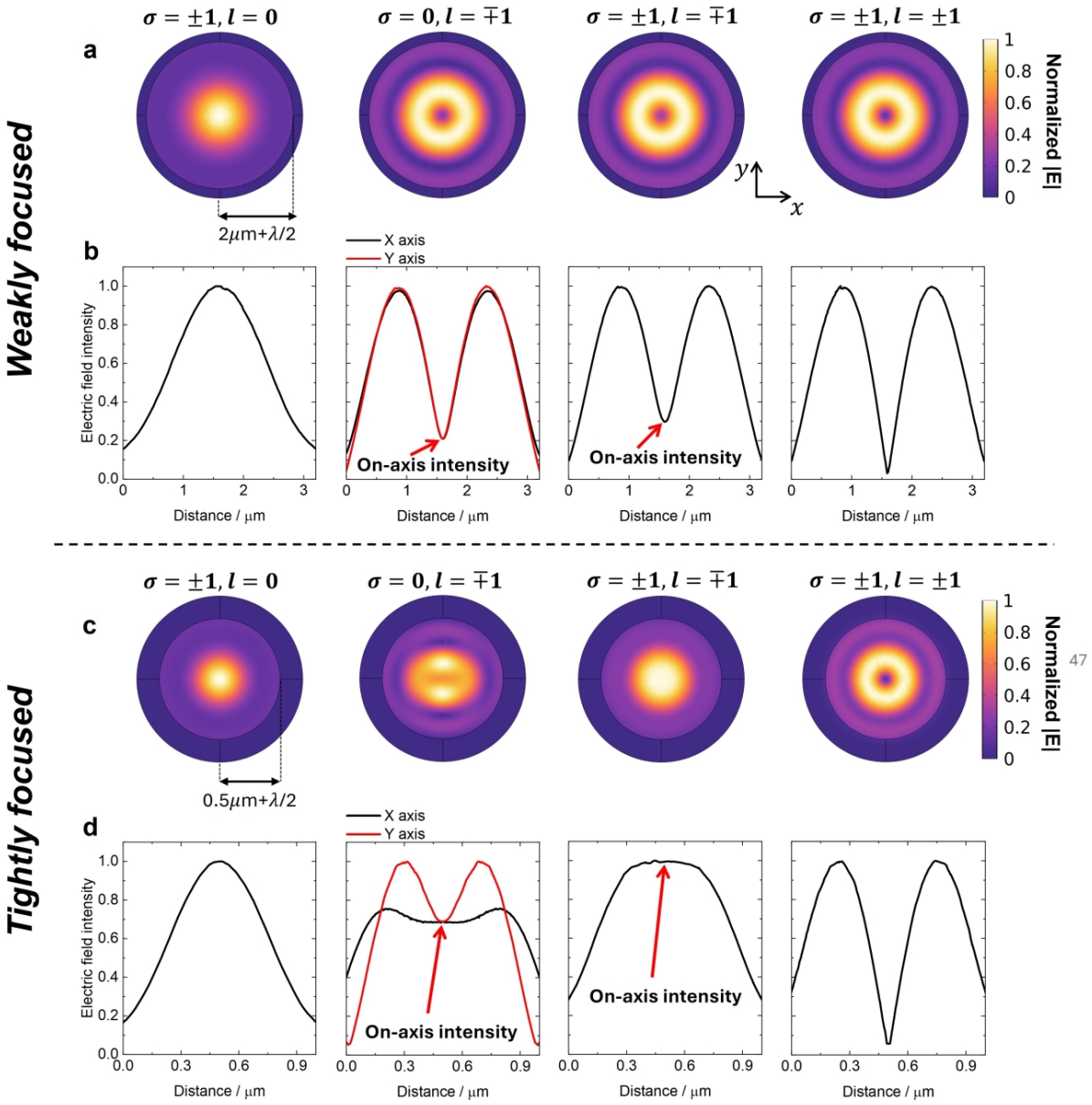

Figure 5.12: Simulations in air for (a,b) weakly-focused (NA=0.3) and (c,d) tightly-focused (NA=0.95) beams. The simulated beams shown here are circularly-polarized Gaussian ($\sigma = \pm 1$, $l = 0$), linearly-polarized (in the x direction) LG beams ($\sigma = 0$, $l = \mp 1$) and circularly-polarized LG beams with antiparallel ($\sigma = \pm 1$, $l = \mp 1$) and parallel ($\sigma = \pm 1$, $l = \pm 1$) SAM and OAM. (a,c) 2D plot of the electric field intensity. (b,d) 1D plot of the 2D plot shown above. $\lambda = 600$ nm.

5.4.2 Dichroism under weak focusing

In this section, the effects of angular momentum in the dichroism were studied using a weakly-focused beam, where effects such as spin-orbit conversion[46, 110] or size matching between the beam and the chiral structure can be ruled out.[104] The

chiroptical properties of the shuriken nanoindentations under weak focusing in water are well-understood,[283] whereas the measurements performed in this chapter are done in air. Therefore, the first steps of this section aim at gaining a thorough understanding of the origin of the chiroptical response of the shurikens in air using conventional chiroptical techniques (ORD and CD) and how the results presented here compared to previously published results in water.[94, 303]

ORD and extinction spectra collected using a linearly-polarized Gaussian beam are displayed in Figure 5.13. The ORD and extinction are consistent with the previously reported chiroptical behaviour of the shuriken structures in water[94, 303] but blue shifted due to the lower refractive index of air compared to water. This confirms the consistency of the observed chiroptical behaviour across different media and the agreement of the data presented here with previous studies. Nevertheless, some differences can be found. In particular, the ORD is weaker in air compared to water and the extinction spectra contain a PIR peak which is less pronounced in air than water.

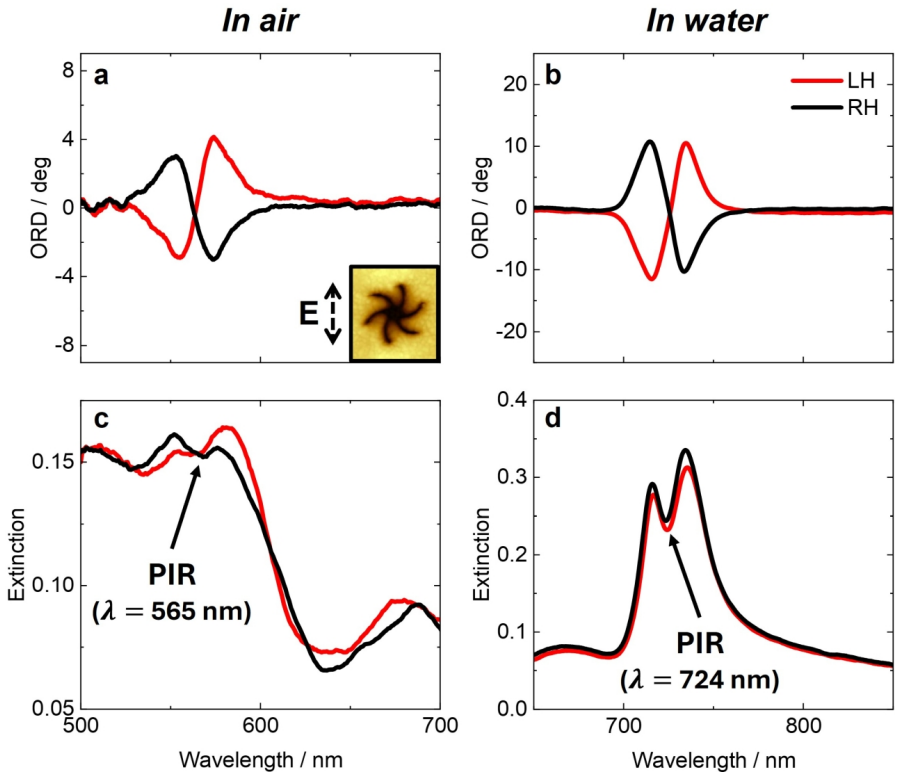

Figure 5.13: (a,b) ORD spectra of LH (red) and RH (black) shuriken structures for measurements in (a) air and (b) water. (c,d) Extinction spectra of LH (red) and RH (black) shuriken structures for measurements in (c) air and (d) water. This data was collected using a linearly-polarized Gaussian beam with the incident polarization shown in (a). The measurements in water were collected by Douglas Murad.

Conventional CD (SAM only) was then measured and it is displayed in Figure 5.13. The measured CD showed a typical line shape observed in a helical oscillator type of chirality[303, 315] with the main peak at 566 nm and broader peak at longer wavelengths. Furthermore, the measured CD is consistent with the CD derived from the Kramers-Kronig relations from ORD, which confirms the consistency of the data across different set-ups.

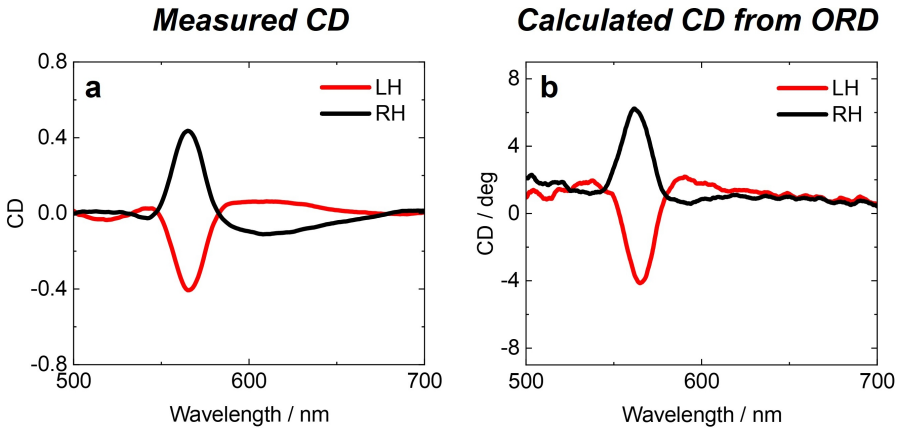

Figure 5.14: (a) Dichroism with SAM only measured at Hokkaido University. (b) Calculated CD from the ORD measured at the University of Glasgow using Kramers-Kronig relation.

As shown in Figure 5.15, spin-dependent extinction measurements on the LH and RH structures show that the dichroism in the shuriken nanoindentations arises due to spin-dependent PIR, in agreement with the previous studies conducted in water.[283] This means that when the handedness of the circularly-polarized light matches that of the structure, there can be near-field coupling between a dipole-active mode (E1) and a dark electric quadrupole (E2), resulting in PIR. When the handedness of the circular polarization does not match that of the structure, the near-field coupling is weak and no PIR occurs. Based on this observation, it is possible to fit the CD spectrum measured in this work using a classical coupled oscillator model, which can be used to mimic the optical properties of plasmonic systems.[272, 283] The classical model used to account for the near-field coupling between the bright and dark modes is a radiating coupled oscillator model described by the coupled differential equations given by[287]

$$\omega_r^{-2}\ddot{p}(t) + \gamma_r\omega_r^{-1}\dot{p}(t) + p(t) = g_r f(t) - \widetilde{k}q(t), \tag{5.76}$$

$$\omega_d^{-2}\ddot{q}(t) + \gamma_d\omega_d^{-1}\dot{q}(t) + q(t) = -\widetilde{k}p(t). \tag{5.77}$$

The bright mode is described by the excitation function $p(t)$, resonance frequency ω_r and damping γ_r. The bright mode is driven by an external force $g_r f(t)$. $f(t)$ represents the external light and g_r is an amplitude coefficient representing the coupling to the external

light. Similarly, the dark mode is described by the excitation function $q(t)$, resonance frequency ω_d and damping γ_d. However, the dark mode is not excited directly by the external light, and it is only excited *via* near-field coupling to the bright mode. The coupling is represented by the complex coupling $\widetilde{k} = k^{-i(\theta-\phi)}$, where k is the magnitude of the coupling and θ and ϕ the phase of the bright and dark modes, respectively.[316]

An expression for the dichroism can be derived by solving the coupled differential equations 5.76 and 5.77 (Appendix D). As shown in Figure 5.15, this provides a good fit of the experimental data for the conventional CD. To account for the helicity of the light, different coupling constants k and g_r amplitude coefficients were used in the fitting process for $\sigma = +1$ and $\sigma = -1$ beams, whereas the other parameters remain the same regardless of the beam helicity. A clear asymmetry was found in the coupling constant k (shown with red arrows in Figure 5.15), justifying that the source of the dichroism is the spin-dependent near-field coupling between bright and dark modes. This agrees with the extinction data in Figure 5.15a,c. Stronger near-field coupling produces PIR. Weaker near-field coupling yields a single peak, corresponding to the absence of PIR.

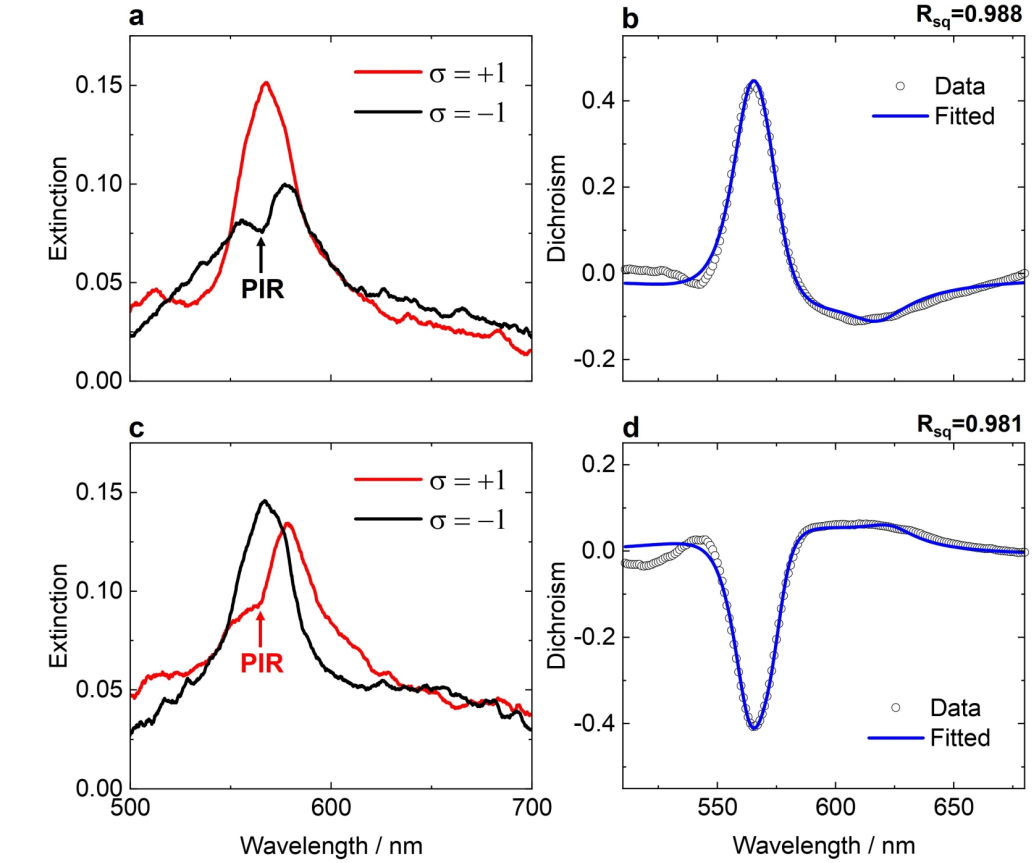

	ω_r	ω_d	γ_r	γ_d	$k_{\sigma=+1}$	$k_{\sigma=-1}$	θ	ϕ	$g_{\sigma=+1}$	$g_{\sigma=-1}$
RH	568	564	0.058	0.029	0.028	0.043	0.060	0.422	0.180	0.181
LH	568	564	0.052	0.022	0.045	0.035	0.044	0.395	0.205	0.205

Figure 5.15: Classical coupled oscillator modelling for (a,b) RH structure and (d,e) LH structure. (a,c) Extinction collected with LCP ($\sigma = +1$, red) and RCP ($\sigma = -1$, black) excitations. (b,d) Fitted curve (blue) of the raw CD data (black open circles) using the classical coupled oscillator model in (e). (e) Schematic of the coupled oscillator model used to fit the CD. (f) Extracted parameters from the fittings for the RH structure in (b) and LH structure in (d), showing an asymmetry in the magnitude of the coupling constant k (red arrows).

Numerical simulations using circularly-polarized plane waves and a periodic structure were performed to confirm that the origin of the observed dichroism arises due to spin-dependent near-field coupling between bright and dark modes. This was done in air but also water for comparison. The simulations show that PIR dip is observed in the simulated extinction spectra and that the dip is less pronounced in air than in water in agreement with the experimentally measured extinction (*cf.* Figure 5.13). Note that the PIR dip in the simulations is also blue shifted by about 10 nm compared to the

experiment (*cf.* Figure 5.13), an effect that has been attributed to the fact that the ideal model has sharper edges compared to the experimental sample.[116] Importantly, the z-component of the electric field at the PIR shows that strong near-field coupling between the structures occurs when the chirality of SAM matches the structure. The coupling is weak for the mismatched combination, showing no interaction between the structures. This effect is particularly strong in water, where the PIR is more pronounced.

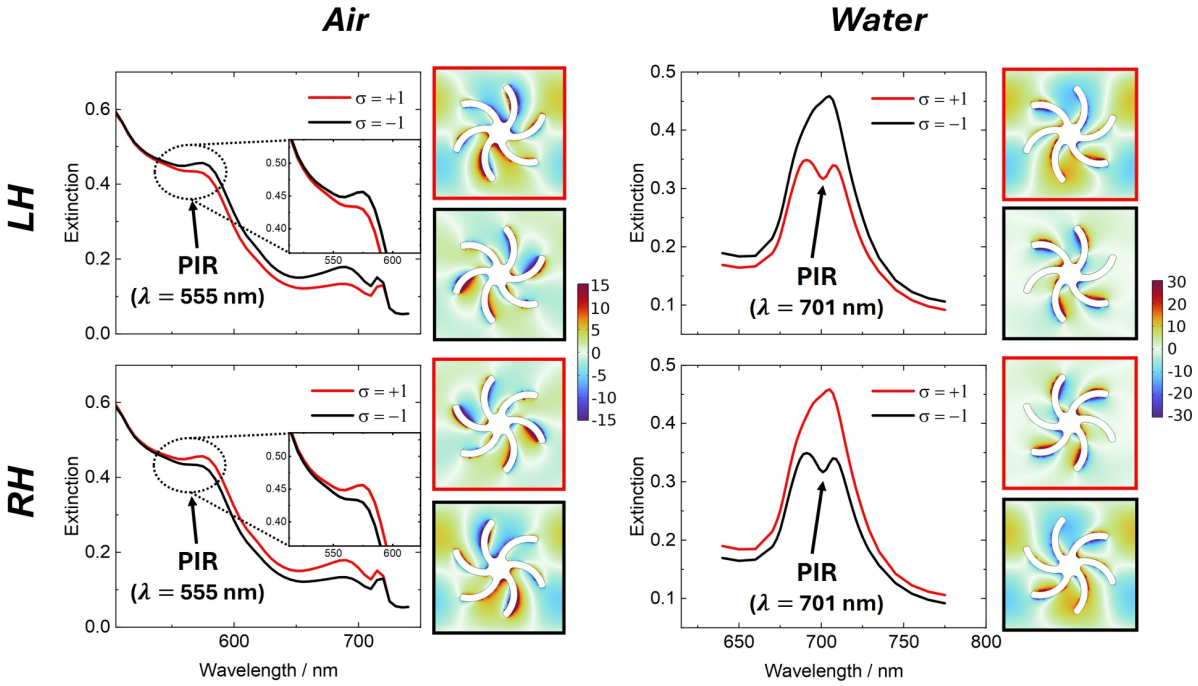

Figure 5.16: Simulated SAM-dependent extinction for $\sigma = +1$ (red) and $\sigma = -1$ (black) for a periodic structure in air and water. The z-component of the electric field at the PIR wavelength is shown in red and black squares for $\sigma = +1$ and $\sigma = -1$ polarizations, respectively.

To confirm that the near-field coupling originates from the periodicity in the structure, the same simulations were repeated without periodic boundary conditions *i.e.* using a single structure. As shown in Figure 5.17, no SAM-dependent PIR was found in the extinction and the electric field shows no near-field interactions, confirming that the observed CD originates from near-field coupling between bright and dark modes in the periodic structure.

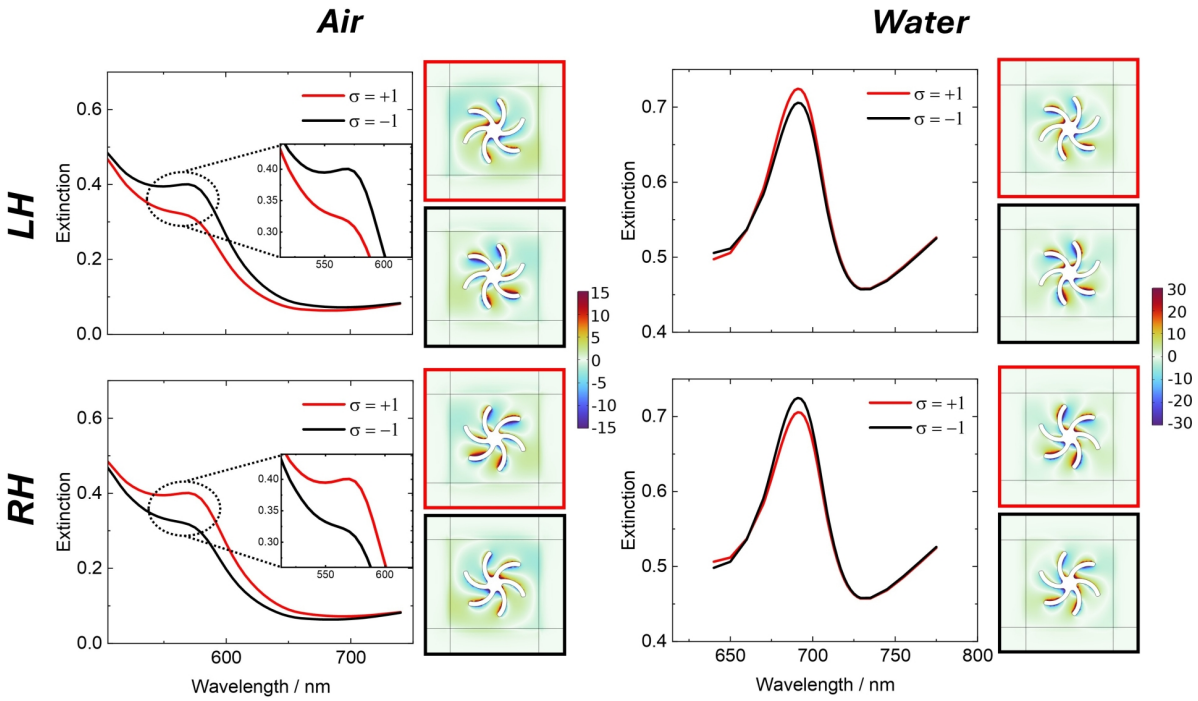

Figure 5.17: Simulated SAM-dependent extinction for $\sigma = +1$ (red) and $\sigma = -1$ (black) for a single structure, showing no PIR dip. The z-component of the electric field at the same wavelengths of Figure 5.16 is shown in red and black squares for $\sigma = +1$ and $\sigma = -1$, respectively.

Figure 5.18 shows the results of the experimental dichroism measurements collected with different combinations of SAM and OAM. Figure 5.18a-c contains the spatial variation across 3 different random sample positions, showing no significant variation across the sample. Figure 5.18d-f contains the averaged dichroism of Figure 5.18a-c, respectively. As it can be seen from the figure, no change in the dichroism was observed with antiparallel combination of OAM ($l = 1$) and SAM, and no helical dichroism was observed for OAM only. This indicates that the dichroism is originating from SAM-only contribution and that OAM of topological charge of 1 has no change in the dichroism under weak focusing.

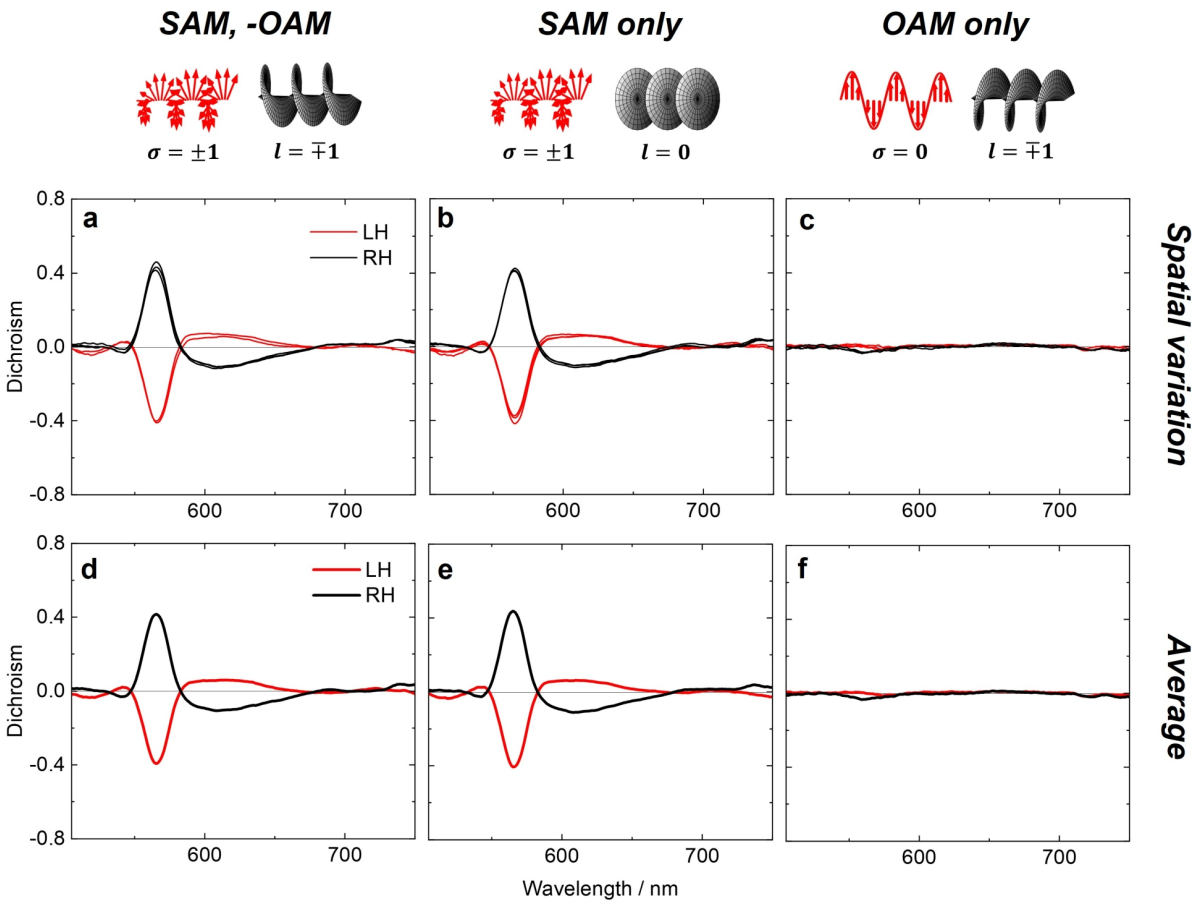

Figure 5.18: Dichroism collected using various combinations of angular momentum for LH (red) and RH (black) shuriken-shaped nanoindentations. (a-c) Spatially-varying dichroism across 3 different random positions in the sample for (a) antiparallel combination of SAM and OAM ($\sigma = \pm 1$, $l = \mp 1$), (b) SAM only ($\sigma = \pm 1$, $l = 0$) and (c) OAM only ($\sigma = 0$, $l = \mp 1$). (d-f) Averaged dichroism obtained from (a-c), respectively.

The results from Figure 5.18 can be understood from the polarization structure of LG beams. The polarization of an arbitrary LG beam is given by[1]

$$\mathbf{E}_{\mathbf{LG}}^{l,p=\mathbf{0}}(\mathbf{r},t) = E_0[\hat{\mathbf{x}}\cos(\omega t - l\phi) + \sigma\hat{\mathbf{y}}\sin(\omega t - l\phi)], \tag{5.78}$$

where $\hat{\mathbf{x}}$ and $\hat{\mathbf{y}}$ are unit vectors in the x and y directions, t time, ϕ azimuthal angle. l is the topological charge and σ the helicity, which change the OAM and SAM of the beam, respectively. Note that in this section weakly-focused beams are used, therefore the electric field is assumed to be in the transverse (xy plane) only.

Equation 5.78 tells us that different polarization distributions are obtained for differ-

[1]This function was provided by Kayn Forbes.

ent combinations of l and σ. Linearly-polarized Gaussian or LG beams have no chirality in their polarization structure over time, as shown in Figure 5.19, which explains why no helical dichroism was observed in the experiment.

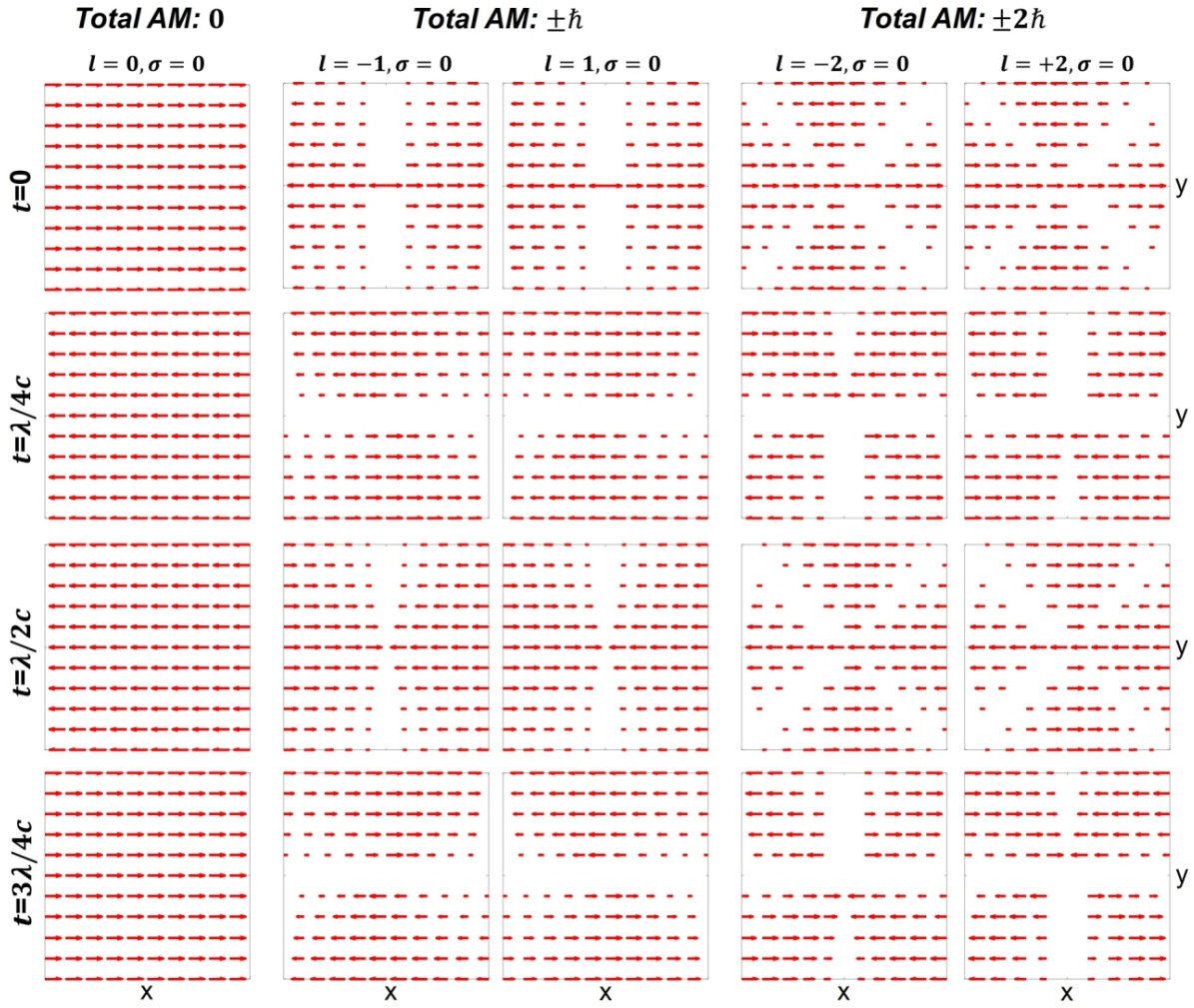

Figure 5.19: Transverse (xy) plane polarization distributions for varying combinations of OAM and SAM in the case of linearly-polarized ($\sigma = 0$) beams as a function of time t. The beam is polarized in the x direction.

In contrast, as shown in Figure 5.20, the polarization structure of circularly-polarized beams $\sigma = \pm 1$ is chiral regardless of the topological charge, as some 'rotational sense' develops over time, which explains the presence of dichroism in the case of circularly-polarized beams in Figure 5.18. The different polarization structures have no effect in the dichroism as demonstrated by the experiments, but the chirality in the polarization structures is necessary for the dichroism to be observed.

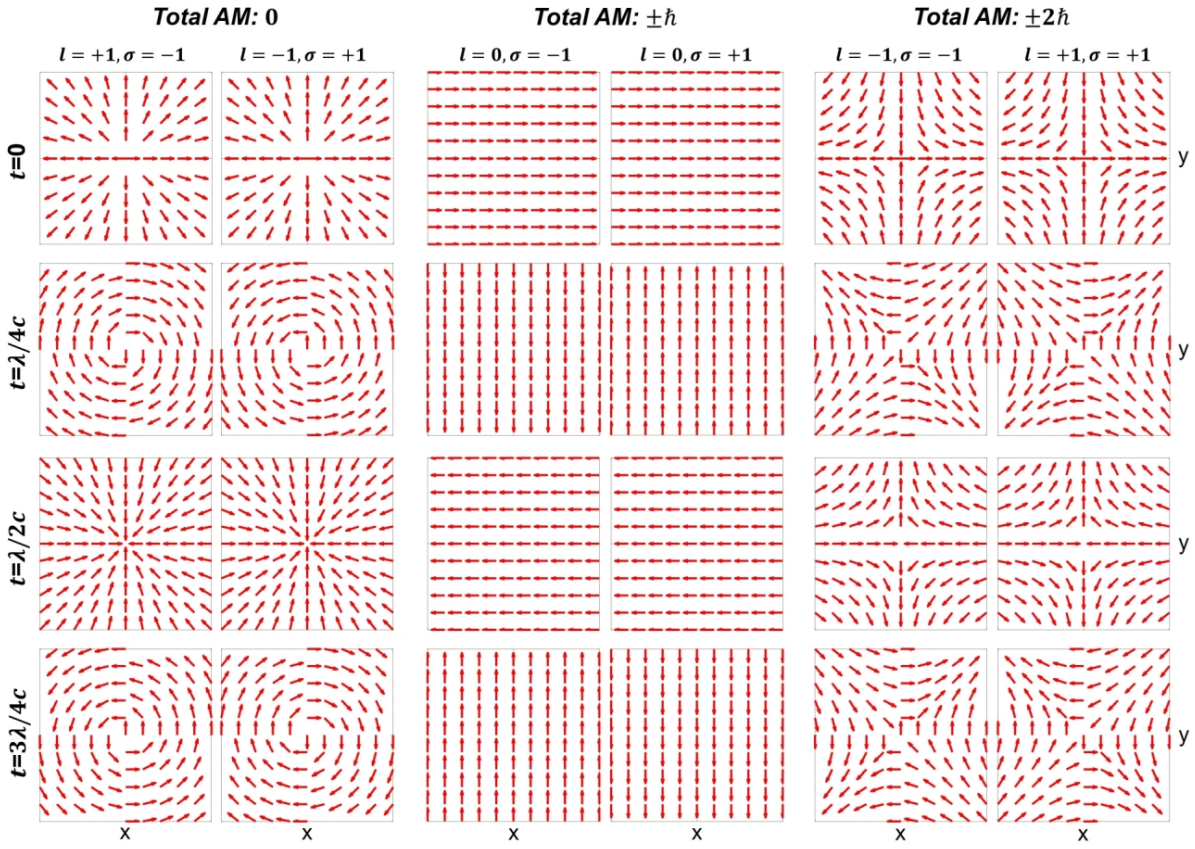

Figure 5.20: Transverse (xy) plane polarization distributions for varying combinations of OAM and SAM in the case of circularly-polarized ($\sigma = \pm 1$) beams as a function of time t.

From the experimental results and the polarization structures of Figures 5.19 and 5.20, it is now clear that the main result from this section is that the presence and absence of dichroism in the shuriken nanoindentations under weak focusing comes down to the polarization structure of the beam being chiral. However, the main question that arises from Figure 5.20 is: *why is the dichroism the same in Figure 5.18 for SAM only and antiparallel combination of SAM and OAM if the polarization distributions shown in Figure 5.20 are different?*, or formulated in a more general perspective: *will the dichroism vary for different total angular momentum content in the beam?* Another main result of this section is that the answer to these questions depends on whether a single or an array of structures is used to measure the dichroism.

Figure 5.21 shows the simulated z-component of the electric field when the beam is centred on a single nanostructure. The results indicate that different modes are excited for different combinations of SAM and OAM, and the symmetry matches the

polarization structure of Figure 5.20. In particular, for circularly-polarized beams, total angular momentum of 0, $\pm\hbar$ and $\pm 2\hbar$ results in a monopole, dipole and quadrupole-like excitations. The symmetry of these modes agrees with previous studies[300, 317, 318] and the work here has rationalized the origin by looking at the polarization structures. Most importantly, the modes are even under inversion for all the cases where OAM is present, indicating the excitation of a quadrupolar mode due to the superior field gradient generated by the LG beams. This is not the case for SAM only, where the modes are odd under inversion, indicating a dipolar excitation for this case.

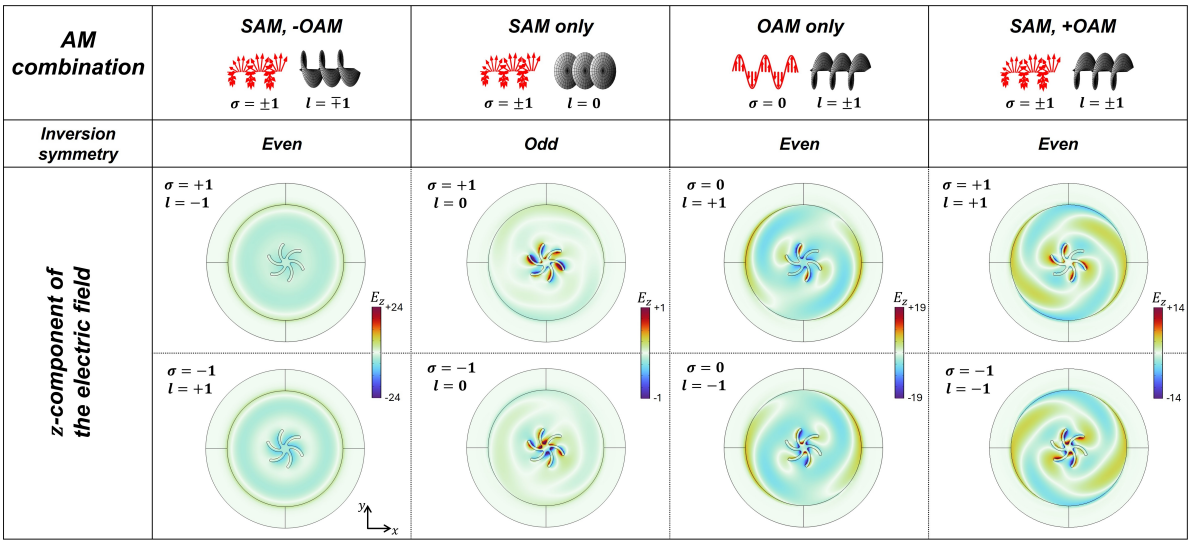

Figure 5.21: Simulation for the weakly-focused beam and shuriken structure. Simulated z-component of the electric field plotted on top of a RH shuriken structure for varying combinations of SAM and OAM (λ=590 nm). The helicity parameter σ and topological charge l are indicated in the upper left corner of each panel.

To replicate the periodicity effects of an array of nanostructures it was not possible to perform simulations with periodic structures, as this would replicate the beam an infinitely amount of times. It was not possible to use an array of nanostructures either due to large number of elements in the mesh and large computational time. Instead, another set of simulations were performed by shifting the centre of the beam with respect to the structure by an amount corresponding to the periodicity of the beam (720 nm). An schematic of this process with all the positions studied is shown in Figure 5.22.

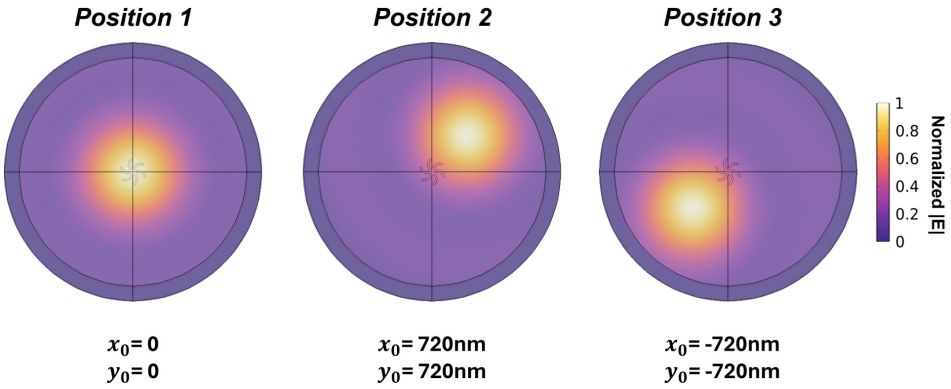

Figure 5.22: Electric field intensity superimposed on a RH shuriken structure to show the different relative beam positions that were simulated. The example here is shown for the Gaussian beam but the same principle applies for the Laguerre-Gaussian beams. Position 1: the beam is centred on the structure. Position 2 (Position 3): the beam is shifted by $x_0 = 720$ nm ($x_0 = -720$ nm) in the x direction and $y_0 = 720$ nm ($y_0 = -720$ nm) in the y direction.

Positions 2 and 3 of Figure 5.22 resulted in the development of a dipolar excitation for all combinations of SAM and OAM, as the z-component is now odd under inversion. This is depicted in Figure 5.23.

Figure 5.23: Simulated z-component of the electric field plotted on top of a RH shuriken structure for varying combinations of SAM and OAM (λ=590 nm) when the centre of the beam is shifted by an x_0 and y_0 amounts in the x and y directions, respectively (positions 2 and 3 of Figure 5.22). The helicity parameter σ and topological charge l are indicated in the upper left corner of each panel.

The individual and averaged g-factors across different beam positions with respect to the structure are shown in Figure 5.24. The helical dichroism (for linearly-polarized LG beam) was found to be weak in agreement with the experiment. In the case of SAM only, the g-factor did not vary significantly by shifting the beam with respect to the structure by an x_0, y_0 amount. This is a consequence of SAM being a *local* property as opposed to OAM which is a *global* property.[319, 320] In the case of parallel and antiparallel combinations of SAM and OAM, the g-factor obtained when the beam is centred on the structure (position 1) is different, corresponding to the specific excitations due to the total angular momentum and quadrupolar mode; but the g-factor is the same as that of SAM only when the beam is off the centre of the structure (positions 2 and 3), corresponding to the dipolar excitation as in the case of SAM only. Averaging over all the positions results in the same g-factor for all the circularly-polarized beams used regardless of the total angular momentum. This agrees with the experimental results of Figure 5.18, as the dichroism did not change in the combination of OAM and SAM. Note that the overall shape does not agree with the experimental one because the periodicity of the structure is not considered in the simulations with focused beams and lattice effects are known to have a strong influence in sharpening the plasmonic resonances.[321]

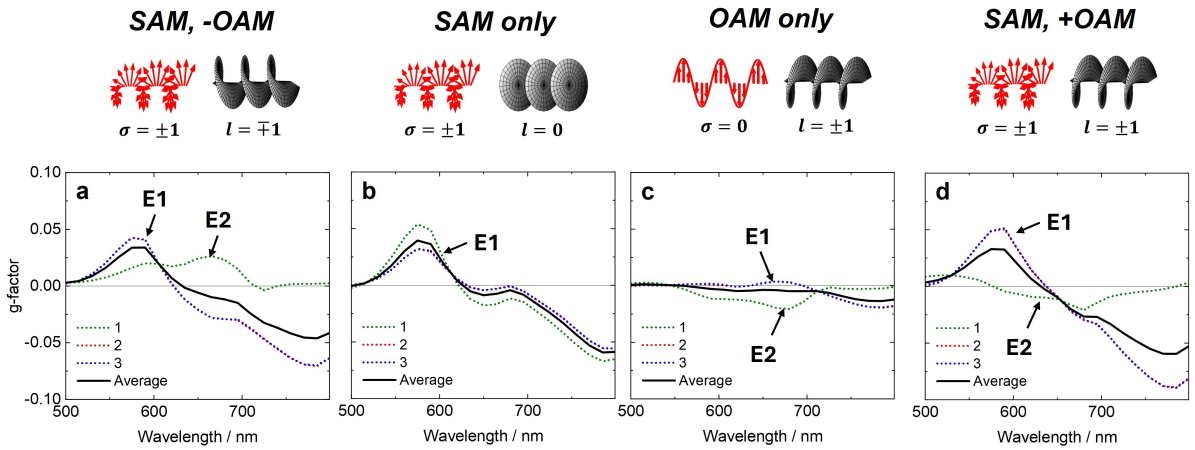

Figure 5.24: Simulated g-factor in the RH structure for varying combinations of SAM and OAM and different beam positions, with the averaged g-factor shown in black. Position 1: beam centred on the structure (green). Position 2: $x_0, y_0 = 720$ nm (red). Position 3: $x_0, y_0 = -720$ nm (blue). E1: electric dipole. E2: electric quadrupole.

In summary, simulations show that different EM modes are excited when the beam is positioned at the centre of the structure, giving rise to a different dichroism. When the structure is off the beam centre it will experience a local electric dipole and no change in the dichroism is observed for the different circularly-polarized beams. For an array of nanostructures and a weakly-focused beam, most of the structures are off the beam centre, which explains why no change is observed for the different circularly-polarized beams used in this work, regardless of the total angular momentum. This is schematically depicted in Figure 5.25.

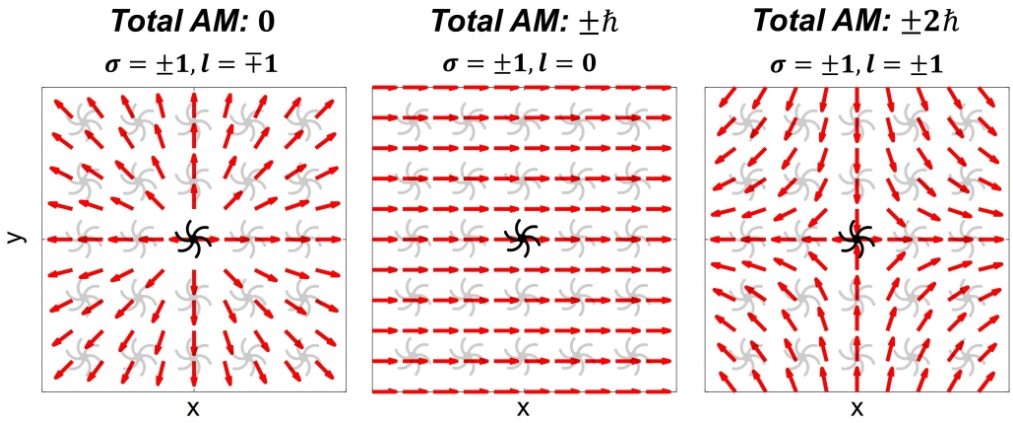

Figure 5.25: Transverse (xy) plane polarization distributions for varying combinations of OAM and SAM in the case of circularly-polarized beams. Structure depicted in black (at the beam centre) experiences the overall polarization distribution. Structures in light grey experience a local dipole. Plotted at time $t = 0$.

Alternatively, the results for weakly-focused beams can be interpreted by looking at the field gradient of LG beams. The field gradient dictates the excitation of the E2 quadrupolar mode *via* which OAM can participate in chiral interactions in the case of paraxial light beams.[13] The gradient in cylindrical coordinates is defined as

$$\nabla \mathbf{E} = \frac{\partial \mathbf{E}}{\partial \rho}\hat{\boldsymbol{\rho}} + \frac{1}{\rho}\frac{\partial \mathbf{E}}{\partial \phi}\hat{\boldsymbol{\phi}} + \frac{\partial \mathbf{E}}{\partial z}\hat{\boldsymbol{z}}, \tag{5.79}$$

where $\hat{\boldsymbol{\rho}}$, $\hat{\boldsymbol{\phi}}$ and $\hat{\boldsymbol{z}}$ are the unit vectors of cylindrical coordinates. Using the paraxial LG beam expression, the gradient of an arbitrary LG beam at the focus ($z = 0$) is therefore given by

$$\nabla \mathbf{E}_{\mathbf{LG}}^{l,p=\mathbf{0}} = \left[\hat{\boldsymbol{\rho}} \left(\frac{|l|}{\rho} - \frac{2\rho}{w_0^2} \right) + \hat{\boldsymbol{\phi}} \frac{il}{\rho} + ik\hat{\boldsymbol{z}} \right] \mathbf{E}_{\mathbf{LG}}^{l,p=\mathbf{0}}. \tag{5.80}$$

From equation 5.80, it is clear that the azimuthal gradient increases for the topological charge but decreases with the radial position ρ, therefore the structures that are positioned outside the beam centre will experience small effects due to the helical wavefronts. Since most of the structures are outside the beam centre this implies that no change is seen due to the OAM in the case of weakly-focused beams.

5.4.3 Dichroism under tight focusing

The dichroism under tight focusing (NA=0.95) was collected using different procedures. The first procedure is the same as that used to collect the dichroism for weakly-focused beams in § 5.4.2 and it involves collecting the dichroism across the visible range and average across random sample positions. The results from this type of measurements are shown in Figure 5.26. First, it can be noticed that the CD has a different appearance in comparison with the weakly-focused case. This is to be expected as the beam spot size of the tightly-focused beam spans slightly more than a single structure so lattice effects and periodicity are expected to be negligible. It can be noticed that the CD has broadened, as resonances broaden in the absence of a lattice.[321] Secondly, the results indicate that some helical dichroism is observed but it is very weak compared to conventional CD. This is likely because of the small spatial overlap between the structure and the LG beam, as the structure has an arm-to-arm distance of $\sim$ 530 nm, which is small compared to the LG beam diameter of $\sim$ 1000 nm.[104] Similar to the weakly-focused beam, no significant difference was found between SAM only and antiparallel combination of SAM and OAM after averaging across random sample positions.

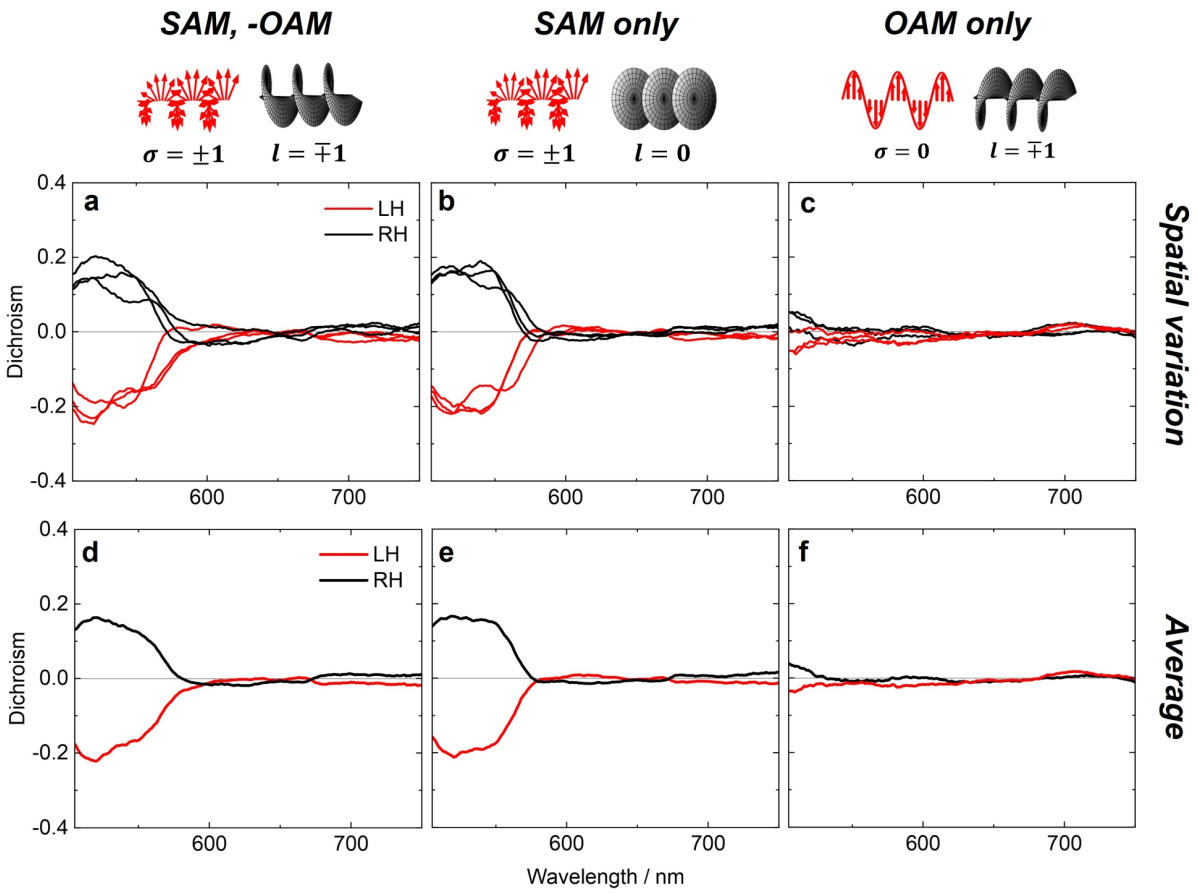

Figure 5.26: Dichroism collected at random sample positions using various combinations of angular momentum for LH (red) and RH (black) shuriken-shaped nanoindentations. (a-c) Spatially-varying dichroism across 3 different random positions in the sample for (a) antiparallel combination of SAM and OAM ($\sigma = \pm 1$, $l = \mp 1$), (b) SAM only ($\sigma = \pm 1$, $l = 0$) and (c) OAM only ($\sigma = 0$, $l = \mp 1$). (d-f) Averaged dichroism obtained from (a-c), respectively.

The classical coupled-oscillator model used to fit dichroism for the weakly-focused beam cannot be applied in this case. As the beam is now tightly focused on a single structure, no near-field coupling between bright and dark modes can occur. As shown in Figure 5.27, this was reflected in the measured extinction, which indicated the absence of PIR for the tightly-focused case.

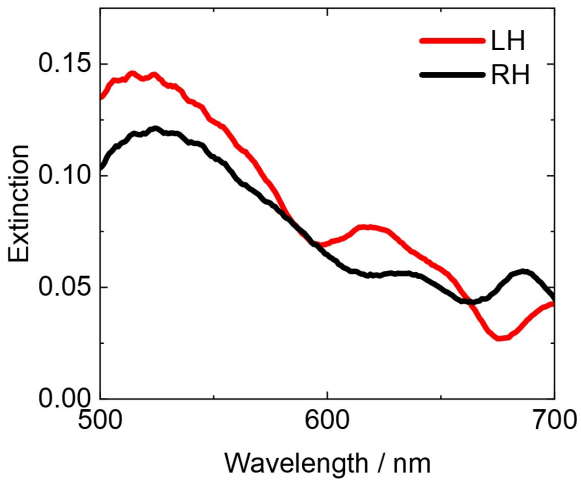

Figure 5.27: Extinction spectra of LH (red) and RH (black) shuriken structures under tight focusing. The data was collected using a linearly-polarized Gaussian beam. The data shows no PIR under the tightly-focused regime.

Another type of measurement was performed by using the piezoelectric stage to create a 2D plot of the dichroism for different wavelengths, as shown in Figure 5.28. From the obtained 2D plot, a circular mask was applied to obtain a value for the average dichroism value of the sample, where the diameter of the circular mask is a multiple of the periodicity of the shuriken nanoindentations.

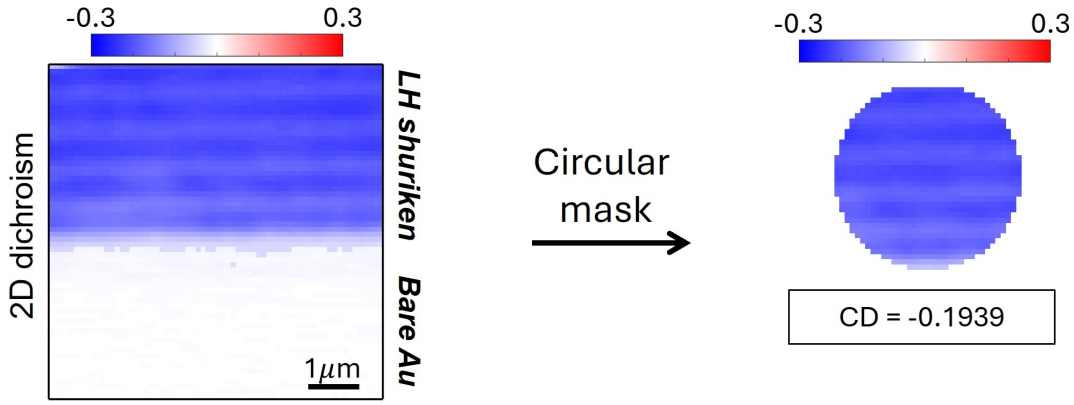

Figure 5.28: 2D plot of the dichroism collected in the LH structure using an excitation wavelength of $\lambda = 516$ nm and $\sigma = \pm 1, l = 0$ beam. A circular mask is applied to obtain an averaged dichroism value for the periodic structure. The distance between the pixels is 100 nm and the scale bar is 1 μm.

Using the procedure of Figure 5.28, it was possible to calculate the averaged dichroism across all sample positions for different wavelength values. The results are shown in Figure 5.29 and, as expected, the averaged dichroism had the same appearance as that

taken at random sample positions.

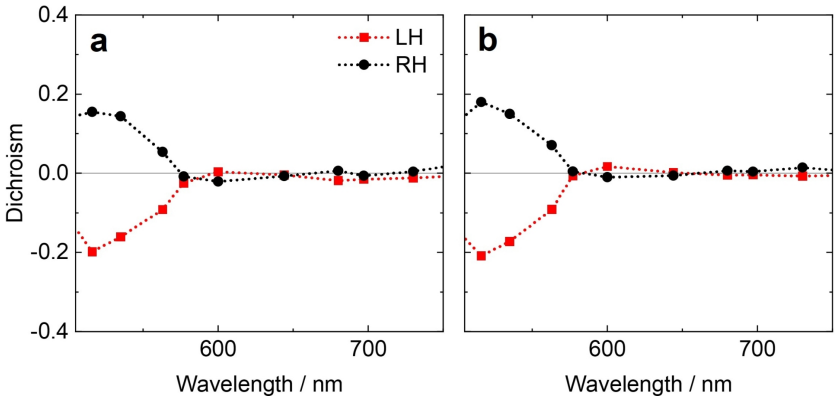

Figure 5.29: Averaged dichroism across different wavelengths for (a) antiparallel combination of SAM and OAM ($\sigma = \pm 1$, $l = \mp 1$) and (b) SAM only ($\sigma = \pm 1, l = 0$) beams.

The main result in the experiments of this chapter is that the dichroism taken directly on the structure was found to be different than the averaged dichroism across all sample positions. The centre of the structure was located using the piezoelectric stage to create a 2D plot of the extinction values for each wavelength. As the nanostructures scatter light stronger than plain gold, larger extinction values are found at the structures. An example of such 2D plot of the extinction is shown in Figure 5.30, showing a pattern of bright (large extinction) spots corresponding to the centre of the nanostructures. The pattern has a periodicity corresponding to that of the shuriken structures (≈720 nm).

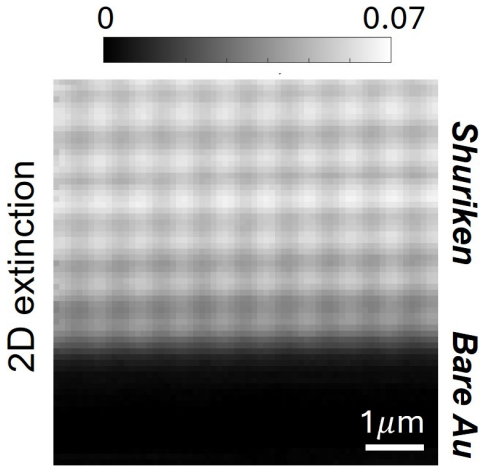

Figure 5.30: 2D plot of the extinction collected using an excitation wavelength of $\lambda = 535$ nm and $l = 0$ beam. The distance between the pixels is 100 nm and the scale bar is 1 μm.

From the large extinction spots in Figure 5.30 it was possible to locate the centre

of the nanostructures within a resolution of 100 nm, which allowed to measure the dichroism on the structure. This resulted in some striking differences, as shown in Figure 5.31. In particular, it is important to notice that the antiparallel combination of OAM and SAM shows some substantial dichroism at the wavelength of $\lambda = 565$ nm, which is where the main peak of the dichroism is observed in the weakly-focused regime. This is not the case for the dichroism collected with SAM only, where the dichroism at this wavelength is almost 0. Note that this change in the dichroism is dynamic and reversible, one just has to turn the Q-plate on/off to add/remove the OAM contribution. Additionally, the helical dichroism was weak, indicating that the optical activity has its origin in the SAM contribution.

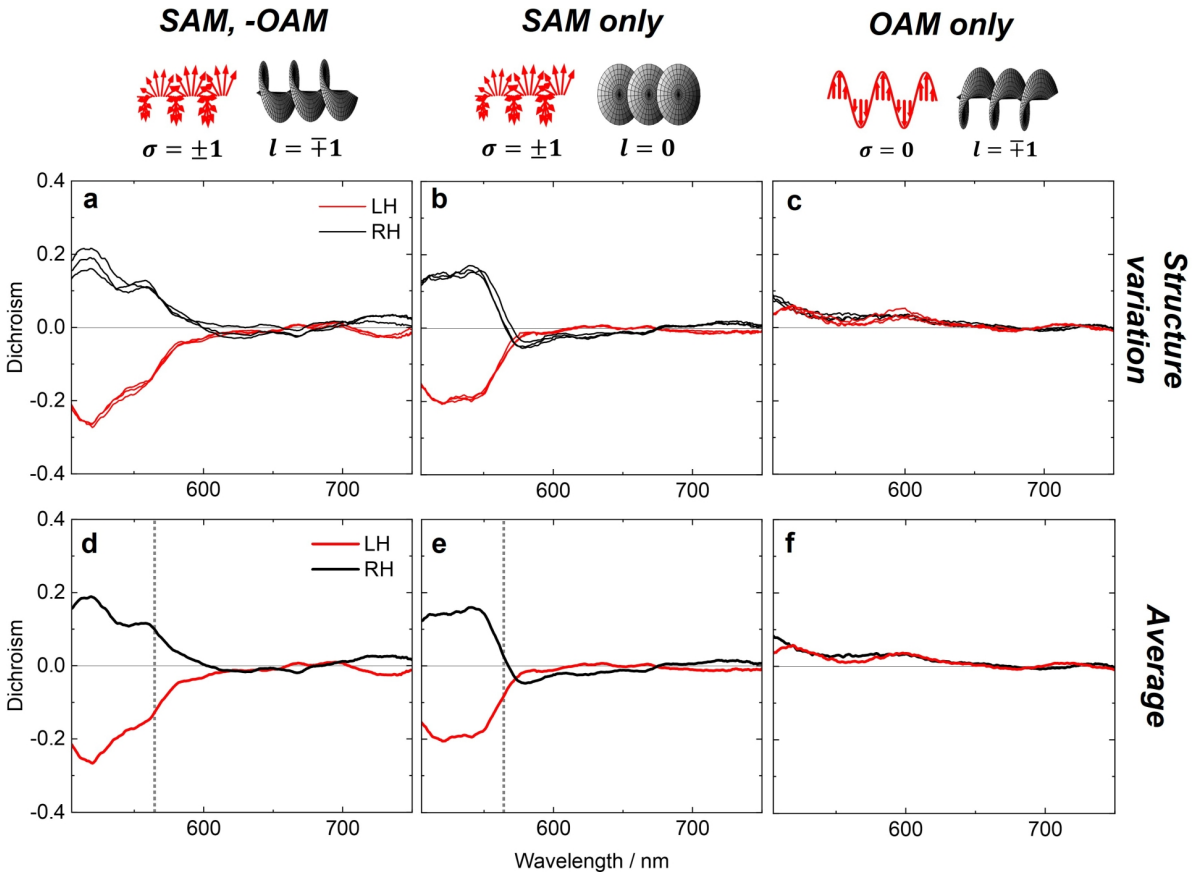

Figure 5.31: Dichroism collected on the structure using various combinations of angular momentum for LH (red) and RH (black) shuriken-shaped nanoindentations. (a-c) Spatially-varying dichroism across 3 different random structures for (a) antiparallel combination of SAM and OAM ($\sigma = \pm 1$, $l = \mp 1$), (b) SAM only ($\sigma = \pm 1$, $l = 0$) and (c) OAM only ($\sigma = 0$, $l = \mp 1$). (d-f) Averaged dichroism obtained from (a-c), respectively. A grey vertical dotted line has been added at $\lambda = 565$ nm where the maximum peak in the dichroism with weak focusing is observed.

The numerical simulations with the tightly-focused beam (shown in Figure 5.32) show the same mode excitations produced as in the weakly-focused case (*cf.* Figure 5.21). As shown here, even though the tightly-focused beam undergoes spin-orbit conversion and the distribution of OAM and SAM changes, the mode symmetry does not change due to the level of focusing, as excitation of these modes depends on the total angular momentum of the beam, but not in the OAM and SAM alone. Most importantly, the modes are even under inversion for all cases where OAM is present, indicating the excitation of a quadrupolar mode. For SAM only, the modes are odd under inversion, indicating a dipolar excitation.

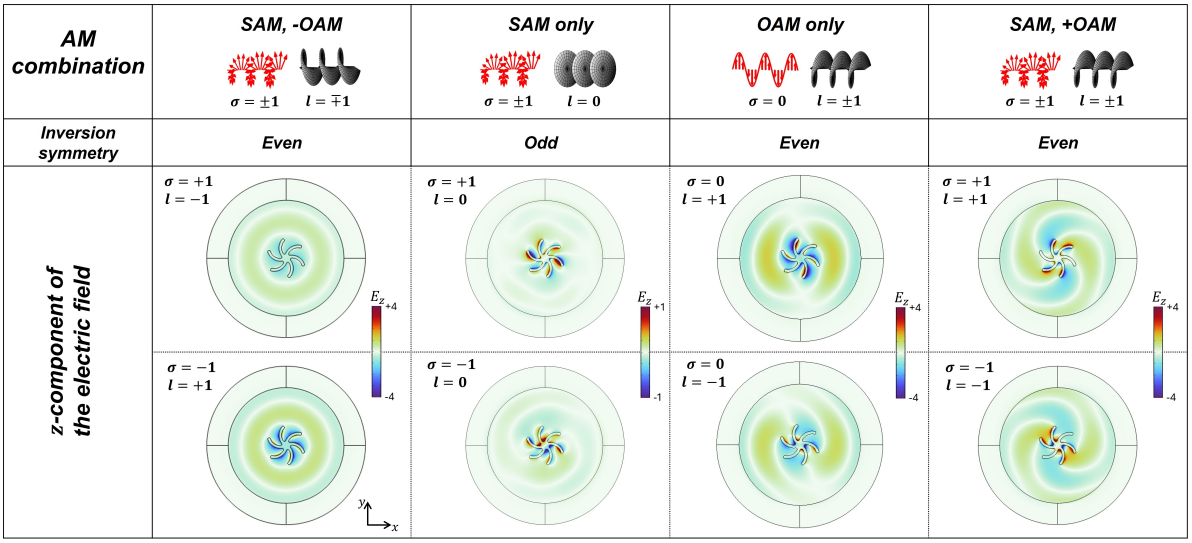

Figure 5.32: Simulation for the tightly-focused beam and shuriken structure. Simulated z-component of the electric field plotted on top of a RH shuriken structure for varying combinations of SAM and OAM (λ=590 nm). The helicity parameter σ and topological charge l are indicated in the upper left corner of each panel.

The excitation of the quadrupolar mode in the simulations in the case of OAM can be understood from theory. Previously, it has been well established that LG beams can excite higher-order modes due to their superior field gradients with respect to Gaussian beams.[99] Therefore, to understand the change in Figure 5.31 we take a look at the electric field gradient of LG beams. Recall that the gradient is given by

$$\nabla \mathbf{E}_{\mathbf{LG}}^{l,p=\mathbf{0}} = \left[\hat{\boldsymbol{\rho}}\left(\frac{|l|}{\rho} - \frac{2\rho}{w_0^2}\right) + \hat{\boldsymbol{\phi}}\frac{il}{\rho} + ik\hat{\boldsymbol{z}}\right]\mathbf{E}_{\mathbf{LG}}^{l,p=\mathbf{0}}, \tag{5.81}$$

which implies that LG beams where $l \neq 0$ will give larger gradients than Gaussian beams, and that this gradient will increase for increasing topological charge. It is a well-known fact across different studies that steep field gradients excite electric quadrupoles (E2), which subsequently modify the chiroptical properties of chiral systems.[322–325] Here it is proposed the dichroism in shuriken nanoindentations arises solely due to SAM contribution, as the helical dichroism collected with OAM only is weak. Due to the absence of PIR in the tightly-focused regime, the dichroism must originate from E1M1 interactions. However, the additional excitation of quadrupolar modes from the steep gradient of LG beams when the beam is tightly focused on the structure modifies the dichroism signal *via* E1E2 interactions, which gives rise to a dichroism signal for the same wavelengths where dichroism is observed due to the near-field coupling of bright and dark modes in the weakly-focused case.

5.5 Conclusions

In this chapter the interaction between light beams carrying varying combinations of SAM and OAM and shuriken-shaped chiral metamaterials have been studied across the visible range. The experiments and simulations for weakly-focused beams indicate no change in the dichroism due to the addition of OAM to the beam and no dichroism with OAM alone. This has been rationalized considering the array effects, polarization distributions and the fact that the dichroism is expected to be the same for the structures off the beam centre.

In the case of tightly-focused beams, however, the beam is now focused on a single shuriken structure. A significant change in the dichroism has been observed using circularly-polarized LG beams ($\sigma = \mp 1$, $l = \pm 1$), and effect that is attributed to the excitation of higher-order modes due to the superior field gradient of LG beams compared to conventional Gaussian beams. As opposed to previous methods where optical activity is changed through geometric modifications,[303] the change in this work is dynamic and it can be simply alternated by switching the Q-plate on/off to add/remove the OAM

contribution. It is important to further notice that the change has been achieved for a structure as small as ∼500 nm in size, but the method is limited by the spatial match between the beam and the structure. Future work could focus on the use of different topological charges, and also on the implementation of a variable phase retarder after the Q-plate. The second one will allow to dynamically alter the final polarization state to (1) act as a half wave plate, generating the parallel combination of SAM and OAM; (2) act as a linear polarizer, generating helical dichroism; (3) maintain the antiparallel combination of SAM and OAM if off.

In summary, the findings of this work simplify the traditional methods of modifying the chiral response which has been previously achieved *via* structural and geometrical design[303] and it envisages orbital angular momentum as a powerful tool for the dynamic modulation of optical activity.

Chapter 5: Summary

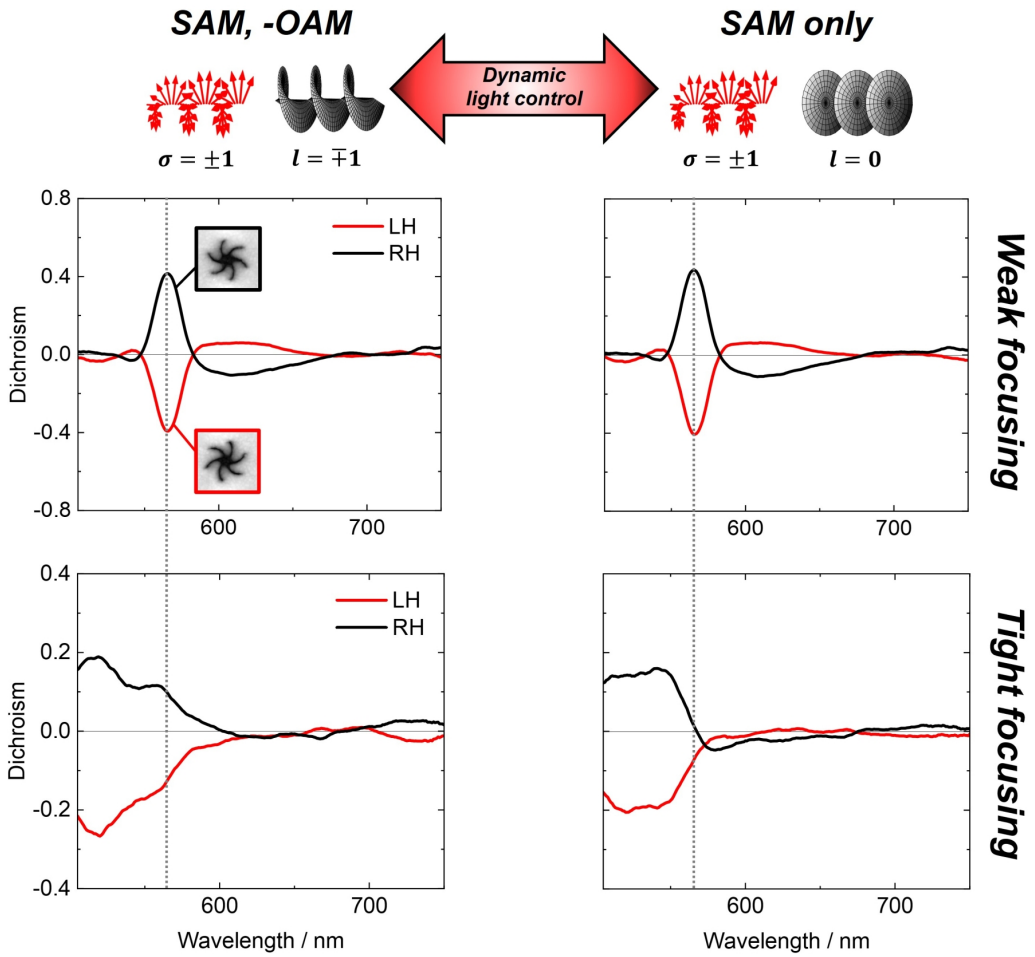

Figure 5.33: Chapter 5 concept figure.

Key findings:

- Orbital angular momentum can excite higher-order modes (E2) due to a superior field gradient.
- Dichroism measurements have been achieved for varying combinations of angular momenta across the visible range in chiral metamaterials.
- Dynamic tuning of the dichroism has been achieved with orbital angular momentum and E1E2 interactions.

Chapter 6

Conclusions and future outlook

In this thesis Laguerre-Gaussian beams and their associated orbital angular momentum have been employed to modify the properties of nanomaterials for two different applications. In the first instance, the torque and azimuthal forces carried by Laguerre-Gaussian beams have been successfully used for the dynamic and spatially-selective modification of the morphology and electronic properties of 2D materials. Numerical simulations have provided a visualization and understanding of the expected forces and torques. The changes in the morphology and properties have been characterized using a wide range of experimental techniques, including Raman spectroscopy, PL spectroscopy, conductance measurements and AFM.

In the second instance of this thesis, Laguerre-Gaussian beams have been investigated for a different application, the tuning of optical activity and chiroptical response in chiral metamaterials. Using theory, numerical simulations and dichroism measurements it has been concluded that the superior field gradients generated by Laguerre-Gaussian beams can be used to dynamically modify the optical activity response in chiral metamaterials. This has been thoroughly investigated using different levels of focusing and different amounts of angular momentum.

In summary, the work performed in this thesis envisages optical orbital angular momentum as a very powerful tool to control the properties of nanomaterials for a wide range of scenarios and applications. The work undertaken in this thesis has been

performed for a fixed topological charge. However, in the realms of orbital angular momentum beams, there is still plenty of room to be explored for different topological charges, alternative beams *e.g.* Bessel or Zernike beams, different polarization structures, in the search for new effects. In the area of 2D materials, there are emerging materials such as 2D hybrid organic-inorganic perovskites[326] that could be explored next.

Overall, it is fascinating to have witnessed the rapid growth in the research of orbital angular momentum of light since its emergence in 1992, and to see how it has expanded into diverse fields and applications. With this thesis, I hope to have sparked some curiosity and contributed, even if just a small part, to this constantly evolving area of study.

Bibliography

1. Parkinson, R. W., Jones, H. M. & Shapiro, I. I. Effects of Solar Radiation Pressure on Earth Satellite Orbits. *Science* **131,** 920–921 (1960).

2. Shapiro, I. I. & Jones, H. M. Perturbations of the Orbit of the Echo Balloon. *Science* **132,** 1484–1486 (1960).

3. Poynting, J. H. The wave motion of a revolving shaft, and a suggestion as to the angular momentum in a beam of circularly polarised light. *Proceedings of the Royal Society of London. Series A, Containing Papers of a Mathematical and Physical Character* **82,** 560–567 (1909).

4. Siegman, A. E. *Lasers* (University Science Books, 1986).

5. Allen, L., Beijersbergen, M. W., Spreeuw, R. J. & Woerdman, J. P. Orbital angular momentum of light and the transformation of Laguerre-Gaussian laser modes. *Phys Rev A* **45,** 8185–8189 (1992).

6. He, H., Friese, M. E. J., Heckenberg, N. R. & Rubinszteindunlop, H. Direct Observation of Transfer of Angular-Momentum to Absorptive Particles from a Laser-Beam with a Phase Singularity. *Physical Review Letters* **75,** 826–829 (1995).

7. Mair, A., Vaziri, A., Weihs, G. & Zeilinger, A. Entanglement of the orbital angular momentum states of photons. *Nature* **412,** 313–316 (2001).

8. Fickler, R. *et al.* Quantum Entanglement of High Angular Momenta. *Science* **338,** 640–643 (2012).

9. Leach, J. *et al.* Quantum Correlations in Optical Angle–Orbital Angular Momentum Variables. *Science* **329,** 662–665 (2010).

10. Gibson, G. *et al.* Free-space information transfer using light beams carrying orbital angular momentum. *Optics Express* **12,** 5448–5456 (2004).

11. Tamburini, F. *et al.* Encoding many channels on the same frequency through radio vorticity: first experimental test. *New Journal of Physics* **14,** 033001 (2012).

12. Wang, J. *et al.* Terabit free-space data transmission employing orbital angular momentum multiplexing. *Nature Photonics* **6,** 488–496 (2012).

13. Forbes, K. A. & Andrews, D. L. Orbital angular momentum of twisted light: chirality and optical activity. *Journal of Physics: Photonics* **3,** 022007 (2021).

14. Maurer, C., Jesacher, A., Bernet, S. & Ritsch-Marte, M. What spatial light modulators can do for optical microscopy. *Laser & Photonics Reviews* **5,** 81–101 (2011).

15. Swartzlander, G. A. Peering into darkness with a vortex spatial filter. *Opt. Lett.* **26,** 497–499 (2001).

16. Balasubramaniam, G. M., Biton, N. & Arnon, S. Imaging through diffuse media using multi-mode vortex beams and deep learning. *Scientific Reports* **12,** 1561 (2022).

17. Hua, Y. *et al.* Visualized quantum 3D orbital-angular-momentum holography. *Chin. Opt. Lett.* **22,** 110501 (2024).

18. Griffiths, D. J. *Introduction to Electrodynamics* (Prentice Hall of India, 1998).

19. Jackson, J. D. *Classical Electrodynamics* (Wiley, 1998).

20. Simon, D. S. *A Guided Tour of Light Beams* (Morgan & Claypool Publishers, 2016).

21. Khare, K., Lochab, P. & Senthilkumaran, P. *Orbital Angular Momentum States of Light* (IOP Publishing, 2020).

22. Novotny, L. & Hecht, B. *Principles of Nano-Optics* 2nd ed. (Cambridge University Press, 2012).

23. Gotte, J. B. & Barnett, S. M. in *The Angular Momentum of Light* (Cambridge University Press, 2012).

24. Allen, L., Barnett, S. M. & Padgett, M. J. *Optical Angular Momentum* (Taylor & Francis Group, 2003).

25. Barnett, S. M., Babiker, M. & Padgett, M. J. Optical orbital angular momentum. *Philos Trans A Math Phys Eng Sci* **375** (2017).

26. Gouy, L. G. *Sur une propriété nouvelle des ondes lumineuses* fre (Gauthier-Villars Paris, Paris, 1890).

27. Barnett, S. M. Optical angular-momentum flux. *Optics B: Quantum and Semiclassical Optics* **4** (2002).

28. Hecht, E. *Optics* 5th edition (Pearson Education, Limited, 2016).

29. Beth, R. A. Mechanical detection and measurement of the angular momentum of light. *Physical Review* **50,** 115–125 (1936).

30. Bazhenov, V. Y., Vasnetsov, M. V. & Soskin, M. S. Laser-Beams with Screw Dislocations in Their Wave-Fronts. *Jetp Letters* **52,** 429–431 (1990).

31. Padgett, M. & Allen, L. Light with a twist in its tail. *Contemporary Physics* **41,** 275–285 (2000).

32. Padgett, M., Courtial, J. & Allen, L. Light's Orbital Angular Momentum. *Physics Today* **57,** 35–40 (2004).

33. Padgett, M. J. & Allen, L. The Poynting Vector in Laguerre-Gaussian Laser Modes. *Optics Communications* **121,** 36–40 (1995).

34. Allen, L. & Padgett, M. J. The Poynting vector in Laguerre-Gaussian beams and the interpretation of their angular momentum density. *Optics Communications* **184,** 67–71 (2000).

35. Durnin, J., Miceli, J. J. & Eberly, J. H. Diffraction-free beams. *Phys. Rev. Lett.* **58,** 1499–1501 (15 1987).

36. Durnin, J. Exact solutions for nondiffracting beams. I. The scalar theory. *J. Opt. Soc. Am. A* **4,** 651–654 (1987).

37. McGloin, D. & Dholakia, K. Bessel beams: Diffraction in a new light. *Contemporary Physics* **46,** 15–28 (2005).

38. Sztul, H. & Alfano, R. The Poynting vector and angular momentum of Airy beams. *Opt. Express* **16,** 9411–9416 (2008).

39. Konwar, S. & Boruah, B. R. Leveraging the orthogonality of Zernike modes for robust free-space optical communication. *Communications Physics* **3,** 203 (2020).

40. Padgett, M. Light's twist. *Proc Math Phys Eng Sci* **470,** 20140633 (2014).

41. Plick, W. N. & Krenn, M. Physical meaning of the radial index of Laguerre-Gauss beams. *Phys. Rev. A* **92,** 063841 (6 2015).

42. Bransden, B. & Joachain, C. *Quantum Mechanics* (Prentice Hall, 2000).

43. Beijersbergen, M., Allen, L., van der Veen, H. & Woerdman, J. Astigmatic laser mode converters and transfer of orbital angular momentum. *Optics Communications* **96,** 123–132 (1993).

44. Bliokh, K. Y. & Nori, F. Transverse and longitudinal angular momenta of light. *Physics Reports* **592,** 1–38 (2015).

45. Bliokh, K. Y., Rodríguez-Fortuño, F. J., Nori, F. & Zayats, A. V. Spin-orbit interactions of light. *Nature Photonics* **9,** 796–808 (2015).

46. Bliokh, K. Y. *et al.* Spin-to-orbital angular momentum conversion in focusing, scattering, and imaging systems. *Opt. Express* **19,** 26132–26149 (2011).

47. Bliokh, K. Y., Aiello, A. & Alonso, M. A. in *The Angular Momentum of Light* (eds Andrews, D. L. & Babiker, M.) 174–245 (Cambridge University Press, 2012).

48. Carretero, L., Acebal, P. & Blaya, S. Kerker's conditions for chiral particles: Enhanced Spin-to–orbital angular momentum conversion of the scattered light. *Journal of Quantitative Spectroscopy & Radiative Transfer* **222,** 60–64 (2019).

49. Marrucci, L. *et al.* Spin-to–orbital conversion of the angular momentum of light and its classical and quantum applications. *Journal of Optics* **13** (2011).

50. Zhou, H., Fu, S. Y., Zhai, Y. W., Yin, C. & Gao, C. Q. Spatial light modulator-based programmable J-plate for the arbitrary spin-to-orbital angular momentum conversion of lights. *Applied Physics B-Lasers and Optics* **125** (2019).

51. Kotlyar, V. V., Nalimov, A. G., Kovalev, A. A., Porfirev, A. P. & Stafeev, S. S. Spin-orbit and orbit-spin conversion in the sharp focus of laser light: Theory and experiment. *Phys. Rev. A* **102,** 033502 (3 2020).

52. Gorodetski, Y., Niv, A., Kleiner, V. & Hasman, E. Observation of the Spin-Based Plasmonic Effect in Nanoscale Structures. *Phys. Rev. Lett.* **101,** 043903 (4 2008).

53. Zhao, Y., Shapiro, D., Mcgloin, D., Chiu, D. T. & Marchesini, S. Direct observation of the transfer of orbital angular momentum to metal particles from a focused circularly polarized Gaussian beam. *Opt. Express* **17,** 23316–23322 (2009).

54. Adachi, H., Akahoshi, S. & Miyakawa, K. Orbital motion of spherical microparticles trapped in diffraction patterns of circularly polarized light. *Phys. Rev. A* **75,** 063409 (6 2007).

55. Zhao, Y., Edgar, J. S., Jeffries, G. D. M., McGloin, D. & Chiu, D. T. Spin-to-Orbital Angular Momentum Conversion in a Strongly Focused Optical Beam. *Phys. Rev. Lett.* **99,** 073901 (7 2007).

56. Stephenson, G. & Radmore, P. M. *Advanced Mathematical Methods for Engineering and Science Students* (Cambridge University Press, 1990).

57. Ashkin, A. Acceleration and Trapping of Particles by Radiation Pressure. *Phys. Rev. Lett.* **24,** 156–159 (4 1970).

58. C., M. J. *A Treatise on Electricity and Magnetism* (Oxford: Oxford University Press, 1998).

59. Neuman, K. C. & Block, S. M. Optical trapping. *Review of Scientific Instruments* **75,** 2787–2809 (2004).

60. Ashkin, A., Dziedzic, J. M., Bjorkholm, J. E. & Chu, S. Observation of a single-beam gradient force optical trap for dielectric particles. *Opt. Lett.* **11,** 288–290 (1986).

61. Maragò, O. M., Jones, P. H., Gucciardi, P. G., Volpe, G. & Ferrari, A. C. Optical trapping and manipulation of nanostructures. *Nature Nanotechnology* **8,** 807–819 (2013).

62. Sneh, T. *et al.* Optical tweezing of microparticles and cells using silicon-photonics-based optical phased arrays. *Nature Communications* **15,** 8493 (2024).

63. Optical trapping and tailoring of exciton-polariton condensates into macroscopic complexes. *Nature Physics* **20,** 22–23 (2024).

64. *Optical Tweezers. Methods and Protocols* (ed Gennerich, A.) (Springer, 2017).

65. Tanaka, M., Tsuboi, Y. & Yuyama, K.-i. Formation of a core–shell droplet in a thermo-responsive ionic liquid/water mixture by using optical tweezers. *Chem. Commun.* **58,** 11787–11790 (84 2022).

66. Fujiwara, H. *et al.* Spin–Orbit Angular-Momentum Transfer from a Nanogap Surface Plasmon to a Trapped Nanodiamond. *Nano Letters* **21,** 6268–6273 (2021).

67. Chen, X. T., Cheng, W. Z., Xie, M. Y. & Zhao, F. L. Optical rotational self-assembly at air-water surface by a single vortex beam. *Results in Physics* **12,** 1172–1176 (2019).

68. O'Neil, A. T. & Padgett, M. J. Three-dimensional optical confinement of micron-sized metal particles and the decoupling of the spin and orbital angular momentum within an optical spanner. *Optics Communications* **185,** 139–143 (2000).

69. O'Neil, A. T., MacVicar, I., Allen, L. & Padgett, M. J. Intrinsic and extrinsic nature of the orbital angular momentum of a light beam. *Physical Review Letters* **88** (2002).

70. Curtis, J. E., Koss, B. A. & Grier, D. G. Dynamic holographic optical tweezers. *Optics Communications* **207,** 169–175 (2002).

71. Garces-Chavez, V. *et al.* Observation of the transfer of the local angular momentum density of a multiringed light beam to an optically trapped particle. *Physical Review Letters* **91** (2003).

72. Leach, J., Keen, S., Padgett, M. J., Saunter, C. & Love, G. D. Direct measurement of the skew angle of the Poynting vector in a helically phased beam. *Opt. Express* **14,** 11919–11924 (2006).

73. Barnett, S. M. *et al.* On the natures of the spin and orbital parts of optical angular momentum. *Journal of Optics* **18,** 064004 (2016).

74. Friese, M. E. J., Nieminen, T. A., Heckenberg, N. R. & Rubinsztein-Dunlop, H. Optical alignment and spinning of laser-trapped microscopic particles. *Nature* **394,** 348–350 (1998).

75. Friese, M. E., Enger, J., Rubinsztein-Dunlop, H. & Heckenberg, N. R. Optical angular-momentum transfer to trapped absorbing particles. *Phys Rev A* **54,** 1593–1596 (1996).

76. Simpson, N. B., Dholakia, K., Allen, L. & Padgett, M. J. Mechanical equivalence of spin and orbital angular momentum of light: an optical spanner. *Opt. Lett.* **22,** 52–54 (1997).

77. Toyoda, K., Miyamoto, K., Aoki, N., Morita, R. & Omatsu, T. Using Optical Vortex To Control the Chirality of Twisted Metal Nanostructures. *Nano Letters* **12,** 3645–3649 (2012).

78. Syubaev, S. *et al.* Chirality of laser-printed plasmonic nanoneedles tunable by tailoring spiral-shape pulses. *Applied Surface Science* **470,** 526–534 (2019).

79. Omatsu, T. *et al.* A New Twist for Materials Science: The Formation of Chiral Structures Using the Angular Momentum of Light. *Advanced Optical Materials* **7** (2019).

80. Fedoruk, M., Meixner, M., Carretero-Palacios, S., Lohmüller, T. & Feldmann, J. Nanolithography by Plasmonic Heating and Optical Manipulation of Gold Nanoparticles. *ACS Nano* **7,** 7648–7653 (2013).

81. Ni, J. *et al.* Three-dimensional chiral microstructures fabricated by structured optical vortices in isotropic material. *Light: Science & Applications* **6,** e17011–e17011 (2017).

82. Barron, L. D. *Molecular Light Scattering and Optical Activity* 2nd ed. (Cambridge University Press, 2004).

83. Eriksson, T., Björkman, S. & Höglund, P. Clinical pharmacology of thalidomide. *European Journal of Clinical Pharmacology* **57,** 365–376 (2001).

84. Arago, M. *Mémoire sur une modification remarquable qu' éprouvent les rayons lumineux dans leur passage à travers certains corps diaphanes, & sur quelques autres phénomènes d'optique* (1811).

85. Anderson, J., Gillen, C., Wright, J., Adams, C. S. & Hughes, I. G. Optical rotation of white light. *American Journal of Physics* **88,** 247–251 (2020).

86. Theron, I. & Cloete, J. The electric quadrupole contribution to the circular birefringence of nonmagnetic anisotropic chiral media: a circular waveguide experiment. *IEEE Transactions on Microwave Theory and Techniques* **44,** 1451–1459 (1996).

87. Kelly, C. *et al.* Chiral Plasmonic Fields Probe Structural Order of Biointerfaces. *Journal of the American Chemical Society* **140,** 8509–8517 (2018).

88. Craig, D. & Thirunamachandran, T. *Molecular Quantum Electrodynamics: An Introduction to Radiation-molecule Interactions* (Dover Publications, 1998).

89. Salam, A. *Molecular Quantum Electrodynamics: Long-Range Intermolecular Interactions* (Wiley, 2009).

90. Brullot, W., Vanbel, M. K., Swusten, T. & Verbiest, T. Resolving enantiomers using the optical angular momentum of twisted light. *Science Advances* **2** (2016).

91. Moscowitz, A. in *Advances in Chemical Physics* 67–112 (John Wiley & Sons, Ltd, 1962).

92. Autschbach, J. Computing chiroptical properties with first-principles theoretical methods: Background and illustrative examples. *Chirality* **21,** E116–E152 (2009).

93. Collins, J. T. *et al.* Chirality and Chiroptical Effects in Metal Nanostructures: Fundamentals and Current Trends. *Advanced Optical Materials* **5,** 1700182 (2017).

94. Tabouillot, V. *et al.* Near-Field Probing of Optical Superchirality with Plasmonic Circularly Polarized Luminescence for Enhanced Bio-Detection. *ACS Photonics* **9,** 3617–3624 (2022).

95. Andrews, D., Romero, L. & Babiker, M. On optical vortex interactions with chiral matter. *Optics Communications* **237,** 133–139 (2004).

96. Araoka, F., Verbiest, T., Clays, K. & Persoons, A. Interactions of twisted light with chiral molecules: An experimental investigation. *Phys. Rev. A* **71,** 055401 (5 2005).

97. Löffler, W., Broer, D. J. & Woerdman, J. P. Circular dichroism of cholesteric polymers and the orbital angular momentum of light. *Phys. Rev. A* **83,** 065801 (6 2011).

98. Babiker, M., Bennett, C. R., Andrews, D. L. & Dávila Romero, L. C. Orbital Angular Momentum Exchange in the Interaction of Twisted Light with Molecules. *Phys. Rev. Lett.* **89,** 143601 (14 2002).

99. Forbes, K. A. & Andrews, D. L. Optical orbital angular momentum: twisted light and chirality. *Opt. Lett.* **43,** 435–438 (2018).

100. Forbes, K. A. & Jones, G. A. Optical vortex dichroism in chiral particles. *Phys. Rev. A* **103,** 053515 (5 2021).

101. Zambrana-Puyalto, X., De Angelis, F. & D'Ambrosio, V. Vortex Circular Dichroism: An experimental technique to assess the scalar/vectorial regime of diffraction [version 2; peer review: 2 approved]. *Open Research Europe* **2** (2024).

102. Power, E. A. & Thirunamachandran, T. Circular dichroism: A general theory based on quantum electrodynamics. *The Journal of Chemical Physics* **60,** 3695–3701 (1974).

103. Ni, J. *et al.* Gigantic vortical differential scattering as a monochromatic probe for multiscale chiral structures. *Proceedings of the National Academy of Sciences* **118,** e2020055118 (2021).

104. Ni, J. *et al.* Giant Helical Dichroism of Single Chiral Nanostructures with Photonic Orbital Angular Momentum. *ACS Nano* **15,** 2893–2900 (2021).

105. Zambrana-Puyalto, X., Vidal, X. & Molina-Terriza, G. Angular momentum-induced circular dichroism in non-chiral nanostructures. *Nature Communications* **5,** 4922 (2014).

106. Iketaki, Y., Watanabe, T., Bokor, N. & Fujii, M. Investigation of the center intensity of first- and second-order Laguerre-Gaussian beams with linear and circular polarization. *Opt. Lett.* **32,** 2357–2359 (2007).

107. Forbes, K. A., Green, D. & Jones, G. A. Relevance of longitudinal fields of paraxial optical vortices. *Journal of Optics* **23,** 075401 (2021).

108. Zambrana-Puyalto, X., Vidal, X., Woźniak, P., Banzer, P. & Molina-Terriza, G. Tailoring Multipolar Mie Scattering with Helicity and Angular Momentum. *ACS Photonics* **5,** 2936–2944 (2018).

109. Rosales-Guzmán, C., Volke-Sepulveda, K. & Torres, J. P. Light with enhanced optical chirality. *Opt. Lett.* **37,** 3486–3488 (2012).

110. Green, D. & Forbes, K. A. Optical chirality of vortex beams at the nanoscale. *Nanoscale* **15,** 540–552 (2 2023).

111. Forbes, K. A. & Jones, G. A. Measures of helicity and chirality of optical vortex beams. *Journal of Optics* **23,** 115401 (2021).

112. Woźniak, P., Leon, I. D., Höflich, K., Leuchs, G. & Banzer, P. Interaction of light carrying orbital angular momentum with a chiral dipolar scatterer. *Optica* **6,** 961–965 (2019).

113. Courant, R. Variational methods for the solution of problems of equilibrium and vibrations. *Bulletin of the American Mathematical Society* **49,** 1–23 (1943).

114. Patoux, A. *et al.* Challenges in nanofabrication for efficient optical metasurfaces. *Scientific Reports* **11,** 5620 (2021).

115. Dong, C. *et al.* Simulation-guided nanofabrication of high-quality practical tungsten probes. *RSC Adv.* **10,** 24280–24287 (41 2020).

116. Hendry, E. *et al.* Ultrasensitive detection and characterization of biomolecules using superchiral fields. *Nature Nanotechnology* **5,** 783–787 (2010).

117. Gilroy, C. *et al.* Roles of Superchirality and Interference in Chiral Plasmonic Biodetection. *The Journal of Physical Chemistry C* **123,** 15195–15203 (2019).

118. Hajji, M. *et al.* Chiral Quantum Metamaterial for Hypersensitive Biomolecule Detection. *ACS Nano* **15,** 19905–19916 (2021).

119. Larson, M. G. & Bengzon, F. *The Finite Element Method: Theory, Implementation and Applications* (Springer, 2013).

120. García-Etxarri, A. *et al.* Strong magnetic response of submicron Silicon particles in the infrared. *Opt. Express* **19,** 4815–4826 (2011).

121. Barnett, S. M. & Loudon, R. The enigma of optical momentum in a medium. *Philosophical Transactions of the Royal Society A: Mathematical, Physical and Engineering Sciences* **368,** 927–939 (2010).

122. Buchanan, M. Minkowski, Abraham and the photon momentum. *Nature Physics* **3,** 73–73 (2007).

123. Minkowski, H. Die Grundgleichungen für die elektromagnetischen Vorgänge in bewegten Körpern. *Nachrichten von der Gesellschaft der Wissenschaften zu Göttingen, Mathematisch-Physikalische Klasse,* 53–111 (1908).

124. Abraham, M. Zur Elektrodynamik bewegter Körper. *Rendiconti del Circolo Matematico di Palermo (1884-1940)* **28,** 1–28 (1909).

125. Barnett, S. M. & Loudon, R. On the electromagnetic force on a dielectric medium. *Journal of Physics B: Atomic, Molecular and Optical Physics* **39,** S671 (2006).

126. Lalaguna, P. L. *et al.* Spatial Control of 2D Nanomaterial Electronic Properties Using Chiral Light Beams. *ACS Nano* **18,** 20401–20411 (2024).

127. Weber, J. W., Calado, V. E. & van de Sanden, M. C. M. Optical constants of graphene measured by spectroscopic ellipsometry. *Applied Physics Letters* **97,** 091904 (2010).

128. Jung, G.-H., Yoo, S. & Park, Q. H. Measuring the optical permittivity of two-dimensional materials without a priori knowledge of electronic transitions. **8,** 263–270 (2019).

129. Querry, M. R. Optical constants. *Contractor Report CRDC-CR-85034* (1985).

130. Radhakrishnan, T. Further studies on the temperature variation of the refractive index of crystals. *Proceedings of the Indian Academy of Sciences - Section A* **33,** 22–34 (1951).

131. De Palma, A. C. *et al.* Strain-dependent luminescence and piezoelectricity in monolayer transition metal dichalcogenides. *Journal of Vacuum Science & Technology B* **38** (2020).

132. Wei, Y., Wang, B., Wu, J., Yang, R. & Dunn, M. L. Bending Rigidity and Gaussian Bending Stiffness of Single-Layered Graphene. *Nano Letters* **13,** 26–30 (2013).

133. Muñoz, E., Singh, A. K., Ribas, M. A., Penev, E. S. & Yakobson, B. I. The ultimate diamond slab: GraphAne versus graphEne. *Diamond and Related Materials* **19,** 368–373 (2010).

134. Lee, H. & Park, J. Y. Height determination of single-layer graphene on mica at controlled humidity using atomic force microscopy. *Review of Scientific Instruments* **90,** 103702 (2019).

135. Yao, Y., Ren, L., Gao, S. & Li, S. Histogram method for reliable thickness measurements of graphene films using atomic force microscopy (AFM). *Journal of Materials Science & Technology* **33,** 815–820 (2017).

136. Alharbi, A. & Shahrjerdi, D. Electronic properties of monolayer tungsten disulfide grown by chemical vapor deposition. *Applied Physics Letters* **109,** 193502 (2016).

137. Pop, E., Varshney, V. & Roy, A. K. Thermal properties of graphene: Fundamentals and applications. *MRS Bulletin* **37,** 1273–1281 (2012).

138. Balandin, A. A. Thermal properties of graphene and nanostructured carbon materials. *Nature Materials* **10,** 569–581 (2011).

139. Sang, Y. *et al.* Measurement of Thermal Conductivity of Suspended and Supported Single-Layer WS2 Using Micro-photoluminescence Spectroscopy. *The Journal of Physical Chemistry C* **126,** 6637–6645 (2022).

140. Novoselov, K. S. *et al.* Two-dimensional atomic crystals. *Proceedings of the National Academy of Sciences* **102,** 10451–10453 (2005).

141. Novoselov, K. S. *et al.* Electric Field Effect in Atomically Thin Carbon Films. *Science* **306,** 666–669 (2004).

142. Cooper, D. R. *et al.* Experimental Review of Graphene. *International Scholarly Research Notices* **2012,** 501686 (2012).

143. Lee, C., Wei, X., Kysar, J. W. & Hone, J. Measurement of the Elastic Properties and Intrinsic Strength of Monolayer Graphene. *Science* **321,** 385–388 (2008).

144. Novoselov, K. S. *et al.* Two-dimensional gas of massless Dirac fermions in graphene. *Nature* **438,** 197–200 (2005).

145. Mak, K. F., Lee, C., Hone, J., Shan, J. & Heinz, T. F. Atomically thin MoS(2): a new direct-gap semiconductor. *Phys Rev Lett* **105,** 136805 (2010).

146. Wang, Q. H., Kalantar-Zadeh, K., Kis, A., Coleman, J. N. & Strano, M. S. Electronics and optoelectronics of two-dimensional transition metal dichalcogenides. *Nature Nanotechnology* **7,** 699–712 (2012).

147. Fortin, E. & Sears, W. M. Photovoltaic effect and optical absorption in MoS2. *J. Phys. Chem. Solids* **43,** 881–884 (1982).

148. Lee, H. S. *et al.* MoS2 Nanosheet Phototransistors with Thickness-Modulated Optical Energy Gap. *Nano Letters* **12,** 3695–3700 (2012).

149. Mak, K. F., He, K., Shan, J. & Heinz, T. F. Control of valley polarization in monolayer MoS2 by optical helicity. *Nature Nanotechnoly* **7,** 494–498 (2012).

150. Xu, X., Yao, W., Xiao, D. & Heinz, T. F. Spin and pseudospins in layered transition metal dichalcogenides. *Nature Physics* **10,** 343–350 (2014).

151. Cao, T. *et al.* Valley-selective circular dichroism of monolayer molybdenum disulphide. *Nat Commun* **3,** 887 (2012).

152. Splendiani, A. *et al.* Emerging photoluminescence in monolayer MoS2. *Nano Lett* **10,** 1271–1275 (2010).

153. Roldán, R., Castellanos-Gomez, A., Cappelluti, E. & Guinea, F. Strain engineering in semiconducting two-dimensional crystals. *Journal of Physics: Condensed Matter* **27,** 313201 (2015).

154. Hosseini, M., Elahi, M., Pourfath, M. & Esseni, D. Strain induced mobility modulation in single-layer MoS2. *Journal of Physics D: Applied Physics* **48,** 375104 (2015).

155. Yu, S., Xiong, H. D., Eshun, K., Yuan, H. & Li, Q. Phase transition, effective mass and carrier mobility of MoS2 monolayer under tensile strain. *Applied Surface Science* **325,** 27–32 (2015).

156. Desai, S. B. *et al.* Strain-Induced Indirect to Direct Bandgap Transition in Multilayer WSe2. *Nano Letters* **14,** 4592–4597 (2014).

157. Dhakal, K. P. *et al.* Local Strain Induced Band Gap Modulation and Photoluminescence Enhancement of Multilayer Transition Metal Dichalcogenides. *Chemistry of Materials* **29,** 5124–5133 (2017).

158. Wang, P.-X. *et al.* Structural Distortion and Bandgap Increase of Two-Dimensional Perovskites Induced by Trifluoromethyl Substitution on Spacer Cations. *The Journal of Physical Chemistry Letters* **11,** 10144–10149 (2020).

159. Wang, G. *et al.* Bending of Multilayer van der Waals Materials. *Phys. Rev. Lett.* **123,** 116101 (11 2019).

160. Kaushik, V., Ahmad, M., Das, P. & Mehta, B. Understanding the Role of 2D Nature on the Junction Properties in WS2 Layers; Effect of AFM Tip Induced Loading Force on Spatially Varying Contact. *Surfaces and Interfaces* **24,** 101131 (2021).

161. Mbayachi, V. B. *et al.* Graphene synthesis, characterization and its applications: A review. *Results in Chemistry* **3,** 100163 (2021).

162. Momma, K. & Izumi, F. *VESTA3* for three-dimensional visualization of crystal, volumetric and morphology data. *Journal of Applied Crystallography* **44,** 1272–1276 (2011).

163. Lv, R. *et al.* Transition metal dichalcogenides and beyond: synthesis, properties, and applications of single- and few-layer nanosheets. *Acc Chem Res* **48,** 56–64 (2015).

164. Kolobov, A. V. & Tominaga, J. *Two-Dimensional Transition-Metal Dichalcogenides* (Springer, 2016).

165. Novoselov, K. S. *et al.* Two-dimensional atomic crystals. *Proceedings of the National Academy of Sciences of the United States of America* **102,** 10451–10453 (2005).

166. Bosi, M. Growth and synthesis of mono and few-layers transition metal dichalcogenides by vapour techniques: a review. *RSC Adv.* **5,** 75500–75518 (92 2015).

167. Lu, G., Yu, K., Wen, Z. & Chen, J. Semiconducting graphene: converting graphene from semimetal to semiconductor. *Nanoscale* **5,** 1353–1368 (4 2013).

168. Balandin, A. A. *et al.* Superior Thermal Conductivity of Single-Layer Graphene. *Nano Letters* **8,** 902–907 (2008).

169. Zhang, Y., Tan, Y.-W., Stormer, H. L. & Kim, P. Experimental observation of the quantum Hall effect and Berry's phase in graphene. *Nature* **438,** 201–204 (2005).

170. Ohno, Y., Maehashi, K. & Matsumoto, K. Label-Free Biosensors Based on Aptamer-Modified Graphene Field-Effect Transistors. *Journal of the American Chemical Society* **132,** 18012–18013 (2010).

171. Mao, S., Lu, G., Yu, K., Bo, Z. & Chen, J. Specific Protein Detection Using Thermally Reduced Graphene Oxide Sheet Decorated with Gold Nanoparticle-Antibody Conjugates. *Advanced Materials* **22,** 3521–3526 (2010).

172. Stankovich, S. *et al.* Graphene-based composite materials. *Nature* **442,** 282–286 (2006).

173. Ramanathan, T. *et al.* Functionalized graphene sheets for polymer nanocomposites. *Nature Nanotechnology* **3,** 327–331 (2008).

174. Semenov, Y. G., Kim, K. W. & Zavada, J. M. Spin field effect transistor with a graphene channel. *Applied Physics Letters* **91,** 153105 (2007).

175. Li, X., Wang, X., Zhang, L., Lee, S. & Dai, H. Chemically Derived, Ultrasmooth Graphene Nanoribbon Semiconductors. *Science* **319,** 1229–1232 (2008).

176. Chernikov, A. *et al.* Exciton binding energy and nonhydrogenic Rydberg series in monolayer WS(2). *Phys Rev Lett* **113,** 076802 (2014).

177. Ugeda, M. M. *et al.* Giant bandgap renormalization and excitonic effects in a monolayer transition metal dichalcogenide semiconductor. *Nat Mater* **13,** 1091–1095 (2014).

178. He, K. *et al.* Tightly bound excitons in monolayer WSe(2). *Phys Rev Lett* **113,** 026803 (2014).

179. Kittle, C. *Introduction to Solid State Physics* 7th edition (Wiley, 1996).

180. Wang, Q. H., Kalantar-Zadeh, K., Kis, A., Coleman, J. N. & Strano, M. S. Electronics and optoelectronics of two-dimensional transition metal dichalcogenides. *Nat Nanotechnol* **7,** 699–712 (2012).

181. Gutierrez, H. R. *et al.* Extraordinary room-temperature photoluminescence in triangular WS2 monolayers. *Nano Lett* **13,** 3447–3454 (2013).

182. Li, Y. *et al.* Accurate identification of layer number for few-layer WS2 and WSe2 via spectroscopic study. *Nanotechnology* **29,** 124001 (2018).

183. Zeng, H. *et al.* Optical signature of symmetry variations and spin-valley coupling in atomically thin tungsten dichalcogenides. *Sci Rep* **3,** 1608 (2013).

184. Mueller, T. & Malic, E. Exciton physics and device application of two-dimensional transition metal dichalcogenide semiconductors. *npj 2D Materials and Applications* **2** (2018).

185. Chernikov, A. *et al.* Exciton Binding Energy and Nonhydrogenic Rydberg Series in Monolayer WS_2. *Phys. Rev. Lett.* **113,** 076802 (7 2014).

186. Kim, M. S. *et al.* Biexciton Emission from Edges and Grain Boundaries of Triangular WS2 Monolayers. *Acs Nano* **10,** 2399–2405 (2016).

187. Srivastava, A. *et al.* Optically active quantum dots in monolayer WSe2. *Nature Nanotechnology* **10,** 491–496 (2015).

188. He, Y. M. *et al.* Single quantum emitters in monolayer semiconductors. *Nature Nanotechnology* **10,** 497–502 (2015).

189. Tonndorf, P. *et al.* Single-photon emission from localized excitons in an atomically thin semiconductor. *Optica* **2,** 347–352 (2015).

190. Fang, H. *et al.* Strong interlayer coupling in van der Waals heterostructures built from single-layer chalcogenides. *Proceedings of the National Academy of Sciences of the United States of America* **111,** 6198–6202 (2014).

191. Rivera, P. *et al.* Observation of long-lived interlayer excitons in monolayer MoSe2-WSe2 heterostructures. *Nature Communications* **6** (2015).

192. Xiao, D., Liu, G. B., Feng, W., Xu, X. & Yao, W. Coupled spin and valley physics in monolayers of MoS2 and other group-VI dichalcogenides. *Phys Rev Lett* **108,** 196802 (2012).

193. Castellanos-Gomez, A. *et al.* Local strain engineering in atomically thin MoS2. *Nano Lett* **13,** 5361–5366 (2013).

194. Castellanos-Gomez, A., van der Zant, H. S. J. & Steele, G. A. Folded MoS2 layers with reduced interlayer coupling. *Nano Research* **7,** 572–578 (2014).

195. Lee, J. *et al.* Switchable, Tunable, and Directable Exciton Funneling in Periodically Wrinkled WS2. *Nano Letters* **21,** 43–50 (2021).

196. Conley, H. J. *et al.* Bandgap engineering of strained monolayer and bilayer MoS2. *Nano Lett* **13,** 3626–3630 (2013).

197. Island, J. O. *et al.* Precise and reversible band gap tuning in single-layer MoSe2 by uniaxial strain. *Nanoscale* **8,** 2589–2593 (5 2016).

198. Lloyd, D. *et al.* Band Gap Engineering with Ultralarge Biaxial Strains in Suspended Monolayer MoS2. *Nano Lett* **16,** 5836–5841 (2016).

199. Hui, Y. Y. *et al.* Exceptional Tunability of Band Energy in a Compressively Strained Trilayer MoS2 Sheet. *ACS Nano* **7,** 7126–7131 (2013).

200. Zhang, Q., Cheng, Y., Gan, L.-Y. & Schwingenschlögl, U. Giant valley drifts in uniaxially strained monolayer MoS_2. *Phys. Rev. B* **88,** 245447 (24 2013).

201. Maniadaki, A., Kopidakis, G. & Remediakis, I. Strain engineering of electronic properties of transition metal dichalcogenide monolayers. *Solid State Communications* **227** (2015).

202. Wang, Y. *et al.* Strain-induced direct–indirect bandgap transition and phonon modulation in monolayer WS2. *Nano Research* **8,** 2562–2572 (2015).

203. Yang, S. X. *et al.* Tuning the Optical, Magnetic, and Electrical Properties of ReSe2 by Nanoscale Strain Engineering. *Nano Letters* **15,** 1660–1666 (2015).

204. Li, Z. *et al.* Efficient strain modulation of 2D materials via polymer encapsulation. *Nature Communications* **11,** 1151 (2020).

205. Xu, K., Cao, P. & Heath, J. R. Scanning Tunneling Microscopy Characterization of the Electrical Properties of Wrinkles in Exfoliated Graphene Monolayers. *Nano Letters* **9,** 4446–4451 (2009).

206. He, X. *et al.* Shear strain induced modulation to the transport properties of graphene. *Applied Physics Letters* **105,** 083108 (2014).

207. Ni, Z. H. *et al.* Uniaxial Strain on Graphene: Raman Spectroscopy Study and Band-Gap Opening. *ACS Nano* **2,** 2301–2305 (2008).

208. Cocco, G., Cadelano, E. & Colombo, L. Gap opening in graphene by shear strain. *Phys. Rev. B* **81,** 241412 (24 2010).

209. Si, C., Sun, Z. & Liu, F. Strain engineering of graphene: a review. *Nanoscale* **8,** 3207–3217 (6 2016).

210. Kuila, T. *et al.* Recent advances in graphene-based biosensors. *Biosensors and Bioelectronics* **26,** 4637–4648 (2011).

211. Fakih, I. *et al.* High resolution potassium sensing with large-area graphene field-effect transistors. *Sensors and Actuators B: Chemical* **291,** 89–95 (2019).

212. Beijersbergen, M. W., Coerwinkel, R. P. C., Kristensen, M. & Woerdman, J. P. Helical-wavefront laser beams produced with a spiral phaseplate. *Optical Communications* **112,** 321–327 (1994).

213. Turnbull, G. A., Robertson, D. A., Smith, G. M., Allen, L. & Padgett, M. J. The generation of free-space Laguerre-Gaussian modes at millimetre-wave frequencies by use of a spiral phaseplate. *Optical Communications* **127,** 183–188 (1996).

214. Kotlyar, V., Kovalev, A., Porfirev, A. & Kozlova, E. Orbital angular momentum of a laser beam behind an off-axis spiral phase plate. *Opt Lett* **44,** 3673–3676 (2019).

215. Arlt, J. Handedness and azimuthal energy flow of optical vortex beams. *Journal of Modern Optics* **50,** 1573–1580 (2003).

216. Heckenberg, N. R., McDuff, R., Smith, C. P. & White, A. G. Generation of optical phase singularities by computer-generated holograms. *Opt. Lett.* **17,** 221–223 (1992).

217. Bazhenov, V. I., Vasnetsov, M. V. & Soskin, M. S. Laser beams with wave front screw dislocations. *Pisma v Zhurnal Eksperimentalnoi i Teoreticheskoi Fiziki* **52,** 1037–1039 (1990).

218. Hashiyada, S. & Tanaka, Y. Y. Rapid modulation of left- and right-handed optical vortices for precise measurements of helical dichroism. *Review of Scientific Instruments* **95,** 053101 (2024).

219. Smith, E. & Dent, G. *Modern Raman Spectroscopy: A Practical Approach* (John Wiley & Sons, Incorporated, Hoboken, UNITED KINGDOM, 2005).

220. Zhang, X., Tan, Q.-H., Wu, J.-B., Shi, W. & Tan, P.-H. Review on the Raman spectroscopy of different types of layered materials. *Nanoscale* **8,** 6435–6450 (12 2016).

221. Yoon, D. & Cheong, H. in *Raman Spectroscopy for Nanomaterials Characterization* (ed Kumar, C. S. S. R.) 191–214 (Springer Berlin Heidelberg, Berlin, Heidelberg, 2012).

222. Wu, J.-B., Lin, M.-L., Cong, X., Liu, H.-N. & Tan, P.-H. Raman spectroscopy of graphene-based materials and its applications in related devices. *Chem. Soc. Rev.* **47,** 1822–1873 (5 2018).

223. Koh, Y. K., Bae, M.-H., Cahill, D. G. & Pop, E. Reliably Counting Atomic Planes of Few-Layer Graphene (n > 4). *ACS Nano* **5,** 269–274 (2011).

224. Calizo, I., Bejenari, I., Rahman, M., Liu, G. & Balandin, A. A. Ultraviolet Raman microscopy of single and multilayer graphene. *Journal of Applied Physics* **106,** 043509 (2009).

225. Berciaud, S., Ryu, S., Brus, L. E. & Heinz, T. F. Probing the Intrinsic Properties of Exfoliated Graphene: Raman Spectroscopy of Free-Standing Monolayers. *Nano Letters* **9,** 346–352 (2009).

226. Das, A. *et al.* Monitoring dopants by Raman scattering in an electrochemically top-gated graphene transistor. *Nature Nanotechnology* **3,** 210–215 (2008).

227. Yoon, D., Son, Y.-W. & Cheong, H. Strain-Dependent Splitting of the Double-Resonance Raman Scattering Band in Graphene. *Phys. Rev. Lett.* **106,** 155502 (15 2011).

228. Frank, O. *et al.* Compression Behavior of Single-Layer Graphenes. *ACS Nano* **4,** 3131–3138 (2010).

229. Ferrari, A. C. & Basko, D. M. Raman spectroscopy as a versatile tool for studying the properties of graphene. *Nature Nanotechnology* **8,** 235–246 (2013).

230. Chen, W. *et al.* Controllable Fabrication of Large-Area Wrinkled Graphene on a Solution Surface. *ACS Applied Materials & Interfaces* **8,** 10977–10984 (2016).

231. Binnig, G., Quate, C. F. & Gerber, C. Atomic Force Microscope. *Phys. Rev. Lett.* **56,** 930–933 (9 1986).

232. Surwade, S. P., Li, Z. & Liu, H. Thermal Oxidation and Unwrinkling of Chemical Vapor Deposition-Grown Graphene. *The Journal of Physical Chemistry C* **116,** 20600–20606 (2012).

233. Zhao, S., Surwade, S. P., Li, Z. & Liu, H. Photochemical oxidation of CVD-grown single layer graphene. *Nanotechnology* **23,** 355703 (2012).

234. McCreary, K. M. *et al.* The Effect of Preparation Conditions on Raman and Photoluminescence of Monolayer WS2. *Sci Rep* **6,** 35154 (2016).

235. He, K., Poole, C., Mak, K. F. & Shan, J. Experimental demonstration of continuous electronic structure tuning via strain in atomically thin MoS2. *Nano Lett* **13,** 2931–2936 (2013).

236. Dai, Z., Liu, L. & Zhang, Z. Strain Engineering of 2D Materials: Issues and Opportunities at the Interface. *Advanced Materials* **31,** 1805417 (2019).

237. Mak, K. F. *et al.* Tightly bound trions in monolayer MoS2. *Nature Materials* **12,** 207–211 (2013).

238. Chowdhury, T. *et al.* Modulation of trion and exciton formation in monolayer WS2 by dielectric and substrate engineering. *2D Materials* **8,** 045032 (2021).

239. Kumar, R. *et al.* Observation of positive trions in α-MoO3/MoS2 van der Waals heterostructures. *Nanoscale* **15,** 12358–12365 (29 2023).

240. Zhu, W. *et al.* Structure and Electronic Transport in Graphene Wrinkles. *Nano Letters* **12,** 3431–3436 (2012).

241. Zhang, D., Li, Z., Klausen, L. H., Li, Q. & Dong, M. Friction behaviors of two-dimensional materials at the nanoscale. *Materials Today Physics* **27,** 100771 (2022).

242. Boyd, D. A. *et al.* Single-step deposition of high-mobility graphene at reduced temperatures. *Nature Communications* **6,** 6620 (2015).

243. Balois-Oguchi, M. V. *et al.* Probing Strain and Doping along a Graphene Wrinkle Using Tip-Enhanced Raman Spectroscopy. *The Journal of Physical Chemistry C* **127,** 5982–5990 (2023).

244. Alexeev, E., Moger, J. & Hendry, E. Photo-induced doping and strain in exfoliated graphene. *Applied Physics Letters* **103,** 151907 (2013).

245. Wang, W., Yang, S. & Wang, A. Observation of the unexpected morphology of graphene wrinkle on copper substrate. *Scientific Reports* **7,** 8244 (2017).

246. Zhang, Y. *et al.* Controlled Growth of High-Quality Monolayer WS2 Layers on Sapphire and Imaging Its Grain Boundary. *ACS Nano* **7,** 8963–8971 (2013).

247. Wei, K., Liu, Y., Yang, H., Cheng, X. A. & Jiang, T. Large range modification of exciton species in monolayer WS2. *Applied Optics* **55,** 6251–6255 (2016).

248. Deng, K. & Ko, W. H. A study of static friction between silicon and silicon compounds. *Journal of Micromechanics and Microengineering* **2,** 14 (1992).

249. Riesz, C. & Weber, H. Friction and wear of sapphire. *Wear* **7,** 67–81 (1964).

250. Liu, K. *et al.* Elastic Properties of Chemical-Vapor-Deposited Monolayer MoS2, WS2, and Their Bilayer Heterostructures. *Nano Letters* **14,** 5097–5103 (2014).

251. Cao, Y. *et al.* Enhancing and quantifying spatial homogeneity in monolayer WS2. *Scientific Reports* **11,** 14831 (2021).

252. Andrei, E. Y. & MacDonald, A. H. Graphene bilayers with a twist. *Nature Materials* **19,** 1265–1275 (2020).

253. Liao, M. *et al.* Precise control of the interlayer twist angle in large scale MoS2 homostructures. *Nature Communications* **11,** 2153 (2020).

254. Liu, K. *et al.* Evolution of interlayer coupling in twisted molybdenum disulfide bilayers. *Nature Communications* **5,** 4966 (2014).

255. Lin, M.-L. *et al.* Moiré Phonons in Twisted Bilayer MoS2. *ACS Nano* **12,** 8770–8780 (2018).

256. Jin, C. *et al.* Observation of moiré excitons in WSe2/WS2 heterostructure superlattices. *Nature* **567,** 76–80 (2019).

257. Poynting, J. H. The wave motion of a revolving shaft, and a suggestion as to the angular momentum in a beam of circularly polarised light. *Proceedings of the Royal Society of London Series a-Containing Papers of a Mathematical and Physical Character* **82,** 560–567 (1909).

258. Rouxel, J. R. *et al.* Hard X-ray helical dichroism of disordered molecular media. *Nature Photonics* **16,** 570–574 (2022).

259. Bégin, J.-L. *et al.* Nonlinear helical dichroism in chiral and achiral molecules. *Nature Photonics* **17,** 82–88 (2023).

260. Cao, Y. *et al.* Photonic Orbital Angular Momentum Dichroism on Three-Dimensional Chiral Oligomers. *ACS Photonics* **10,** 1873–1881 (2023).

261. Greenfield, N. J. Using circular dichroism spectra to estimate protein secondary structure. *Nature Protocols* **1,** 2876–2890 (2006).

262. Whitmore, L. & Wallace, B. A. Protein secondary structure analyses from circular dichroism spectroscopy: Methods and reference databases. *Biopolymers* **89,** 392–400 (2008).

263. Miyahara, T. & Nakatsuji, H. Indicator of the Stacking Interaction in the DNA Double-Helical Structure: ChiraSac Study. *The Journal of Physical Chemistry A* **119,** 8269–8278 (2015).

264. Bishop, G. R. & Chaires, J. B. Characterization of DNA Structures by Circular Dichroism. *Current Protocols in Nucleic Acid Chemistry* **11,** 7.11.1–7.11.8 (2002).

265. Zhang, H. *et al.* In situ monitoring of molecular aggregation using circular dichroism. *Nature communications* **9,** 4961 (2018).

266. Knoppe, S. & Bürgi, T. Chirality in Thiolate-Protected Gold Clusters. *Accounts of Chemical Research* **47,** 1318–1326 (2014).

267. Dierking, I. Chiral Liquid Crystals: Structures, Phases, Effects. *Symmetry* **6,** 444–472 (2014).

268. Zhang, S., Genov, D. A., Wang, Y., Liu, M. & Zhang, X. Plasmon-Induced Transparency in Metamaterials. *Phys. Rev. Lett.* **101,** 047401 (4 2008).

269. Limonov, M. F., Rybin, M. V., Poddubny, A. N. & Kivshar, Y. S. Fano resonances in photonics. *Nature Photonics* **11,** 543–554 (2017).

270. Luk'yanchuk, B. *et al.* The Fano resonance in plasmonic nanostructures and metamaterials. *Nature Materials* **9,** 707–715 (2010).

271. Hwang, Y., Lee, S., Kim, S., Lin, J. & Yuan, X.-C. Effects of Fano Resonance on Optical Chirality of Planar Plasmonic Nanodevices. *ACS Photonics* **5,** 4538–4544 (2018).

272. Gu, J. *et al.* Active control of electromagnetically induced transparency analogue in terahertz metamaterials. *Nature Communications* **3,** 1151 (2012).

273. Smith, D. D., Chang, H., Fuller, K. A., Rosenberger, A. T. & Boyd, R. W. Coupled-resonator-induced transparency. *Phys. Rev. A* **69,** 063804 (6 2004).

274. Pendry, J. B. A Chiral Route to Negative Refraction. *Science* **306,** 1353–1355 (2004).

275. Plum, E. *et al.* Metamaterial with negative index due to chirality. *Phys. Rev. B* **79,** 035407 (3 2009).

276. Zhou, J. *et al.* Negative refractive index due to chirality. *Phys. Rev. B* **79,** 121104 (12 2009).

277. Zhang, S. *et al.* Negative Refractive Index in Chiral Metamaterials. *Phys. Rev. Lett.* **102,** 023901 (2 2009).

278. Ma, C. *et al.* All-optical tunable slow-light based on an analogue of electromagnetically induced transparency in a hybrid metamaterial. *Nanoscale Adv.* **3,** 5636–5641 (19 2021).

279. Raza, S. & Bozhevolnyi, S. I. Slow-light plasmonic metamaterial based on dressed-state analog of electromagnetically induced transparency. *Opt. Lett.* **40,** 4253–4256 (2015).

280. Anker, J. N. *et al.* Biosensing with plasmonic nanosensors. *Nature Materials* **7,** 442–453 (2008).

281. Liu, N. *et al.* Planar Metamaterial Analogue of Electromagnetically Induced Transparency for Plasmonic Sensing. *Nano Letters* **10,** 1103–1107 (2010).

282. Kabashin, A. V. *et al.* Plasmonic nanorod metamaterials for biosensing. *Nature Materials* **8,** 867–871 (2009).

283. Kelly, C. *et al.* Controlling Metamaterial Transparency with Superchiral Fields. *ACS Photonics* **5,** 535–543 (2018).

284. Boller, K.-J., Imamo ğlu, A. & Harris, S. E. Observation of electromagnetically induced transparency. *Phys. Rev. Lett.* **66,** 2593–2596 (20 1991).

285. Harris, S. E. Electromagnetically Induced Transparency. *Physics Today* **50,** 36–42 (1997).

286. Liu, N. *et al.* Plasmonic analogue of electromagnetically induced transparency at the Drude damping limit. *Nature Materials* **8,** 758–762 (2009).

287. Tassin, P. *et al.* Electromagnetically Induced Transparency and Absorption in Metamaterials: The Radiating Two-Oscillator Model and Its Experimental Confirmation. *Phys. Rev. Lett.* **109,** 187401 (18 2012).

288. Yu, C.-L. *et al.* High Circular Polarized Nanolaser with Chiral Gammadion Metal Cavity. *Scientific Reports* **10,** 7880 (2020).

289. Passaseo, A., Esposito, M., Cuscunà, M. & Tasco, V. Materials and 3D Designs of Helix Nanostructures for Chirality at Optical Frequencies. *Advanced Optical Materials* **5,** 1601079 (2017).

290. Schäferling, M., Dregely, D., Hentschel, M. & Giessen, H. Tailoring Enhanced Optical Chirality: Design Principles for Chiral Plasmonic Nanostructures. *Phys. Rev. X* **2,** 031010 (3 2012).

291. Wu, A., Tanaka, Y. Y. & Shimura, T. Giant chiroptical response of twisted metal nanorods due to strong plasmon coupling. *APL Photonics* **6,** 126104 (2021).

292. Tang, Y., Sun, L. & Cohen, A. E. Chiroptical hot spots in twisted nanowire plasmonic oscillators. *Applied Physics Letters* **102,** 043103 (2013).

293. Wu, Z. & Zheng, Y. Moiré Chiral Metamaterials. *Advanced Optical Materials* **5,** 1700034 (2017).

294. Kuroki, S., Ishida, T. & Tatsuma, T. Effects of plasmon coupling on circular dichroism of chiral nanoparticle arrays. *The Journal of Chemical Physics* **160,** 064702 (2024).

295. Cui, N. *et al.* High Electric Field-Enhanced Terahertz Metamaterials with Bowtie Triangle Rings: Modeling, Mechanism, and Carbohydrate Antigen 125 Detection. *The Journal of Physical Chemistry C* **125,** 19374–19381 (2021).

296. Tang, Y. & Cohen, A. E. Enhanced Enantioselectivity in Excitation of Chiral Molecules by Superchiral Light. *Science* **332,** 333–336 (2011).

297. Kakkar, T. *et al.* Superchiral near fields detect virus structure. *Light: Science & Applications* **9,** 195 (2020).

298. Li, W. *et al.* Circularly polarized light detection with hot electrons in chiral plasmonic metamaterials. *Nature Communications* **6,** 8379 (2015).

299. Mohammadi, E. *et al.* Accessible Superchiral Near-Fields Driven by Tailored Electric and Magnetic Resonances in All-Dielectric Nanostructures. *ACS Photonics* **6,** 1939–1946 (2019).

300. Arikawa, T. *et al.* Transfer of orbital angular momentum of light to plasmonic excitations in metamaterials. *Science Advances* **6,** eaay1977 (2020).

301. Liu, S. *et al.* Tailoring Optical Vortical Dichroism with Stereometamaterials. *Laser & Photonics Reviews* **16,** 2100518 (2022).

302. Gadegaard, N., Mosler, S. & Larsen, N. B. Biomimetic Polymer Nanostructures by Injection Molding. *Macromolecular Materials and Engineering* **288,** 76–83 (2003).

303. Karimullah, A. S. *et al.* Disposable Plasmonics: Plastic Templated Plasmonic Metamaterials with Tunable Chirality. *Advanced Materials* **27,** 5610–5616 (2015).

304. Marrucci, L., Manzo, C. & Paparo, D. Optical Spin-to-Orbital Angular Momentum Conversion in Inhomogeneous Anisotropic Media. *Phys. Rev. Lett.* **96,** 163905 (16 2006).

305. Fu, S. & Gao, C. *Optical Vortex Beams: Fundamentals and Techniques* (Springer Nature Singapore, Singapore, 2023).

306. Rubano, A., Cardano, F., Piccirillo, B. & Marrucci, L. Q-plate technology: a progress review [Invited]. *J. Opt. Soc. Am. B* **36,** D70–D87 (2019).

307. Kong, F. *et al.* Controlling the orbital angular momentum of high harmonic vortices. *Nature Communications* **8,** 14970 (2017).

308. Sato, K. Measurement of Magneto-Optical Kerr Effect Using Piezo-Birefringent Modulator. *Japanese Journal of Applied Physics* **20,** 2403 (1981).

309. Rakić, A. D., Djurišić, A. B., Elazar, J. M. & Majewski, M. L. Optical properties of metallic films for vertical-cavity optoelectronic devices. *Appl. Opt.* **37,** 5271–5283 (1998).

310. Sultanova, N., Kasarova, S. & Nikolov, I. Dispersion Properties of Optical Polymers. *ACTA PHYSICA POLONICA A* **116,** 585–587 (2009).

311. Richards, B. & Wolf, E. Proceedings of the Royal Society A: Mathematical, Physical and Engineering Sciences. *Proceedings of the Royal Society of London. Series A. Mathematical and Physical Sciences* **253** (1959).

312. Zhan, Q. Cylindrical vector beams: from mathematical concepts to applications. *Adv. Opt. Photon.* **1,** 1–57 (2009).

313. Zhan, Q. *Vectorial Optical Fields* (WORLD SCIENTIFIC, 2014).

314. Ganic, D., Gan, X. & Gu, M. Focusing of doughnut laser beams by a high numerical-aperture objective in free space. *Opt. Express* **11,** 2747–2752 (2003).

315. Wu, Z., Chen, X., Wang, M., Dong, J. & Zheng, Y. High-Performance Ultrathin Active Chiral Metamaterials. *ACS Nano* **12,** 5030–5041 (2018).

316. Taubert, R., Hentschel, M., Kästel, J. & Giessen, H. Classical Analog of Electromagnetically Induced Absorption in Plasmonics. *Nano Letters* **12,** 1367–1371 (2012).

317. Tanaka, D. *et al.* Multipole Excitation of Localized Plasmon Resonance in Asymmetrically Coated Core–Shell Nanoparticles Using Optical Vortices. *Laser & Photonics Reviews* **18,** 2300536 (2024).

318. Sakai, K., Nomura, K., Yamamoto, T. & Sasaki, K. Excitation of Multipole Plasmons by Optical Vortex Beams. *Scientific Reports* **5,** 8431 (2015).

319. Courtial, J., Zambrini, R., Dennis, M. R. & Vasnetsov, M. Angular momentum of optical vortex arrays. *Opt. Express* **14,** 938–949 (2006).

320. Allen, L. & Padgett, M. Equivalent geometric transformations for spin and orbital angular momentum of light. *Journal of Modern Optics* **54,** 487–491 (2007).

321. Kravets, V. G., Kabashin, A. V., Barnes, W. L. & Grigorenko, A. N. Plasmonic Surface Lattice Resonances: A Review of Properties and Applications. *Chemical Reviews* **118,** 5912–5951 (2018).

322. Wu, T., Zhang, W., Wang, R. & Zhang, X. A giant chiroptical effect caused by the electric quadrupole. *Nanoscale* **9,** 5110–5118 (16 2017).

323. Wang, H. & Zhao, Y. Plasmon-enhanced chiral absorption through electric dipole–electric quadrupole interaction. *Journal of Optics* **26,** 085002 (2024).

324. Efrima, S. Raman optical activity of molecules adsorbed on metal surfaces: Theory. *The Journal of Chemical Physics* **83,** 1356–1362 (1985).

325. Tullius, R. *et al.* "Superchiral" Spectroscopy: Detection of Protein Higher Order Hierarchical Structure with Chiral Plasmonic Nanostructures. *Journal of the American Chemical Society* **137,** 8380–8383 (2015).

326. Brenner, T. M., Egger, D. A., Kronik, L., Hodes, G. & Cahen, D. Hybrid organic—inorganic perovskites: low-cost semiconductors with intriguing charge-transport properties. *Nature Reviews Materials* **1,** 15007 (2016).

Appendix A

MATLAB code to generate Laguerre-Gaussian beams

The following code generates plots of Laguerre-Gaussian beams in MATLAB by using the expression in cylindrical coordinates.

```
clear all
close all

%This code plots OAM beams as a function of m and p, where m is the
   orbtal angular momentum
 %and p+1 is the number of concentric rings, using the LG beam
    equation in
 %cylindrical coordinates

%Paula Laborda, 20/4/2022


%% OAM beam parameters

m = -2;
p = 0;

%m: orbtal angular momentum
```

```
%p+1: number of concentric rings

%Cylindrical coordinates
%z = height above xy plane
%rho: radial coordinate
%phi: azimuth

%% Initial parameters

N = 800;

resolution=150;
resolution_rho = 15;
if m==0
    resolution_rho = 7;
   resolution_phi = 60;
else
    resolution_rho = 15;
resolution_phi = 10000;
end
step=2*pi/resolution;
rho=linspace(0, N, resolution_rho);
phi=linspace(-pi,pi, resolution_phi);
lambda = 400; %wavelength
k = 2*pi/lambda; %wavevector
w_0 = lambda/2; %beam waist
z_R = pi*w_0^(2)/lambda; %Rayleigh range
z=0; %z at the focal point
beam_waist = @(w_0, z, z_R) sqrt(w_0.^2*(1+(z./z_R).^2));
chi_function = @(a,b) atan(a./b);
R_z = @(z_R,z) (z_R.^(2)+z.^(2))./z; %rayleigh range

%% Normalization constant
%From Gotte:
```

```
C_mp = sqrt((2.^((abs(m)+1)).*(factorial(p))/(pi.*factorial(p+abs(m)))
    ));%normalization constant for Laguerre-Gaussian mode

%C_mp = sqrt(2/(pi*factorial(m)*factorial(p)))*min(m,p)
%C_mp = sqrt((2*(factorial(p))/(pi.*factorial(p+abs(m)))));%
    normalization constant for Laguerre-Gaussian mode
%C_mp=1;


%% Laguerre Polynomial

syms f(u) g(u) h(u) L_polynomial(u)


f(u) = exp(-u);
g(u) = exp(u);
h(u) = diff(f(u)*u^(min(abs(m),p)+abs(m-p)),min(abs(m),p));
L_polynomial(u) = (u^(-abs(m-p))*h(u)*g(u))/factorial(min(abs(m),p));

%% Laguerre-Gaussian beam

[Rho,Phi]=meshgrid(rho,phi(1:end));



%From Gotte:
LG = @(z, rho, phi) C_mp./(sqrt(beam_waist(w_0, z, z_R))).*(rho.*sqrt
    (2)./beam_waist(w_0, z, z_R)).^(abs(m)).*exp(-rho.^(2)./(beam_waist
    (w_0, z, z_R)).^2).*double(L_polynomial(2.*rho.^(2)./(beam_waist(
    w_0, z, z_R)).^2)).*exp(-1i.*k.*(rho.^(2)./(2.*(R_z(z_R,z))))).*exp
    (1i.*(m).*phi).*exp(-1i.*(abs(m)+2*p+1).*chi_function(z,z_R));


%From comsol:
```

```
%LG = @(z, rho, phi) C_mp.*w_0./(beam_waist(w_0, z, z_R)).*(rho.*sqrt
    (2)./beam_waist(w_0, z, z_R)).^(m).*exp(-rho.^(2)./(beam_waist(w_0,
     z, z_R)).^2).*double(L_polynomial(2.*rho.^(2)./(beam_waist(w_0, z,
     z_R)).^2)).*exp(-1i.*k.*(rho.^(2).*z./(2.*(R_z(z_R,z))))).*exp(-1i
    .*(m).*phi).*exp(-1i.*(m+2*p+1).*chi_function(z,z_R)).*(-1).^(min(m
    ,p));



LH_beam_2D = LG(z, Rho, Phi);

%Conversion from cylindrical coordinates to cartesian coordinates
[X,Y] = pol2cart(Phi,Rho);



%Intensity distribution
figure()
surf(X,Y,abs(LH_beam_2D).^2)
title('Intensity distribution')


%Phase

figure()

angle_part = angle(LH_beam_2D);

if m~=0
max_value=max(max(angle_part));
min_value=min(min(angle_part));

angle_part((angle_part >  3.1412) | (angle_part < -3.1412)) = NaN;
end
```

```
S=surf(X,Y,angle_part)
%zlim([-pi,pi])
title('Phase')

if m~=0
S.EdgeColor = 'none';
hold on
spacing = 10;  % play around so it fits the size of your data set
for i = 1: spacing:length(X(:,1))
    plot3(X(i,:), Y(i,:), angle_part(i,:),'-k');
    plot3(X(i,:), Y(i,:), angle_part(i,:),'-k');
end
hold off
end



%Phasefront
figure()
C = X;
W1=surf(X,Y, angle_part,C)
hold on
W2=surf(X,Y,angle_part+2*pi,C)
W3=surf(X,Y,angle_part+4*pi,C)
W4=surf(X,Y,angle_part+6*pi,C)
hold off
title('wavefront')
colormap gray;
% colormap hot;

%load('Blue_colormap.mat')
%colormap(gca, Blue);
```

```
%shading interp

if m~=0
W1.EdgeColor = 'none';
W2.EdgeColor = 'none';
W3.EdgeColor = 'none';
W4.EdgeColor = 'none';

hold on
spacing = 200;  % play around so it fits the size of your data set
for i = 1: spacing:length(X(:,1))
    plot3(X(i,:), Y(i,:), angle_part(i,:),'-k');
    plot3(X(i,:), Y(i,:), angle_part(i,:)+2*pi,'-k');
    plot3(X(i,:), Y(i,:), angle_part(i,:)+4*pi,'-k');
    plot3(X(i,:), Y(i,:), angle_part(i,:)+6*pi,'-k');
end



spacing2=2
for i = 1: spacing2:length(X(1,:))
    plot3(X(:,i), Y(:,i), angle_part(:,i),'-k');
    plot3(X(:,i), Y(:,i), angle_part(:,i)+2*pi,'-k');
    plot3(X(:,i), Y(:,i), angle_part(:,i)+4*pi,'-k');
    plot3(X(:,i), Y(:,i), angle_part(:,i)+6*pi,'-k');
end
end
s.CData = X.^2 + Y.^2;
set(gca,'visible','off')
%set(h,'edgecolor','r','facecolor',[.1 .9 .1])

xlabel('X');
ylabel('Y');
zlabel('Z');
```

As mentioned in Chapter 2, Laguerre-Gaussian beams can also be generated by

combining Hermite-Gaussian modes.

Mathematically, the combination of $h+j$ HG modes to yield LG modes of arbitrary order h and j is done as follows.[23]

$$LG_{hj}(x,y,z) = \sum_{t=0}^{h+j} i^t b(h,j,t) HG_{h+j-t,t}(x,y,z), \tag{A.1}$$

where $b(h,j,t)$ is a coefficient described in reference [23] and the term i^t shifts the HG beams to generate the LG beam. Now, the topological charge l and radial mode p are given by $l = h - j$ and $p = \min(h,j)$, respectively. The MATLAB code presented below uses equation A.1 and it was used to generate the images in Figures 2.3, 2.8 and 2.10.

```
close all
clear all

%Laguerre-Gaussian modes expressed as a combination of Hermite-
    Gaussian modes

% Orbital angular momentum: |n-l|
% Number of concentric rings: min(n,l)


%% Hermite-Gaussian beam parameters

lambda = 532; %wavelength in nm
N = 900;
%N=4500; %to visualize phase
resolution = 200; %number of data points
x=linspace(-N, N,resolution);
y=x;
[X,Y]=meshgrid(x,y);
n=2; %order in x for HG mode
l=1; %order in y for HG mode
plot_HG = 1; %1 if you want to plot all HG modes used in the script


%% Beam parameters

C_nl = sqrt(2/(pi*factorial(n)*factorial(l)))*2^(-(n+l)/2);
w_0 = lambda/2; %beam waist at focal point
k = 2*pi/lambda; %wavevector
z_R = pi*w_0^2/lambda; %Rayleigh range
z=0; %value along propagation axis
beam_waist = @(w_0, z, z_R) sqrt(w_0.^2*(1+(z./z_R).^2));
chi_function = @(a,b) atan(a./b);
```

```
%% Hermite Polynomial

syms f(u) g(u) h(u) H(u)

f(u) = exp(-u.^2);
g(u) = exp(u.^2);
h_x(u) = diff(f(u),n);
h_y(u) = diff(f(u),l);

H_x(u) = (-1)^n*g*h_x;
H_y(u) = (-1)^l*g*h_y;


%% Laguerre-Gaussian plot

LG_mode = 0;

for t=0:(n+l)

    C_nl = sqrt(2/(pi*factorial(n+l-t)*factorial(t)))*2^(-(n+l)/2); %
        normalization constant


    %Hermite polynomials
    syms f(u) g(u) h(u) H(u)

    f(u) = exp(-u.^2);
    g(u) = exp(u.^2);
    h_x(u) = diff(f(u),n+l-t);
    h_y(u) = diff(f(u),t);

    H_x(u) = (-1)^(n+l-t)*g*h_x;
    H_y(u) = (-1)^(t)*g*h_y;
```

```
    %Hermite-Gaussian beam function:
    HG_2D = @(x, y, z) C_nl./(beam_waist(w_0, z, z_R)).*exp(-1i*k*(x
        .^(2)+y.^(2))/(2.*((z_R^2+z.^2)/z))).*exp(-((y.^(2)+x.^(2))./
        beam_waist(w_0, z, z_R).^2)).*exp(-1i*(n+l+0.5).*chi_function(z
        ,z_R)).*double(H_x((sqrt(2).*x./beam_waist(w_0, z, z_R)))).*
        double(H_y((sqrt(2).*y./beam_waist(w_0, z, z_R))));

    HG_beam_2D = HG_2D(X,Y,z);
    jj=t+1;
    HG(jj).HG_beam = HG_beam_2D;

    if plot_HG==1
         figure()
         surf(X,Y,abs(HG_beam_2D))
         xlabel('X')
         ylabel('Y')
         title(['Hermite-Gaussian mode: HG_', num2str(n+l-t), '_',
             num2str(t), ', z=', num2str(z)])
         set(gca,'visible','off')
         shading interp
    end

    %coefficient for LG mode
    syms R(s)
    R(s) = diff((1-s)^(n)*(1+s)^(l),t);
    B_nlt = sqrt((factorial(n+l-t)*factorial(t))/(2^(n+l)*factorial(n)
        *factorial(l)))*(1/factorial(t))*R(0);

    %Laguerre-Gaussian expressed as a sum of Hermite-Gaussian modes:
    LG_mode = LG_mode + (1i).^(t).*double(B_nlt).*HG_beam_2D;
    %(1i).^(t)
end

%allHG = [HG.HG_beam]; %structure file containing the HG modes used to
```

```
    generate LG mode

%% Plotting the LG modes
figure()
surf(X,Y,abs(LG_mode).^2)
xlabel('X')
ylabel('Y')
zlabel('Intensity distribution')
set(gca,'visible','off')
title(['Result: Laguerre Gaussian mode, z=', num2str(z), ', L=',
   num2str(abs(n-l))])
set(gca,'visible','off')
shading interp
colormap gray;



figure()
surf(X,Y,angle(LG_mode))
xlabel('X')
ylabel('Y')
zlabel('Phase')
set(gca,'visible','off')
colormap gray;
shading interp
colorbar('Ticks',[-3,3],'TickLabels',{'-\pi','\pi'},'Fontsize',30)
title('Laguerre Gaussian mode: phase)')
```

Appendix B

MATLAB code for γ-ray removal

```
%% Script used to remove gamma rays
%Author: Paula Laborda Lalaguna, 28/3/2022
%Input file extension: .asc
%Example of filename: linear1-2
    _acc200_ExT3_T22p5deg_TC330_1P85_2P180_1QWP359_2QWP359_A0_10.40.56
%The number of acquisitions has to be after the first underscore for
    the
%code to work properly

%Enter file name without extension in 'filename_noext'. If empty:
%filename_noext='', the code asks the user to select as many files as
%wanted.
%save=1, if you want to save the file. Saved as wavelength, PL
    intensity. It will be saved in the folder gamma_removed


%%


clear all
close all
```

```
%% User parameters

filename_noext='';
extension = '.asc'
filename = strcat(filename_noext, extension);
save = 1;
threshold = 2;
colors = ['r','b','k','m','g'];


if isempty(filename_noext)
    [filename_array,pathname] = uigetfile('*.txt','Multiselect','ON');
    cd(pathname)
else
    filename_array = filename;
end



if ischar(filename_array)
    num_files = 1;
else
    num_files = length(filename_array);
end



% for ii=1:num_files
%   if ischar(filename_array)
%       filename = filename_array;
%   else
%       filename = filename_array{ii};
%   end
% end
```

```
for ii=1:num_files
     if ischar(filename_array)
          filename = filename_array;
     else
          filename = filename_array{ii};
     end


%% Raw data


%finds the number of acquisitions
[~, basename, ext] = fileparts(filename);
parts = strsplit(basename, '_');
acc = parts(2);
acc = cell2mat(acc);
acc = str2double(acc(4:end));
data = readtable(filename, 'MultipleDelimsAsOne', true,'FileType','
   text');



PL = data.Var2;
PL = PL/acc;
eV = 1239.841984./data.Var1;

% h=figure('Name', ['Raw data', num2str(ii)],'Position
   ',[100,200,600,500]);
% plot(eV, PL, 'Color', colors(1));


%% Gamma ray removal
```

```
for ii=1:length(PL)
    check = PL(ii)
    try
        if (check > (PL(ii-1)+threshold) || check > (PL(ii+1)+
            threshold))
            PL_2(ii) = PL_2(ii-1);
        else
            PL_2(ii) = PL(ii);
        end
    catch
        PL_2(ii) = PL(ii);
    end
end


% figure('Name', ['Gamma rays removed', num2str(ii)],'Position
    ',[100,200,600,500]);
% p=plot(eV, PL_2,'Color',colors(2));

%% Both the raw data and gamma rays removed

figure('Name', 'Comparison','Position',[100,200,600,500]);
plot(eV, PL,eV,PL_2);


gamma = [];
gamma(:,1) = data.Var1;
gamma(:,2) = PL_2';


%save test.txt x y -ascii

if save==1
    if not(isfolder([pathname,'gamma_removed']))
    mkdir gamma_removed
```

```
    end
    try
        cd gamma_removed
    catch
    end
    writematrix(gamma, [basename,'_gammaremoved.txt'],'Delimiter',' ')
end
end
```

Appendix C

Maximum intensity and radius of maximum intensity in Laguerre-Gaussian beams

The intensity of a Laguerre-Gaussian beam with radial mode $p = 0$ is given by

$$I(r) = |E(r)|^2 = \frac{2}{\pi|l|!} A e^{\frac{-2r^2}{w_0^2}} \left(\frac{r\sqrt{2}}{w_0}\right)^{2|l|}, \tag{C.1}$$

where r is beam radius, w_0 beam waist (assuming $z = 0$, at the focal point), l the topological charge and A an amplitude constant.

The derivative dI/dr is given by

$$\begin{aligned}
\frac{dI}{dr} &= \frac{2}{\pi|l|!} A \Big(\frac{-4r}{w_0^2}\Big) e^{\frac{-2r^2}{w_0^2}} \left(\frac{r\sqrt{2}}{w_0}\right)^{2|l|} + \frac{2}{\pi|l|!} A e^{\frac{-2r^2}{w_0^2}} \left(\frac{\sqrt{2}}{w_0}\right)^{2|l|} 2|l| r^{2|l|-1} = \\
&= \frac{2}{\pi|l|!} A e^{\frac{-2r^2}{w_0^2}} \left(\frac{\sqrt{2}}{w_0}\right)^{2|l|} \Big[\frac{-4r}{w_0^2} r^{2|l|} + 2|l| r^{2|l|-1}\Big] \\
&= \frac{2}{\pi|l|!} A e^{\frac{-2r^2}{w_0^2}} \left(\frac{\sqrt{2}}{w_0}\right)^{2|l|} \Big[\frac{-4r^{2|l|+1}}{w_0^2} + 2|l| r^{2|l|-1}\Big],
\end{aligned} \tag{C.2}$$

where we have employed the chain rule.

To find the maximum we can solve $dI/dr = 0$.

$$\frac{dI}{dr} = 0 \rightarrow \frac{-4r^{2|l|+1}}{w_0^2} + 2|l|r^{2|l|-1} = 0$$

$$\frac{4r^{2|l|+1}}{w_0^2} = 2|l|r^{2|l|-1}$$

$$\frac{4r^{2|l|+1}}{w_0^2} = 2|l|r^{2|l|-1}$$

$$\frac{2r^{2|l|+1}}{w_0^2|l|r^{2|l|-1}} = 1$$

$$\frac{2r^2}{w_0^2|l|} = 1.$$

Solving for r we obtain

$$r^2 = \frac{w_0^2}{2}|l|$$

$$\boxed{r_{max} = \frac{\sqrt{2}w_0}{2}\sqrt{|l|}.} \tag{C.3}$$

Equation C.3 shows the radius at which the intensity of an LG beam is maximum. The maximum intensity is calculated by substituting C.3 into equation C.1:

$$I_{max}(r_{max}) = \frac{2}{\pi|l|!}Ae^{\frac{-2r_{max}^2}{w_0^2}}\left(\frac{r_{max}\sqrt{2}}{w_0}\right)^{2|l|}$$

$$\boxed{I_{max}(r_{max}) = \frac{2}{\pi|l|!}Ae^{-|l|}\sqrt{|l|}^{2|l|}.} \tag{C.4}$$

Appendix D

Coupled-oscillator modelling

In this section an expression to fit dichroism data using a classical radiating coupled oscillator system is derived. A classical two-coupled oscillator system with a driving force acting only on one of the oscillators can be described by the differential equations[283, 287]

$$\omega_r^{-2}\ddot{p}(t) + \gamma_r\omega_r^{-1}\dot{p}(t) + p(t) = g_r f(t) - \widetilde{k}q(t), \tag{D.1}$$

$$\omega_d^{-2}\ddot{q}(t) + \gamma_d\omega_d^{-1}\dot{q}(t) + q(t) = -\widetilde{k}p(t). \tag{D.2}$$

In equations D.1 and D.2, the bright oscillator is described by the excitation function $p(t)$, resonance frequency ω_r and damping γ_r. The bright mode is driven by an external force $g_r f(t)$. In our case, $f(t)$ represents the external light and g_r is an amplitude coefficient representing the coupling to the external light. Similarly, the dark mode is described by the excitation function $q(t)$, resonance frequency ω_d and damping γ_d. The dark mode is not excited directly by the external light, and it is only excited *via* near-field coupling to the bright mode. The coupling is represented by the complex coupling $\widetilde{k} = k^{-i(\theta-\phi)}$, where k is the magnitude of the coupling and θ and ϕ the phase of the bright and dark modes, respectively.[316]

The general solutions to equations D.1 and D.2 have the form

$$p(t) = P(\omega)e^{-i\omega t}e^{-i\theta}, \tag{D.3}$$

$$q(t) = Q(\omega)e^{-i\omega t}e^{-i\phi}, \tag{D.4}$$

and the force $f(t)$ is given by $f(t) = F(\omega)e^{-i\omega t}$. Therefore, we obtain

$$\begin{cases} P(\omega)e^{-i\theta}D_r(\omega) = gF(\omega) - \widetilde{k}Q(\omega)e^{-i\phi}, \\ Q(\omega)e^{-i\phi}D_d(\omega) = -\widetilde{k}P(\omega)e^{-i\theta}, \end{cases} \tag{D.5}$$

where $D_r(\omega) = 1 - (\frac{\omega}{\omega_r})^2 - i\gamma_r(\frac{\omega}{\omega_r})$ and $D_d(\omega) = 1 - (\frac{\omega}{\omega_d})^2 - i\gamma_d(\frac{\omega}{\omega_d})$.

Solving by substitution of $Q(\omega)$ into $P(\omega)$ gives and expression for $P(\omega)$.

$$P(\omega) = \frac{F(\omega)gD_d(\omega)}{e^{-i\theta}(D_r(\omega)D_d(\omega) - \widetilde{k}^2)}) \tag{D.6}$$

As the force $F(\omega)$ in our case is due to the electric field $E(\omega)$ and the susceptibility is $\chi(\omega) = P(\omega)/E(\omega)$, the susceptibility becomes

$$\chi(\omega) = \frac{gD_d(\omega)}{e^{-i\theta}(D_r(\omega)D_d(\omega) - \widetilde{k}^2)}. \tag{D.7}$$

From the susceptibility, the refractive index can be derived as

$$n = \sqrt{\chi(\omega) + 1}. \tag{D.8}$$

The reflectivity can be derived from the refractive index *via*

$$R = \left|\frac{n_{air} - n}{n_{air} + n}\right|^2, \tag{D.9}$$

where n_{air} is the refractive index of the surrounding medium (in our case air). The circular dichroism can now be expressed as the difference in reflectivity between LCP

and RCP beams,

$$\mathrm{CD} = 2\Big(\frac{R_{LCP} - R_{RCP}}{R_{LCP} + R_{RCP}}\Big). \tag{D.10}$$

The fitting parameters used to fit the experimental CD in Section 5.4.2 of Chapter 5 are ω_r, ω_d, γ_r, γ_d, k, θ, ϕ and g. To account for the beam chirality in the dichroism, different fitting parameters were used for k and g for LCP ($\sigma = +1$) and RCP ($\sigma = -1$), so the susceptibility becomes

$$\chi_{\sigma=\pm1}(\omega) = \frac{g_{\sigma=\pm1} D_d(\omega)}{e^{-i\theta}(D_r(\omega)D_d(\omega) - \widetilde{k}^2_{\sigma=\pm1})}, \tag{D.11}$$

from which the refractive indices, reflectivity and CD can be derived.